
Test of Lorentz invariance: exploiting the potential of air showers at ultra-high energy

DISSERTATION
zur Erlangung des Grades eines Doktors
der Naturwissenschaften

vorgelegt von
Fabian Dünkel, M.Sc.

Eingereicht bei der Naturwissenschaftlich-Technischen Fakultät
der Universität Siegen

Siegen, März 2024

Betreuer und erster Gutachter:
Prof. Dr. Markus Risse

Zweiter Gutachter:
Prof. Dr. Markus Cristinziani

Tag der mündlichen Prüfung:
09.07.2024

Abstract

In extensive air showers induced by ultra-high-energy (UHE) cosmic rays, secondary particles are produced with energies far above those accessible by other means. These extreme energies can be used to search for new physics beyond the current Standard Model of particle physics. In this work, the effects of isotropic, nonbirefringent Lorentz violation in the photon sector are investigated. In the case of a photon velocity smaller than the maximum attainable velocity of standard Dirac fermions, vacuum Cherenkov radiation becomes possible. For photon velocities greater than the maximum attainable velocity of standard Dirac fermions, photon decay is introduced together with a change in the decay time of neutral pions. Implementing these Lorentz-violating effects in air-shower simulations, a significant reduction of the average atmospheric depth of the shower maximum $\langle X_{\max} \rangle$ is obtained in both cases. Based on measurements of $\langle X_{\max} \rangle$ and its shower-to-shower fluctuations $\sigma(X_{\max})$, a new two-sided bound on Lorentz violation exploiting the high energies of particles in air showers is presented. The impact of Lorentz violation on the number of muons in air showers is also discussed.

Zusammenfassung

In ausgedehnten Luftschauern, die durch ultrahochenergetische kosmische Strahlung ausgelöst werden, werden Sekundärteilchen mit Energien erzeugt, die weit über denen liegen, die auf andere Weise erreichbar sind. Diese extremen Energien können zur Suche nach neuer Physik jenseits des aktuellen Standardmodells der Teilchenphysik genutzt werden. In dieser Arbeit werden die Auswirkungen einer isotropen, nicht doppelbrechenden Verletzung der Lorentzinvarianz im Photonensektor untersucht. Im Falle einer Photonengeschwindigkeit, die kleiner ist als die maximal erreichbare Geschwindigkeit von Standard-Dirac-Fermionen, wird Vakuum-Cherenkov-Strahlung möglich. Bei Photonengeschwindigkeiten, die größer sind als die maximal erreichbare Geschwindigkeit von Standard-Dirac-Fermionen, wird Photonenzerfall zusammen mit einer Änderung der Zerfallszeit neutraler Pionen eingeführt. Durch die Implementierung dieser Lorentzinvarianzverletzenden Effekte in Luftschauersimulationen wird in beiden Fällen eine signifikante Reduzierung der durchschnittlichen atmosphärischen Tiefe des Schauermaximums $\langle X_{\max} \rangle$ ausgelöst. Mit Hilfe von Messungen von $\langle X_{\max} \rangle$ und den Schwankungen $\sigma(X_{\max})$ zwischen Luftschauern wird eine neue zweiseitige Grenze auf die Verletzung der Lorentzinvarianz aufgestellt, welche die hohen Energien von Teilchen in Luftschauern ausnutzt. Der Einfluss der Verletzung der Lorentzinvarianz auf die Anzahl der Myonen in Luftschauern wird ebenfalls diskutiert.

Contents

| | | |
|----------|---|-----------|
| 1 | Cosmic Rays | 1 |
| 1.1 | History of astroparticle physics | 1 |
| 1.2 | The cosmic ray energy spectrum | 5 |
| 1.3 | Cosmic-ray sources and acceleration | 9 |
| 1.4 | Cosmic-ray composition | 13 |
| 2 | Ultra-high energy air showers | 17 |
| 2.1 | Air shower development | 17 |
| 2.1.1 | Photon-induced showers and the Heitler model | 18 |
| 2.1.2 | Development of hadron induced air showers | 19 |
| 2.2 | Air shower detection | 24 |
| 3 | The Pierre Auger Observatory | 27 |
| 3.1 | The fluorescence detector | 28 |
| 3.1.1 | FD event reconstruction | 30 |
| 3.2 | The Surface Detector | 33 |
| 3.2.1 | SD event reconstruction | 34 |
| 3.3 | Additional components of the Observatory | 38 |
| 4 | Lorentz Violation | 41 |
| 4.1 | The Standard Model of particle physics | 41 |
| 4.2 | Introduction to Lorentz Violation | 43 |
| 4.3 | Lorentz Violation in the Standard Model Extension | 45 |
| 4.3.1 | Lorentz Violation for $\kappa < 0$ | 47 |
| 4.3.2 | Lorentz Violation for $\kappa > 0$ | 49 |
| 4.4 | Bounds on LV from cosmic ray observations | 51 |
| 4.5 | Changes in extensive air showers due to LV | 52 |
| 5 | Used software, simulations and data | 57 |
| 5.1 | CONEX | 57 |
| 5.1.1 | Modifications for $\kappa < 0$ | 58 |
| 5.1.2 | Modifications for $\kappa > 0$ | 59 |
| 5.2 | Auger data samples | 61 |
| 5.3 | Preparation of air shower data and simulations | 61 |
| 5.3.1 | Two-dimensional contours of Auger Data | 63 |
| 5.3.2 | Combination of Simulations | 63 |
| 6 | Analysis of simulated air showers | 69 |
| 6.1 | General Method | 69 |

| | | |
|----------|---|------------|
| 6.2 | Results for $\kappa < 0$ | 70 |
| 6.2.1 | Changes in X_{\max} | 70 |
| 6.2.2 | New limit on $\kappa < 0$ using X_{\max} measurements | 75 |
| 6.2.3 | Changes in N_{μ} | 80 |
| 6.2.4 | Changes in the correlation between X_{\max} and N_{μ} | 83 |
| 6.2.5 | Differences between hadronic interaction models | 88 |
| 6.3 | Results for $\kappa > 0$ | 91 |
| 6.3.1 | Changes in X_{\max} | 92 |
| 6.3.2 | New limit on $\kappa > 0$ using X_{\max} measurements | 96 |
| 6.3.3 | Changes in N_{μ} | 101 |
| 6.3.4 | Changes in the correlation between X_{\max} and N_{μ} | 103 |
| 6.3.5 | Differences between hadronic interaction models | 105 |
| 6.4 | Outlook | 107 |
| 7 | Conclusion | 109 |
| A | Code | 111 |
| B | Additional Figures | 123 |
| C | Additional Tables | 137 |
| | Bibliography | 139 |

Chapter 1

Cosmic Rays

Astroparticle physics is a field of science concerned with the study of elementary particles of extraterrestrial origin. It lies at the intersection of particle physics, astronomy and cosmology, emerging after the discovery of cosmic rays. A short history of the discovery of cosmic rays is summarized in Sec. 1.1. The discovery of cosmic rays (CRs) took place more than a century ago with the detection of particles from outer space arriving at the Earth. The majority of cosmic rays consists of ionized atomic nuclei, although other particles such as electrons, positrons, gamma rays, neutrinos and antiprotons also arrive. In this chapter, the nuclear component of cosmic rays is discussed, with a focus on different features of cosmic rays. The energy spectrum of cosmic rays is described in Sec. 1.2. Prospective cosmic ray sources and acceleration mechanisms, as well as the anisotropies in their arrival directions are summarized in Sec. 1.3. In Sec. 1.4, our current knowledge about the cosmic ray composition up to the highest energies is covered.

1.1 History of astroparticle physics

In 1896, spontaneous radioactivity was discovered by Antoine Henri Becquerel [Bec96], followed by the discovery of the radioactive decays of polonium and radium by Marie and Pierre Curie [CCB98] in 1898. Charged electroscopes in the presence of radioactive material discharged, which led to the conclusion that charged particles were emitted in the decay.

The insulation of electroscopes was improved by Julius Elster and Hans Geitel [EG00] and Charles Thomson Rees Wilson [Wil01]. Since the improved electroscopes still discharged, it was concluded that this discharge was due to ionizing radiation from outside the instrument. A common assumption for the origin of this radiation were radioactive decays in the crust of the Earth. One of the first suggestions of an extra-terrestrial origin of this radiation was made by Wilson [Wil01]. His measurements of ionisation in tunnels however showed no reduction in radiation, thus not supporting an extra-terrestrial origin.

In 1909, Theodor Wulf measured the rate of ionisation at the base and top of the Eiffel tower [Wul09] in order to determine the variation of radiation

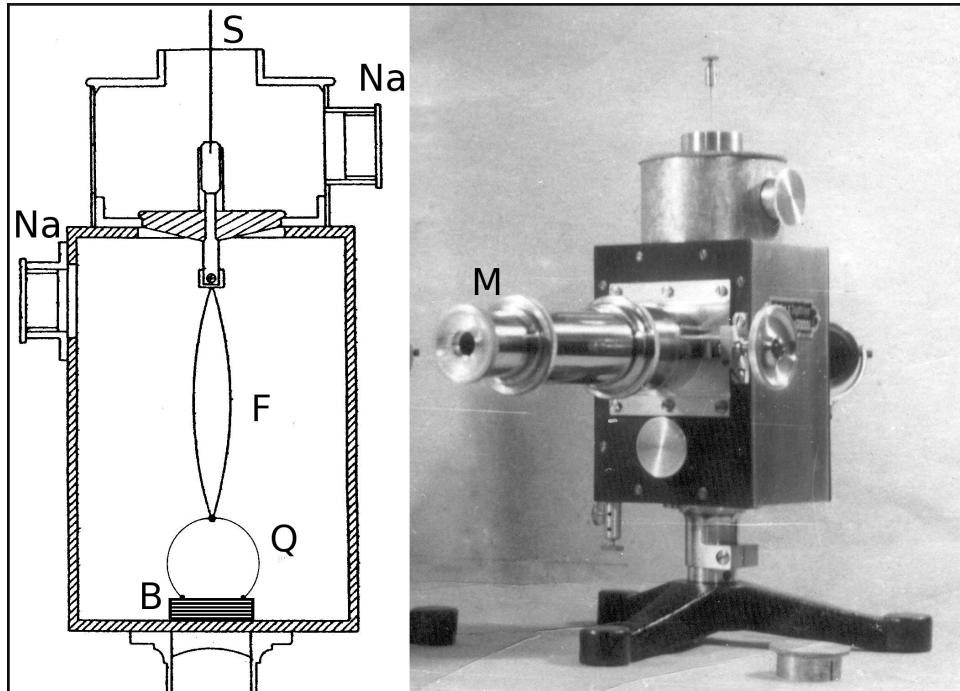


FIGURE 1.1: Shown on the left is the cross section of the electroscopes developed and used by Wulf, on the right a picture of the same. The electric charge of the metal filaments (F) held by a quartz string (Q) can be determined from the spread of the filament through the microscope (M). The quartz strings are connected to an amber insulator (B) and the chambers can be connected to a sodium-drying device by two openings (Na). Image taken from [FS12].

with altitude and gain insights about its origin. While the ionisation rate decreased, the decrease was lower than expected for a purely terrestrial origin. A schematic illustration as well as a picture of the type of electroscopes used by Wulf is displayed in Fig. 1.1.

In the same year, Karl Bergwitz measured a decrease in ionisation to 24 % at an altitude of 1300 m, which was consistent with radiation produced in the Earth's crust [Ber10]. His results were questioned due to damage to the electroscopes during the flight [Goc11].

The first discovery of cosmic rays is attributed to Victor Hess, who in 1912 noticed that, after an initial decrease in ionisation rates, an electroscopes loses its charge faster the higher up in the atmosphere it was [Hes12]. Hess attributed his findings to highly penetrating radiation entering the atmosphere from above. His measurements were confirmed later by Werner Kolhörster up to a height of 9.2 km [Kol13; Kol14] and by Robert Andrews Millikan, who measured up to increasing altitudes of up to 15 km using specially designed instruments attached to sounding balloons [MB26]. The results of ionisation measurements by both Hess and Kolhörster are shown in Fig. 1.2. Millikan also first used the term "cosmic rays", as he thought gamma rays to be the source of the measured radiation. A short time later, Jacob Clay measured the

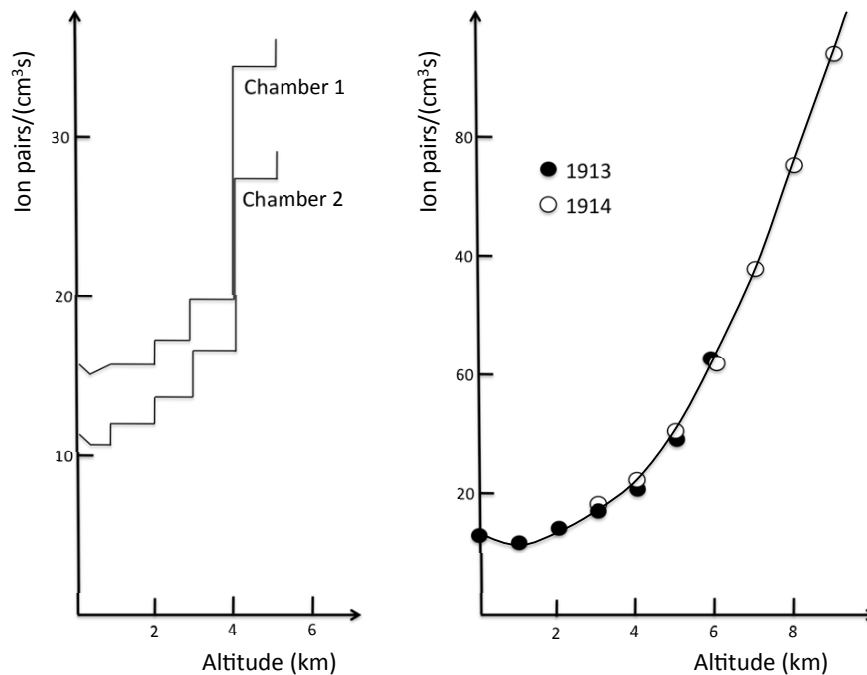


FIGURE 1.2: Measurements of the atmospheric ionisation in different altitudes. The results of the balloon flights by Viktor Hess [Hes12] are shown on the left. On the right, Werner Kolhörster's results are shown, extending the measurements to altitudes up to 9.2 km and confirming the results of Hess [Kol13; Kol14]. Image taken from [CD11].

dependence of cosmic rays on the geomagnetic latitude [Cla27; Cla28] and Walther Bothe and Kolhörster performed coincidence counting of ionizing radiation in the atmosphere [BK29]. Their results pointed towards massive, charged particles as the source of the ionizing radiation instead of gamma rays.

In 1938, observations of coincident signals in particle detectors were done by Pierre Auger at sea level, as well as in an altitude of 3500 m at the Jungfrau-joch in Switzerland [Aug+39]. Those observations showed a high number of coincident events at distances of up to 300 m, which can be seen in Fig. 1.3. He came to the conclusion that those coincident events had to originate from the same source. He proposed a very-high-energy cosmic particle, which induced an avalanche of secondary particles, called an air-shower. From his measurements he also concluded an energy of 10^{15} eV for the primary particle, orders of magnitude above energies reached by terrestrial particle accelerators of the time.

The extremely high energies of cosmic rays have been confirmed by subsequent experiments. The first particle with an energy of 100 EeV was observed in 1962 by John Linsley at the Volcano Ranch experiment in New

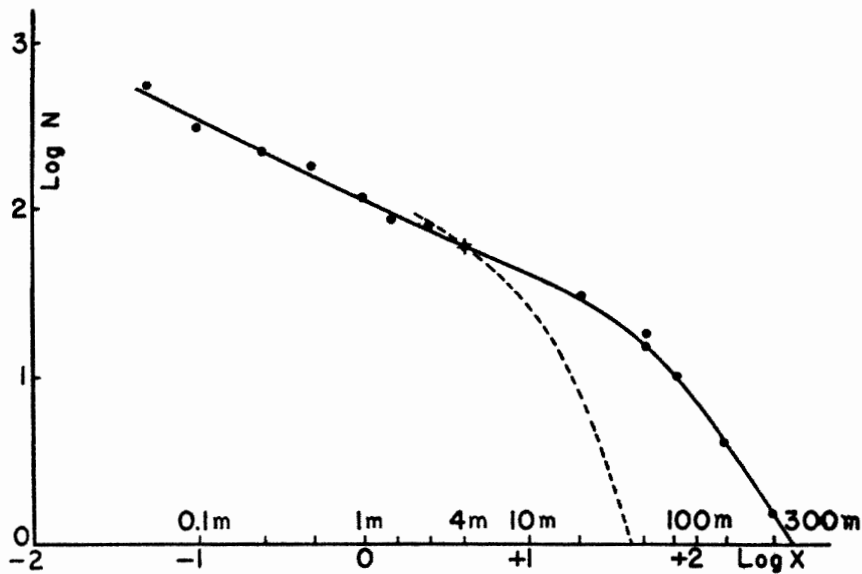


FIGURE 1.3: Measurements of the number of coincident events in two detectors in different distances [Aug+39]. The x-axis corresponds to the distance between the detectors in meters, the y-axis to the number of measured coincident events. The solid line shows the interpolation between measurements (dots), while the dashed line corresponds to the prediction of coincident events made by Hans Euler. Auger explained the increased rate at high distances through the production of highly penetrating "mesotrons" (mesons) in the shower.

Mexico [Lin63]. The highest energy cosmic ray to date, the "Oh-My-God-Particle", has been observed by the Fly's Eye air-shower detector in Utah with a primary particle energy of 320 EeV [Bir+95]. The detection of a particle at these energies was puzzling, as a strong flux suppression due to interactions of high-energy cosmic rays with the cosmic microwave background (CMB) was expected [Gre60; ZK66]. One solution for this apparent tension is the emission of the cosmic ray by a relatively close source.

Direct observations of cosmic rays were made significantly more effective with the first satellite-based experiments, beginning in 1959 with experiments measuring charged radiation aboard the Russian Luna missions as well as the American Explorer satellites. Those types of experiments now could observe cosmic rays before any interaction in the Earth's atmosphere, enabling precise measurements of the energy and the particle type of the cosmic rays. The first measurements of cosmic X-rays and gamma rays by satellite experiments were done in the 1960s and 1970s by, e.g, Explorer XI [KC62] and the Uhuru satellite [Gia+71]. This made it possible to determine the directions of cosmic ray sources, such as the Galactic Center, the Crab Nebula and the binary systems Vela X-1 and Cygnus X-3 [Gru20].

With the reconstruction of the arrival directions of the cosmic rays, it became possible to analyze the processes inside astronomical objects through the lens of the cosmic rays emitted by them, giving rise to the field of particle astrophysics. As the production of cosmic rays at high energies requires extreme conditions, important information about the processes inside those objects can be gained this way.

1.2 The cosmic ray energy spectrum

The energy spectrum of cosmic rays (CRs) covers several orders of magnitude, both in energy and in flux. The energy range extends from below 1 GeV up to the highest energies around 100 EeV, spanning more than 11 orders of magnitude. The particle flux can roughly be described by a power law $\frac{d\Phi}{dE} \sim E^\alpha$ with a spectral index $\alpha \approx -3$ [Swo01]. As a consequence, the flux spans a range of more than 30 orders of magnitude. The dependency of CR flux on energy can be seen in Fig. 1.4.

To observe CRs of different energies, different techniques are used. At lower CR energies below the TeV range, the particle flux is very large, with multiple particles per square meter and second. At energies below the GeV range, the CR flux is suppressed by a magnetic field generated by solar activity, which deflects charged particles entering the solar system from outside. However, cosmic rays in the form of electrons, protons and a minor fraction of heavier nuclei are produced by the sun itself in this energy range [TT04], contributing to the overall spectrum. As solar activity is time dependent, the low-energy CR flux fluctuates. The particle flux decreases to one particle per square meter and year in the PeV range. Below this energy, direct detection of CRs using experiments based on balloons and satellites can be used. These experiments use a combination of multiple detectors, such as calorimeters, magnetic spectrometers, Cherenkov detectors and transition radiation detectors. This makes it possible to precisely measure properties of the particle, e.g. energy, mass or charge. Examples for some recent space-based experiments are PAMELA [Pic+07] and the AMS experiment [Bat98] on the International Space Station (ISS), some balloon-based experiments are BESS-Polar [Yos+04], CREAM [Ahn+07] and TRACER [Mül+08].

At energies above the PeV range however, the flux becomes so low that direct detection becomes impractical due to rapidly increasing costs for detectors large enough to compensate for the lower particle flux. Thus primary CRs with energies above several PeV have to be measured through indirect observation methods using ground-based detectors. These detectors exploit the interaction of CRs in the atmosphere, which leads to the generation of atmospheric air-showers. These air-showers consist of a large number of secondary particles, of which a fraction may reach the ground. From the measurement of the secondary particles arriving at ground level, the primary particle can be reconstructed. The depth of the shower in the atmosphere depends on the primary particle energy, hence detectors at high elevations

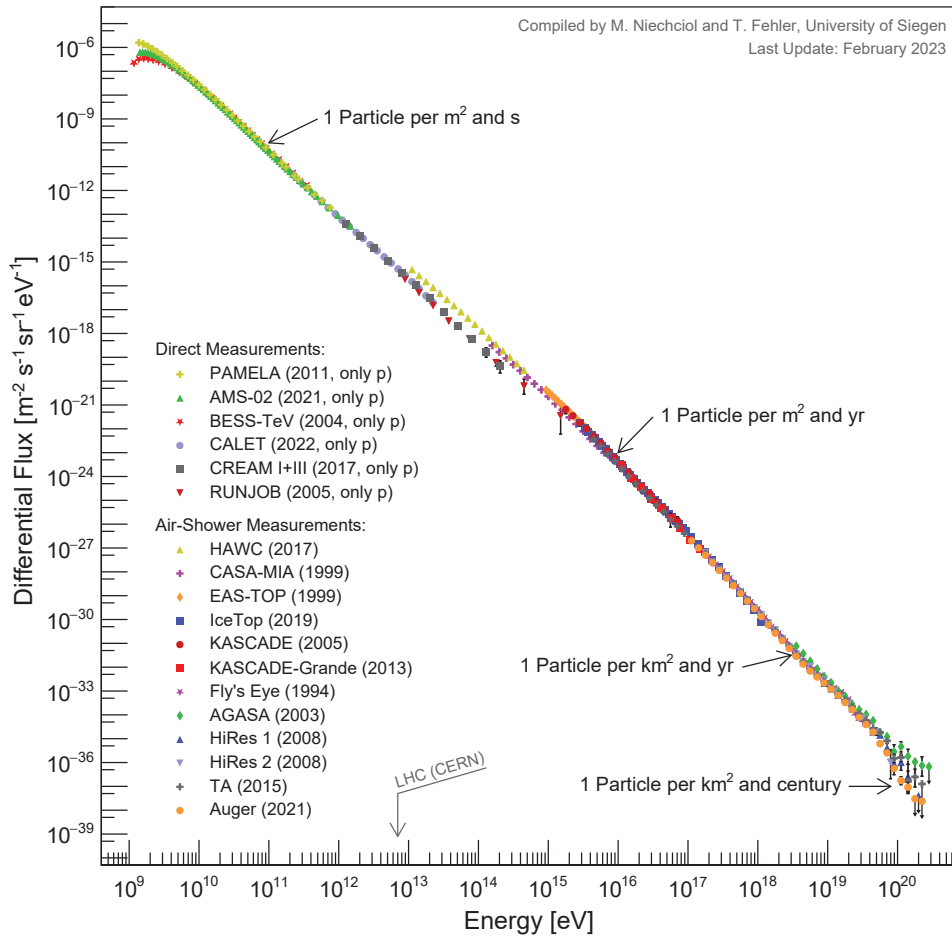


FIGURE 1.4: The cosmic-ray energy spectrum, aggregated from both direct measurements and indirect measurements using air-showers in the Earth's atmosphere [Nie]. Covered are 11 orders of magnitude in energy and 32 orders of magnitude in CR flux. Marked are significant milestones of particle fluxes as well as the energy reached by protons accelerated by the LHC.

are used to study CRs in the PeV energy range, while higher energy CRs can also be studied using detectors at lower elevations. Examples of such detectors sampling shower particles at ground level are KASCADE [Ant+03], KASCADE-Grande [Ape+10], Ice-Top [Abb+13] as well as the surface detectors of the Pierre Auger Observatory [Aab+15b] and the Telescope Array (TA) [Abu+12].

Complementary to the ground-level observations, fluorescence light emitted by nitrogen atoms in the atmosphere, which were excited by secondary particles, is measured by, e.g., the fluorescence detectors of the Auger Observatory and TA, as well as the historic Fly's Eye experiment [Abu+00]. Another method to analyze air-shower development is through the measurement of radio signals generated through both the Askaryan effect and geomagnetic charge separation [Hue13], used by both Tunka-Rex [Bez+15] and

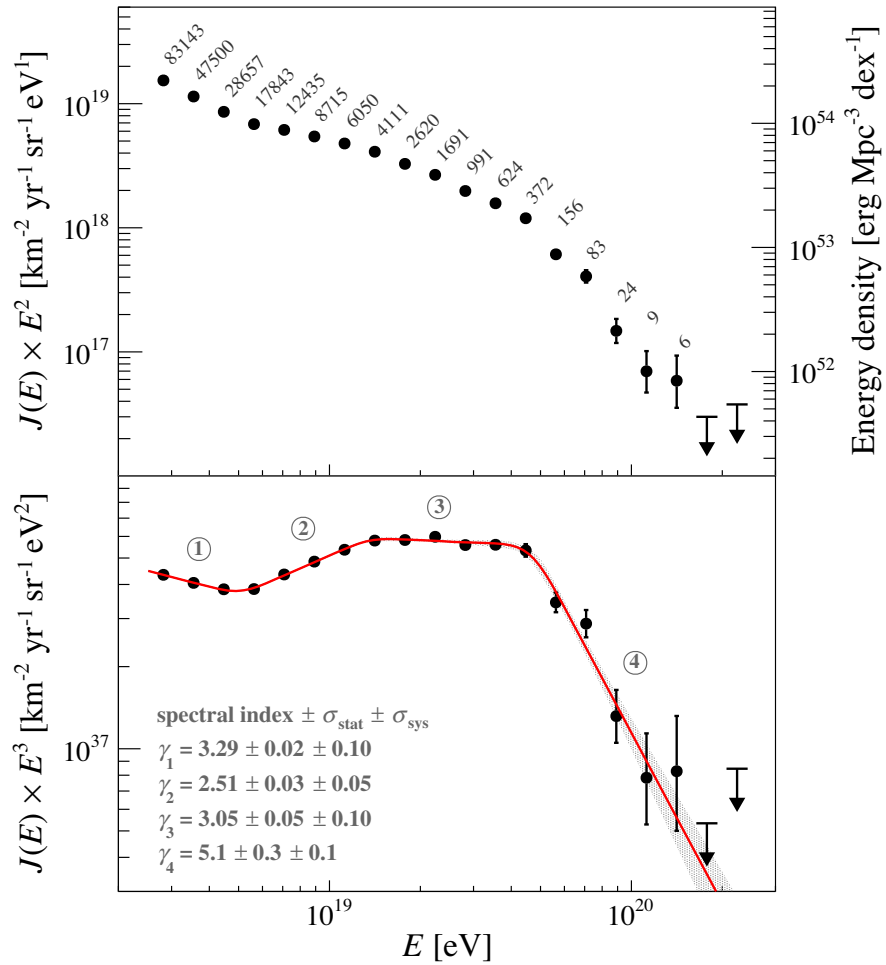


FIGURE 1.5: The CR energy spectrum as observed by the Pierre Auger Observatory [Aab+20c]. In the top plot, the CR energy spectrum is scaled by E^2 , as well as the number of events observed in each bin is noted. In the bottom plot, the CR energy spectrum is scaled by E^3 and fitted with a sequence of four power laws, showing how the spectral index changes with the different energy ranges.

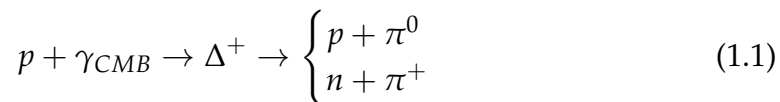
AERA [Kel11]. The detection of air Cherenkov radiation is used for gamma-ray astronomy by experiments like H.E.S.S. [OH23], MAGIC [Fer06] or the future Cherenkov Telescope Array (CTA) [Act+11]. At the highest energies above the EeV range, the CR flux drops to less than one particle per square kilometer and year. To compensate for this, ground based detector arrays like the Pierre Auger Observatory or TA cover hundreds and even thousands of square kilometers to gather enough events to make statistical analysis possible [MR18].

While the energy spectrum roughly follows a power law, on closer inspection several features become noticeable. Below the energy of 4 PeV, the spectrum has a slope of $\alpha \simeq -2.7$. At 4 PeV, the spectrum steepens to $\alpha \simeq -3$, a feature which is commonly called "knee". At an energy of 20 PeV, a minor

hardening of the spectrum, called the "low energy ankle", appears, where the spectral index α changes from $\alpha < -3$ to $\alpha > -3$. The spectrum steepens again at the "second knee" at 0.1 EeV, where the spectral index increases to $\alpha \simeq -3.3$. The spectral index stays constant up to an energy of 5 EeV, where the spectrum hardens to a decreased spectral index of $\alpha \simeq -2.6$, which is called the "ankle". At energies above 40 EeV, the flux is further suppressed, with a spectral index of $\alpha < -4$. At the highest energies, an exponential decrease or even a final cutoff at 200 EeV may exist, however the statistics are too small to gain conclusive results.

Additional features in the ultra-high-energy (UHE) regime can be seen in recent results of the Pierre Auger Observatory [Aab+20c], which are displayed in Fig 1.5. At 13 EeV, the spectrum softens from $\alpha \simeq -2.5$ to $\alpha \simeq -3.1$ with a further softening to $\alpha \simeq -5.1$ at energies above 50 EeV.

The origins of those features are related to the mechanisms of CR production, propagation and interactions in the interstellar medium, as well as the types of CR sources, all of which are still the subject of current research. The shape of the spectrum is thus used as an indicator for various open questions in both astrophysics and particle physics. Both the first and second knee can be explained by a rigidity-dependent steepening of the spectrum. At the first knee at an energy of 4 PeV, the proton spectrum steepens, with the suppression of heavier elements occurring at energies of $4Z$ PeV, scaling with the atomic number Z . The second knee at 0.1 EeV then coincides with the steepening of the Fe spectrum at 4×26 PeV. Such rigidity dependence can be obtained from both galactic sources [Pet61] or from CRs escaping the galaxy above a certain energy threshold due to diffusion and drift effects [Ptu+93]. The ankle can be explained by a transition from galactic to extragalactic CRs happening between the second knee and the ankle. Above the ankle, CRs show no correlation with the galactic plane or the galactic center, indicating an extragalactic origin [MR18]. The Greisen-Zatsepin-Kuzmin (GZK) effect, named after the predictions of Greisen [Gre60], Zatsepin and Kuzmin [ZK66] in 1966, can explain the strong flux suppression at 40 EeV. Proposed shortly after the discovery of the cosmic microwave background (CMB), the GZK effect posits an interaction of primary UHECR protons with photons from the CMB:



The resonance energy of this interaction is 1232 MeV, resulting from the mass of the delta baryon. Together with the temperature of the CMB of $T_{CMB} = 2.72548 \pm 0.00057$ K [Fix09], this results in a GZK cutoff at energies of 50 – 60 EeV for protons, with respectively higher cutoff energies for heavier nuclei. While the GZK effect explains the steepening of the spectrum, no independent evidence for this process has been found so far. Another possible cause for the flux suppression is a limitation in the acceleration mechanisms,

resulting in similar spectral features [MR18]. So far no unambiguous answer to the origin of the flux suppression at the highest energies has been found.

1.3 Cosmic-ray sources and acceleration

Different acceleration mechanisms and sources are proposed for CRs at different energies of the CR spectrum. While the particle source and the acceleration mechanism are in principle distinct, it is generally assumed that CRs are accelerated in or near the source. At the lower end of the spectrum, the Sun is a source of CRs. The generation of CRs in the Sun is due to acceleration of particles in time-dependent magnetic fields. The sites of those magnetic fields can be seen as sunspots and are suitable to accelerate CRs to energies up to the GeV range [Gru20]. The identification of the sources of extra-solar CRs is more complicated, since charged particles are deflected by galactic magnetic fields, making it impossible to determine the origin of a CR from the arrival direction at Earth. However, the spectral shape implies that CR acceleration is a non-thermal process and requires some kind of active acceleration mechanism in order to maintain the power law dependency over multiple orders of magnitude.

At energies below the ankle, CRs are probably of mainly galactic origin, with supernova remnants (SNR) within the galaxy being a promising candidate acceleration mechanism. Here CRs are accelerated by the shock fronts of SNRs, which are the ejected envelopes of supernovae, expanding over timescales of 10 000 years. Typically, the outer front is decelerated by interactions with the interstellar medium, leading to a velocity difference between the outer and inner shock fronts. The CR particle may repeatedly get scattered back and forth between the two shock fronts, gaining energy on every reflection with the inner front and losing energy on every reflection with the outer front. Overall, the energy gained is greater than the lost energy, leading to a relative energy gain $\frac{\Delta E}{E}$ proportional to the ratio between the velocity difference between the shock fronts Δv and its velocity v [Gru20]:

$$\frac{\Delta E}{E} \approx 2 \frac{\Delta v}{v} \quad (1.2)$$

This mechanism is called first-order Fermi acceleration, first being proposed by Enrico Fermi [Fer49]. It can account for the acceleration of CRs to energies of up to the EeV range and provides a spectrum which matches the observations by CR measurements [Bel78].

A possible acceleration site using a similar mechanism are magnetized molecular clouds. These clouds include randomly moving magnetic mirrors, which can repeatedly reflect charged particles, granting them increasing energy. This mechanism is similar to the reflection at shock fronts of SNRs, and it is named second-order Fermi acceleration [Fer49]. However, due to the lower velocities of the magnetic clouds fronts this is an inefficient process. Its energy gain per interaction is lower than first order Fermi acceleration with

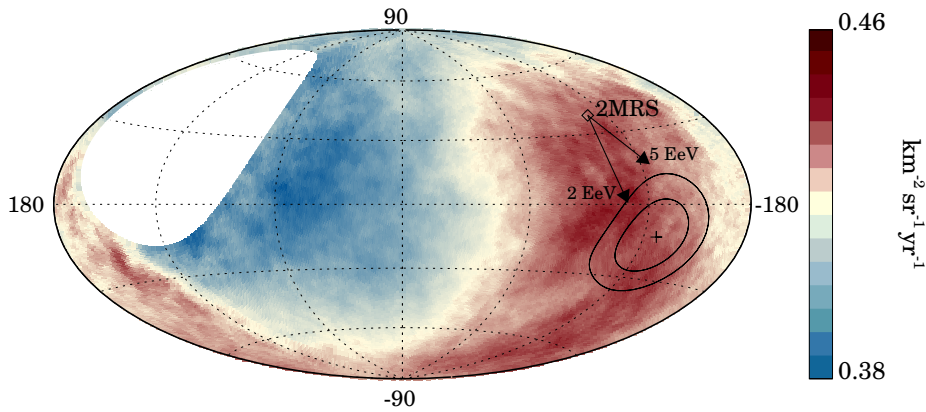


FIGURE 1.6: Flux of CRs with energies above 8 EeV by arrival direction in galactic coordinates as measured by the Pierre Auger Observatory [Aab+18a]. The direction of the reconstructed dipole is indicated by the cross, the surrounding ellipses denote the 68% CL and 95% CL regions. The direction of the flux weighted dipole of galaxies in the 2MRS catalog [Huc+12] is denoted by the diamond. The two arrows show the modifications to the dipole moment due to the Galactic magnetic field as modeled in [Ade+16] for particles with E/Z of 5 EeV and 2 EeV respectively. Image taken from [MR18].

a relative energy gain $\frac{\Delta E}{E}$ proportional to the square of the ratio between the cloud velocity u and its velocity v [Gru20]:

$$\frac{\Delta E}{E} \approx 2 \frac{u^2}{v^2} \quad (1.3)$$

There has been first evidence for CR acceleration in SNRs through the discovery of photons with energies exceeding 100 TeV from the direction of the Crab Nebula [Ame+19], which is the remnant of SN1054, a supernova observed in 1054 by Chinese and Japanese astronomers. Interactions of primary cosmic rays with matter surrounding the SNR are expected to produce photons of the observed energies.

At energies above the ankle, CRs are generally assumed to be of extragalactic origin. This hypothesis is additionally supported by the observation of a dipole structure in the UHECR arrival directions by the Pierre Auger Observatory [Aab+17a; Rou21]. For energies above 8 EeV, a dipolar amplitude of 6.5% has been detected, pointing 125° away from the Galactic Center. While a minor dipolar anisotropy can be explained by the movement of the observer in relation to the frame of the CRs, this would lead to a dipolar anisotropy of only 0.6% [KS06], one order of magnitude smaller than observed. The propagation of CRs in extra-galactic turbulent magnetic fields leading to the observed anisotropy is another currently proposed explanation. The direction of the anisotropy is consistent with the distribution of nearby galaxies in the 2MRS catalog [Huc+12], when the deflection

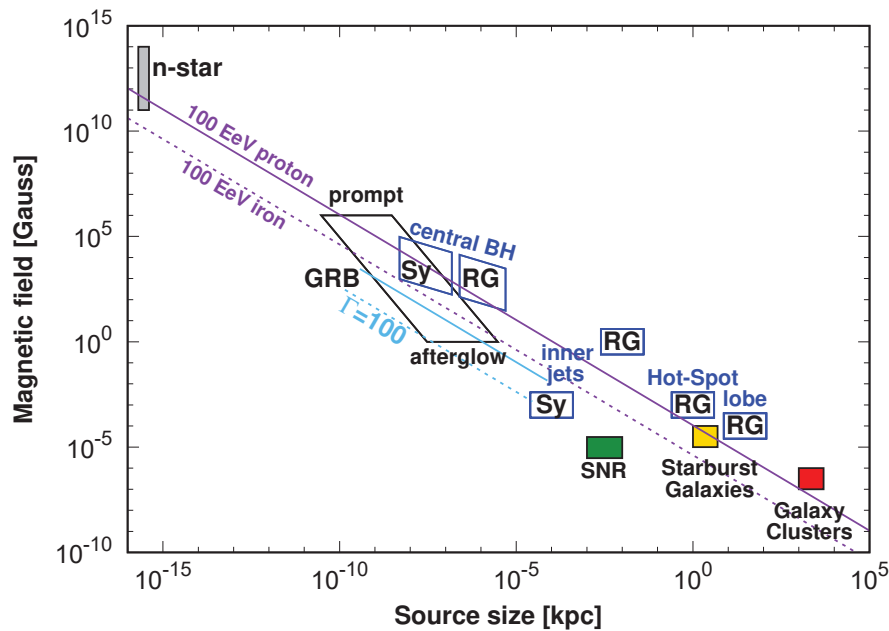


FIGURE 1.7: The Hillas plot shows size and magnetic field strength of possible UHECR source candidates [MR18]. The solid and dashed purple lines indicate the necessary source parameters needed to accelerate protons and iron respectively to energies above 100 EeV. For sources with relativistic jets, e.g. GRBs, the shifted lines for the case of a boost of $\Gamma = 100$ are shown in cyan, indicating the relaxed parameters in size and magnetic field. Shown sources are Neutron stars (n-star), GRBs, AGNs involving both radio-quiet Seyfert galaxies (Sy) and radio galaxies (RG) with acceleration both in the inner black hole (BH) or the inner jets, and the hot-spots and radio lobes of Fanaroff-Riley Class II galaxies. The parameters of SNRs as well as the acceleration of CRs in large scale shocks in starburst galaxies and galaxy clusters are also displayed.

of charged particles in the galactic magnetic field is taken into account. The measured dipolar anisotropy as well as the expected arrival directions of CRs produced by the 2MRS sources are shown in Fig. 1.6.

This does however not settle the question of the mechanism accelerating CRs to the highest energies. In fact, not a single class of sources may be responsible for the UHECR flux, but a combination of different source types. To constrain possible sources, a simple relation between the maximum achievable energy E_{\max} , its size L and its average magnetic field strength B can be used:

$$E_{\max} = \Gamma e Z B L \quad (1.4)$$

For further acceleration, the Larmor radius of the particle has to be smaller

than the acceleration, thus a stronger magnetic field as well as a larger acceleration region both lead to higher maximum energies. The relation also takes a boost Γ in relation to the observer into account, which is the case if the acceleration takes place in a relativistic jet. Eq. 1.4 is also known as the Hillas criterion with the associated Hillas plot classifying different sources by magnetic field strength and size [Hil84]. In Fig. 1.7, such a Hillas plot with currently assumed possible UHECR source candidates is shown. Different source candidates with the associated source sizes as well as magnetic field strengths are plotted. For an acceleration of protons and iron primaries to energies above 100 EeV, sources have to fulfill the Hillas criterion from Eq. 1.4 by reaching the area above the purple continuous and dotted lines respectively. For boosted sources, such as GRBs and AGN jets, this criterion is relaxed by the boost Γ , which is indicated by the cyan parallel lines. For lower energies, those lines would be appropriately shifted down according to the difference in CR energy.

One possible source of CRs are active galactic nuclei (AGN), which are found at the center of active galaxies. These typically are supermassive black holes surrounded by an accretion disk. These black holes can generate magnetic fields with strengths of several hundred Gauss while the accretion disks span up to 10^{-5} pc. In addition to acceleration in the inner region, CRs should also be able to be accelerated in the giant radio lobes of AGNs. With these parameters, AGN should be able to accelerate CRs to energies above 100 EeV. However, only the closest of those sources are expected to contribute to the highest energies, as energy losses from synchrotron radiation and GZK suppression should restrict the signal from distant sources. This close horizon leads to only a small number of radio galaxies as possible source candidates which should result in a measurable excess of UHECRs from their directions [Mar01].

Another proposed source of UHECRs are the mergers of binary neutron star (BNS) systems. During the merging process, turbulent magnetic fields of extreme magnitude can be formed, which are predicted to be able to accelerate CRs to energies of multiple EeV [Kim19]. Mergers of different binary systems, such as binary black holes or of a neutron star and a normal star, are also speculated to produce high-energy CRs in a similar fashion. However, the acceleration in those systems is less efficient than in BNS systems. Due to the transitory nature of these events, experimental confirmation of these acceleration mechanisms is difficult.

Gamma-ray bursts (GRBs) are amongst the most-energetic astrophysical events observed. Most GRBs seem to be released by hypernovae, where an extremely massive star collapses into a black hole. Another subgroup of GRBs seems to originate from the mergers of BNS systems. For all GRBs, the energies of the producing event are massive, and CRs could be accelerated in the resulting ultra-relativistic winds to energies reaching 100 EeV. Thus GRBs are another possible candidate for UHECR acceleration [Wax95]. However, the mechanisms producing UHECRs in GRBs would also produce neutrinos, which have so far not been able to be measured [Abb+22]. While

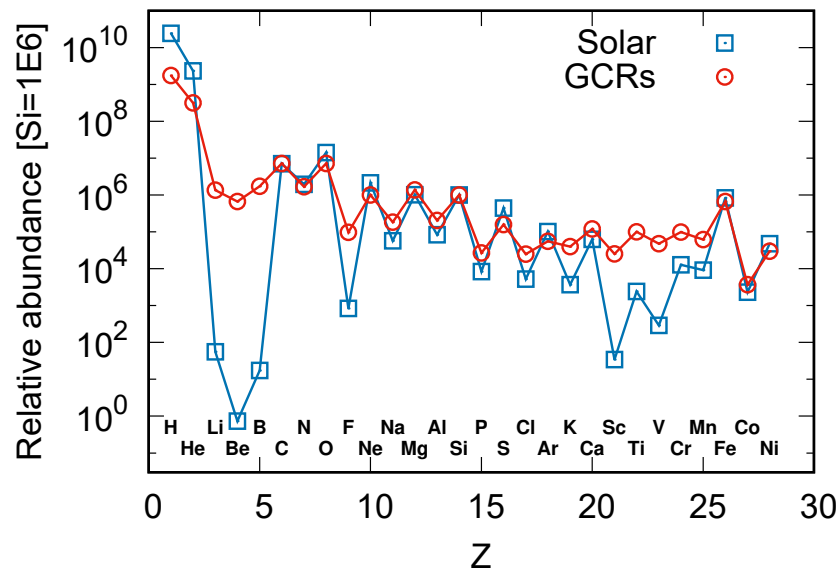


FIGURE 1.8: The relative abundances of elements up to nickel (Ni) in the solar system [Lod03] and from galactic CRs at low energies [Lav+13]. The relative abundances are normalized to 10^6 for silicon (Si, $Z = 14$). Image taken from [MR18].

this does not exclude GRBs as a source, it does restrict production in GRBs to only a fraction of the total flux.

1.4 Cosmic-ray composition

The composition of CRs at the lower end of the energy spectrum at around 100 GeV has been thoroughly examined through direct measurements by both balloon and satellite experiments. CRs arriving at Earth are, with a fraction of $\approx 99\%$, overwhelmingly hadronic, the remaining $\approx 1\%$ of flux are mostly electrons contributed by the solar wind. An extremely low flux of antiparticles such as antiprotons ($\approx 0.01\%$) and positrons ($\approx 0.1\%$) has also been found, which is consistent with the expectation of generation of antiparticles in collisions of CRs with matter in the interstellar medium. Here, we focus primarily on the hadronic CRs.

In Fig. 1.8, the measured relative abundances of elements up to a atomic number of $Z = 28$ in both the solar system as well as in low energy galactic CRs are displayed. Overall, the composition of the solar system has many similar features to that of CRs. The most abundant elements are hydrogen (i.e. protons, H) and helium (He) with respective relative abundances of $\approx 85\%$ and $\approx 12\%$ [Gru20]. Heavier elements with $Z \geq 3$ account for the remaining 3% of hadronic CRs. Generally, elements with an even atomic number are more abundant than their uneven neighbors, which is explained by the higher stability of nuclear configurations with even proton and neutron

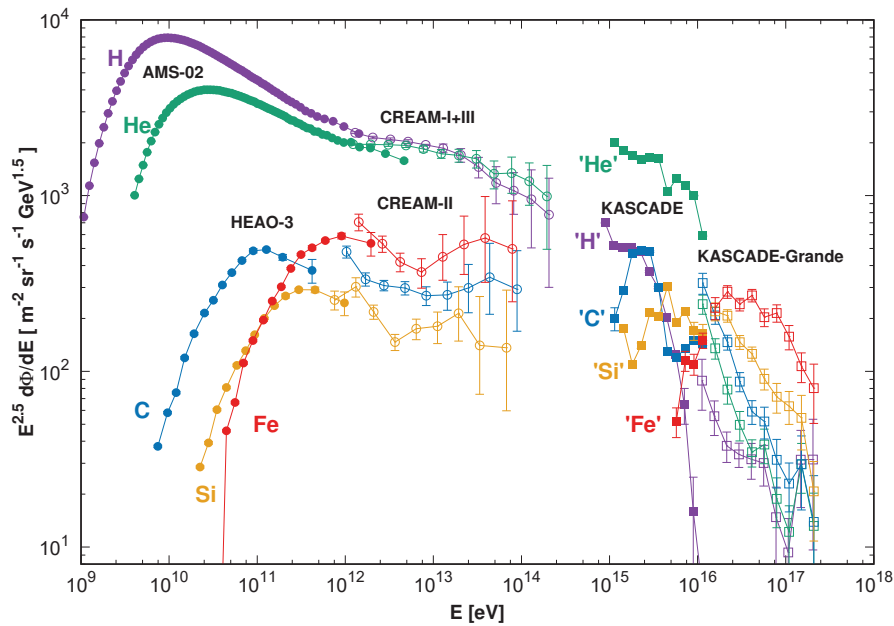


FIGURE 1.9: Cosmic ray spectra of different elements [MR18] in the energy range between 1 GeV and 0.2 EeV. Below the knee, the spectrum is measured by the satellite experiments AMS-02 [Agu+15b; Agu+15a] and HEAO-3 [Eng+90] and the balloon flights CREAM-I, CREAM-II and CREAM-III [Yoo+17; Ahn+09]. For energies above the knee, results from the Air-shower experiments KASCADE [Ape+09] as well as KASCADE-Grande [Ape+13] are shown, where the elements are taken as representative of the flux of their respective mass ranges due to the indirect detection method.

numbers as well as the prevalence of helium burning processes in the production of heavier elements through stellar nucleosynthesis [Bur+57]. Iron is also relatively abundant, since it is the heaviest element which can be produced through exothermal processes in stellar evolution due to having the lowest energy per nucleon. Elements heavier than iron are believed to be produced in supernova explosions and neutron star mergers through neutron capture processes, and thus their abundance is low.

The most pronounced difference between abundances in the solar system and in galactic CRs is that elements which have a significant underabundance in the solar system are more common in galactic cosmic rays. These elements are typically produced as spallation products of more common heavier elements which react with the gas in the interstellar medium. The elements lithium (Li), beryllium (Be) and boron (B) for example can be produced in the spallation of the much more abundant elements carbon (C), nitrogen (N) and oxygen (O), while fluorine (F) is produced in the spallation of neon (NE) and the elements from scandium (Sc) to mangan (Mn) can result from the spallation of iron (Fe) and nickel (Ni) [WBM97].

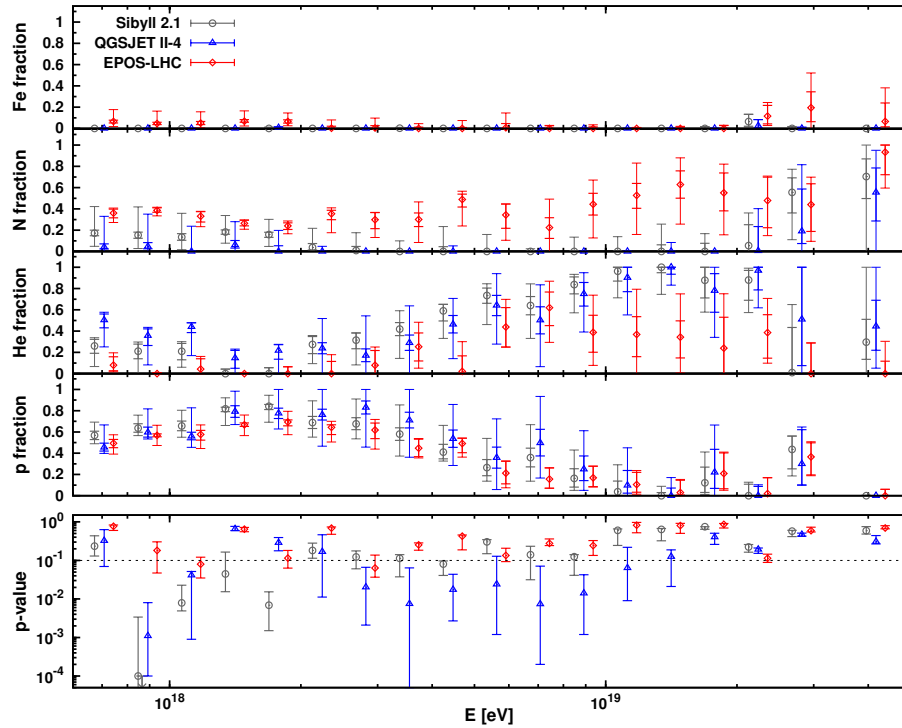


FIGURE 1.10: Fractions of elements of four different elemental mass groups as determined by the Pierre Auger Observatory [Aab+14b]. Results are shown for the three hadronic interaction models EPOS-LHC, QGSJET-II-04 and Sibyll 2.1. In the upper panels, the fractions of individual elements are shown, the lower panel shows the p-values of the fits.

Both acceleration mechanisms as well as the deflection of CRs during propagation due to (extra-)galactic magnetic fields are rigidity dependent. Thus, a change in the elemental abundances in CRs with different energies is expected, with the fraction of heavier elements increasing for higher energies. In Fig. 1.9, the flux of different CR components in relation to the energy is shown. The flux of hydrogen and helium below the knee was measured by AMS-02 aboard the international Space Station [Agu+15b; Agu+15a] as well as the balloon flights CREAM-I and CREAM-III [Yoo+17]. The flux of the heavier elements carbon, silicon and iron below the knee was measured by the HEAO-3 satellite [Eng+90] as well as CREAM-II [Ahn+09]. At energies above the knee, the air-shower arrays KASCADE [Ape+09] and KASCADE-Grande [Ape+13] were used to determine CR fluxes. As air-shower experiments cannot directly measure the primary particle type, the components were determined using a fit to the observed electron and muon numbers at the ground using a model with five elemental components (H, He, C, Si, Fe). It follows that the displayed flux of an element is representative of an entire mass group (e.g. the shown flux of C could be closer to the cumulative flux of C, N and O) and depends on the hadronic model used in the simulations.

At low energies, the spectrum is dominated by H with an increasing fraction of He and heavier elements for higher energies. He is more abundant than H at energies above 100 GeV. Above 10 PeV, the spectrum is dominated by heavy elements in the mass range of Fe. The strong suppression of the H flux at ≈ 4 PeV coincides with the knee, the suppression of heavier elements seen is consistent with an effect depending on particle rigidity, steepening at energies of $\approx 4 Z$ PeV with the suppression of iron beginning at 100 PeV, supporting this interpretation of the second knee.

For CRs of even higher energies, one method of reconstructing the elemental composition is by performing combined fits of air-shower simulations of different elements to X_{\max} measurements. The elemental composition of CRs with energies in the EeV range reconstructed by the Pierre Auger Observatory using different hadronic interaction models [Aab+14b] is shown in Fig. 1.10. Although there are significant differences between the models, such as the comparatively high nitrogen fraction derived with EPOS-LHC, the reconstructions have some common features. In particular, the proton fraction again dominates the 1 – 5 EeV range where the flux of heavy elements is again suppressed. Above the ankle at 5 EeV, heavier compositions are favored with the proton fraction vanishing, although the exact composition varies between models. With Sibyll 2.1 and QGSJET-II-04, a helium-dominated composition is obtained, while a significant nitrogen fraction at the highest energies is gained with EPOS-LHC. A significant contribution of iron-like particles is not seen at any energy in the investigated range for all models [Aab+17c].

Chapter 2

Ultra-high energy air showers

When energetic cosmic rays interact with the atmosphere of the Earth, cascades of energetic particles, called air showers, are produced. In Sec. 2.1, the general development of typical air showers induced by CRs is discussed. The Heitler model, a simplified model used to describe purely electromagnetic showers is introduced in Sec. 2.1.1. In Sec. 2.1.2, the more complex development of air showers initiated by a hadronic primary particle is covered. These showers can then be detected using ground-based experiments, which is the topic of Sec. 2.2.

2.1 Air shower development

Cosmic rays approaching Earth first enter the Earth's magnetic field before entering the atmosphere. For charged particles with energies above ≈ 1 GeV this results in deflection, which leads to an energy- and latitude-dependent anisotropy in the arrival directions of particles. Particles with lower energies are deflected more strongly and may become trapped in the magnetic field inside the Van Allen radiation belts [Gru20]. These particles then are reflected between the Earth's magnetic poles until they either escape into space or are absorbed in the atmosphere close to the poles, which can be seen in the form of auroras. Particles with enough energy to penetrate the magnetic field then enter the Earth's atmosphere, where they interact with the constituent molecules of air, mainly nitrogen and oxygen. Repeated re-interaction of secondaries results in a cascade of highly energetic particles propagating through the atmosphere, called (extensive) air shower. All constituent particles move with a velocity close to the speed of light c in the approximate direction of the primary particle, as only minor transverse momenta are introduced in collisions. Those particles form the shower front, a slightly curved disk moving along the shower axis, given by the direction of the primary particle.

The distance along the shower axis is measured as the atmospheric depth X in g cm^{-2} , which measures the amount of air which is traversed along the shower axis. It is gained by integration of the density of air (g cm^{-3}) along the traversed path (cm). The total vertical column density of the atmosphere is about 1000 g cm^{-2} , corresponding to the pressure at sea level of

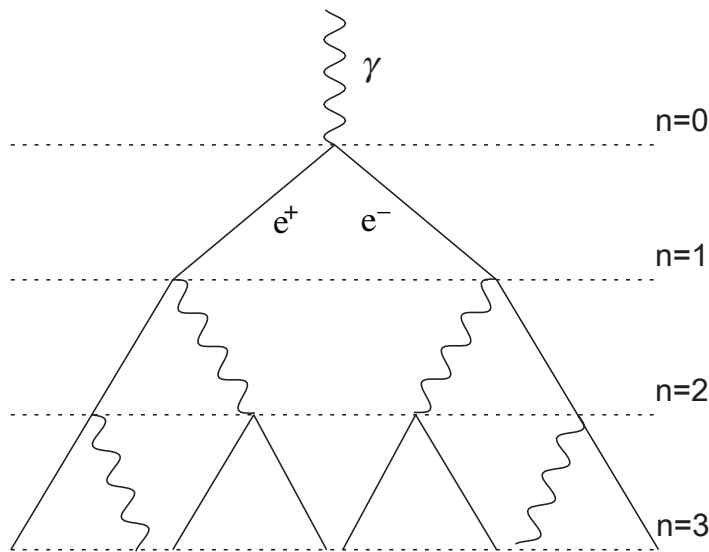


FIGURE 2.1: Schematic depiction of the Heitler model adapted from [Mat05a]. Shown is the shower development over the first four interaction lengths. Electrons and positrons are depicted as straight lines, photons as wavy lines.

≈ 1 bar [Gru20]. Radiation lengths of charged cosmic rays as well as photons in air are in the order of several tens of g cm^{-2} , thus the atmosphere is opaque to them, with interactions almost guaranteed.

2.1.1 Photon-induced showers and the Heitler model

While hadronic showers are relevant in the later sections, the shower principle can be explained with the simpler case of a purely electromagnetic shower induced by a photon. The photon in the atmosphere interacts with the electromagnetic charge of the atomic nuclei and undergoes pair production, producing an electron-positron pair. Those electrons and positrons, in the following referred to together as electrons, in turn interact with the air, producing photons via Bremsstrahlung, with energy losses via other interactions only becoming relevant at energies below the 100 MeV range. If those photons are of sufficient energy, they undergo pair production again, resulting in a cascade effect.

A simplified model of the development of electromagnetic air showers was developed by Walter Heitler [Hei54]. In the Heitler model, it is assumed that every interaction happens after an interaction length λ with each secondary particle inheriting half the energy of the initial particle. For photons and electrons the interaction length in air is about 25 g cm^{-2} , allowing for up to 40 interactions over the total column density for a vertical shower. After n interaction lengths, a shower initiated by a photon with energy E_0 has reached an atmospheric depth of $X_n = n\lambda$, consisting of $N = 2^n$ particles

with an energy of $E_n = E_0 \cdot 2^{-n}$ each. The maximal number of particles is reached when the energy per particle drops lower than the critical energy E_{crit} . Below this energy, Bremsstrahlung is no longer the dominant process for energy loss of electrons and positrons, thus stopping further shower development. Primary photon energy, critical energy and the maximum number of particles are thus related through the expression [MR18]:

$$E_0 = N_{\text{max}} E_{\text{crit}} \quad (2.1)$$

The atmospheric depth at which the shower reaches its maximal size is then given by [Mat05a]:

$$X_{\text{max}} = \frac{\lambda}{\ln 2} \ln(N_{\text{max}}) = \frac{\lambda}{\ln 2} \ln\left(\frac{E_0}{E_{\text{crit}}}\right) \quad (2.2)$$

The rate at which the depth of the shower maximum X_{max} increases with energy is given by the elongation rate D , which is defined as the derivative of X_{max} with respect to $\log_{10}(E_0)$:

$$D = \frac{dX_{\text{max}}}{d \log_{10}(E_0)} = \frac{\ln(10)}{\ln(2)} \lambda \quad (2.3)$$

While this relatively simple model cannot predict the exact shower development, the predictions for the dependence of the shower size on E_0 as well as for the elongation rate of electromagnetic showers agree with more complex simulations.

2.1.2 Development of hadron induced air showers

The development of showers initiated by a hadronic cosmic ray is more complicated, as an increased number of different particle types can be produced inside the shower. A schematic depiction of the components of an air shower as well as of the different particles produced in the shower is depicted in Fig. 2.2.

Hadronic component

The primary hadron typically interacts with atomic nuclei in the air in collisions via the strong interaction, producing a large number of secondary particles in each collision. For a proton traversing air, the radiation length is $\approx 90 \text{ g cm}^{-2}$ [Gru20]. As the total atmospheric depth traversed is at least 11 times higher than this, interaction of the primary particle with the air is practically guaranteed. While the radiation length of protons is larger than that of photons, the overall development of the shower is faster due to the higher number of particles produced in each interaction.

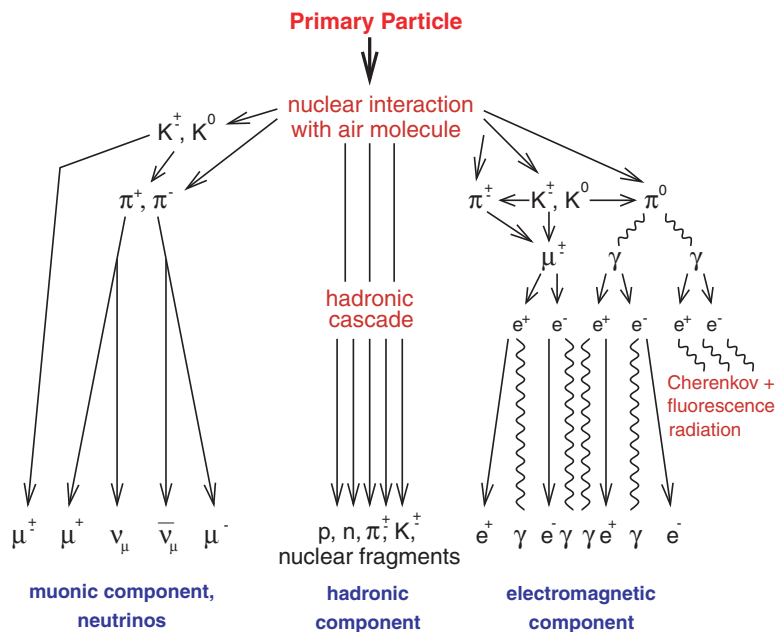


FIGURE 2.2: Schematic depiction of the shower development and the individual shower components [HRR03].

The hadronic interactions produce mostly pions, as those are the lightest hadrons, and a smaller number of kaons. All three types of pions are produced in roughly similar fractions. Neutral pions decay almost instantaneously into photon pairs, feeding into the electromagnetic component. Charged pions have larger decay lengths, which leads to them interacting multiple times with the atmosphere before decaying into pairs of muons, which feeds the muonic component, and neutrinos. Neutrinos do not contribute to the further development of the shower due to their extremely small interaction cross sections, and are thus typically not observed [MR18].

This early air shower development can be described by a simplified model similar to the Heitler model. In that model, each interaction happens after a fixed interaction length, producing a fixed number of secondary particles. Only the charged pions re-interact, while the neutral pions decay into photons without further hadronic interactions. This reduces the total energy carried by charged pions in a shower with a primary particle of energy E_0 after n generations to [Mat05a]:

$$E_{\pi^\pm, \text{tot}} = \left(\frac{2}{3}\right)^n E_0 \quad (2.4)$$

Repeated interactions of pions with air happen as long as they are above a critical energy, below which the decay length $\gamma c \tau_{\pi^\pm}$ drops to values lower than the mean distance traversed before interaction with the atmosphere. For a shower with a primary energy of 10^{17} eV this is the case after $n = 6$ interaction lengths, where $E_{\pi^\pm, \text{tot}}$ is reduced to only 9% of the primary particle.

The remaining energy is channeled into the electromagnetic component of the shower through the decay of the produced neutral pions [Mat05a].

Electromagnetic component

The electromagnetic component contains the majority of the number of particles produced in an air shower. The initial particles of the electromagnetic sub-showers are mainly produced by the decay of neutral pions into photon pairs, steadily feeding energy into the electromagnetic component in the early stage of the shower. In addition to this, there are minor contributions from the decay of charged muons. After this, the individual electromagnetic sub-showers develop like the purely electromagnetic showers discussed above. Since a majority of the primary particle energy is transferred into the electromagnetic component, it is also the component containing the greatest number of particles and is thus crucial to the overall development of the air shower. In fact, some shower properties, such as the elongation rate can be described reasonably well by only taking account the electromagnetic development of the shower and the first hadronic interactions [Mat05a; MR18].

Muonic component

The muonic component is produced by the decay of charged pions which have reached energies at which decay becomes more probable than repeated interaction. The range of muons in the atmosphere is mostly determined by their relatively long lifetime $\tau_\mu \approx 2.2 \mu\text{s}$, as the energy loss of relativistic muons in air is low ($\approx 1.8 \text{ GeV}$). Thus, the muonic component is the most penetrating part of the shower, with its size staying almost constant after reaching the maximum. This results in a relatively high number of muons reaching the ground, accounting for 80% of all charged secondary particles at sea level [Gru20].

Longitudinal shower development

The longitudinal development of the entire hadronic shower is more complex than that of a purely electromagnetic one, due to the hadronic component feeding both the electromagnetic and muonic components as well as interactions and decays competing against each other [MR18].

As the majority of the energy of the shower is contained in the electromagnetic component, the longitudinal development of the shower is mainly determined by the longitudinal development of the electromagnetic component. This can be parameterized through a Gaisser-Hillas function [GH77] given by:

$$N_e = N_{\text{max}} \left(\frac{X - X_1}{X_{\text{max}} - X_1} \right)^{\frac{X_{\text{max}} - X_1}{\lambda}} e^{-\frac{X_{\text{max}} - X}{\lambda}} \quad (2.5)$$

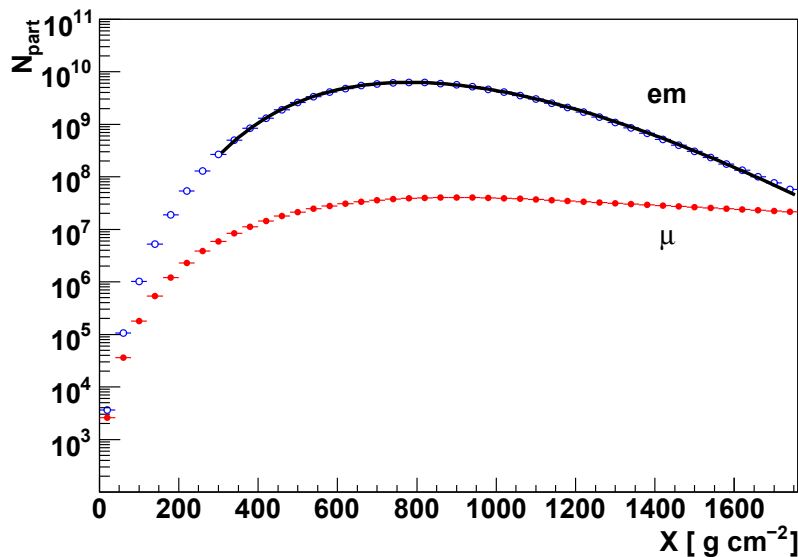


FIGURE 2.3: Average longitudinal profile of the electromagnetic (blue) and muonic (red) components of simulated showers initiated by a 10 EeV proton [Abr+09]. The solid black line shows a Gaisser-Hillas function fitted to the electromagnetic component.

In this function, N_{\max} describes the maximal number of particles and X_{\max} the atmospheric depth at which this maximum is reached. X_1 is the atmospheric depth of the first interaction and $\lambda \sim 70 \text{ g cm}^{-2}$ the effective attenuation length.

The simulated development of the number of particles in both the electromagnetic and muonic component, as well as a fit to a Gaisser-Hillas function are displayed in Fig. 2.3. The electromagnetic component consists of a large number of particles, with the number steadily increasing until a maximum N_{\max} at atmospheric depth X_{\max} is reached. The number of particles in the muonic component also rapidly increases in the early stages of the shower. In contrast to the electromagnetic component, the number of muons only slightly decreases after its maximum is reached, resulting in much higher penetration.

Lateral distribution of secondary particles

For a ground-based experiment, the lateral distribution of particles at ground level is of great interest for the shower reconstruction. The particle densities of the different shower components at ground level in relation of the distance to the shower core is seen in Fig. 2.4. Again, electrons visibly outnumber the other shower components, while all shower components have a wide distribution, with particles still being measured at distances of hundreds of meters or kilometers from the shower axis. Of the three distributions, the muon distribution shows the highest densities at large lateral distances, due to the

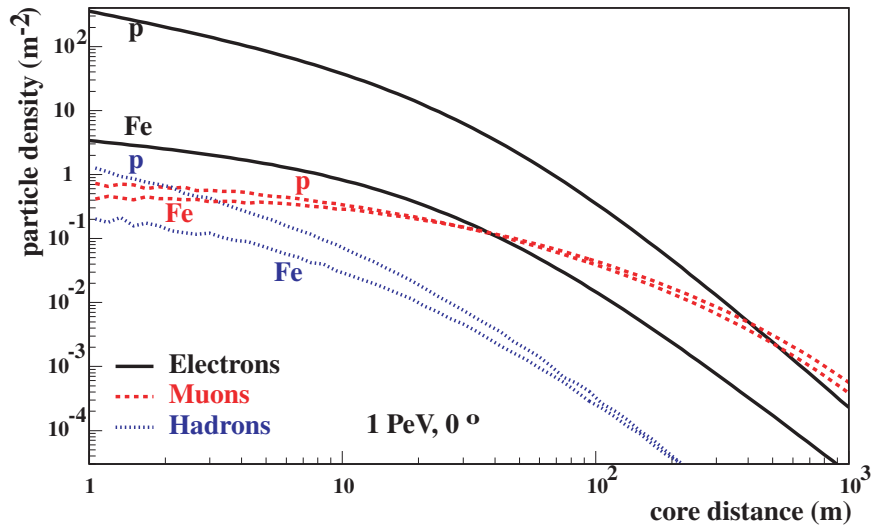


FIGURE 2.4: Lateral distribution of particle densities of the different air shower components in showers initiated by different primary particles [HRR03]. The values were derived from MC simulations of vertical showers with a primary energy of 1 PeV using CORSIKA [Hec+98].

production of muons very early in the shower development, where small transverse momenta can lead to a large displacement on the ground. Thus, with a higher distance from the shower axis, the proportion of measured muons increases.

The superposition model for heavy nuclei

The mass of the primary particle also impacts the shower development, as the first interaction depends on the cross section of the particle-collision with air. For particles heavier than the proton, the superposition model can be used to understand the shower behaviour. In the superposition model, a shower initiated by a particle with energy E_0 consisting of A nucleons is considered to be a superposition of A proton showers with energies E_0/A each. From this, a dependence of the average depth of the shower maximum $\langle X_{\max} \rangle$ on the primary particle mass follows [MR18]:

$$\langle X_{\max}^A(E) \rangle = \langle X_{\max}^p(E_0/A) \rangle \quad (2.6)$$

This also implies that the elongation rate does not depend on the mass of the primary particle, if a constant elongation rate of the proton is assumed. In this case, any changes in elongation rate measured relate to a change in primary particle composition. If the elongation rate of the photon changes at an energy E , these changes can be seen for heavier particles at higher energies $A \cdot E$.

The superposition model also predicts a decrease in the fluctuations of the shower maximum between showers $\sigma(X_{\max})$ for higher mass primaries. For a proton shower, the spread of X_{\max} is mostly determined by fluctuations of the depth of the first interaction, with additional contributions from fluctuations in the development of the subsequent electromagnetic component. For a higher-mass particle, the fluctuations of the superimposed protons are largely averaged out, leading to a significant decrease in $\sigma(X_{\max})$. For example, the fluctuations of showers induced by 100 EeV protons are $\sigma(X_{\max}^p) \approx 60 \text{ g cm}^{-2}$, those of iron only a third of this value with $\sigma(X_{\max}^{Fe}) \approx 20 \text{ g cm}^{-2}$. These features of the superposition model give a good approximation of the shower development and can be reproduced in numerical shower simulations [MR18].

2.2 Air shower detection

To detect air showers in the atmosphere, several techniques are used. These can be grouped into two categories: In the first category, the secondary particles reaching the ground are detected by an array of particle detectors. The second category is the detection of electromagnetic emission produced by the electromagnetic component of the shower during propagation through the atmosphere. Different types of radiation have been used for these measurements, such as fluorescence light emitted by excited air molecules, Cherenkov light and radio emission. With all methods, the direction of the primary particle can be reconstructed by measuring the arrival times of signals, the primary particle energy can be reconstructed by the integration of all measured signal strengths. For a ground based measurement this involves adding up all measured particles, when measuring the propagation in the atmosphere, the total measured electromagnetic radiation gives a measure of the total shower energy. A sketch of the different detection methods and their interactions with the air shower can be seen in Fig. 2.5.

While various different types of detectors can be used for air-showers arrays, most current experiments use either water Cherenkov detectors or scintillation detectors. For shower reconstruction, the electron-muon ratio can be determined for experiments using detection methods with different responses to muons and electrons. Different methods to obtain this are the use of absorbers between detectors, which absorb vastly more electrons than muons, as well as the use of different detectors with inherently different responses to electrons and muons. The depth of the shower maximum X_{\max} can also be estimated by analyzing the arrival time at individual detectors, although this is significantly less precise than measurements from atmospheric radiation.

To compensate the low flux of cosmic rays at the highest energies, the area covered by the experiment has to be large. For measurements at the ground, this necessitates building large arrays of detectors, covering up to several thousands of km^2 , with detectors spaced according to the technique used as

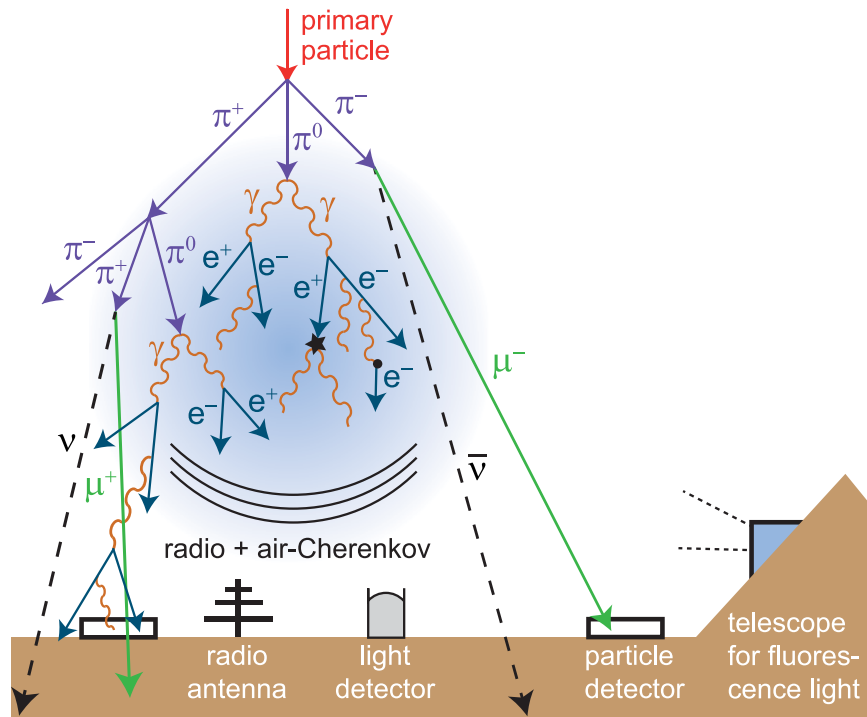


FIGURE 2.5: A sketch of different detection techniques of air showers [Sch17].

well as the targeted energies, where higher energies need larger areas while for lower energies a denser spacing is preferred. This spacing can range from several meters (e.g. 13 m at KASCADE [Ape+10]) to more than a kilometer (e.g. 1.5 km at the Pierre Auger Observatory [Aab+15b]). Experiments observing the fluorescence light in air or Cherenkov light can measure a large volume of air with only a single telescope, capable of measuring showers in distances of tens of kilometers.

Fluorescence detectors exploit the light emitted by nitrogen nuclei which were excited by the passing shower front. They provide very high sensitivity for both the total energy of the shower, as well as the depth of the shower maximum X_{\max} . The reconstruction of the shower is also less dependent on the hadronic interaction models than measurements of particles at the ground. However, the sensitivity to the muonic component of the shower is poor, as the fluorescence is dominated by the electromagnetic component.

Cherenkov detectors detect the passage of particles faster than the speed of light in the medium the particle travels in. This technique is used in dense media such as ice and water to detect neutrino-induced particle cascades [Ach+06; Avr+22], but can also be applied to air showers. Similar to fluorescence detectors, Cherenkov detectors are mostly sensitive to the electromagnetic component of air showers due to the high energy-to-mass ratio of electrons and positrons. Because of this, they are used for gamma astronomy and detecting photon-induced air showers. For gamma-ray energies above ≈ 50 GeV, imaging atmospheric Cherenkov telescopes such as

H.E.S.S. [OH23] and MAGIC [Fer06] are used to measure the Cherenkov light emitted by the shower [Fun15]. For even higher energies above 1 PeV, arrays of photomultipliers have been used to measure atmospheric Cherenkov light at experiments like Tunka-133 [Pro+14]. The intensity of the Cherenkov light is proportional to the energy of the electromagnetic component, resulting in accurate measurements of the shower energy, similar to fluorescence detection.

An additional method for measurements of air showers is the detection of radio emission from air showers. Radio emission in air showers is mainly generated by the deflection of relativistic electrons in the geomagnetic field, its amplitude depends on both the total shower energy and the angle between the shower axis and the geomagnetic field. These emissions can be measured by arrays of radio antennae, which are often attached to existing cosmic-ray experiments. Work is still done on the reconstruction of air showers from radio measurements, with the achieved precision for measurements of energy and shower position being comparable to other measurements techniques [Sch17].

Another approach to studying air showers is the measurement of light emitted by the air shower from above using balloons or satellites. This is currently explored by the EUSO program [Cas18]. Currently, a prototype in the form of the Mini-EUSO observatory is aboard the ISS [Bac+21], dedicated satellite experiments are also planned. Advantages of space-based observations of air showers are the coverage of a large amount of atmosphere, as well as uniform coverage of all arrival directions. On the other hand, satellite experiments have strict constraints the detector parameters and the increased exposure of such experiments currently results in a lower precision compared to ground based experiments, especially for the shower depth X_{\max} [Ber+14].

Chapter 3

The Pierre Auger Observatory

In this chapter, the Pierre Auger Observatory is introduced to give context to the air shower data used in the later chapters of this work. The idea of the Pierre Auger Observatory was hatched in 1991 by James Cronin and Alan Watson in Dublin at the International Cosmic Ray Conference. Due to the rapidly decreasing flux of cosmic ray particles with increasing energy, a detector covering a very large area would be needed for measurements at the highest energies. The Pierre Auger Collaboration was officially founded in 1999, the construction of the Observatory started in 2002, with the first data taken in 2004. The detector covers a total area of $\approx 3000 \text{ km}^2$ and is located in the remote countryside near the city of Malargüe in Argentina [Aab+15b].

The Pierre Auger Observatory has a hybrid detector design, combining multiple detection techniques for increased accuracy. The first component of the detector is a large Surface Detector (SD) to detect secondary air-shower particles at ground level, consisting of 1660 water Cherenkov detectors. Complementing this, the Fluorescence Detector (FD) is used to measure the fluorescence light produced by the passage of the air shower through the atmosphere. The FD component of the Observatory consists of 24 fluorescence telescopes at 4 sites overlooking the SD array. Additional fluorescence telescopes as well as a denser SD array are installed near the Coihueco site for measurements of air showers at lower energies [Aab+15b]. The layout of the Observatory with its primary components is shown in Fig. 3.1. Fluorescence light produced by passing air showers is detected by the FD, which enables precise measurements of shower energy and development, but is restricted to observations to clear, moonless nights, resulting in a duty cycle of $\approx 15\%$. Sec. 3.1 covers the FD component of the Pierre Auger Observatory. The SD measures secondary particles at the ground with a duty cycle of $\approx 100\%$ and is covered in Sec. 3.2.

Additional components of the Pierre Auger Observatory, such as the High Elevation Auger Telescopes (HEAT) and the infill array used to measure showers of lower energies as well as the Auger Engineering Radio Array (AERA) are discussed in Sec. 3.3.

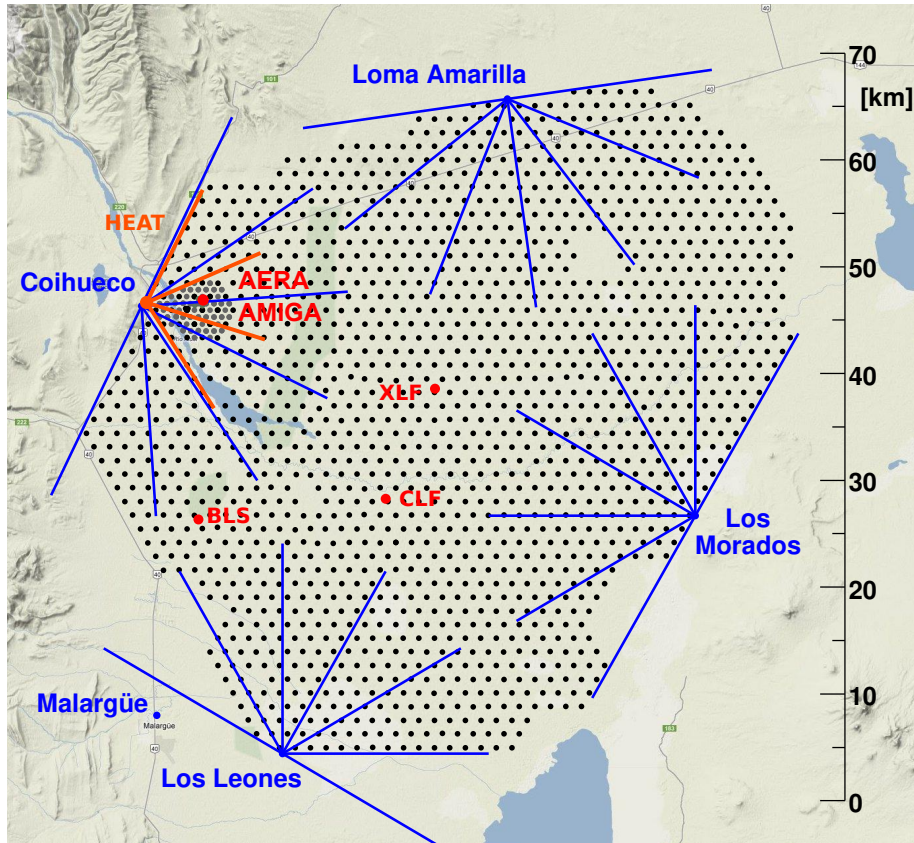


FIGURE 3.1: Layout of the Pierre Auger Observatory [Veb20]. The black markers correspond to the 1660 detector stations of the SD. The four sites of the FD as well as the field of view of individual telescopes are marked in blue, with the additional high-elevation telescopes of HEAT at Coihueco marked in dark orange. Also shown are the 750 m array and AERA near Coihueco, as well as laser (XLF, CLF) and weather balloon launching (BLS) facilities.

3.1 The fluorescence detector

The FD of the Pierre Auger Observatory consists of 24 fluorescence telescopes, which are located at the four sites Coihueco, Loma Amarilla, Los Morados and Los Leones. At each site, six telescopes with a field of view of $30^\circ \times 30^\circ$ are installed, for a total field of view of 30° in elevation and 180° in azimuth [Abr+10a]. The telescopes are pointed towards the center of the array, overlooking the entire SD area, which can also be seen in Fig. 3.1. Fig. 3.2 shows both a photograph of the building housing the fluorescence telescopes at Los Morados as well as a schematic view of one such building.

The FD is used to detect the air-fluorescence of extensive air showers. The fluorescence light is produced when the charged particles in the air shower lose energy by exciting nitrogen molecules contained in the atmosphere. The excited nitrogen molecules can then return to their ground state, radiating the absorbed energy in the form of fluorescence light in the UV range with

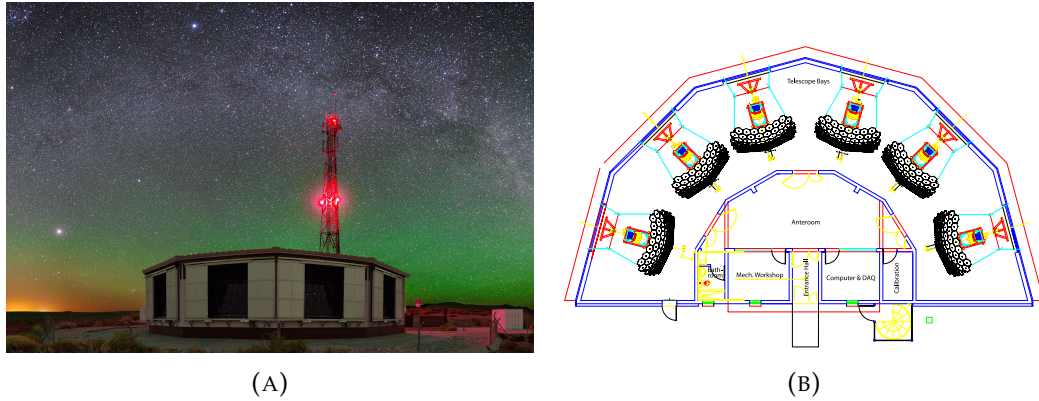


FIGURE 3.2: (A) The FD building at Los Morados at night [Pie20]. (B) Schematic layout of a FD detector location with six fluorescence telescopes [Abr+10a].

wavelengths between 300 nm and 430 nm. The number of photons produced in this way is proportional to the total amount of energy deposited in the atmosphere and depends on atmospheric conditions, such as humidity, pressure and air temperature. Through measurements of the fluorescence light emission along the shower axis, the profile of the energy deposited in dependence on the atmospheric depth $\frac{dE}{dX}(X)$ can be determined. Through integration, the total energy of the shower can be inferred, as long as the fraction of energy carried away by the muonic component as well as neutrinos ($\approx 10\%$) are taken into account [Abr+10a]. The dependence of the fluorescence yield on atmospheric conditions has been studied intensively. For instance, the fluorescence yield of the 337 nm band in dry air in standard atmospheric conditions of 1013 hPa and 20 °C is $5.61 \pm 0.06_{\text{stat}} \pm 0.22_{\text{sys}}$ photons per MeV [Ave+13]. Due to this dependence, monitoring of atmospheric conditions is of extreme importance. Each of the four FD station is outfitted with a weather station monitoring air pressure, humidity and temperature. Four lidar stations installed at the FD sites are used in addition to this to monitor the aerosol density above the Observatory. To gain a model of the atmosphere above the detector, measurements with weather balloons at the balloon launching site (BLS), marked in Fig.3.1, were carried out. Data from the balloon flights was later used to validate satellite data from the Global Data Assimilation System (GDAS) and subsequently replaced by the same [Aab+15b]. To prevent changes in in the optical system of the telescopes due to temperature variations, they are housed in clean, climate controlled buildings [Abr+10a].

A schematic view of a fluorescence telescope is shown in Fig. 3.3a. The design of the FD is based on the Schmidt telescope [Sch38], correcting for both spherical and coma aberration. When no data is taken, e.g. during the day or during thunderstorms, the shutter system is closed to protect the detector. During measurements, the fluorescence light enters the telescope through the aperture system, which is fitted with an UV filter as well as a Schmidt optics corrector ring. The filter absorbs light outside the target range between

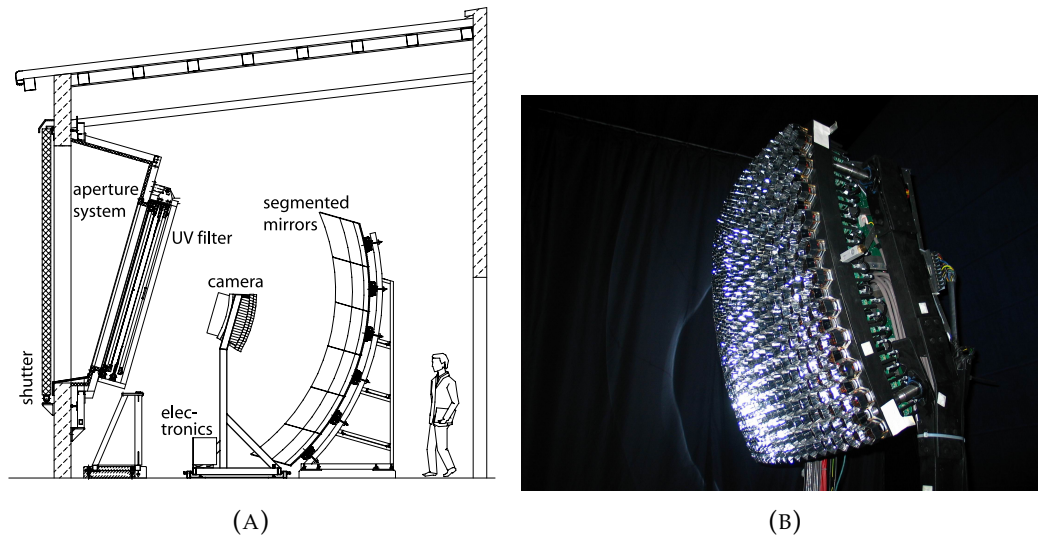


FIGURE 3.3: (A) Schematic depiction of a fluorescence telescope, with main components labeled [Abr+10a]. (B) Photo of the Camera module of a fluorescence telescope [Pie15a].

290 nm and 430 nm for the fluorescence spectrum of molecular nitrogen, reducing background noise. A segmented mirror with an area of $\approx 13 \text{ m}^2$ and a spherical radius of 3400 mm collects the fluorescence light, reflecting it onto the camera. Two different designs are used for the segmented mirrors. At Los Leones and Los Morados, the mirrors of the 12 telescopes consist of 36 rectangular anodized aluminium mirrors. At Coihueco and Loma Amarilla, the telescopes are segmented into 60 hexagonal mirrors of coated glass. The mirror segments are aligned to the intended shape of a sphere with the center of curvature along the optical axis of the telescope using a laser [Abr+10a].

The camera, displayed in Fig. 3.3b, consists of 440 hexagonal pixels, arranged in 20 rows and 22 columns. The pixels of the camera are implemented through PMTs mounted inside a milled aluminium block. Each pixel has an angular diameter of 1.5° , for a total field of view of 30° in azimuth and 28.1° in elevation. The maximum angular resolution of the telescope of 1.5° is defined by the pixel size. When an air shower traverses the field of view of the telescope, the emitted fluorescence light is reflected onto the camera, creating a track corresponding to the changing position of the front of the air shower [Abr+10a].

3.1.1 FD event reconstruction

The reconstruction of events measured by the FD consists of two parts. First, the shower geometry is reconstructed to determine location and direction of the shower. The second step is the reconstruction of the shower energy and profile. Showers are measured by the FD as a series of triggered pixels in the FD camera. For the geometry reconstruction, the timing information of each pixel is used, indicated in Fig. 3.4a by the changing colors from violet for early pixels to red for the late pixels. The first step is the determination

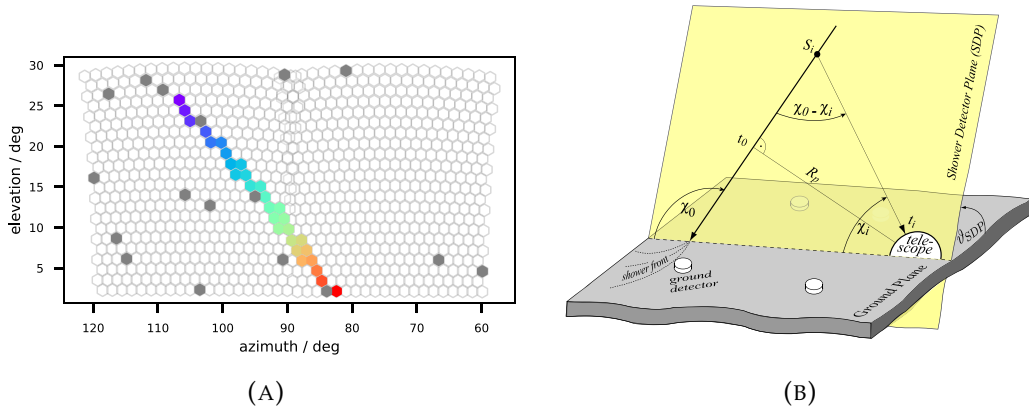


FIGURE 3.4: (A) Camera view of an event measured by the FD telescope at Coihueco. The time at which each pixel is activated is indicated by the colors, with violet pixels being early and red pixels late occurrences. Grey pixels indicate coincident signals excluded from the event reconstruction [Abd+23]. (B) Schematic depiction of the shower as seen from the FD telescope and the shower detector plane [Abr+10a].

of the shower-detector-plane (SDP), which is the plane containing both the shower axis and the FD telescope, as sketched in Fig. 3.4b. The SDP is found by fitting a straight line through the triggered FD camera pixels [Abr+10a; Aab+15b].

The position of the shower axis is reconstructed using the timing information of the individual pixels of the FD camera. The position of the axis within the SDP is fully described by two parameters, the minimum distance between shower axis and FD telescope R_p and the angle χ_0 between shower axis and the horizontal line in the SDP. For each pixel pointing in a direction with an angle χ_i to the horizontal line in the SDP the arrival time t_i of the signal can be expressed in terms of R_p , χ_0 and the arrival time at the point of the closest approach t_0 by [Abr+10a]:

$$t_i = t_0 + \frac{R_p}{c} \tan\left(\frac{\chi_0 - \chi_i}{2}\right) \quad (3.1)$$

The parameters R_p and χ_0 are reconstructed by fitting the timing information of all pixels to the expected values according to this function. The accuracy of this reconstruction suffers if the measured tracks are short or if the shower geometry results in similar angular speed $d\chi/dt$ over the entire track. This uncertainty is then propagated to other shower parameters, such as the reconstructed shower energy. To mitigate this, timing information from matched events measured by the SD is also incorporated into the fit in the so called hybrid reconstruction, adding additional timing information at the ground. Due to the high duty cycle of the SD, this is possible for most FD events. The hybrid reconstruction results in a resolution of 0.6° for the arrival direction and 50 m for the location of the shower core [Abr+10a].

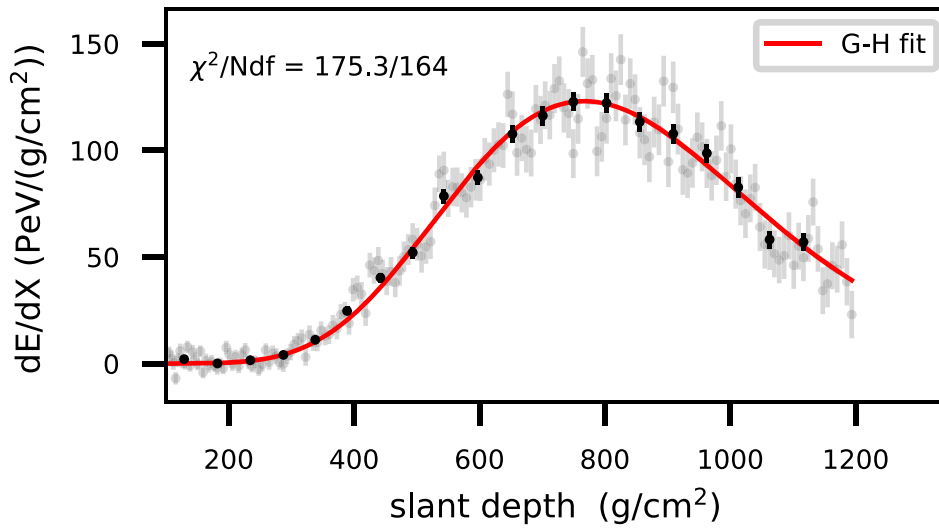


FIGURE 3.5: Reconstruction of the longitudinal profile of a shower measured by the FD [Abd+23]. The line overlaying the measurements is the fitted Gaisser-Hillas function.

The shower profile is reconstructed by converting the signal measured by the FD camera to a slant depth dependent calorimetric energy deposit along the shower axis. The first step in this is the conversion from the PMT signal of a single pixel to the amount of light at the aperture. For this both absolute and a relative calibration methods are used. One absolute calibration involves mounting a light source with a diameter of 2.5 m on the aperture, called the drum for its shape. This source provides a known uniform flux of monochrome light in the UV spectrum which is used to calibrate the response of the PMTs [Bra+13; Aab+17b]. This is cross-checked by measuring the light scattered from a remote laser shot. This results in a known number of photons reaching each pixel of the FD camera used for calibration [Abr+10a].

A relative calibration of the FD is done before and after each night of operation to track the short and long term detector performance. Three positions of the detector are illuminated to measure detector response, transmissibility of the filter and reflectivity of the mirror components [Abr+10a].

After reconstruction of the light at the aperture, the intensity at the shower axis is reconstructed. The intensity of the fluorescence light is decreased by attenuation in the atmosphere by scattering on atmospheric particles and aerosols, and it has to be disentangled from the contribution of noise by other light sources, such as direct and indirect Cherenkov light and multiple-scattered light. The light intensity gained this way can then be transformed into a calorimetric energy deposit profile [Ung+08].

The calorimetric energy of a shower as well as the atmospheric depth of the shower maximum X_{\max} are reconstructed by fitting a Gaisser-Hillas-Function (see Eq. (2.5)) to the longitudinal shower profile (Fig. 3.5). The

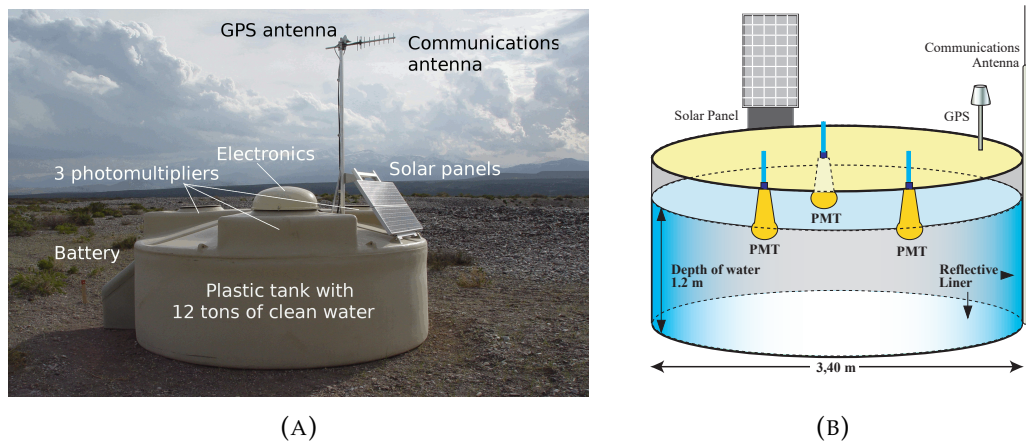


FIGURE 3.6: A water Cherenkov detector station of the Pierre Auger Observatory. (A) Photograph of a deployed SD station. Main hardware components visible from the outside, as well as the position of the photomultipliers inside the tank, are labeled. Image taken from [Pie15b]. (B) Schematic view of an SD station filled with pure water, adapted from [Kei04].

calorimetric energy of the shower is gained by integrating over the total traversed depth, while X_{\max} is a parameter gained from the fit. The total energy of the shower is estimated by accounting for the fraction of energy carried away by particles invisible to the FD, e.g. high-energy muons or neutrinos, which account for about 10% of the total energy, depending on the type of the primary particle. The energy resolution of the FD reconstruction given by the event-to-event fluctuations is in the order of 10%, while the uncertainty of X_{\max} is less than 20 g cm^{-2} [Ung+08; Abr+10a].

3.2 The Surface Detector

The SD is an array of 1660 water Cherenkov detector stations covering a total area of $\approx 3000 \text{ km}^2$. With the exception of technical issues, the detector stations have a duty cycle of 100%, accounting for the largest fraction of all data taken by the Pierre Auger Observatory. Each station is positioned at a distance of 1500 m from its neighbors, forming a hexagonal grid. This distance was chosen as a compromise between cost of the array and the energy efficiency, as a denser array enables the measurement of lower energies but also increases the number of detector stations. With the chosen spacing, a trigger efficiency of 100% is reached for energies above $3 \times 10^{18} \text{ eV}$ [All+08].

Each SD station is designed to work autonomously and not depend on other parts of the detector. The largest component of each station is a cylindrical water tank with a diameter of 3.6 m, which is filled with 12000 l of pure water to a height of 1.2 m. The thickness of the polyethylene tank walls is 13 mm, with the outer third of the walls consisting of beige material while the inner two thirds are black. The outer color is chosen to blend in with

the surroundings while the black inner layer is for light absorption, ensuring opaqueness of the tank. In addition to this, an opaque, reflective liner is installed inside each tank, enclosing the water volume. This both prevents the contamination or loss of water and is a secondary precaution against light leaks into the water volume. Three hatches are installed at the roof of the tank, providing access to its interior. A photograph of a deployed detector tank with labeled components can be seen in Fig.3.6a. Cherenkov light produced by secondary air shower particles is used for their detection. After diffuse reflection at the tank liner, the Cherenkov light can be measured by three photomultiplier tubes (PMTs) installed at the top of the tank. Each PMT is placed below one of the hatches in a distance of 1.2 m from the center of the tank and pointed downward to protect from direct exposure to the Cherenkov light (see Fig. 3.6b). The signals from the PMTs are sent to the read-out electronics, enclosed inside a dome on top of one of the hatches. All electronic components are powered by a battery system housed in the shadow of the tank which is recharged using solar panels. A communications antenna is used to provide a link to the Central Data Acquisition System (CDAS) of the Pierre Auger Observatory. The exact position and timing of each detector station is determined using a GPS antenna mounted next to the communications antenna [All+08].

When a signal is measured by an SD station, it needs to pass five trigger levels to be considered a physical event which can be reconstructed. The first two levels of the trigger system are requirements on the signal strength locally evaluated at the SD station. The trigger levels three to five take the entire array into account and impose increasingly strict conditions on the coincidence of simultaneously triggered SD stations, testing if the signal times are compatible with those produced by a moving shower front. After passing all trigger levels, 99.9% of events also pass the full shower reconstruction [Abr+10b].

3.2.1 SD event reconstruction

For the reconstruction of arrival direction, position and size of the shower, time, signal strength as well as the accurate 3D position of each triggered SD station is necessary. For reconstruction of the shower geometry, a fit to the start time of the signals is done. A rough approximation for the arrival direction can be gained by fitting the signal start times to a plane front as depicted in Fig. 3.7a. In this simple approximation, the shower is modeled by a flat shower front traveling in the direction $-\hat{a}$ given by the shower axis and impacting the ground at the position \vec{x}_b . The position of \vec{x}_b is the signal-weighted center-of-mass of all stations of the event, with the time t_b of the shower plane passing through \vec{x}_b . If the shower plane is assumed to be moving at the speed of light, the time $t_{sh}(\vec{x})$ of the shower plane passing through an arbitrary point \vec{x} is described by the projection of this point on the shower axis [Aab+20b]:

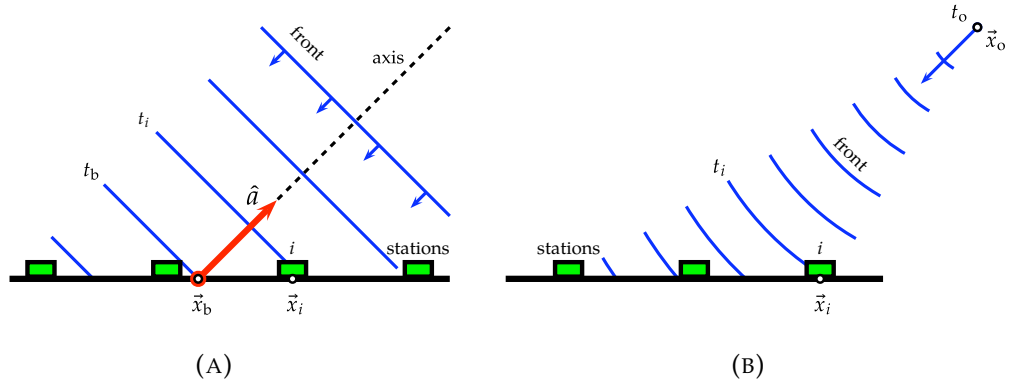


FIGURE 3.7: Schematic depictions of the air shower development from [Aab+20b]. (A) Approximation in a planar front described by the shower axis \hat{a} and the barycenter \vec{x}_b . (B) Spherical shower development originating at a center point \vec{x}_o at the time t_o .

$$c t_{\text{sh}}(\vec{x}) = c t_b - \hat{a} \cdot (\vec{x} - \vec{x}_b) \quad (3.2)$$

This equation is solved by choosing a "seed triangle" of stations from which an analytical solution is derived. The seed triangle is the combination of one station and its two nearest neighbors, all of which have passed the local trigger level and are in a triangular configuration. From all possible seed triangles in an event the one with the highest sum of signals is used [Aab+20b].

A curved shower front is used for a more precise reconstruction, with the radius of the curvature being an additional free parameter. The reconstructed shower is then defined by the direction of the shower axis \hat{a} , the intersection point of shower axis and ground \vec{x}_c and the impact time t_c . The barycenter \vec{x}_b is taken as an approximation of the impact point \vec{x}_c for the start of the fit. This corresponds to two free parameters for the shower direction as well as one free parameter for t_c and the curvature of the shower front.

The reconstruction framework approximates the shower to a spherical wavefront originating at a virtual origin point \vec{x}_o at time t_o , as displayed in Fig. 3.7b, inflating with the speed of light as it propagates through the atmosphere towards the ground. The arrival time of the shower front is given by [Aab+20b]

$$c t_{\text{sh}}(\vec{x}) = c t_o - |\vec{x} - \vec{x}_o|, \quad (3.3)$$

which is independent of the impact point \vec{x}_c and the shower axis. The shower axis \hat{a} can be determined in this framework as the normalized direction from \vec{x}_c towards \vec{x}_o [Aab+20b].

If five or more triggered stations are contained in a event, the curvature is taken as a free parameter, for events with less stations there is not enough

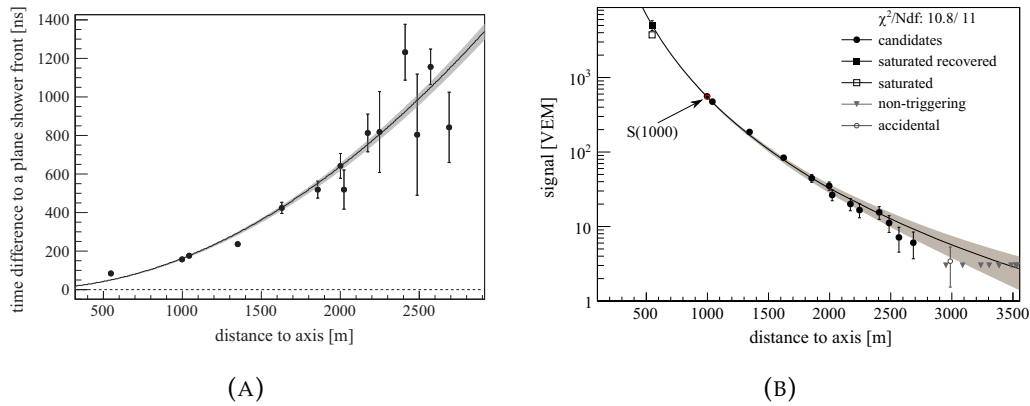


FIGURE 3.8: Shower behavior of extensive air showers at ground in dependence on the distance from the shower axis. In both plots, points with error bars correspond to triggered stations, the black line is the result of the model fit and the shaded area represents its uncertainties. (A) Delay of the signal start times compared to a plane shower front [Aab+15b]. (B) Signal size in VEM [Aab+15b].

information to solve for the curvature, thus a fixed curvature determined from events with a higher number of stations is used [Aab+20b].

An example of such a shower reconstruction is displayed in Fig. 3.8a, showing the difference in the arrival times at stations in dependence on the distance from the reconstructed shower axis.

The signal strength in dependence of the distance r between a detector station and the shower axis is described by the lateral distribution function (LDF). Through a fit of the signals measured by the SD to the LDF, a more precise measure of the position of the shower core \vec{x}_c can be determined. For this fit, the signal strength $S(r)$ is expressed in terms of the shower size estimator $S(r_{\text{opt}})$ and the LDF $f_{\text{LDF}}(r)$ [Aab+20b]:

$$S(r) = S(r_{\text{opt}})f_{\text{LDF}}(r) \quad (3.4)$$

The LDF $f_{\text{LDF}}(r)$ is normalized to $f_{\text{LDF}}(r_{\text{opt}}) = 1$. The optimal distance value is chosen to minimize the shower-to-shower variations in $S(r_{\text{opt}})$ and depends on the geometry of the array. For the Pierre Auger Observatory, this optimal value is close to 1000 m and the corresponding shower size estimator $S(r_{\text{opt}})$ at $r_{\text{opt}} = 1000$ m is referred to as $S(1000)$ [Aab+20b].

The function used to describe the LDF is chosen empirically and is a modified version of the Nishimura-Kamata-Greisen (NKG) function [KN58; Gre56]

$$f_{\text{LDF}}(r) = \left(\frac{r}{r_{\text{opt}}}\right)^{\beta} + \left(\frac{r+r_s}{r_{\text{opt}}+r_s}\right)^{\beta+\gamma} \quad (3.5)$$

with the fixed parameter $r_s = 700$ m.

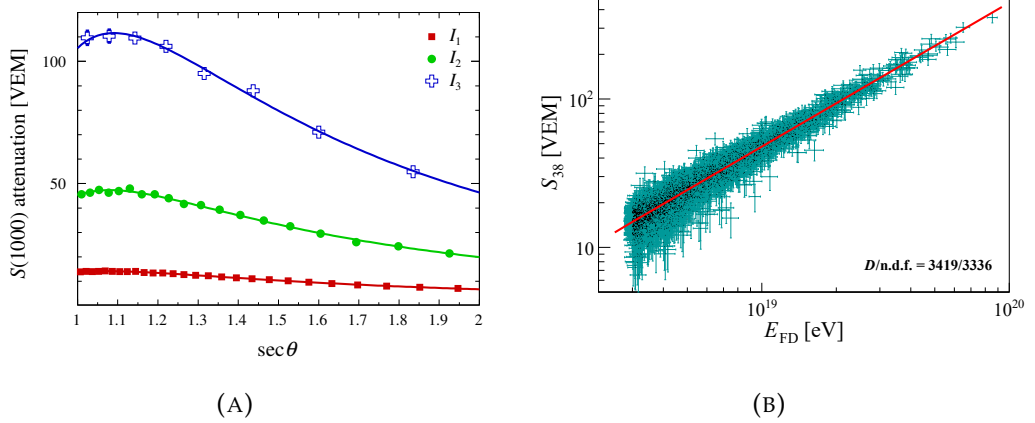


FIGURE 3.9: (A) $S(1000)$ as a function of $\sec(\theta)$ as described in Eq. (3.6) [Aab+20a]. The lines correspond to the fits at intensities associated with the approximate energies 3×10^{18} eV (I_1), 8×10^{18} eV (I_2) and 2×10^{19} eV (I_3). The dots correspond to the data gained using the CIC method. (B) Correlation between S_{38} and E_{FD} [Aab+20a]. The red line is the best fit of the data points with the function given in Eq. (3.7).

The slope parameter β can be reconstructed from fits for events containing two or more stations within a radius of $400 \text{ m} < r < 1600 \text{ m}$ with a necessary separation. The parameter γ is fitted for events with at least two stations within a radius of $1000 \text{ m} < r < 2000 \text{ m}$. Both parameters are parametrized as functions of the zenith angle and $S(1000)$ [Aab+20b]. An example of the signal sizes obtained using this reconstruction and those measured, expressed in VEM, in dependence of the distance of the detector station from the shower axis is shown in Fig. 3.8b.

The energy reconstruction of the SD is done through cross-calibration with FD data and is done in two steps. First, $S(1000)$, which depends on the zenith angle θ , is transformed into the zenith independent quantity S_{38} using the constant intensity cut (CIC) method [Her+61], which exploits the isotropic flux of CRs. The dependence of $S(1000)$ on θ is due to inclined showers propagating through a larger amount atmosphere. For showers which are below the shower maximum, this leads to a further attenuation before reaching the ground. The transformed shower estimator S_{38} can be thought of as $S(1000)$ of the same shower, had it arrived with a zenith angle of $\theta = 38^\circ$. The relation between $S(1000)$ and S_{38} is expressed as a third-order polynomial in $x = \cos^2(\theta) - \cos^2(38^\circ)$ [Aab+20a]:

$$S(1000) = S_{38} \left(1 + ax + bx^2 + cx^3 \right) \quad (3.6)$$

In the second step, the shower size estimator S_{38} is converted to an estimator for the shower energy by comparing S_{38} and the energy measurement E_{FD} of the FD for events measured by both SD and FD, after cuts to ensure a

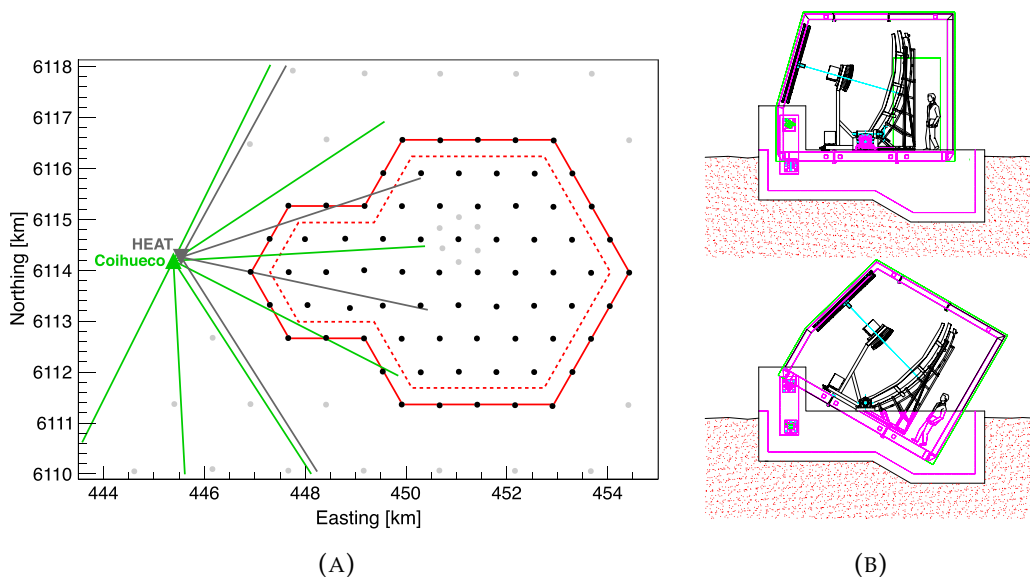


FIGURE 3.10: (A) Layout of the 750 m infill array of AMIGA and HEAT near Coihueco [Abr+22]. (B) Cross section of a HEAT telescope in both horizontal and tilted configuration [Mat11].

good quality of data for events measured by both detectors. The correlation between S_{38} and E_{FD} is described by the power law

$$E_{FD} = AS_{38}^B. \quad (3.7)$$

The parameters A and B of the power law are determined by performing a maximum-likelihood fit to the chosen events, as is seen in Fig. 3.9b. The total uncertainty of the SD energy $E_{SD} \equiv AS_{38}^B$ reconstructed in this way is 14 %, independent of the energy, and is dominated by the uncertainty in the FD calibration [Aab+20a].

3.3 Additional components of the Observatory

In addition to the FD and SD, several other components related to air shower measurements, calibration and development of new detection techniques are present at the Pierre Auger Observatory. An upgrade of the whole detector, called AugerPrime, is also currently being deployed to incorporate additional detection techniques.

The standard Auger hybrid detector is designed to detect CRs with energies above 10^{18} eV. However, the energy region below is also of high interest due to the transition from galactic sources to extragalactic sources. For measurements of lower energy CRs, the low-energy enhancements of the Auger Muons and Infill for the Ground Array (AMIGA) and High Elevation Auger Telescopes (HEAT) are added to the array. AMIGA covers an area of 27.5 km^2

near the Coihueco FD site and consists of additional detector stations with a denser grid with a spacing of 750 m (SD-750 m). These detector stations differ from the basic design of the SD array only in the addition of a muon counter. The denser spacing of detectors makes the reconstruction of lower-energy air showers possible, which otherwise would have too few triggered stations for reconstruction. The muon detectors, buried in a depth of 2.3 m below the detector tanks, are used to determine the strength of the muonic component, which can be used to gain information on the elemental composition of measured cosmic rays [Aab+15b; Bot21].

The second component of the low-energy extension of the Pierre Auger Observatory are the High Elevation Auger Telescopes (HEAT), which are three additional telescopes installed near the Coihueco FD site. These telescopes are built very similar to those of the FD, but are fitted with a hydraulics system to tilt them up to 29° upwards. Tilted in this way, HEAT is able to measure showers of lower energies which would die out before reaching the field of view covered by the Coihueco FD. Combined with the FD, an elevation range of 58° is covered, allowing the reconstruction of showers of much lower energies than those only measured by the FD [Aab+15b; Mat11].

The Auger Engineering Radio Array (AERA) is built to explore the radio emissions of air showers and is located inside the SD-750 m array near the Coihueco FD site. It consists of 153 radio stations deployed on an area of about 17 km^2 . Each station is fitted with two logarithmic-periodic dipole antennas (LPDA) or two butterfly antennas oriented in north-south and east-west direction and the detector stations are installed with different spacing. The purpose of AERA is the evaluation of advantages of different radio detection techniques for air showers as well as a determination of the capabilities of the reconstruction of shower parameters (e.g. energy, arrival direction, primary particle mass) using radio techniques [Aab+18b; Sch16].

Currently the Pierre Auger Observatory is being upgraded to improve the measurement capabilities, especially in the composition reconstruction at highest energies. The upgrade, also called 'AugerPrime', affects all components of the Observatory. The duty cycle of the FD shall be increased by lowering the supplied high voltage to the camera, making measurements in nights with higher background illumination possible. Each of the SD stations shall be outfitted with a surface scintillation detector (SSD), a radio detector, a fourth PMT and an upgrade to the station electronics. The fourth PMT increases the dynamic range of the detector while the upgraded electronics make higher sampling rates possible. The SSD is fitted on top of the tank and serves in tandem with the water Cherenkov detector to better distinguish muonic and electromagnetic components of showers, enabling a more precise reconstruction of the primary particle type. The radio detector, based on the findings of AERA, is a fourth detection channel installed at each SD station, primarily measuring the electromagnetic component of the shower [Aab+16a; Ber23; Cas19].

Chapter 4

Lorentz Violation

This chapter covers the general concept of theories introducing Lorentz Violation (LV) as well as the specific case of LV in the photon sector and its expected effects on extensive air showers. It starts with Sec. 4.1 on the Standard Model of particle physics (SM) and continues with a short introduction to the concept of LV in Sec. 4.2. Some examples of theoretical frameworks allowing for LV are given as well as possible approaches to test Lorentz invariance. The following sections focus on the specific case of isotropic, nonbirefringent LV in the photon sector, which is discussed in this work. In Sec. 4.3 the process of obtaining LV in the framework of the Standard Model Extension (SME) is explained. In Secs. 4.3.1 and 4.3.2 the respective effects of a negative/ positive LV parameter κ are discussed. A short review of current limits on isotropic, nonbirefringent LV in the photon sector derived from direct CR observations is given in Sec. 4.4. The expected changes in the development of air showers initiated by UHECR due to LV are discussed in Sec. 4.5.

4.1 The Standard Model of particle physics

The Standard Model of particle physics (SM) is used to describe all known elementary particles and their interactions. A representation of the particles of the SM is shown in Fig. 4.1. Elementary particles fall into two groups, fermions with spin $1/2$ and bosons with integer spins. Fermions are the matter particles and are subdivided into quarks and leptons. Both quarks and leptons are further subdivided into three generations, also called flavors, with higher generations having larger masses. Each generation of quarks has one quark with a charge of $+2/3e$ (up, charm, top) and one with a charge of $-1/3e$ (down, strange, bottom). Each lepton generation consists of one charged lepton (electron, muon, tau) and the corresponding neutral particles, the neutrinos. While neutrinos are massless in the SM, experimental evidence (e.g. neutrino oscillations and neutrino mixing) exists for a non-zero neutrino mass [Gri08; Wor+22].

Interactions between the matter particles are mediated by the bosons. The gluon is the gauge boson of the strong force, affecting all quarks. All charged particles interact via the electromagnetic force through the photon. The W

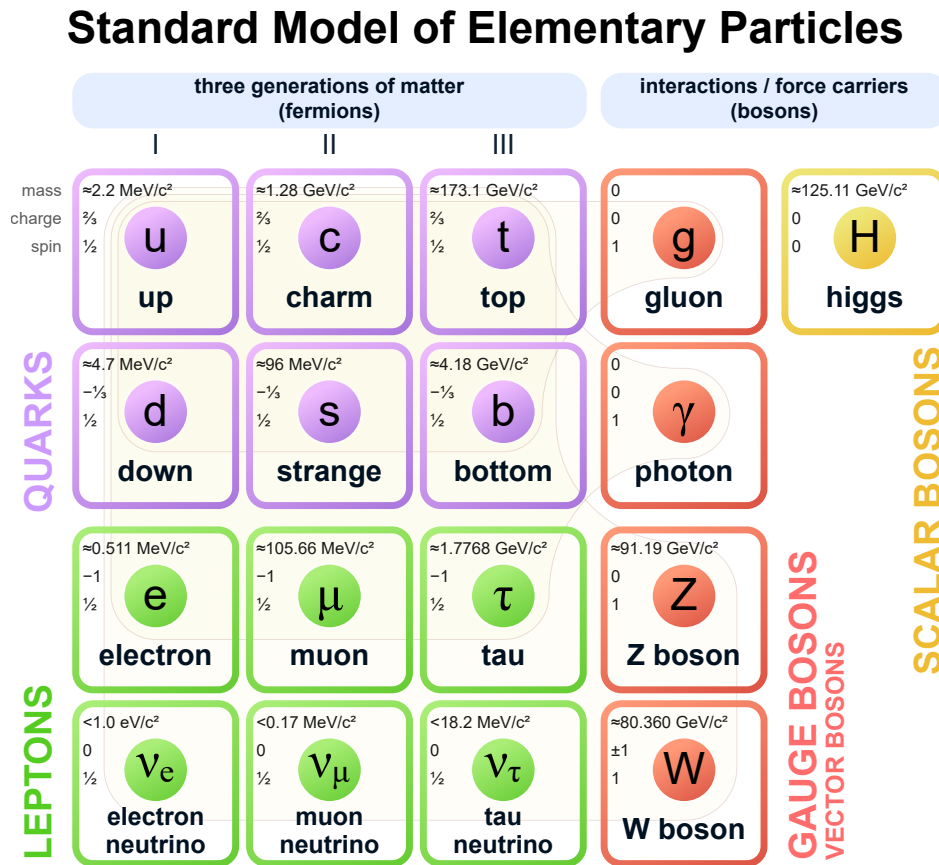


FIGURE 4.1: The particles of the Standard Model of particle physics [Wik19]. The particles are divided into six quarks and six leptons, which are further divided into three generations or flavours each. The forces between those particles are mediated by four gauge bosons and the Higgs boson.

and Z bosons interact with all matter particles through the weak force. Gluons and photons are massless, while W and Z bosons are massive particles. The particles gain their masses through spontaneous symmetry breaking due to the Higgs field and the associated Higgs boson [Gri08; Wor+22].

Each of the fundamental interactions can be described by a Lagrangian \mathcal{L} , which incorporates the local gauge symmetries. The Lagrangian for Quantum Electrodynamics (QED), which will be relevant in the later sections of this chapter, is given by [PS95]

$$\mathcal{L}_{\text{QED}} = -\frac{1}{4}F^{\mu\nu}F_{\mu\nu} + \bar{\psi} [\gamma^\mu(i\partial_\mu - eA_\mu) - m] \psi, \quad (4.1)$$

with the electromagnetic vector potential A_μ and the electromagnetic field tensor $F^{\mu\nu} = \partial_\mu A_\nu - \partial_\nu A_\mu$.

Charge conjugation (C), parity (P) and time reversal (T) are all symmetries which hold in the electromagnetic and strong interaction, but are broken by

the weak interaction. While the individual symmetries C, P and T may be broken, CPT symmetry is conserved in the SM. In addition to this, the SM is Lorentz invariant in combination with special relativity, i.e. all processes are the same for all observers independent of movement [CK97; Add+22].

The predictions of the SM are continuously tested and confirmed by, e.g., particle collider experiments such as the Large Hadron Collider (LHC). In fact, measurements at the LHC suggest that there may be no new physics interacting with SM particles up to energy scales up to $\approx 10^{17}$ eV [Bea+19].

On the other hand, there are observations in astrophysics and cosmology which do not agree with the expectations of the SM. The standard cosmological model, also called Λ CDM model, predicts a fraction of only $\approx 4\%$ of the total energy in the universe to be in the form of baryonic matter. Dark matter makes up $\approx 22\%$ of the total energy, a number derived from its gravitational effects on spacetime in, e.g., the dynamics of galaxies. The remaining energy is contained in dark energy, which does not have gravitational effects, but influences the expansion of the universe [Hea08]. In the SM, there are no candidates for dark-matter particles, inviting new theories.

Another issue is the mass of the neutrinos, which are massless in the SM. Neutrino oscillations, which are impossible with massless neutrinos have been experimentally confirmed through many experiments, e.g. by measuring the neutrino flux of the sun, of nuclear reactors or at accelerator experiments. The nonzero neutrino masses are integrated in e.g. the seesaw mechanism, in which the SM is a low-energy effective theory of the full theory [GM08].

4.2 Introduction to Lorentz Violation

The Standard Model of particle physics (SM), introduced in the previous section, provides a quantum mechanical theory of all particles and fundamental forces except gravity, while Einstein's theory of relativity provides a classical description of gravity. In this description of the universe, Lorentz symmetry is preserved. The predictions of both the SM as well as relativity have been extremely successful and were tested to very high precision. But the SM does not give a complete description of all observed phenomena, as it lacks explanations for, e.g., gravity on the quantum scale or the existence of dark matter. There is a great number of approaches to establish a more fundamental theory incorporating these phenomena and unifying the SM and relativity, many of which allow a deviation from exact Lorentz symmetry. Examples of approaches aiming to explain quantum gravity (QG) and allowing LV are string theory [KS89], spacetime foam [Ame+97], Loop quantum gravity [AMU02], noncommutative field theory [Car+01] and brane-world theories [MPR00].

There are many different theoretical frameworks which result in LV and can be experimentally tested. A relatively simple way to a theory incorporating LV is the modification of the dispersion relation for particles. In this

approach, the Lorentz invariant dispersion law $E^2 = p^2 + m^2$ is replaced by a function $E^2 = F(p, m)$. In most approaches of this kind, the rest frame of the CMB is taken as the preferred frame. To correspond to observations, Lorentz invariance has to hold for low energies and momenta and the dispersion relation has to reduce to $E^2 = p^2 + m^2$. A preferred way to express the modification is as an expansion around $p = 0$, which leads to the expression [Mat05b]:

$$E^2 = p^2 + m^2 + F_i^{(1)} p^i + F_{ij}^{(2)} p^i p^j + F_{ijk}^{(3)} p^i p^j p^k + \dots \quad (4.2)$$

The coefficients $F_{ijk\dots n}^{(n)}$ are constant and can be chosen arbitrarily, with the order n of the first non-zero term depending on the underlying theory, but typically leading only to small modifications. These coefficients can vary between particle species, with different dispersion relations for each. For simplification, rotational invariance is often assumed and the coefficients rewritten to factor out the Planck energy E_{Pl} , rewriting Eq. (4.2) with dimensionless parameters $f^{(n)}$:

$$E^2 = p^2 + m^2 + E_{Pl} f^{(1)} |p| + f^{(2)} p^2 + E_{Pl}^{-1} f^{(3)} |p|^3 + \dots \quad (4.3)$$

A conservative approach to tests of LV from QG involves effective field theories (EFTs). When the SM and relativity are expressed as EFTs [BT19], LV can be achieved by the introduction of additional tensors.

A theory in which adding potential Lorentz violating terms to the SM is possible was derived by Colladay and Kostelecky, called the minimal Standard Model Extension (mSME) or just SME [CK98]. The added terms are either CPT-even or CPT-odd and differ depending on the type of LV implemented. For fermions, for example, the CPT-odd added LV terms are of the form [Mat05b]

$$-a_\mu \bar{\psi} \gamma^\mu \psi - b_\mu \bar{\psi} \gamma_5 \gamma^\mu \psi \quad (4.4)$$

with the fermion spinor ψ and an individual set of coefficients for each particle species.

In the photon sector, LV in the SME framework is given by the terms

$$-\frac{1}{4} (k_F)_{\mu\nu\rho\sigma} F^{\mu\nu} F^{\rho\sigma} + \frac{1}{2} (k_A F)^\mu \epsilon_{\mu\nu\rho\sigma} A^\nu F^{\rho\sigma}. \quad (4.5)$$

The k_F term is CPT-even while the $k_A F$ term is CPT-odd and leads to an unstable theory as well as vacuum birefringence [Mat05b]. In this work, CPT-even LV in the photon sector and its effects are treated in Sec. 4.3.

With steadily improving sensitivity of instruments and a variety of theories allowing for LV various different techniques can be used to test Lorentz invariance, with some examples of such experiments given here. Measurements of a sidereal variation due to a movement of the Earth to a Lorentz

violating background field have been done using the movements of particles confined in a Penning trap [BG86] for long periods of time [Mit+99] or through the comparison of atomic clocks based of different elements (see, e.g., [Bea+00; Bea+02; Phi+01]). Another terrestrial experiment to constrain LV is the study of the resonant frequency of cavity resonators, which will vary with orientation of the cavity in the case of LV (see, e.g., [Mat05b] for a list of experiments).

While terrestrial experiments are mostly concerned with low-energy processes, astrophysical tests can be used to probe the effects of LV at much higher energies. With a modified dispersion relation, the velocity of the photon becomes dependent on its energy. For two simultaneously emitted photons with different energies from an astrophysical source, the difference in the time of flight increases with distance. Thus, the observation of the arrival time of photons from distant sources such as GRBs, AGNs and pulsars can be used to constrain LV [Ell+00]. A similar approach is applied to constrain birefringence arising from LV. This LV-induced birefringence leads to a depolarisation of linearly polarized light. The observation of linearly polarized light from distant sources can thus be used to gain bounds on the corresponding LV parameter [JLM06]. Another possible effect of LV is a change in the interactions of elementary particles, which can manifest, e.g., in the appearance of new threshold reactions or the shift of thresholds for reactions in comparison to the SM. The implementation of two of those effects, photon decay and vacuum Cherenkov (VCh) radiation in the framework of the SME are discussed in greater depth in Sec. 4.3.1 and Sec. 4.3.2. Photon decay is forbidden in the SM and becomes allowed above a given energy threshold in the case of LV, thus the measurement of high-energy photons from distant sources gives a lower bound on this threshold energy and the corresponding LV parameter [KR08]. VCh radiation is the emission of photons for charged particles above a given threshold energy, leading to rapid energy loss, where direct observations of charged CRs can be used to obtain bounds on LV [KR08]. For a regularly updated list of bounds on LV derived by different methods, see [KR11].

4.3 Lorentz Violation in the Standard Model Extension

LV can be achieved by adding a single term to the Lagrange density, which breaks Lorentz invariance but preserves CPT and gauge invariance [CN83; KM02]:

$$\begin{aligned}
\mathcal{L} = & \underbrace{-\frac{1}{4}F^{\mu\nu}F_{\mu\nu} + \bar{\psi} [\gamma^\mu (i\partial_\mu - eA_\mu) - m] \psi}_{\text{standard QED}} \\
& \underbrace{-\frac{1}{4}(k_F)_{\mu\nu\rho\sigma}F^{\mu\nu}F^{\rho\sigma}}_{\text{CPT-even LV term}}
\end{aligned} \tag{4.6}$$

Natural units ($\hbar = c = 1$) are used throughout this chapter, as well as the Minkowski metric $g_{\mu\nu}(x) = \eta_{\mu\nu} = [\text{diag}(+1, -1, -1, -1)]_{\mu\nu}$. The added term depends on the tensor $(k_F)_{\mu\nu\rho\sigma}$, which consists of twenty independent components, as it is under the same symmetry restrictions as the Riemann tensor. Of those components, one corresponds to an unobservable double trace changing the normalisation of the photon field. Ten components produce birefringence, which is very strongly constrained by current cosmological observations [Fri+20]. Eight components lead to a direction-dependent modification of Lorentz invariance. In this work, only nonbirefringent, isotropic LV is considered. In this case, only one last independent component of $(k_F)_{\mu\nu\rho\sigma}$ remains, which is defined as follows [KS11a]:

$$\begin{aligned}
(k_F)_{\mu\nu\rho\sigma} &= \frac{1}{2} (\eta_{\mu\rho}\tilde{\kappa}_{\nu\sigma} - \eta_{\mu\sigma}\tilde{\kappa}_{\nu\rho} + \eta_{\nu\sigma}\tilde{\kappa}_{\mu\rho} - \eta_{\nu\rho}\tilde{\kappa}_{\mu\sigma}) \\
\tilde{\kappa}_{\mu\nu} &= \frac{\kappa}{2} [\text{diag}(3, 1, 1, 1)]_{\mu\nu}
\end{aligned} \tag{4.7}$$

The first line of Eq. (4.7) ensures nonbirefringence and the second gives isotropy. The deformation parameter κ (also referred to as $\tilde{\kappa}_{tr}$ in the literature, see e.g. [KR11; KS08; KM02]) is restricted to the half-open interval $(-1, 1]$ [KS11b].

The phase velocity of the photon is given as

$$v_\gamma = \frac{\omega}{|\vec{k}|} = \sqrt{\frac{1-\kappa}{1+\kappa}}c. \tag{4.8}$$

In this equation, c , still equal to one in the unit system used here, but added for greater clarity, refers to the maximum attainable velocity of a massive Dirac Fermion in Eq. (4.6). The photon phase velocity v_γ is greater than c in the case of negative values of κ , smaller than c in the case of positive values of κ and exactly c in the SM case of $\kappa = 0$. For non-zero values of κ , certain processes which are prohibited in Lorentz-invariant theories become possible.

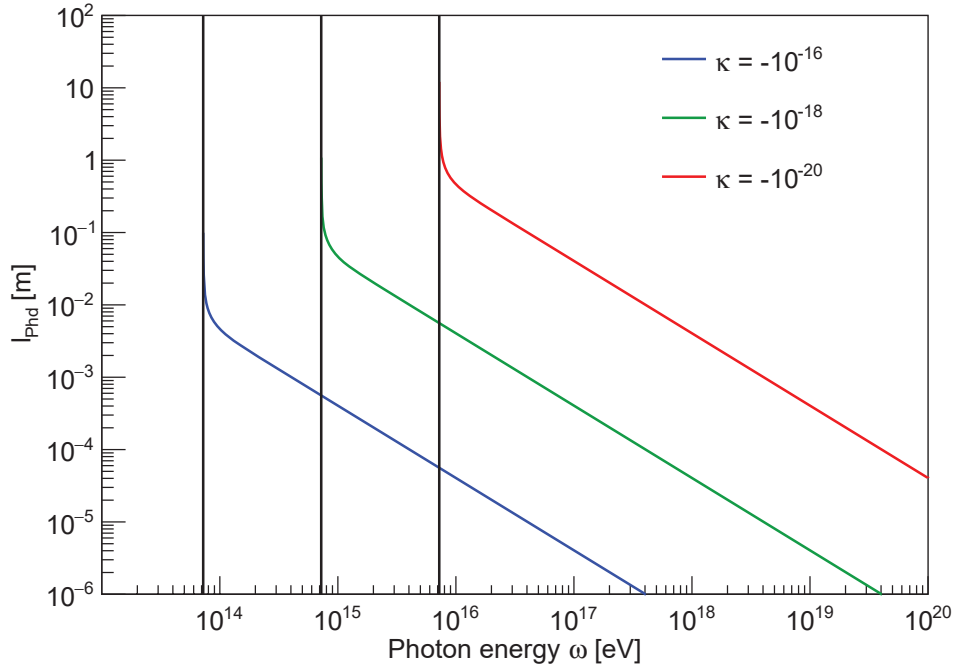


FIGURE 4.2: The photon decay length l_{PhD} due to LV induced photon decay dependent on photon energy ω . Values of $\kappa = -10^{-16}$, $\kappa = -10^{-18}$ and $\kappa = -10^{-20}$ are used. The threshold energies $\omega_{\text{th}}(\kappa)$ for the respective values of κ are marked by the vertical lines.

4.3.1 Lorentz Violation for $\kappa < 0$

In the case of negative values of κ , two processes which differ from the SM description have to be taken into account, which are explained in this section. The first process is the decay of the nonstandard photon into an electron-positron pair

$$\tilde{\gamma} \rightarrow e^+ + e^-, \quad (4.9)$$

which becomes allowed in this LV theory at sufficiently high energies. The energy threshold for photon decay $\omega_{\text{th}}(\kappa)$ is described in [KS08] as

$$\omega_{\text{th}}(\kappa) = 2 m_e \sqrt{\frac{1 - \kappa}{-2\kappa}} \simeq \frac{2 m_e}{\sqrt{-2\kappa}}. \quad (4.10)$$

In this description of $\omega_{\text{th}}(\kappa)$ and for the remaining part of this section, $m_e = 511 \text{ keV}$ denotes the rest mass of the electron. The decay rate Γ_{PhD} of a photon above the energy threshold $\omega_{\text{th}}(\kappa)$ is given by

$$\Gamma_{\text{PhD}} = \frac{\alpha}{3} \frac{-\kappa}{1 - \kappa^2} \sqrt{\omega^2 - \omega_{\text{th}}^2} \left[2 + \frac{\omega_{\text{th}}^2}{\omega^2} \right], \quad (4.11)$$

with the fine structure constant $\alpha = \frac{e^2}{4\pi} \approx \frac{1}{137}$ [DK15]. The decay length

$l_{\text{PhD}} = \frac{1}{\Gamma_{\text{PhD}}}$ of a photon in relation to its energy ω is presented in Fig. 4.2 for several values of κ . The photon decay length l_{PhD} decreases to the scale of meters or even centimeters right above the threshold energy $\omega_{\text{th}}(\kappa)$, corresponding to an effectively instantaneous decay in the context of this work.

The energies of the particles produced by the photon decay lie in the range $[E_-, E_+]$, given by [DK15]:

$$E_{\pm} = \frac{\omega}{2} \left[1 \pm \sqrt{\frac{1+\kappa}{1-\kappa} \left(1 - \frac{\omega_{\text{th}}^2}{\omega^2} \right)} \right] \quad (4.12)$$

The differential energy spectrum for the produced electrons is symmetric around $\omega/2$ and is given by:

$$\frac{d\Gamma_{\text{PhD}}}{dE} = \frac{-\alpha\omega}{\sqrt{\frac{1+\kappa}{1-\kappa}} (1+\kappa)^2} \left[\frac{2\kappa}{\omega^2} E^2 - \frac{2\kappa}{\omega} E + \frac{\kappa}{1-\kappa} - \frac{(1+\kappa)m_e^2}{\omega^2} \right] \quad (4.13)$$

The second particle, the positron, carries the remaining energy of the photon, due to the symmetry of the electron energy spectrum it is following the same energy distribution as the electron.

In addition to the addition of photon decay, the decay time τ of the neutral pion into two nonstandard photons,

$$\pi^0 \rightarrow \tilde{\gamma} + \tilde{\gamma}, \quad (4.14)$$

is modified. The magnitude of this modification depends on the pion energy E_{π^0} and the LV parameter κ [DKR16; Kli18]:

$$\tau(E_{\pi^0}, \kappa) = \frac{\tau_{\text{SM}}}{g(E_{\pi^0}, \kappa)} \quad (4.15)$$

The decay time of the neutral pion in the non-LV theory is represented by τ_{SM} , while $g(E_{\pi^0}, \kappa)$ is the modification factor defined as:

$$g(E_{\pi^0}, \kappa) = \begin{cases} \frac{\sqrt{1-\kappa^2}}{(1-\kappa)^3} \left[1 - \frac{(E_{\pi^0})^2 - (m_{\pi^0})^2}{(E_{\pi^0}^{\text{cut}})^2 - (m_{\pi^0})^2} \right]^2 & \text{for } E_{\pi^0} < E_{\pi^0}^{\text{cut}}, \\ 0 & \text{otherwise.} \end{cases} \quad (4.16)$$

The pion cutoff energy $E_{\pi^0}^{\text{cut}}$ is given by [Kli18]:

$$E_{\pi^0}^{\text{cut}} = m_{\pi^0} \sqrt{\frac{1-\kappa}{-2\kappa}} \simeq \frac{m_{\pi^0}}{\sqrt{-2\kappa}} = \frac{m_{\pi^0}}{2m_e} \omega_{\text{th}}(\kappa) \approx 132 \omega_{\text{th}}(\kappa) \quad (4.17)$$

The dominating decay channel of the neutral pion in the SM is the decay into a photon pair ($\pi^0 \rightarrow \gamma + \gamma$) with a branching ratio of 98.823(34) %. The second largest decay channel is the decay into electron, positron and photon ($\pi^0 \rightarrow e^+ + e^- + \gamma$), due to the internal conversion of one photon into an electron-positron pair, with a branching ratio of 1.174(35) % [Wor+22]. The decay with the third highest probability involves internal conversion of both photons into electron-positron pairs ($\pi^0 \rightarrow e^+ + e^- + e^+ + e^-$) and has only a branching ratio of $(3.34 \pm 0.16) \times 10^{-5}$. Thus, the decay of neutral pions is suppressed for LV with $\kappa < 0$, with the neutral pions becoming effectively stable above the cutoff energy $E_{\pi^0}^{\text{cut}}$.

The photon threshold energy ω_{th} gained from Eq. (4.10) is used here as well as the values of the rest masses of the neutral pion ($m_{\pi^0} \approx 135 \text{ MeV}$) and the electron ($m_e = 511 \text{ keV}$). Due to the higher pion mass, the pion cutoff energy $E_{\pi^0}^{\text{cut}}$ is about two orders of magnitude greater than the energy threshold for photon decay $\omega_{\text{th}}(\kappa)$. The modification of the neutral pion decay time leads to a decrease in the decay rate with energy, until the neutral pion becomes stable above the cutoff energy $E_{\pi^0}^{\text{cut}}$.

4.3.2 Lorentz Violation for $\kappa > 0$

In the case of positive values of κ , Vacuum Cherenkov (VCh) radiation, i.e., the emission of photons by charged particles above a given threshold energy $E_{\text{VCh}}^{\text{th}}(\kappa)$, becomes possible. This threshold is imposed by the conservation of energy and momentum and is described by [DK15]

$$E_{\text{VCh}}^{\text{th}}(\kappa) = m \sqrt{\frac{1+\kappa}{2\kappa}} \simeq \frac{m}{\sqrt{2\kappa}}. \quad (4.18)$$

Charged particles with a mass m above the threshold $E_{\text{VCh}}^{\text{th}}(\kappa)$ continuously radiate photons with the differential emission rate $\frac{d\Gamma_{\text{VCh}}}{d\omega}$ [DK15]:

$$\frac{d\Gamma_{\text{VCh}}}{d\omega} = \frac{\alpha Z^2}{E \sqrt{E^2 - m^2}} \left[\frac{2\kappa E}{1 - \kappa^2} (E - \omega) - \frac{m^2}{1 - \kappa} + \frac{\kappa}{(1 - \kappa^2)(1 - \kappa)} \omega^2 \right] \quad (4.19)$$

The differential emission rate $\frac{d\Gamma}{d\omega}$ depends on the charge of the particle Z in units of the proton charge e and the photon energy ω .

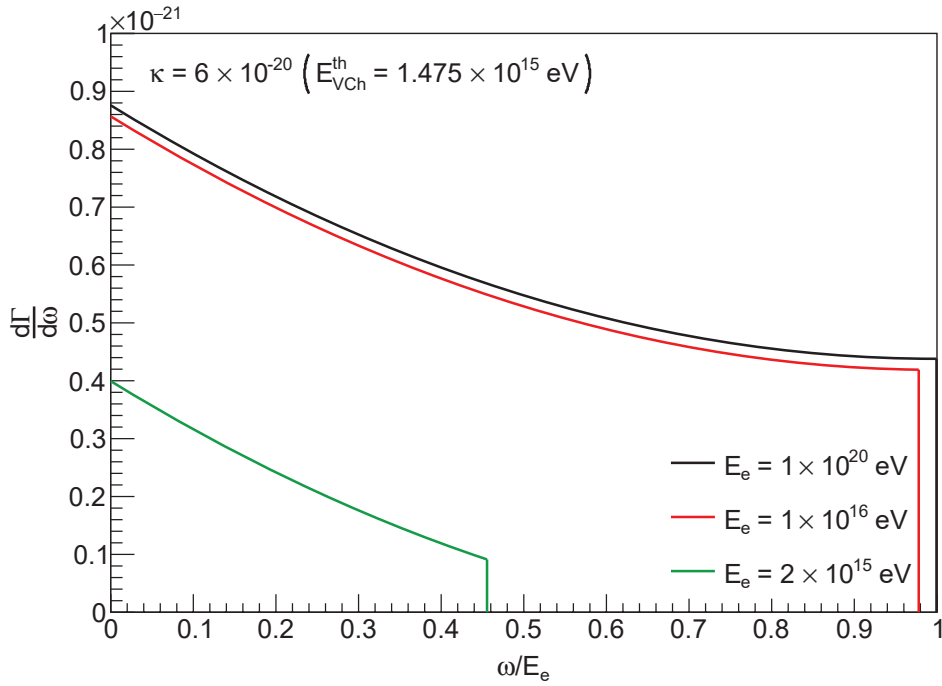


FIGURE 4.3: Differential emission rates of VCh photons in dependence of the energy fraction ω/E_e inherited from a primary electron for $\kappa = 6 \times 10^{-20}$ and different electron energies E_e .

The maximum energy of the radiated photon is given by the upper bound ω_{\max} , which results from energy-momentum conservation and prevents a divergence of radiated power [DK15]:

$$\omega_{\max} = \left(\frac{1 - \kappa}{\kappa} \right) \left[\sqrt{\frac{1 + \kappa}{1 - \kappa}} \sqrt{E^2 - m^2} - E \right]. \quad (4.20)$$

The differential photon spectrum in relation on the relative energy of the emitted photon is displayed in Fig. 4.3. A noteworthy feature of the spectrum is the low slope of the distribution for high primary particle energies, with only a factor of two between the emission rates at the highest and lowest allowed energies. This leads to a significant probability for the production of high energy photons. In addition to this, the maximum energy of the emitted photon is a significant portion of the primary particle energy, especially for high energy primary particles, where almost 100% of the primary particle energy can be emitted via one VCh photon. This no longer holds for electron energies near the VCh energy threshold $E_{VCh}^{th}(\kappa)$, where the maximum energy approaches zero as the electron energy approaches $E_{VCh}^{th}(\kappa)$.

The power radiated through VCh photons can be gained by integration of the differential energy spectrum with the inserted factor ω [KS08]:

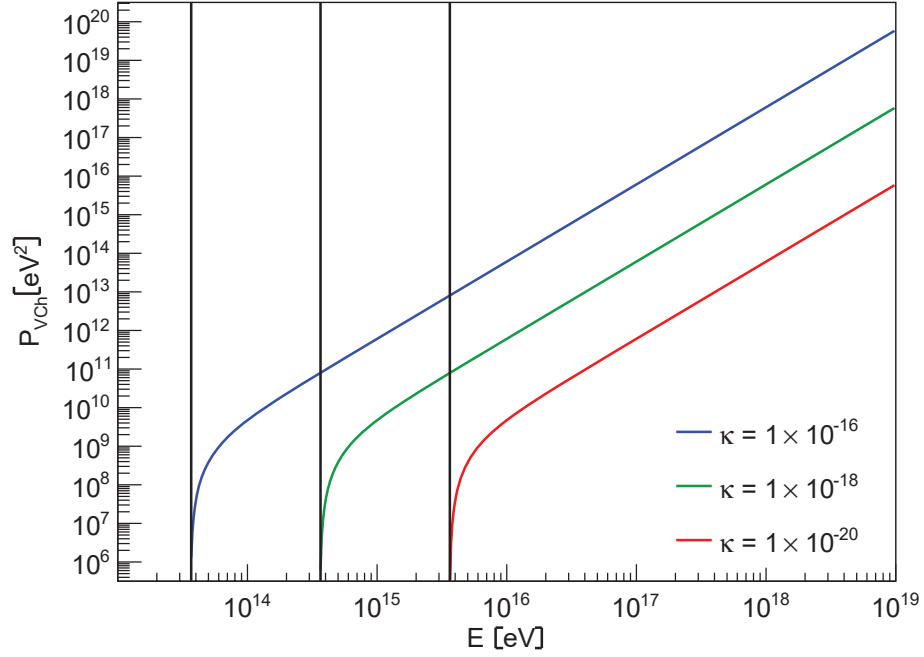


FIGURE 4.4: Rate of emitted energy from a electron emitting VCh radiation in relation to the electron energy for different values of κ . The energy thresholds of VCh radiation for different κ is marked by the black vertical lines.

$$\begin{aligned}
 P_{\text{VCh}}(E) &= \frac{\alpha}{24\kappa^3 E \sqrt{E^2 - m^2}} \left(\sqrt{\frac{1-\kappa}{1+\kappa}} E - \sqrt{E^2 - m^2} \right)^2 \\
 &\times \left[(8\kappa^2 + 8\kappa + 12) E^2 - (1 + \kappa) \right. \\
 &\left. \times \left(6(1 + 2\kappa) m^2 + 4(3 + 4\kappa) \sqrt{\frac{1-\kappa}{1+\kappa}} E \sqrt{E^2 - m^2} \right) \right] \quad (4.21)
 \end{aligned}$$

The energy emission rate for electrons of different energies with different values κ is displayed in Fig. 4.4. The radiated energy increases rapidly after the energy threshold $E_{\text{VCh}}^{\text{th}}$, slowing to an increase quadratic in energy at higher energies.

4.4 Bounds on LV from cosmic ray observations

The processes described in the previous sections lead to restrictions on the maximum energies of certain cosmic ray particles arriving at Earth, which can be used to test the LV theory. For $\kappa < 0$, photons above the threshold energy $\omega_{\text{th}}(\kappa)$ defined in Eq. (4.10) decay rapidly into electron-positron pairs

and would thus be unable to be observed at Earth. The observation of UHE photons by terrestrial experiments can thus be used to set bounds on κ . Measurements of a gamma ray with a primary energy of $\omega = 30$ TeV done by the H.E.S.S. Cherenkov telescope array [Aha+06] result in a lower limit on κ of [KS08]:

$$\kappa > -9 \times 10^{-16} \quad (98 \% \text{ CL}) . \quad (4.22)$$

This lower limit has been improved by exploiting the decrease of the shower maximum $\langle X_{\text{max}} \rangle$ caused by LV in [KNR17], showing the sensitivity of air shower observations to LV. The comparison between the values of $\langle X_{\text{max}} \rangle$ gained from LV shower simulations to air shower observations was done under the assumption of a pure proton composition. This was done as the composition of CRs is uncertain, with protons leading to the most conservative bounds. The result from this analysis improved the limit gained from primary photon observations by a factor of 3000 to:

$$\kappa > -3 \times 10^{-19} \quad (98 \% \text{ CL}) . \quad (4.23)$$

In the case of $\kappa > 0$, charged particles above the threshold energy given by Eq. (4.18) rapidly lose energy due to VCh radiation. Such particles are consequently unable to reach Earth at energies above the given threshold. Reversely, any observation of those particles implies a threshold energy higher than the energy of the observed particle. This has been used to set an upper bound on κ using measurements done by the Pierre Auger Observatory of UHE cosmic rays in the order of $E_{\text{prim}} = 150$ EeV [Abr+08]. Under the conservative assumption of an iron nucleus as primary particle, this results in an upper bound of [KS08]:

$$\kappa < 6 \times 10^{-21} \quad (98 \% \text{ CL}) . \quad (4.24)$$

4.5 Changes in extensive air showers due to LV

The additional processes introduced due to LV lead to significant changes in the development of extensive air showers. In both cases of $\kappa < 0$ and $\kappa > 0$ those differences are mainly situated in the electromagnetic part of the shower.

For $\kappa < 0$, photons in the early stages of the shower with energies above the energy threshold for photon decay ω_{th} can occur. This leads to a faster development of the electromagnetic component and a faster overall shower development. This in turn leads to a shorter electromagnetic component of the shower, resulting in an overall shorter shower with a smaller atmospheric depth of the shower maximum X_{max} .

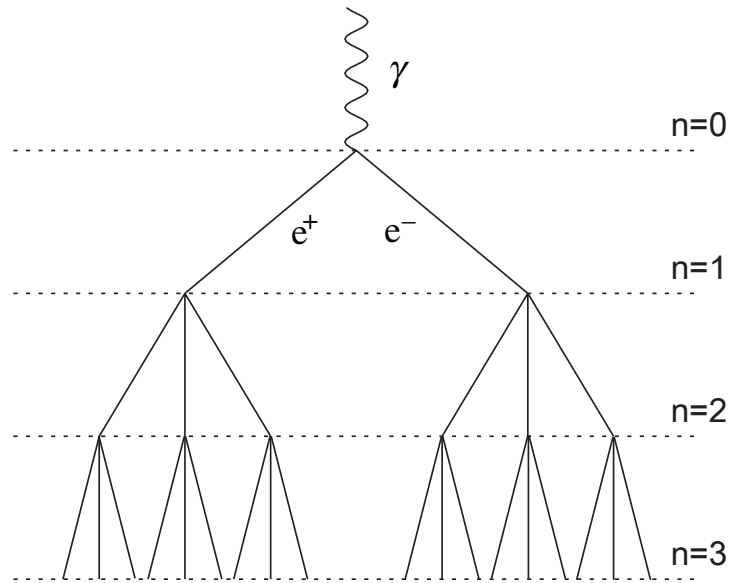


FIGURE 4.5: Schematic depiction of the Heitler model modified to include photon decay. Shown is the shower development over the first three interaction lengths. Electrons and positrons are depicted as straight lines, the initial photon as a wavy line. While the initial photon is depicted for illustration purposes, all photons decay immediately into electron-positron pairs, leading to a multiplicity of three at each vertex after the first interaction.

This change can be approximately modeled in a modified version of the Heitler model, the process of which is also described in [DKR16]. Ordinarily, each photon "decays" into an electron-positron pair via pair production, while each of the charged particles emits a photon after the interaction length λ . With the implementation of photon decay, each photon with an energy $\omega_0 > \omega_{\text{th}}$ decays into an electron-positron pair rapidly. As an example, a photon right above ω_{th} for $\kappa = -10^{-20}$ has an interaction length of less than 1 m, which translates to a traversed atmospheric depth of $\approx 0.12 \text{ g cm}^{-2}$ with the density of air at sea level and even less at higher altitudes, where the first interactions of the shower occur and the air is less dense. In comparison to the typical interaction length of 25 g cm^{-2} for electromagnetic interactions discussed in Sec. 2.1.1, this decay is practically instantaneous. This applies both to the first photons in the electromagnetic cascade, which were produced by the neutral pion decay, and photons produced via Bremsstrahlung inside the shower.

For each generation of the electromagnetic cascade in which a photon is produced via Bremsstrahlung with an energy above ω_{th} , the process is thus modified to $e^\pm \rightarrow e^\pm + \tilde{\gamma} \rightarrow e^\pm + (e^+ + e^-)$. The three resulting particles have the relative energies $1/2$, $1/4$ and $1/4$ respectively, but for a simplified

treatment a relative energy of $1/3$ each is assumed here. A schematic view of this model is depicted in Fig. 4.5. With these assumptions, the energy of each particle in each generation changes for a primary photon with $\omega_0 > \omega_{\text{th}}$. The first photon decays instantly, thus the zeroth generation consists of two leptons with $E_0 = \omega_0/2$. For each following generation for which $E > \omega_{\text{th}}$ holds, the particle energy can be described by

$$E_n = \frac{\omega_0/2}{3^n}. \quad (4.25)$$

As soon as the particle energy falls below ω_{th} , the shower develops conventionally, as described in Sec. 2.1.1. The atmospheric depth of the shower maximum in the case of $\omega_0/2 > \omega_{\text{th}} > E_{\text{crit}}$ can thus be described by splitting the shower into two parts, above and below ω_{th} , with different elongation rates:

$$X_{\text{max}} = \frac{\lambda}{\ln 3} \ln \left(\frac{\omega_0/2}{\omega_{\text{th}}} \right) + \frac{\lambda}{\ln 2} \ln \left(\frac{\omega_{\text{th}}}{E_{\text{crit}}} \right) \quad (4.26)$$

The first part of this equation describes the shower behaviour above ω_{th} and the second part describes the standard behaviour of the shower for energies below ω_{th} . For $\omega_0 > \omega_{\text{th}} > \omega_0/2 > E_{\text{crit}}$ only the initial photon decays, leading to

$$X_{\text{max}} = \frac{\lambda}{\ln 2} \ln \left(\frac{\omega_0/2}{E_{\text{crit}}} \right). \quad (4.27)$$

For $\omega_0 < \omega_{\text{th}}$ no photon decay occurs and the conventional description of the Heitler model as given in Eq. (2.2) holds.

In addition to photon decay, the lifetime of high energy neutral pions increases due to LV. This leads to an overall decrease in decays of neutral pions into electron-positron pairs. These pions can then travel further through the atmosphere, undergoing additional hadronic interactions, which would otherwise be impossible. In the simplified model introduced in Sec. 2.1.2, there is no energy transfer from the hadronic component to the electromagnetic component as long as $E_{\pi^0} > E_{\pi^0}^{\text{cut}}$ is satisfied. As explained in Sec. 2.1.2, hadronic interactions produce multiple secondary particles with larger interaction lengths than electromagnetic interactions in the shower. With this in mind, the delay of energy transfer from the hadronic component to the electromagnetic component of the shower speeds up the shower development, again leading to shorter showers. Additionally, the average energy of neutral pions decaying into photon pairs will decrease, which leads to a higher number of electromagnetic subshowers initiated by lower-energy photons. This can reduce the effect of the photon decay on the air shower development, as less generations in the electromagnetic shower contain photons above the energy threshold ω_{th} .

In the case of $\kappa > 0$, VCh radiation also occurs mainly in the electromagnetic component of the shower. The reason for this is the combination of the low mass of the electron and the relatively high possible energies of the first particles of the electromagnetic component of the air shower. The scale of the interaction lengths is the same as for photon decay, i.e. meters and below, and is thus assumed to be quasi-instantaneous in the context of air shower development. The quasi-instantaneous radiation of photons leads to a higher energy loss of the first electrons and positrons than what would conventionally happen due to Bremsstrahlung. This results in a fast conversion of the kinetic energies of those charged particles to photons emitted through VCh radiation. Overall, the LV shower has an early electromagnetic component consisting of more photons than the SM shower, with the energy distributed over more individual particles. A description of VCh radiation in the Heitler model is not practical, as one lepton may emit any number of VCh photons with energies which may be highly varying.

Additionally the type of primary particles arriving at Earth are restricted because of VCh radiation at high energies. For protons, the maximum energy of a primary particle arriving at Earth is given by the energy threshold for VCh radiation:

$$E_{\text{VCh,p}}^{\text{th}} = \frac{m_{\text{p}}}{m_{e^{\pm}}} E_{\text{VCh},e^{\pm}}^{\text{th}}(\kappa) \approx 1800 E_{\text{VCh},e^{\pm}}^{\text{th}}(\kappa) \quad (4.28)$$

Protons above this threshold would quickly lose energy through VCh radiation and thus not be observable at Earth. The same holds true for higher mass primaries, where the energy threshold for energy loss through VCh radiation is proportional to the particle mass A :

$$E_{\text{VCh,nucleus}}^{\text{th}} \approx A E_{\text{VCh,p}}^{\text{th}} \quad (4.29)$$

This leads to primary particles with progressively higher masses dominating the composition of cosmic rays at the highest energies under the assumption of a positive κ , with a total cutoff of the spectrum at the threshold energy of the highest mass primary particles.

Secondary particles other than electrons produced in the early stages of the shower development may also be affected by VCh radiation. In particular, muons and pions are probable candidates for early VCh production, as it is possible for them to inherit large fractions of the primary particle energy and they possess masses lower than the proton. These high energies are needed, as the energy thresholds for VCh described in Eq. (4.18) are proportional to the mass of the particle. This leads to the following energy thresholds for muons and pions:

$$E_{\text{VCh},\mu^{\pm}}^{\text{th}} = \frac{m_{\mu^{\pm}}}{m_{e^{\pm}}} E_{\text{VCh},e^{\pm}}^{\text{th}}(\kappa) \approx 200 E_{\text{VCh},e^{\pm}}^{\text{th}}(\kappa) \quad (4.30)$$

$$E_{\text{VCh},\pi^\pm}^{\text{th}} = \frac{m_{\pi^\pm}}{m_{e^\pm}} E_{\text{VCh},e^\pm}^{\text{th}}(\kappa) \approx 270 E_{\text{VCh},e^\pm}^{\text{th}}(\kappa) \quad (4.31)$$

Those energy thresholds are less than one decade below the energy threshold for protons. It follows that for a shower initiated by a primary particle closely below its energy threshold $E_{\text{VCh},p}^{\text{th}}$, a secondary pion (muon) would have to inherit more than 15% (11%) of the primary particle energy to undergo VCh radiation. While this is not impossible, such events are rare and thus expected to only have a minor impact on the average shower development. For primary particles with lower energies, the number of non-electron particles undergoing VCh radiation further decreases and becomes zero for primary particles with energies of less than the VCh threshold energy $E_{\text{VCh},\pi^\pm}^{\text{th}}$ of the muon.

Chapter 5

Used software, simulations and data

To analyze the impact of LV on the development of air showers, a full Monte Carlo (MC) approach as in [KNR17] is used. The MC code CONEX [Ber+07; Pie+06], v2r7p50, was used, with appropriate modifications to implement LV. The simulation code as well as the implemented modifications are explained in Sec. 5.1. Hadronic interactions are simulated with the three high-energy interaction models EPOS LHC [Pie+15] and QGSJET-II-04 [Ost11] as well as with SIBYLL 2.3d [Rie+20]. For all settings not explicitly mentioned, the defaults provided by the CONEX code are used. To be able to compare the simulated air showers to observation, X_{\max} measurements taken by the Pierre Auger Observatory are used, as documented in Sec. 5.2. In the last part of this chapter, Sec. 5.3, the preparation of both simulations and Auger measurements for the analysis in Ch. 6 is explained.

5.1 CONEX

CONEX is a fast, one-dimensional hybrid shower simulation code. It combines MC simulations of the high-energy hadronic interactions with a fast numerical approach for less-energetic secondary particles. Particles above a threshold are treated in the standard MC way like they would be by e.g. CORSIKA [Hec+98]. For lower energies, the cascades initiated by secondary particles are described using cascade equations. This results in both a high efficiency and high accuracy. CONEX was chosen in preference over a full MC simulation program like CORSIKA because of the much faster computation of showers at the energies of interest in this work ($E > 10^{18}$ eV). While a shower simulated with CORSIKA at energies above 10^{18} eV may typically take hours to simulate, simulation with CONEX takes only times in the order of tens of seconds, although simulation time increases with modification. All modifications are done inside the `conex_sub.F` source file and can be found in the appendix A with their respective positions in the original file noted.

5.1.1 Modifications for $\kappa < 0$

In this section, the changes added to the CONEX code to implement photon decay and modified neutral pion decay are discussed.

Modifications for photon decay are implemented in the EGS4 section of the code by adding an instantaneous decay of photons above the threshold energy defined in Eq. (4.10). When a photon above threshold is detected, it is replaced by an electron-positron pair. This is done inside the SHOW subroutine of the EGS4 code as displayed in the appendix A.1. The energy of the photon is divided up over the resulting particles according to the differential energy spectrum of the electron given in Eq. (4.13). The integrated energy spectrum is used to draw energy values according to the differential energy spectrum and is derived by integration of Eq. (4.13) from E_- to E :

$$\begin{aligned} \Gamma(E) &= \int_{E_-}^E \frac{d\Gamma_{\text{PhD}}}{dE'} dE' = \frac{-\alpha\omega}{\sqrt{\frac{1+\kappa}{1-\kappa}} (1 + \kappa^2)} \\ &\times \left[\frac{2\kappa}{3\omega^2} (E^3 - E_-^3) - \frac{\kappa}{\omega} (E^2 - E_-^2) \right. \\ &\left. + \left(\frac{\kappa}{1-\kappa} - \frac{(1+\kappa)m_e^2}{\omega^2} \right) (E - E_-) \right] \end{aligned} \quad (5.1)$$

Here E is the energy of the electron, E_- is the minimum energy of the electron defined by Eq. (4.12) and ω is the energy of the initial photon. The fine-structure-constant $\alpha = \frac{1}{137}$ and the mass of the electron $m_e \approx 511$ keV are also used. For this, a uniformly distributed random number is drawn and transformed to fit the differential energy spectrum using the normalized integrated energy spectrum $\Gamma(E)/\Gamma(E_+)$. The energy E_{e^-} of the first secondary particle, arbitrarily chosen to be the electron, is drawn using the subroutine `lvdrawrandomenergy` displayed in the appendix A.5. The output of one million calls to the `lvdrawrandomenergy` subroutine is displayed in Fig. 5.1, showing good agreement between the distribution of drawn values and the target distribution $\frac{d\Gamma_{\text{PhD}}}{dE}$. After drawing the secondary particle energy, the photon is effectively converted into an electron by changing the particle ID to -1 and the particle energy is set to the drawn value. The second produced particle is generated by adding an identical particle on top of the EGS4 stack, but changing particle id to 1 and energy to $E_{e^+} = \omega - E_{e^-}$.

The modified decay time of the neutral pion is implemented by adding a multiplicative factor g as given by Eq. (4.16) to the pion decay time. This is done in the propagation routine, where the decay time of the pion is also determined in the standard CONEX code. The code used to accomplish this can be viewed in the appendix A.4.

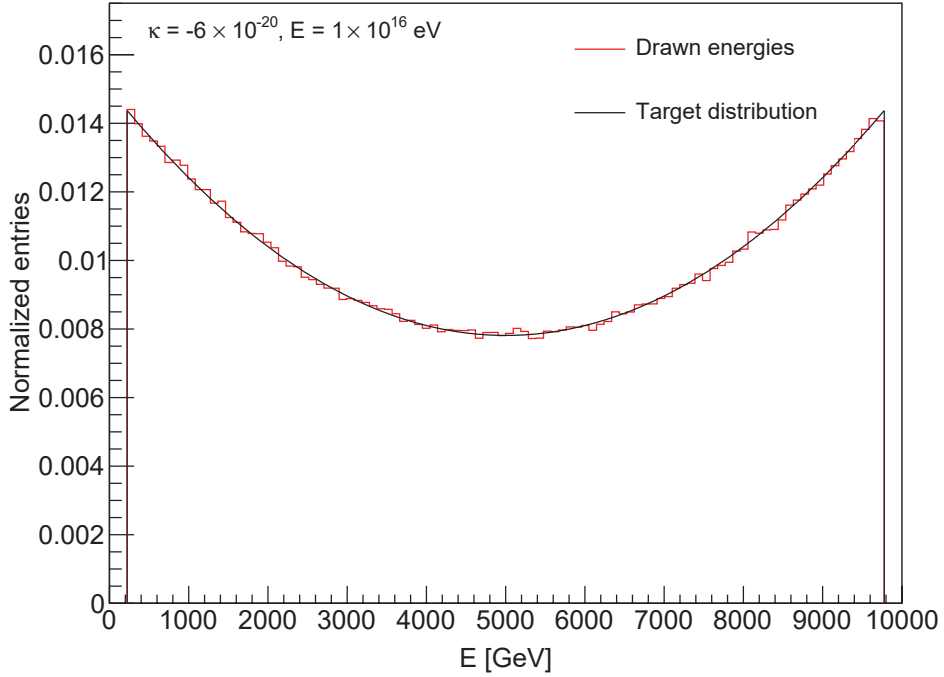


FIGURE 5.1: Comparison between 1000000 energy values for an electron produced by photon decay drawn by `lvdrawrandomenergy` (red) and the differential energy spectrum $\frac{d\Gamma_{\text{phD}}}{dE}$ (black). The values were drawn for a primary photon energy $\omega = 10^{16} \text{ eV}$ and $\kappa = -6 \times 10^{-20}$.

5.1.2 Modifications for $\kappa > 0$

For values of $\kappa > 0$, VCh radiation for electrons and positrons is achieved by adding an additional, instantaneous "decay" of electrons/positrons above the threshold energy given by Eq. (4.18). This "decay" replaces the original electrons/positrons and produces a photon with an energy according to the distribution given in Eq. (4.19) as well as an electrons/positrons with accordingly reduced energy. This is accomplished similarly to the photon decay in the $\kappa < 0$ case, by adding a section of code into the EGS4 section of CONEX. There, any electron or positron above the threshold energy produces a photon with an energy according to Eq. (4.19), reducing its energy by the same amount, which is shown in appendix A.6. The photon energy is drawn in the subroutine `lvdrawrandomenergy`, modified for $\kappa > 0$ and using the integrated energy spectrum Γ_{VCh} :

$$\Gamma_{\text{VCh}}(\omega) = \frac{\alpha Z^2}{E\sqrt{E^2 - m^2}} \left[\frac{2\kappa E\omega}{1 - \kappa^2} \left(E - \frac{\omega}{2} \right) - \frac{m^2}{1 - \kappa} \omega + \frac{\kappa}{3(1 - \kappa^2)(1 - \kappa)} \omega^3 \right] \quad (5.2)$$

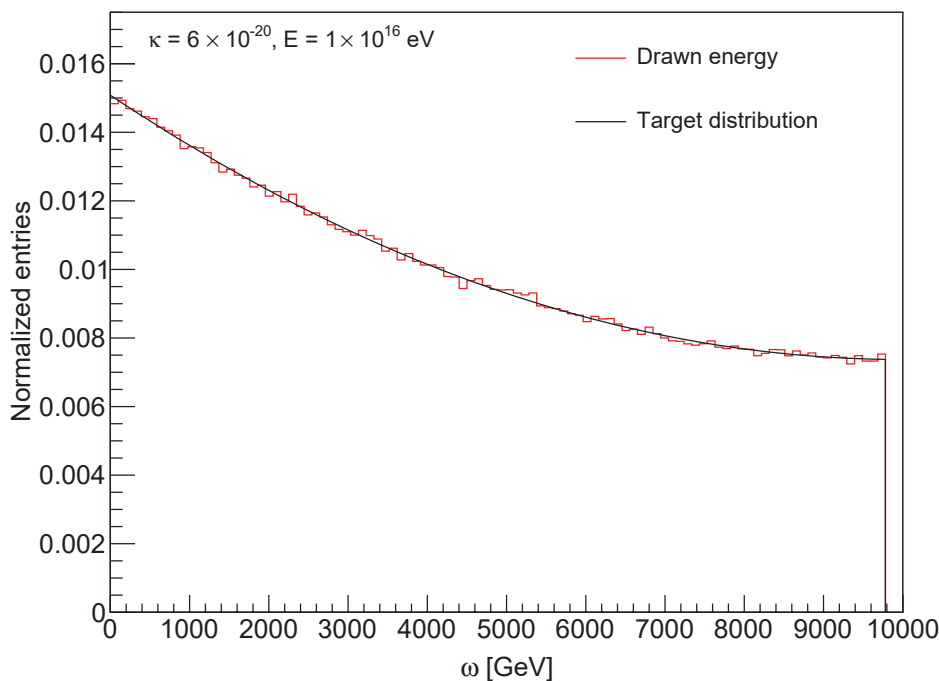


FIGURE 5.2: Comparison between 1000000 values for a VCh photon drawn by `lvdrawrandomenergy` (red) and the differential energy spectrum $\frac{d\Gamma_{\text{phD}}}{dE}$ (black). The values were drawn for a primary electron with energy $E = 10^{16}$ eV and $\kappa = 6 \times 10^{-20}$.

As in the case of $\kappa < 0$, the energy of the produced photon is drawn using a random number and transforming it onto the energy via the normalized integrated energy spectrum $\Gamma_{\text{VCh}}(\omega)/\Gamma_{\text{VCh}}(\omega_{\text{max}})$, with the maximum photon energy ω_{max} defined by Eq. (4.20). The code for this can be seen in the appendix A.12 and a comparison between 1000000 VCh photon energies drawn and the expected distribution is shown in Fig 5.2. The generation of a photon with the drawn energy is done in EGS4 by duplicating the initial particle, changing the ID of the first particle to that of the photon (0) and adjusting the energies of both particles.

The implementation of VCh radiation for charged particles other than electrons/positrons is not as straightforward. Here, during propagation the energy of VCh candidate particles is compared to their respective energy thresholds. For energies above threshold, a flag is set to replace the SM interaction with VCh radiation, the code adding this for muons and pions is found in appendix A.7, A.8 and A.9. The radiation of a VCh photon is done in an added subroutine.

The subroutine for the VCh radiation of particles other than electrons or positrons is called `VCPionInteraction`, due to it overwhelmingly being applied to pions, and is documented in the appendix A.13. As particles outside the electromagnetic shower are not processed by the EGS4 section of

the CONEX code, the VCh radiation is implemented via an additional decay mode `imode = 100`, which is set in the propagation method for particles above their respective VCh energy thresholds. Particles with this decay mode are processed by a modified version of the existing CONEX code for QBall-production, which fulfills in principle the same function as the EGS4 implementation: drawing an energy using `1vdrawrandomenergy` and producing a photon with this energy while reducing primary particle energy by the same amount.

5.2 Auger data samples

The X_{\max} data used here was taken by the Pierre Auger Observatory and covers the measurement period for December 2004 to December 2017 [Yus19]. This data sample consists only of hybrid events, observed both by the fluorescence telescopes and at least one surface detector station. The combination of both observations leads to an increased precision in the X_{\max} measurement, which is the main observable examined in this work. Even though data from the Pierre Auger Observatory was used here, in principle data taken by any experiment measuring the X_{\max} distribution of UHECR can be used to perform the steps in the analysis.

The Auger data sample consists of $\langle X_{\max} \rangle$ and $\sigma(X_{\max})$ measurements for energies above $10^{17.2}$ eV with their respective statistical and systematic errors, with events binned by their reconstructed primary particle energies. The energy bins have a width of 0.1 in $\log_{10}(E)$ with a total of 25 bins. The last bin includes all events with an energy of $10^{19.6}$ eV or greater instead of the usual bin width. This last bin is generally excluded in this analysis, since it covers a wider energy range and has, with only 35 observed events, a poor statistical accuracy. A table containing the used X_{\max} moments is shown in Tab. 5.1.

For this analysis, only measurements from the Pierre Auger Observatory are used, as measurements from the Telescope array (TA) are not corrected for detector effects [Abb+18], possibly skewing the analysis. In addition to this, TA measurements and Auger measurements have found to be consistent within their uncertainties [Ung16; Yus23].

5.3 Preparation of air shower data and simulations

In this section, the processing of both the X_{\max} data taken by the Pierre Auger Observatory as well as the simulations produced using the modified version of CONEX is explained. In Sec. 5.3.1 both $\langle X_{\max} \rangle$ and $\sigma(X_{\max})$ values of showers observed by the Pierre Auger Observatory are taken and used to derive two-dimensional confidence intervals on $\langle X_{\max} \rangle / \sigma(X_{\max})$ for each measured primary particle energy bin. In Sec. 5.3.2, the combination of simulated showers with different primary particle masses to replicate arbitrary primary particle compositions is shown.

| $\langle \log_{10}(E/\text{eV}) \rangle$ | # of events | $\langle X_{\text{max}} \rangle [\text{g cm}^{-2}]$ | | | $\sigma(X_{\text{max}}) [\text{g cm}^{-2}]$ | | |
|--|-------------|---|------------------------|--------------------------|---|------------------------|--------------------------|
| | | mean | σ_{stat} | $\sigma_{\text{sys,up}}$ | mean | σ_{stat} | $\sigma_{\text{sys,up}}$ |
| 17.26 | 1052 | 665.5 | 2.61 | 9.52 | 60.6 | 3.9 | 2.79 |
| 17.35 | 1617 | 680.2 | 2.08 | 9.17 | 64.7 | 3.0 | 2.68 |
| 17.45 | 2264 | 682.2 | 1.61 | 8.86 | 58.3 | 2.5 | 2.58 |
| 17.55 | 2565 | 688.9 | 1.61 | 8.58 | 59.1 | 2.5 | 2.47 |
| 17.65 | 2620 | 694.8 | 1.3 | 8.33 | 56.3 | 2.0 | 2.37 |
| 17.75 | 2320 | 705.0 | 1.65 | 8.06 | 60.5 | 2.6 | 2.27 |
| 17.85 | 7303 | 712.3 | 1.0 | 7.63 | 58.3 | 1.3 | 2.16 |
| 17.95 | 6232 | 720.3 | 1.1 | 7.49 | 58.9 | 1.5 | 2.15 |
| 18.05 | 5022 | 728.7 | 1.2 | 7.38 | 59.6 | 1.8 | 2.27 |
| 18.15 | 4095 | 736.1 | 1.2 | 7.31 | 59.1 | 1.6 | 2.31 |
| 18.25 | 3255 | 742.8 | 1.3 | 7.27 | 58.0 | 1.7 | 2.29 |
| 18.35 | 2527 | 748.0 | 1.5 | 7.26 | 56.7 | 2.1 | 2.22 |
| 18.45 | 1933 | 752.8 | 1.6 | 7.29 | 54.0 | 2.1 | 2.12 |
| 18.55 | 1347 | 755.2 | 1.8 | 7.34 | 51.2 | 2.2 | 1.98 |
| 18.65 | 1007 | 760.8 | 2.0 | 7.43 | 54.5 | 2.8 | 1.83 |
| 18.75 | 707 | 757.2 | 1.9 | 7.54 | 43.5 | 2.5 | 1.66 |
| 18.85 | 560 | 763.2 | 2.0 | 7.67 | 42.0 | 2.4 | 1.51 |
| 18.95 | 417 | 766.0 | 2.4 | 7.83 | 38.6 | 2.9 | 1.36 |
| 19.05 | 321 | 770.1 | 2.6 | 8.01 | 39.3 | 3.2 | 1.25 |
| 19.15 | 253 | 770.7 | 2.6 | 8.21 | 34.8 | 3.4 | 1.17 |
| 19.25 | 159 | 777.2 | 3.5 | 8.44 | 41.3 | 5.2 | 1.14 |
| 19.35 | 122 | 776.3 | 3.2 | 8.68 | 33.9 | 4.1 | 1.17 |
| 19.44 | 80 | 775.7 | 4.5 | 8.92 | 37.1 | 5.2 | 1.26 |
| 19.55 | 50 | 783.7 | 4.2 | 9.22 | 26.6 | 5.1 | 1.45 |
| 19.73 | 35 | 776.2 | 4.8 | 9.75 | 25.3 | 4.2 | 2.02 |

TABLE 5.1: Auger X_{max} moments published in [Yus19].

5.3.1 Two-dimensional contours of Auger Data

Previous analyses investigating isotropic, nonbirefringent LV in the photon sector (e.g., [KNR17]) employed a one-dimensional approach which compared only $\langle X_{\max} \rangle$ values of LV simulations to measurements. Here, this approach is extended to also include $\sigma(X_{\max})$ in the comparison. While a separate treatment of both observables is possible, it is more precise to do a simultaneous comparison. This is an expansion from one dimension to two dimensions, and thus a two dimensional confidence interval or confidence region has to be defined. In previous analyses (e.g., [KR08; KNR17]), a confidence level of 98 % was used, for reasons of comparability this is also adopted here.

To gain the combined probability density distributions, two assumptions are made about the underlying distributions of both statistical and systematic errors of $\langle X_{\max} \rangle$ and $\sigma(X_{\max})$. For statistical errors, a normal distribution is assumed. Mean and standard deviation of the distributions are given by the mean and the statistical error of the respective observable. As the systematic errors do not change between measurements, a split uniform distribution was chosen for those instead of a normal distribution. The distribution is split into the intervals $[m - \sigma_{\text{sys,low}}, m]$ and $[m, m + \sigma_{\text{sys,high}}]$ for an observable with a mean m and systematic errors of $\sigma_{\text{sys,low}}$ and $\sigma_{\text{sys,high}}$. The distribution is split in such a way that there is a 50 % probability for values both above and below the mean value. No correlations between the error distributions for $\langle X_{\max} \rangle$ and $\sigma(X_{\max})$ or statistical and systematic errors were assumed.

The two-dimensional confidence interval is generated numerically using a toy MC model. This is achieved by first generating a large number (10^{10}) of values randomly distributed according to the probability density distributions of both observables. The generated values are binned in both $\langle X_{\max} \rangle$ and $\sigma(X_{\max})$. The bins containing the highest number of entries are added to the two-dimensional confidence interval, until 98 % of all entries are contained in it. The result of this process for two of the energy bins of the X_{\max} data taken by the Pierre Auger Observatory [Yus19] can be seen in Fig. 5.3. The bins have widths of $0.06 \frac{\text{g}}{\text{cm}^2}$ for $\langle X_{\max} \rangle$ and $0.02 \frac{\text{g}}{\text{cm}^2}$ for $\sigma_{\text{sys,high}}$, any finer binning would not result in any increase in the precision of the analysis, as the X_{\max} values given by data only include a precision of $0.1 \frac{\text{g}}{\text{cm}^2}$.

In principle, this method can be used to gain two-dimensional confidence intervals for measurements taken by any experiment measuring the atmospheric depth of the shower maximum X_{\max} of large numbers of air showers, as long as either the entire set of X_{\max} with associated primary particle energies or $\langle X_{\max} \rangle$ and $\sigma(X_{\max})$ are available.

5.3.2 Combination of Simulations

The composition of cosmic-ray particles, especially at high energies, is a subject which is currently actively investigated, as discussed in Sec. 1.4. While

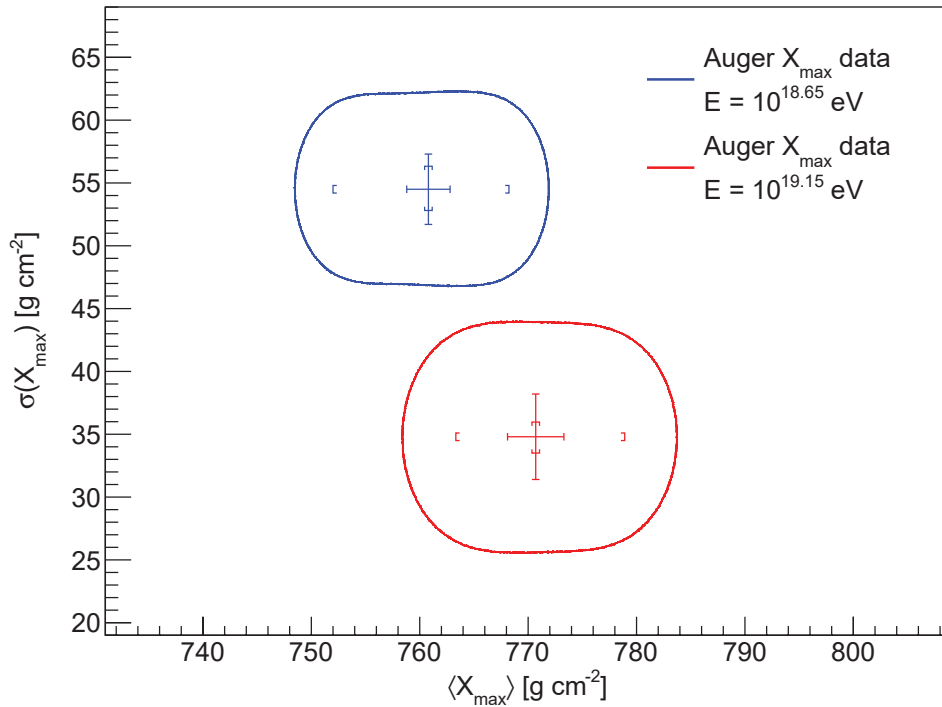


FIGURE 5.3: The range of all possible $\langle X_{\max} \rangle / \sigma(X_{\max})$ -values inside the contours of the two-dimensional confidence interval derived from Auger X_{\max} data. The contours are shown for select energy bins, statistical errors are indicated by lines, systematic errors by brackets.

the composition tends to shift towards heavier particles with increasing energy, the exact fractions are uncertain. In addition to this, changes in the shower development, such as those implemented here for LV, would have to be taken into account, which makes a composition obtained under an SM assumption not transferable to the LV case. Thus, no a-priori assumption about the primary particle composition is made here, which leads to any combination of particles in the mass range $1 \leq A \leq 56$ being allowed. Heavier particles are excluded, since they only occur in trace amounts in CRs and no significant contribution of those elements is expected.

To account for any possible composition of primary particles while also simplifying the analysis, selected elements were chosen as representatives of their respective mass ranges. Chosen were protons (mass number $A = 1$), helium nuclei ($A = 4$), oxygen nuclei ($A = 16$) and iron nuclei ($A = 56$) for the case of $\kappa < 0$ and protons, helium, lithium ($A = 7$), beryllium ($A = 9$), boron ($A = 11$), nitrogen ($A = 14$), silicon ($A = 28$) and iron nuclei for $\kappa > 0$. The greater number of low-mass elements simulated for $\kappa > 0$ is due to the lower masses progressively becoming excluded from the possible compositions at higher energies and greater values of κ , as explained in Sec. 4.5. Important observables used for the analysis described in Cha. 6 are $\langle X_{\max} \rangle$ and $\sigma(X_{\max})$, both of which are derived from the distribution of the values of X_{\max} in a given sample. For $\langle X_{\max} \rangle$, the mean value of the X_{\max}

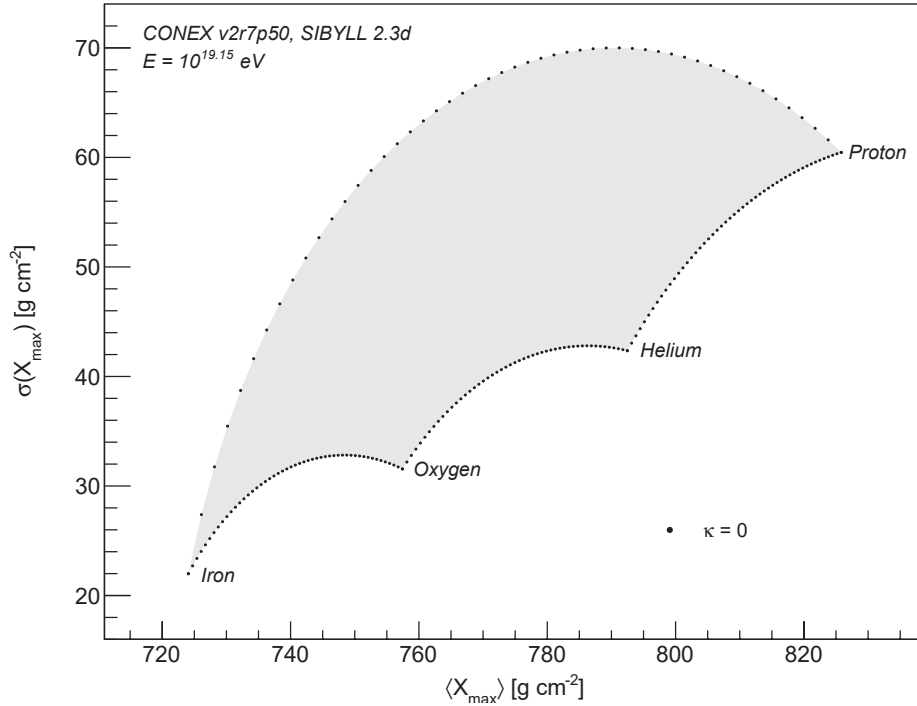
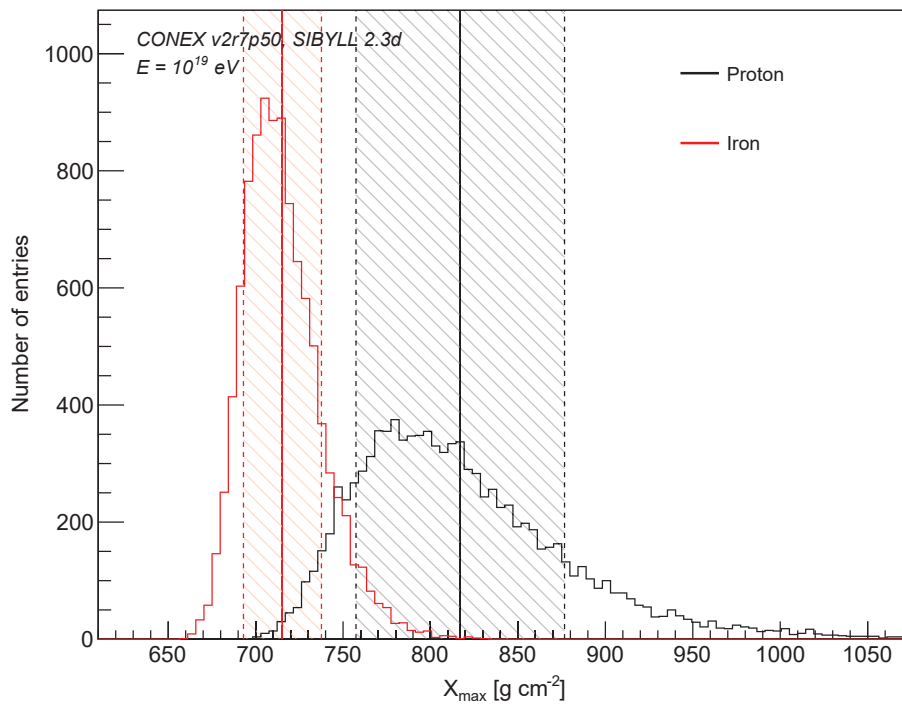


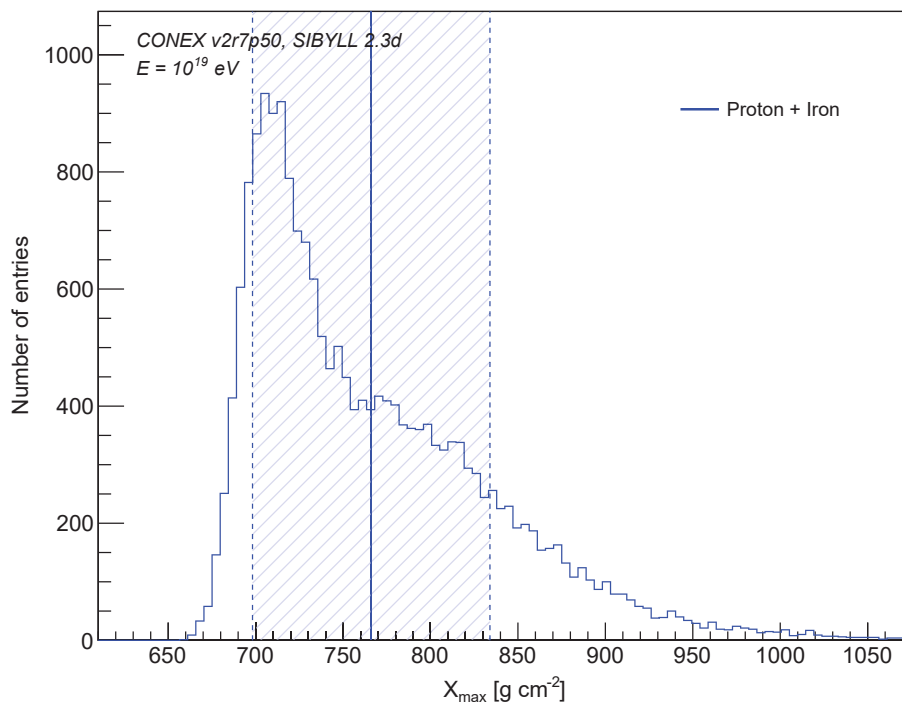
FIGURE 5.4: The range of all possible $\langle X_{\max} \rangle / \sigma(X_{\max})$ -values for combinations of simulated air showers induced by primary protons, helium, oxygen and iron nuclei for $\kappa = 0$ and a primary particle energy of $10^{19.15}$ eV. Displayed are only proton-helium, helium-oxygen, oxygen-iron and iron-proton combinations, since all other possible combinations of those four elements produce $\langle X_{\max} \rangle / \sigma(X_{\max})$ -values inside the umbrella-shaped area defined by those. Any point is differing 2% in composition from the neighboring points.

distribution is taken, while $\sigma(X_{\max})$ describes the width of the same distribution. For a pure composition, only simulations for the respective primary particle are taken into account. For any other composition, simulations for different primary particles are weighted to their respective fraction of the overall composition. Those weighted simulations are then combined to form the cumulative X_{\max} distribution. The values for $\langle X_{\max} \rangle$ and $\sigma(X_{\max})$ can be extracted from this distribution.

The resulting $\langle X_{\max} \rangle / \sigma(X_{\max})$ -combinations for a fixed value of energy and $\kappa = 0$ are displayed in Fig. 5.4. The area covered by the allowed values has a distinctive, umbrella-like shape, with pure compositions at the tips of the shape. This shape is due to the different behaviour of $\langle X_{\max} \rangle$ and $\sigma(X_{\max})$ under combination of different primary particle masses. The resulting $\langle X_{\max} \rangle$ value of any combination has the same value as the weighted mean of the $\langle X_{\max} \rangle$ values of all components. In contrast to this, the value of $\sigma(X_{\max})$ for any combination of different masses is always greater than the weighted mean of the $\sigma(X_{\max})$ values of all components. Due to the difference in $\langle X_{\max} \rangle$ between showers resulting from particles of different masses, the X_{\max} distribution becomes wider once different masses are introduced.



(A)



(B)

FIGURE 5.5: Distributions of X_{\max} for simulated showers initiated by protons and iron nuclei (A), as well as the sum of both distributions (B). The primary particle energy is $E = 10^{19}$ eV in both cases. The mean values of each distribution are marked by the vertical continuous lines, the corresponding 1σ widths are shown by the shaded areas.

An example of this for showers initiated only by protons and iron nuclei as well as by a mixture of 50 % of both is shown in Fig. 5.5. This example shows the extreme case of a combination of particles with the highest difference in mass. The value of $\langle X_{\max} \rangle$ changes from 817 g cm^{-2} and 715 g cm^{-2} for the individual X_{\max} distributions for protons and iron to 766 g cm^{-2} for the combined distribution, which is the expected mean of the individual values. For $\sigma(X_{\max})$, the values preceding combination are 59.6 g cm^{-2} and 22.3 g cm^{-2} for protons and iron respectively, this increases to 67.8 g cm^{-2} for the combined distribution, more than 8 g cm^{-2} more than for protons, the wider of the two initial distributions.

The area covered by all possible compositions, marked grey in Fig. 5.4, is confined by two-particle-type compositions of particles with neighboring mass numbers as well as the proton-iron combinations, which are the dotted points at the edges of the area. Any composition of more than two of the chosen primary particles is contained inside those bounds. This is used to reduce the number of examined compositions. For n primary particles combined in s equidistant steps, the number of operations decreases from $\mathcal{O}(s^n)$ for a full simulation of all possible combinations to $\mathcal{O}(s \cdot n)$ operations for just the edges.

The compositions used as an outline of all possible composition were taken in steps of 2 % between neighboring two-particle compositions. The different primary particles were chosen because they are roughly equidistant in $\ln A$, with additional primary particles added for $\kappa > 0$ for higher precision once lower mass primaries become excluded due to VCh radiation, as discussed in Sec. 4.5. This leads, due to the superposition principle described in Sec. 2.1.2, to roughly equidistant values of $\langle X_{\max} \rangle$ for those particles at the same energy, which results in a good coverage of possible $\langle X_{\max} \rangle / \sigma(X_{\max})$ combinations with a low number of simulated primary particles. Increasing the number of primary particle masses simulated leads to additional tips between the tips of previously adjacent particles of the umbrella seen in e.g. Fig. 5.4. It was tested if adding additional simulated primary particles with different masses changes the limits derived in Sec. 6.2.2 and Sec. 6.3.2. For $\kappa < 0$, there are no changes to the limit on κ , as the additional particles only add additional information in a $\langle X_{\max} \rangle / \sigma(X_{\max})$ region of no relevance to this specific analysis. The impact of the choice of allowed primary particles for $\kappa > 0$ is discussed in Sec. 6.3.2.

Chapter 6

Analysis of simulated air showers

In this chapter, the effects of LV on air showers simulated with the modified versions of CONEX are discussed. First, the general method used to derive new limits on LV is explained in Sec. 6.1.

Sec. 6.2 treats the case of $\kappa < 0$, where the changes are dominated by the introduction of photon decay, leading to a significant impact on both the longitudinal development of the shower as well as the number of muons in the shower. Changes in the longitudinal shower development are the topic of Sec. 6.2.1. The results of this section are used in Sec. 6.2.2 to significantly improve previous limits on $\kappa < 0$. In Sec. 6.2.3, the changes in the muon number are discussed, followed by Sec. 6.2.4, where the resulting changes in the correlation between shower depth and muon number are investigated.

In Sec. 6.3, the case of $\kappa > 0$ is treated similarly. The effects of the introduction of VCh radiation into the shower on the longitudinal shower development are discussed in Sec. 6.3.1, and used in Sec. 6.3.2 to derive a new limit on κ . The effects of LV on the muon number in the shower are shown in Sec. 6.3.3. In Sec. 6.3.4, the changes in the correlation between shower depth and muon number through VCh radiation are discussed.

6.1 General Method

In previous works discussed in Sec. 4.4, direct observations were used to set bounds on isotropic, nonbirefringent LV [KS08]. The bound on $\kappa < 0$ was improved by studying the impact of LV on the air shower development in [KNR17], exploiting changes in the atmospheric depth of the shower maximum $\langle X_{\max} \rangle$ caused by LV. To gain a conservative determination of the limit, a pure composition of only protons was assumed. Those previous limits are also discussed in Sec. 4.4. In this work, this method is expanded to take into account additional observables, the most prominent being $\sigma(X_{\max})$, the fluctuations in the atmospheric depth of the shower maximum. As $\sigma(X_{\max})$ is found to be stable in regards to LV, but differs for primary particles with different mass numbers A (see Sec. 2.1.2), it is a natural candidate to aid in restricting possible primary particle compositions. This makes a deviation from the assumption of the pure proton composition possible.

No assumptions about the composition of cosmic rays are made here, so all possible compositions have to be taken into account. This is accomplished by choosing several different mass numbers (e.g., $A = 1, 4, 16$ and 56 for $\kappa < 0$) representative of their respective mass ranges, and then combining those representatives for any possible combination. For the following analysis, possible combinations of $\langle X_{\max} \rangle$ and $\sigma(X_{\max})$ are of interest. The process of extracting the range of possible $\langle X_{\max} \rangle / \sigma(X_{\max})$ combinations from simulations for pure primary particles is described in detail in Sec. 5.3.2.

6.2 Results for $\kappa < 0$

The introduction of LV processes into the shower, particularly the decay of the nonstandard photon, is expected to cause significant changes in its development, as discussed in Sec. 4.5. The observables analyzed in this work were chosen because they are expected to be sensitive to those changes. Significant changes in the atmospheric depth of the shower maximum X_{\max} due to LV are shown in Sec. 6.2.1. Significant discrepancies between air shower measurements and simulations for values of κ at the previously established bound [KNR17] can be seen when comparing both the mean of the atmospheric depth of the shower maximum $\langle X_{\max} \rangle$ and its fluctuations $\sigma(X_{\max})$. This is used to improve previous limits in Sec. 6.2.2. Significant changes can also be observed in the number of muons produced in the shower, which directly translates to the number of muons N_{μ} observable at ground level. This is discussed in Sec. 6.2.3. The impact of LV with $\kappa < 0$ on the correlation between the shower parameters X_{\max} and N_{μ} , as well as possible approaches to exploit these changes in searches for LV, is covered in Sec. 6.2.4. The differences in shower development between different hadronic interaction models are discussed in Sec. 6.3.5.

6.2.1 Changes in X_{\max}

The expected changes of the interactions taking place inside the air showers are discussed in Sec. 4.5. Those changed interactions lead to a noticeable decrease in the elongation rate (rate of change of $\langle X_{\max} \rangle$ with increasing energy) of the shower at highest energies. This in turn leads to a lower atmospheric depth of the shower maximum $\langle X_{\max} \rangle$ in comparison to the SM case. This effect can be seen in Fig. 6.1, where the distributions of X_{\max} values for three sets of showers simulated for primary protons with an energy of 10^{19} eV and LV parameters of $\kappa = 0$ (SM), $\kappa = -1 \times 10^{21}$ and $\kappa = -1 \times 10^{19}$ chosen as an example. For both depicted values of κ , the effects of LV on the shower development are visible at the shown energy, with the mean value of the X_{\max} distribution ($\langle X_{\max} \rangle$) decreasing for larger values of κ . In addition to that, the distribution becomes slightly more narrow, which can be seen especially in the shown distributions below the maximum, which corresponds to a decrease in the fluctuations between showers ($\sigma(X_{\max})$). The magnitude of these effects as well as the dependence on κ , primary particle energy and primary particle type are discussed in the following paragraphs.

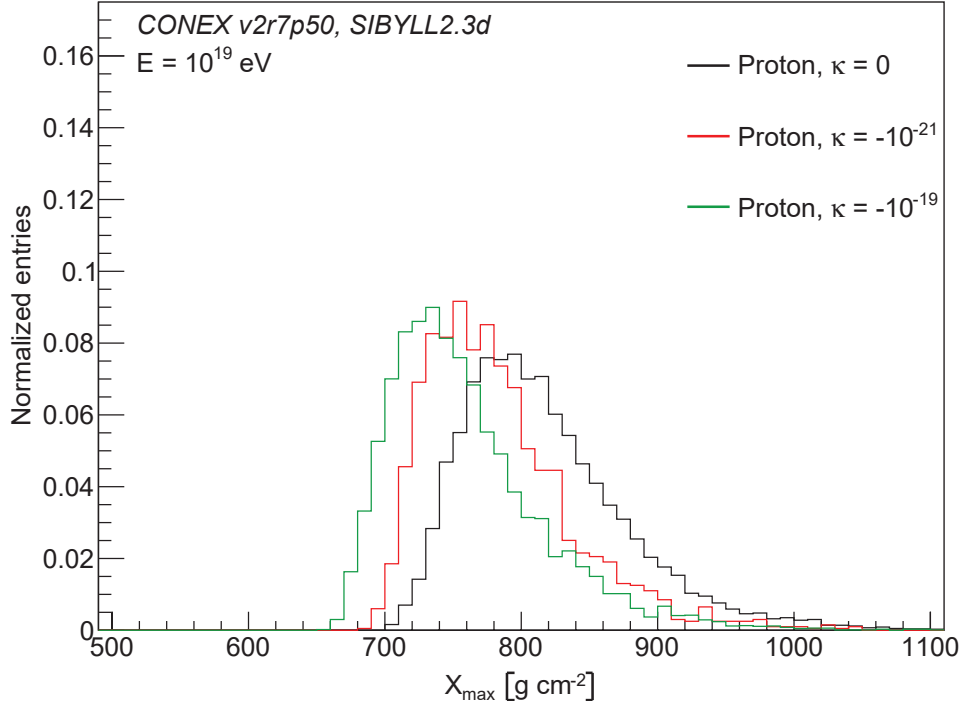


FIGURE 6.1: The distribution of simulated values of X_{\max} for primary protons with an energy of 10^{19} eV for the absence of LV ($\kappa = 0$) and for different values of $\kappa < 0$.

The changes in $\langle X_{\max} \rangle$ for $\kappa = -1 \times 10^{21}$ and $\kappa = -1 \times 10^{19}$ over the energy range covered by this analysis are displayed in Fig. 6.2. Several distinctive features are added to the development of $\langle X_{\max} \rangle$ with energy. The most obvious of those is the decrease in the elongation rate at the highest energies in the case of $\kappa < 0$ in comparison to $\kappa = 0$. In the SM case the elongation rate stays at an approximate value of 55 g cm^{-2} per decade in energy through the entire energy range, independent of the primary mass. In the case of LV, the elongation rate decreases to $\approx 35 \text{ g cm}^{-2}$ per decade in energy above an energy threshold of

$$E_{\text{ER}}^{\text{th}}(A, \kappa) \approx sA\omega_{\gamma}^{\text{th}}(\kappa) \quad (6.1)$$

with the atomic mass number A of the primary particle, a factor $s \approx 10$ and the energy threshold for photon decay $\omega_{\gamma}^{\text{th}}(\kappa)$ from Eq. (4.10). The factor s depends on the energies of the highest-energy photons in the shower in relation to the primary particle energy, as LV only becomes relevant to the shower development as photons of sufficient energy occur in the shower.

As an example, for $\kappa = -1 \times 10^{21}$, which corresponds to a threshold energy of $E_{\gamma}^{\text{th}} = 2.3 \times 10^{16}$ eV, the average number of photon decays per proton induced shower is 0.66 at a primary particle energy of $E = 10^{17.5}$ eV, with no photon decay occurring in 1154 of 2000 simulated showers. At this energy, even of those showers that are affected by photon decay, most only experience a single photon decay (528 out of the 846 showers with photon decay),

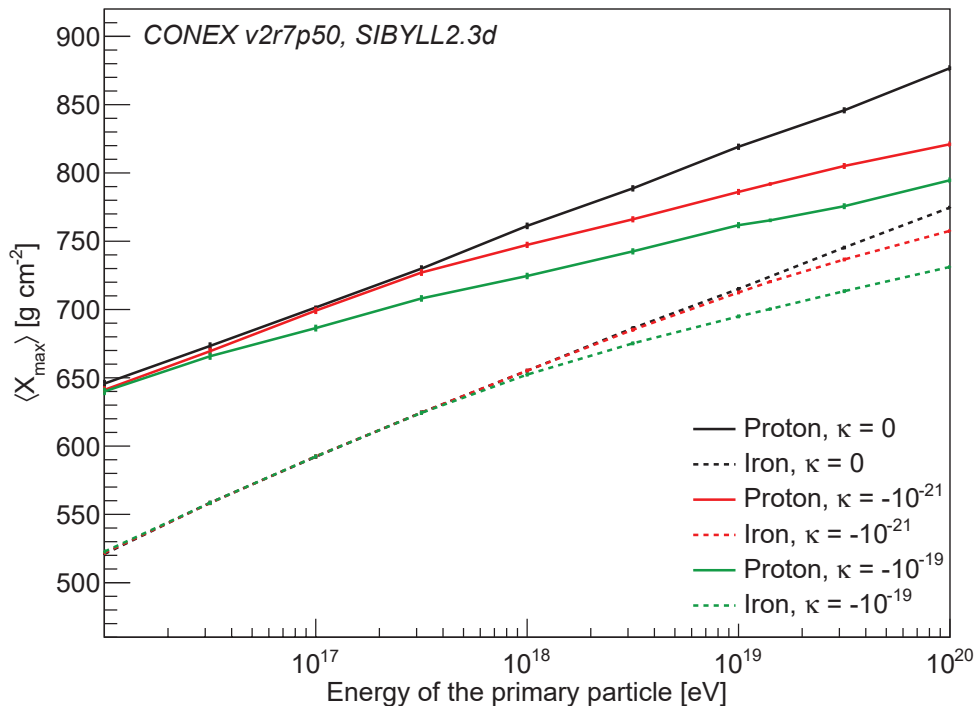


FIGURE 6.2: The simulated values of $\langle X_{\max} \rangle$ as a function of the primary energy for primary protons and iron nuclei for the absence of LV ($\kappa = 0$) and for different values of $\kappa < 0$.

which only leads to a small overall change in $\langle X_{\max} \rangle$ of 6 g cm^{-2} at this energy. The average number of photon decays in each shower increases with increasing primary particle energy to 3.89 decays at $E = 10^{18} \text{ eV}$, which leads to a change in $\langle X_{\max} \rangle$ of 14 g cm^{-2} , and 17.40 decays at $E = 10^{18.5} \text{ eV}$, leading to a change in $\langle X_{\max} \rangle$ of 21 g cm^{-2} . With higher primary particle energy, the number of photon decays increases an approximate factor of 12 for each decade in primary particle energy, while the difference in $\langle X_{\max} \rangle$ increases with $\ln E$.

While the threshold of the change in elongation rate is dependent on κ , the elongation rate above the threshold is not, leading to $\langle X_{\max} \rangle$ values for different values of κ remaining parallel at energies above the higher $E_{\text{ER}}^{\text{th}}$. This can be understood through the modified Heitler model introduced in Sec. 4.5. With an increase in primary particle energy, the starting energy of the electromagnetic subshowers increases, for which the atmospheric depth increases with the decreased elongation rate. In fact, the relative change in elongation rate predicted by the modified Heitler model, $\ln 2 / \ln 3 = 0.631$, closely matches the change in elongation rate for modified simulated air showers, $35 \text{ g cm}^{-2} / 55 \text{ g cm}^{-2} = 0.636$.

The difference in $\langle X_{\max} \rangle$ between the SM and the LV case for a given primary mass is thus dependent on both the energy of the primary particle as well as the value of κ . At the highest energies, differences of the order 50 g cm^{-2} and more can be seen. This value is large in comparison to the resolution of X_{\max} measurable by current experiments and should thus produce

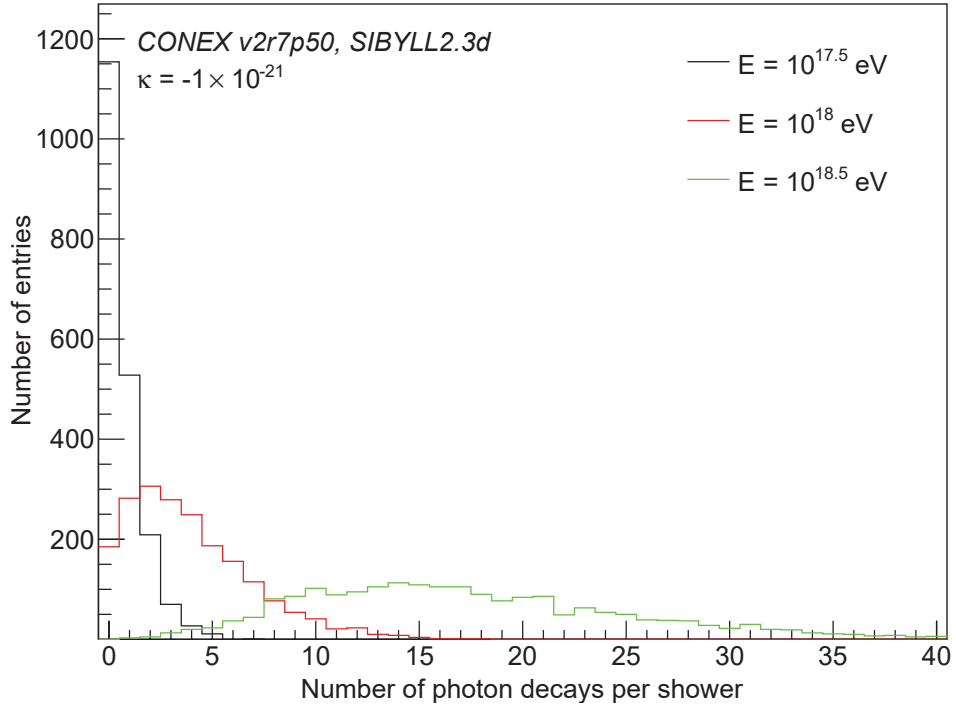


FIGURE 6.3: Distribution of the number of photon decays per shower for 2000 showers simulated with $\kappa = -1 \times 10^{21}$ and different energies of a primary proton.

measurable signals in the case of LV. The resolution of the X_{\max} measurements of the Pierre Auger Observatory for example is 25 g cm^{-2} at $10^{17.8}$ eV, improving with higher energies to 15 g cm^{-2} above $10^{19.3}$ eV [Aab+14a].

Another effect of the introduction of LV into the shower development is a decrease in the difference between $\langle X_{\max} \rangle$ values of different primary particles. According to the superposition principle explained in Sec. 2.1, a shower initiated by a particle with an atomic mass number A and energy E can be approximated by A showers of energy $\frac{E}{A}$. This leads to lower energies of secondary particles produced in a shower of higher mass primary particles with the same primary particle energy. Due to this effect, photons above E_{γ}^{th} appear only at higher energies for higher mass primary particles [KNR17], which leads to the factor A in the energy threshold for changes in X_{\max} given in Eq. 6.1.

Due to the difference in $E_{\text{ER}}^{\text{th}}$ for primary particles of different masses, there is a range of energies where showers initiated by lower-mass primary particles are already affected by changes due to LV, while showers of higher mass particles display no changes in development caused by LV, due to their lower secondary particle energies. In this energy range, the $\langle X_{\max} \rangle$ values of both types of showers approach each other at higher energies until the higher mass showers are also above their respective $E_{\text{ER}}^{\text{th}}$. Above this energy, the difference in $\langle X_{\max} \rangle$ between showers initiated by different primaries does not change further, since the elongation rate is again the same. This effect can, e.g., be seen in Fig. 6.2 for showers initiated by protons ($A = 1$) and iron

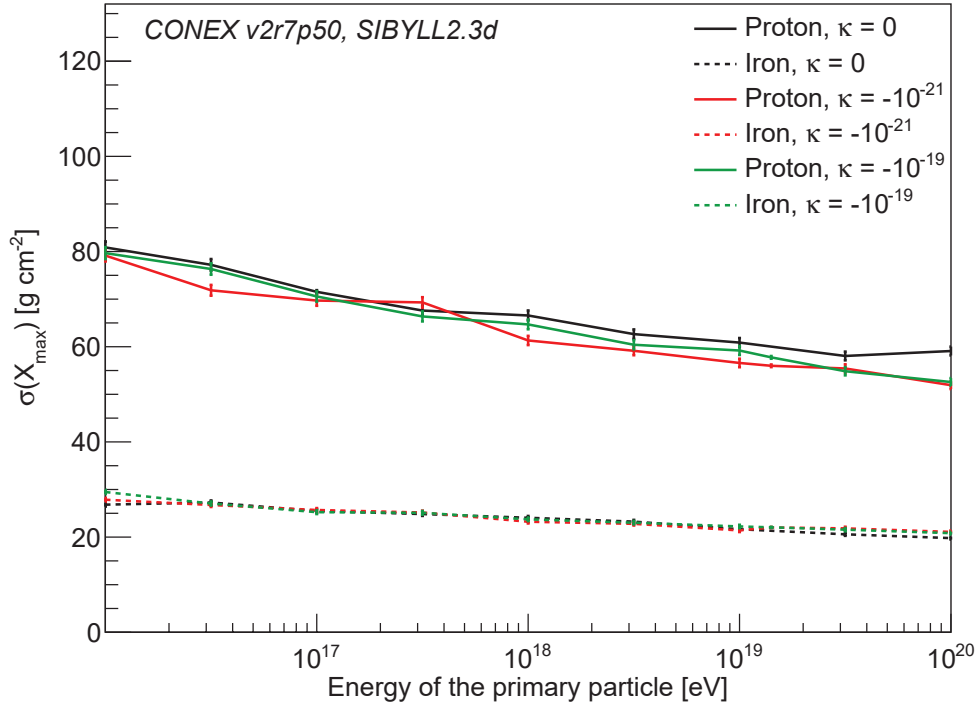


FIGURE 6.4: The simulated values of $\sigma(X_{\max})$ as a function of the primary energy for primary protons and iron nuclei for the absence of LV ($\kappa = 0$) and for different values of $\kappa < 0$.

nuclei ($A = 56$), simulated with $\kappa = -1 \times 10^{19}$. The visible change of $\langle X_{\max} \rangle$ occurs at $E \approx 10^{16.5}$ eV for protons, while the showers initiated by iron nuclei are changed at energies above $E \approx 10^{17.75}$ eV. In this energy range, the difference in $\langle X_{\max} \rangle$ between both particles decreases from $\approx 120 \text{ g cm}^{-2}$ at $E = 10^{16.5}$ eV to $\approx 75 \text{ g cm}^{-2}$ at $E = 10^{18}$ eV, due to the difference in elongation rates. This same effect can be seen for any value of κ , with the energy thresholds shifting with κ according to Eq. 6.1.

A second important value used to describe shower behaviour used in this analysis are the shower-to-shower fluctuations $\sigma(X_{\max})$. The impact of LV of different magnitudes on the $\sigma(X_{\max})$ values of shower simulations can be seen in Fig. 6.4. There are no changes as significant as the changes in $\langle X_{\max} \rangle$ seen here. Above $E_{\text{ER}}^{\text{th}}$, $\sigma(X_{\max})$ of proton induced showers decreases over the next decade of energy until a difference of approximately 4 g cm^{-2} between SM simulations and simulations with LV, independent of the value of κ . The errors of the differences in each energy bin are of the order 0.7 g cm^{-2} , which makes this a difference of $\approx 4\sigma$ when taking into account only a single bin, with the significance increasing with the number of energies above the threshold taken into account. For heavier primaries, the changes in $\sigma(X_{\max})$ are further reduced until the difference between simulations with SM and LV becomes compatible with zero for iron primaries. This relatively low change is due to $\sigma(X_{\max})$ being dominated by the first interaction of the shower [MR18], which is hadronic and unaffected by LV. An explanation for the minor decrease in $\sigma(X_{\max})$ can be found in the shortening in the initial phase of the electromagnetic sub-showers due to photon decay. Since the

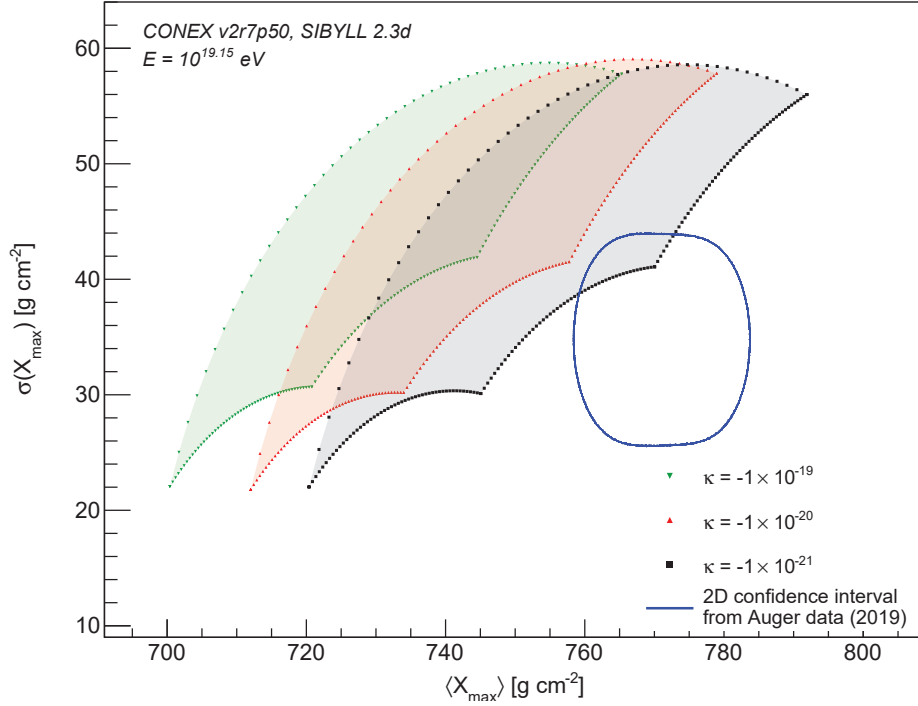


FIGURE 6.5: Comparison of the $\langle X_{\max} \rangle$ - $\sigma(X_{\max})$ -combinations derived by simulations which incorporate LV to the 2D confidence intervals given by the measurements of the Pierre Auger Observatory [Yus19] for different values for κ and a primary particle energy of $10^{19.15}$ eV.

photons above E_{γ}^{th} decay instantly instead of interacting after a randomly distributed time the fluctuations in the electromagnetic sub-shower decrease, leading to a minor decrease in the fluctuations of the overall shower. Showers initiated by heavier particles have a higher multiplicity of photons with lower fluctuations, which decreases the impact of LV on $\sigma(X_{\max})$ for those showers.

6.2.2 New limit on $\kappa < 0$ using X_{\max} measurements

In this section, the changes in the showers presented in Sec. 6.2.1 are used to derive new bounds on $\kappa < 0$, improving previous limits. This new limit on $\kappa < 0$ was already published in [DNR21]. The limit on κ is gained by comparing the sets of simulated values obtained from the combined simulations which are produced as explained in Sec. 5.3.2 to the confidence regions derived from measurements taken by the Pierre Auger Observatory described in Sec. 5.3.1. This comparison is done for each value of κ and each primary particle energy separately. For each of those comparisons, all possible combinations of $\langle X_{\max} \rangle$ and $\sigma(X_{\max})$ produced by combinations of simulations of showers with different primary particles are compared to the confidence region derived from Auger data.

An illustration of this comparison for a primary particle energy of $E =$

$10^{19.15}$ eV and differing values of κ can be seen in Fig. 6.5. This specific energy bin was chosen for demonstration as it is in the energy range between $10^{18.9}$ eV and $10^{19.2}$ eV which is of particular importance to determine the new bounds, as this energy range shows the differences between simulations and data for the largest values of κ . Both the decrease in $\langle X_{\max} \rangle$, discussed in Sec. 6.2.1, as well as the stability of $\sigma(X_{\max})$ with respect to changes in κ can be seen in this figure. The lighter particles are influenced by LV for all values of κ at this energy, which is reflected in a decrease of $\approx 20 \text{ g cm}^{-2}$ in $\langle X_{\max} \rangle$ with each decade in κ . Iron showers, located at the lower tip of the umbrella-plots, are just starting to be influenced by LV with $\kappa = -1 \times 10^{-21}$ at $E = 10^{19.15}$ eV, which can be seen in the lower difference in $\langle X_{\max} \rangle$ between iron showers simulated with $\kappa = -1 \times 10^{-20}$ and $\kappa = -1 \times 10^{-21}$.

These comparisons are done repeatedly for different values of κ for all energy bins. For each of those comparisons, it is determined if there is a possible simulated primary particle composition matching Auger data within the given confidence level, which is illustrated by overlap between two areas (simulated vs. observed) in Figs. 6.5 to 6.7. Reversely, if there is no primary particle combination which fits the Auger measurements, indicated by no overlap between both areas, as seen in Fig. 6.7 this κ does not fit the measurements and can thus be excluded. For any value of κ , one excluded energy bin is sufficient to exclude this κ .

The number of simulated compositions at the edge of the $\langle X_{\max} \rangle$ - $\sigma(X_{\max})$ parameter space for all energy bins at selected values of κ is shown in Tab. 6.1 for CONEX simulations run using SIBYLL 2.3d. As a value of κ can be excluded at an energy if there are no matching compositions, the relevant entries are those in which zero accepted compositions are found. Only the outline of the $\langle X_{\max} \rangle$ - $\sigma(X_{\max})$ values covered by simulations, as described in Sec. 5.3.2, is checked for overlap with the confidence region of the associated energy bin, as these are sufficient to determine overlap between both regions. For low κ and low energies, the confidence region fits into the umbrella spanned by the $\langle X_{\max} \rangle$ - $\sigma(X_{\max})$ values of the simulated showers. This is caused by a decrease of the uncertainties of the measurements by the Pierre Auger Observatory at lower energies, leading to smaller confidence intervals. This can be seen in Fig. 6.6 for $E = 10^{17.55}$ eV, where there is no overlap between the edge of the $\langle X_{\max} \rangle$ - $\sigma(X_{\max})$ parameter space of simulations and the Auger confidence region, as the confidence region is enveloped by the region covered by the simulations. This results in a "false" zero for $\kappa = -1 \times 10^{-21}$ and $\kappa = 0$ when only checking the outline of simulations, which has to be excluded from the analysis. Only once LV is introduced, $\langle X_{\max} \rangle$ is lowered, resulting in an overlap between the outline of the umbrella and the confidence region. The entries where the confidence region is entirely inside the region covered by simulations, which are found at low values of κ and low primary particle energies, are marked with X in the table. For this analysis, the two highest-energy bins (above $10^{19.50}$ eV) are also excluded due to the comparably small statistics.

The zero values corresponding to no overlap between simulations and

| Bin # | $\log_{10}(E/\text{eV})$ | $\kappa =$ | | | | |
|-------|--------------------------|----------------------|----------------------|----------------------|----------------------|----|
| | | -1×10^{-19} | -1×10^{-20} | -6×10^{-21} | -1×10^{-21} | 0 |
| 0 | 17.26 | 27 | 4 | 8 | 6 | X |
| 1 | 17.35 | 36 | 12 | 10 | X | X |
| 2 | 17.45 | 22 | X | X | X | X |
| 3 | 17.55 | 37 | X | X | X | X |
| 4 | 17.65 | 28 | 7 | 3 | X | X |
| 5 | 17.75 | 49 | 22 | 8 | X | X |
| 6 | 17.85 | 32 | 11 | 8 | X | X |
| 7 | 17.95 | 35 | 17 | 13 | X | X |
| 8 | 18.05 | 26 | 34 | 31 | 7 | X |
| 9 | 18.15 | 14 | 36 | 36 | 14 | X |
| 10 | 18.25 | 4 | 35 | 37 | 23 | 6 |
| 11 | 18.35 | 0 | 32 | 39 | 30 | 9 |
| 12 | 18.45 | 0 | 19 | 33 | 34 | 12 |
| 13 | 18.55 | 0 | 12 | 26 | 33 | 12 |
| 14 | 18.65 | 0 | 29 | 39 | 45 | 7 |
| 15 | 18.75 | 0 | 0 | 18 | 33 | 31 |
| 16 | 18.85 | 0 | 0 | 4 | 26 | 32 |
| 17 | 18.95 | 0 | 0 | 0 | 25 | 32 |
| 18 | 19.05 | 0 | 0 | 12 | 32 | 34 |
| 19 | 19.15 | 0 | 0 | 2 | 26 | 29 |
| 20 | 19.25 | 0 | 30 | 48 | 55 | 37 |
| 21 | 19.35 | 0 | 0 | 17 | 39 | 38 |
| 22 | 19.44 | 0 | 48 | 54 | 63 | 49 |
| 23 | 19.55 | 0 | 0 | 0 | 30 | 38 |
| 24 | 19.73 | 0 | 0 | 3 | 48 | 55 |

TABLE 6.1: Number of points in the contour around the $\langle X_{\text{max}} \rangle - \sigma(X_{\text{max}})$ values allowed by all compositions simulated using CONEX with the hadronic interaction model SIBYLL 2.3d inside the Auger confidence region determined from recent X_{max} moments published in [Yus19]. Selected values of $\kappa < 0$ are shown with decreasing strength of LV from left to right. For each value of κ , the comparison is done separately for each energy bin of the measurements from the Pierre Auger Observatory. Entries where the Auger confidence region is entirely inside the region covered by simulated showers are marked with an X. The two highest energy bins are excluded from the analysis due to low statistics, but listed here for completeness.

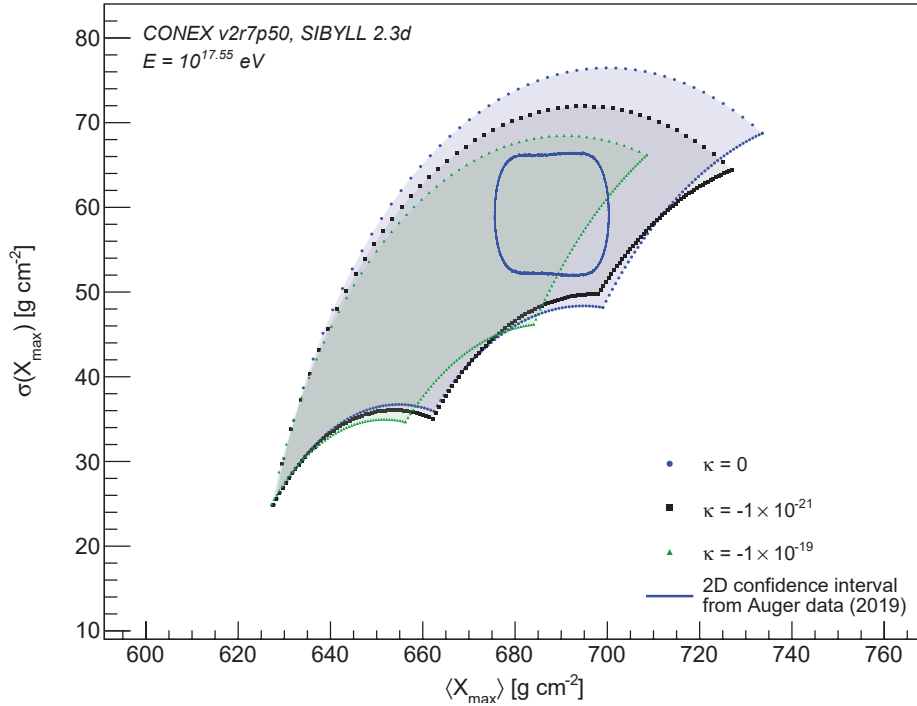


FIGURE 6.6: Comparison of the $\langle X_{\max} \rangle$ - $\sigma(X_{\max})$ -combinations derived by simulations to the 2D confidence intervals given by the measurements of the Pierre Auger Observatory for different values of κ and a primary particle energy of $10^{17.55}$ eV.

measurements are found at higher energies ($E > 10^{18.3}$ eV) and larger values of κ . For $\kappa = -1 \times 10^{-19}$, all energy bins above $10^{18.3}$ eV show no overlap, as do the energy bins between $10^{18.7}$ eV and $10^{19.2}$ eV for $\kappa = -1 \times 10^{-20}$. For $\kappa = -6 \times 10^{-21}$, only one energy bin shows no overlap between simulations and data, any smaller value of κ has some simulated primary particle combinations matching the confidence region for all energies. Plots of the comparison between simulations and data for energy bins 0 to 23 can be found in appendix B.9, B.10 and B.11.

These tests of compatibility between simulations and data are repeated, scanning over different values of κ and energy bins, until a value κ_{crit} is found where all $\kappa \leq \kappa_{\text{crit}}$ do not fit the measurements while all $\kappa > \kappa_{\text{crit}}$ do. For the hadronic interaction model SIBYLL 2.3d, as shown above, this results in the new bound

$$\kappa > \kappa_{\text{crit}} = -6 \times 10^{-21} \quad (98\% \text{ CL}). \quad (6.2)$$

The new bound of $\kappa_{\text{crit}} = -6 \times 10^{-21}$ improves the previous bound determined in [KNR17] by a factor 50. One reason for this improvement is the increase in the number of showers observed by the Pierre Auger Observatory between the data used in the previous analysis [Aab+14a] and here, leading to a decrease in statistical uncertainties. The second factor in the improvement of the bounds is the new method used. In appendix C.1,

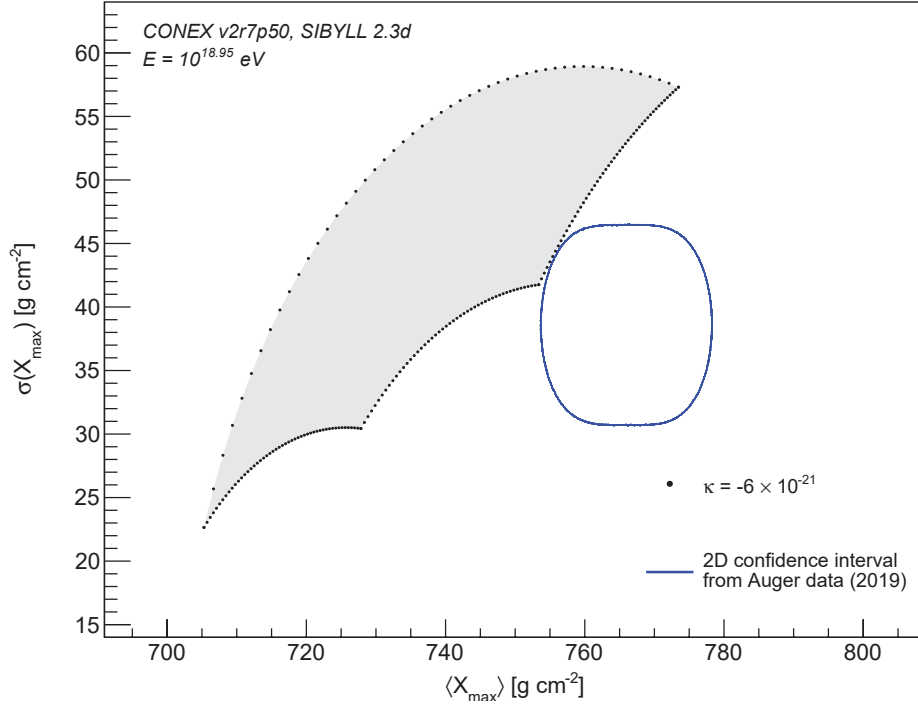


FIGURE 6.7: Comparison of the $\langle X_{\max} \rangle$ - $\sigma(X_{\max})$ -combinations derived by LV simulations to the 2D confidence interval given by the measurements of the Pierre Auger Observatory for $\kappa = -6 \times 10^{-21}$ and a primary particle energy of $10^{18.95}$ eV.

the results of the analysis, repeated for the previously used X_{\max} moments from the Pierre Auger Observatory, are displayed. There, the energy range starts at a higher energy of $10^{17.8}$ eV, as only data from the FD and the 1500 m SD array is used, while the later measurements include measurements from the low-energy extensions of the Observatory. The last energy bin above $10^{19.5}$ eV is again excluded. At energies of $10^{17.85}$ eV and $10^{18.05}$ eV, as well as for $\kappa = 0$, the confidence region is again fitting into the outline of the umbrella spanned by the $\langle X_{\max} \rangle$ - $\sigma(X_{\max})$ values of the simulations, which is marked by X in the table. For $\kappa = -1 \times 10^{-19}$, this leaves eight energy bins in which there is no overlap between data and simulations, thoroughly excluding this value of κ . For $\kappa = -1 \times 10^{-20}$, only bin 10 at an energy of $E = 10^{18.85}$ eV shows no simulated compositions matching the confidence region, while $\kappa = -6 \times 10^{-21}$ shows overlap for all investigated energies. Thus, $\kappa = -1 \times 10^{-20}$ can be excluded while $\kappa = -6 \times 10^{-21}$ cannot, resulting in a bound of $\kappa_{\text{crit}} = -1 \times 10^{-20}$ for the previously used X_{\max} moments, which is an improvement by a factor of 30 from the previous lower limit of $\kappa > -3 \times 10^{-19}$. The remaining improvement is due to the increased amount of showers measured by the Pierre Auger Observatory.

An example of a comparison near the bound is shown in Fig. 6.7, which depicts the allowed $\langle X_{\max} \rangle$ - $\sigma(X_{\max})$ values of simulations and data in the energy range crucial for the determination of the new bounds. The simulations with $\langle X_{\max} \rangle$ - $\sigma(X_{\max})$ values closest to the two-dimensional confidence region are those which are mainly helium. The first composition inside the

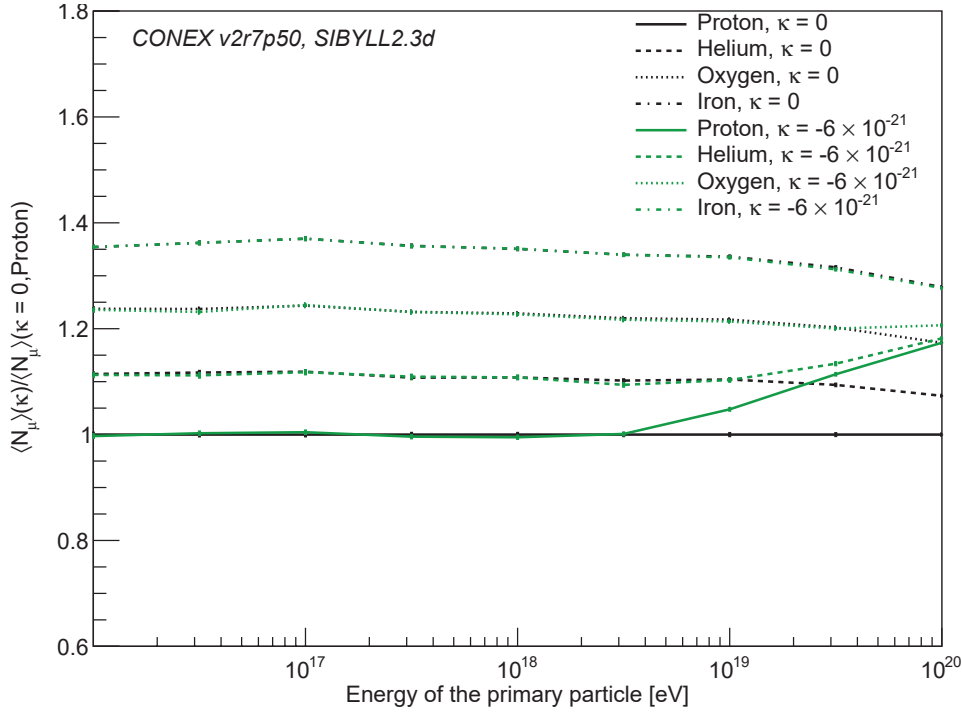


FIGURE 6.8: The simulated values of $\langle N_\mu \rangle$ as a function of the primary energy for different primary particles in the absence of LV ($\kappa = 0$) and for $\kappa < 0$. All values are normalized to the value of $\langle N_\mu \rangle$ for unmodified protons at the corresponding energy, to show the relative effect of LV on the muon number.

region is a 100% helium composition. A CR composition consisting of only helium is generally not assumed to be the case, thus further improvements of the gained bounds are possible by constraining possible primary particle compositions, e.g., by using observables sensitive to the primary particle mass, such as the number of muons contained in the shower.

6.2.3 Changes in N_μ

The effect of LV on the number of muons measured at ground level N_μ is also investigated to check the potential for further improvements on the bounds of κ through the inclusion of an additional observable. While $\langle X_{\max} \rangle$ decreases at equal energies with increasing mass of the primary particle of air showers, N_μ increases with an increase in primary particle mass. The mean number of muons $\langle N_\mu \rangle$ simulated for different energies and primary particle masses is displayed in Fig. 6.8, normalized to the value of $\langle N_\mu \rangle$ for protons in the $\kappa = 0$ case for each energy. Simulations for both the case of $\kappa = 0$ as well as $\kappa < 0$ are shown. Simulations were done with a zenith angle of $\Theta = 45^\circ$, the muon number was taken at a vertical depth of 875 g cm^{-2} , which corresponds to a slant depth of $875 \text{ g cm}^{-2} \cos(\frac{\pi}{4})^{-1} \approx 1237.4 \text{ g cm}^{-2}$. In a one-dimensional shower simulation code like CONEX, this fixed zenith angle has no impact on the shower development, but fixes the slant depth of the theoretical detector for all showers, as the muon number is dependent on

the slant depth of the shower. The energy threshold above which muons in the shower are simulated was set to 1 GeV.

Similar to $\langle X_{\max} \rangle$, deviations between $\langle N_{\mu} \rangle$ values for the SM and LV cases are seen at the highest energies, with the difference becoming larger for higher energy values. The relative increase of $\langle N_{\mu} \rangle$ for proton induced showers at $E = 10^{20}$ eV amounts to $\approx 18\%$. The increase in $\langle N_{\mu} \rangle$ is roughly linear to the logarithmic energy, increasing by $\approx 13\%$ per decade in primary particle energy. As pions can inherit a significant fraction of the primary particle energy, the effects of the modified pion decay can be seen at primary particle energies which are not much higher than the pion cutoff energy $E_{\pi^0}^{\text{cut}}$ introduced in Eq. (4.17). For protons simulated with $\kappa = -6 \times 10^{-21}$, effects on $\langle N_{\mu} \rangle$ due to LV appear at energies above $10^{18.5}$ eV, which is less than a decade greater than the pion cutoff energy $E_{\pi^0}^{\text{cut}}(\kappa = -6 \times 10^{-21}) = 1.23 \times 10^{18}$ eV. These changes in $\langle N_{\mu} \rangle$ also appear at higher energies for heavier primary particles due to the superposition principle. As $\langle N_{\mu} \rangle$ increases only at higher energies for heavier primaries, but heavier primaries produce higher values of $\langle N_{\mu} \rangle$ in the SM, this leads to $\langle N_{\mu} \rangle$ gradually becoming the same value for primary particles of different masses at the highest energies. This effect can be seen for primary protons and helium in Fig. 6.8, for higher energies the increase in $\langle N_{\mu} \rangle$ of lighter primary particles leads to it approaching $\langle N_{\mu} \rangle$ of heavier primary particles. This effect is even more pronounced for larger values of κ , as changes due to LV occur at lower primary particle energies.

While changes in $\langle X_{\max} \rangle$ are dominated by the effects of photon decay in the electromagnetic sub-showers, the effect on $\langle N_{\mu} \rangle$ is dominated by the changes in the neutral pion decay time. This is due to the electrons, positrons and photons in this part of the shower typically not producing any more muons. It follows that the addition of photon decay cannot change the rate of muon production on the shower. Studies using simulations only incorporating photon decay and no changes to the pion decay rate were done to confirm this. In Fig. 6.9 the changes in $\langle N_{\mu} \rangle$ in relation to the SM is depicted for both the full implementation of LV into the shower at $\kappa = -6 \times 10^{-21}$, as well as for a partial implementation, which only adds photon decay to the simulation while not modifying the decay time of the neutral pion. The changes in $\sigma(N_{\mu})$, $\langle X_{\max} \rangle$ as well as $\sigma(X_{\max})$ are shown in appendix B.6, B.7 and B.8, where no changes are seen in X_{\max} , while $\sigma(N_{\mu})$ is also only affected in simulation with the modified neutral pion decay.

As the neutral pion becomes effectively stable for any energy above the threshold energy $E_{\pi^0}^{\text{cut}}$ described in Sec. 4.3.1, further hadronic interactions become possible, producing additional secondary particles such as charged pions which themselves can re-interact or decay into pairs of muons and muon neutrinos, which is responsible for the increase in $\langle N_{\mu} \rangle$.

The change in $\langle N_{\mu} \rangle$ is of additional interest as there is a currently unexplained excess of muons measured in comparison to predictions made using all hadronic interaction models [Aab+15a], which could be explained by LV, as is proposed in e.g. [Tom17]. However, the increase in $\langle N_{\mu} \rangle$ induced by LV

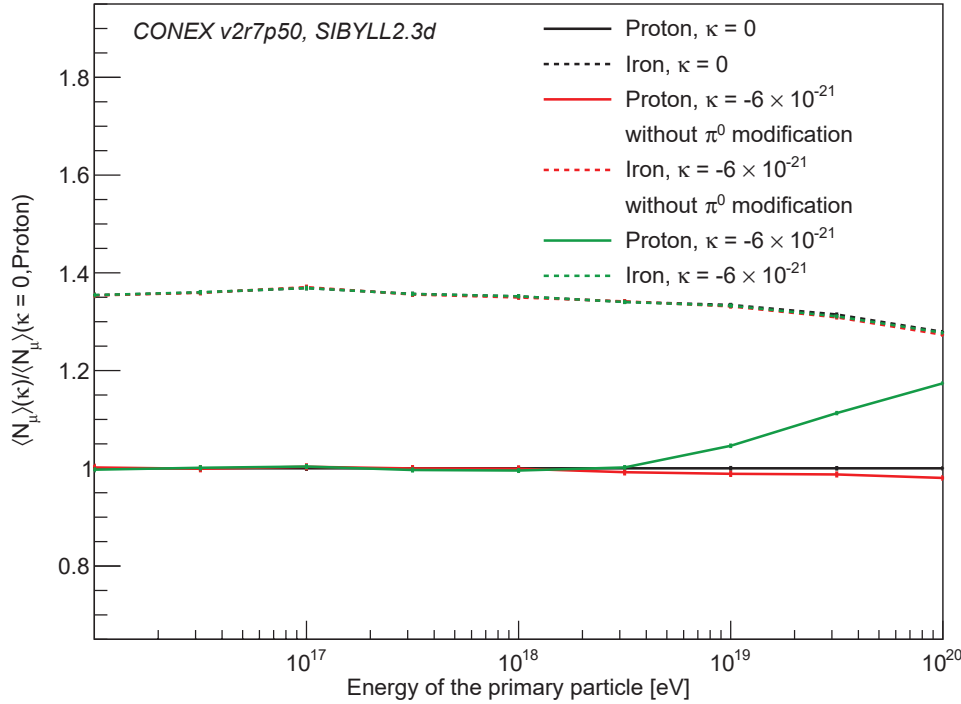


FIGURE 6.9: The simulated values of $\langle N_\mu \rangle$ as a function of the primary energy for different primary particles in the absence of LV ($\kappa = 0$) and for $\kappa = -6 \times 10^{-21}$. All values are normalized to the value of $\langle N_\mu \rangle$ for unmodified protons at the corresponding energy, to show the relative effect of LV on the muon number. Depicted is also the result of a partial modification of the CONEX code, incorporating only photon decay and no modification of the pion decay time.

at the levels still allowed by the limits on κ derived in this work is still lower than the excess seen. Thus, even in the case of LV, it could only be a partial contributor to the measured muon excess.

The relative effect of LV on shower-to-shower fluctuations $\sigma(N_\mu)$ of the muon number are shown in Fig. 6.10. Again, values are normalized to the value of $\sigma(N_\mu)$ for an unmodified shower induced by a proton of the respective energy. Changes of $\sigma(N_\mu)$ due to LV can be seen for energies above the same energy threshold as for changes in $\langle N_\mu \rangle$, showing a decrease in $\sigma(N_\mu)$ for simulations incorporating LV. This decrease is significant, reducing $\sigma(N_\mu)$ by $\approx 34\%$ for primary protons at an energy of 10^{20} eV. The slope of this decrease is most pronounced at energies right above the threshold for the effect and less steep at higher energies. For the example of primary protons simulated with $\kappa = -6 \times 10^{-21}$, there is $\approx 15\%$ difference in the decrease of $\sigma(N_\mu)$ between $E = 10^{18.5}$ eV and $E = 10^{19}$ eV, with only $\approx 2\%$ difference between $E = 10^{19.5}$ eV and $E = 10^{20}$ eV. For primary particles of higher masses, this decrease begins at higher energies, which scale linearly with the particle mass A , and is thus also less pronounced.

The combination of the decrease in $\sigma(N_\mu)$ and increase in $\langle N_\mu \rangle$ leads to a

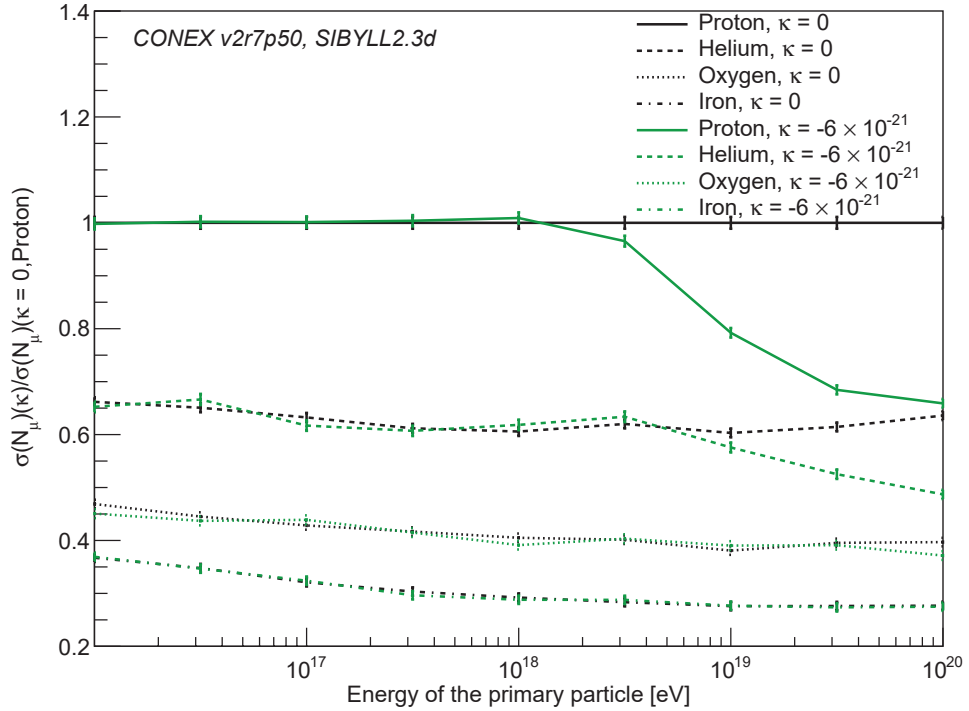


FIGURE 6.10: The simulated values of $\sigma(N_\mu)$ as a function of the primary energy for different primary particles in the absence of LV ($\kappa = 0$) and for $\kappa < 0$. All values are normalized to the value of $\sigma(N_\mu)$ for unmodified protons at the corresponding energy, to show the relative effect of LV on the muon number.

much smaller relative width of N_μ values. The relative width of N_μ decreases by more than 40% for protons at the highest energy simulated with $\kappa = -6 \times 10^{-21}$ compared to $\kappa = 0$.

6.2.4 Changes in the correlation between X_{\max} and N_μ

With changes due to LV observed in both X_{\max} and N_μ , the impact of LV on the correlation between both observables is also of interest. Using this correlation to determine the purity of the mass composition was proposed in [YR12]. The correlation between X_{\max} and N_μ was examined for simulations of pure and mixed compositions, as well as for measured air shower data. The SD of the Pierre Auger Observatory does not measure N_μ directly, thus the correlated observable $S(1000)$ is used instead in [Aab+16b]. Muons contribute a majority of $S(1000)$, the total signal at a core distance of 1000 m for showers with an energy of 10^{19} eV at the examined zenith angles between 20° and 60° [Keg13]. Thus, $S(1000)$, scaled to a zenith angle of 38° and an energy of 10^{19} eV to correct for energy and inclination dependence, was used in [Aab+16b] as a stand-in for N_μ . It was found that observations cannot be reproduced by simulations of pure compositions, independent of the mass of the primary particle.

The compositions examined here are both pure compositions and the maximally mixed composition of 50% protons and 50% iron nuclei, representing

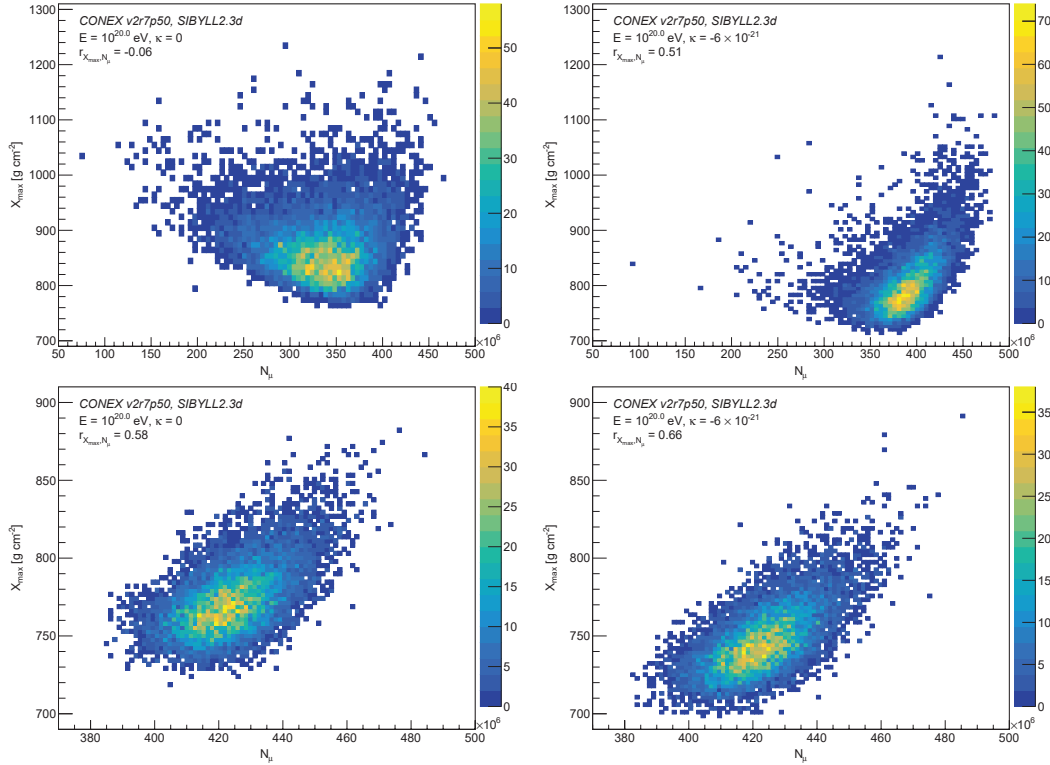


FIGURE 6.11: Visual example of the changes in the distribution of X_{\max} and the number of muons observed at ground level N_{μ} and their correlation for $\kappa = 0$ (left) and $\kappa = -6 \times 10^{-21}$ (right) and an energy of 10^{20} eV. Shown are pure compositions with CRs consisting of 100 % protons (top) or 100 % iron nuclei (bottom).

pure compositions at both ends of the possible primary masses as well as an example of the effects on a mixed composition. To describe the correlation between X_{\max} and N_{μ} , the Pearson correlation coefficient $r(X_{\max}, N_{\mu})$ is used, which is defined as:

$$r(X_{\max}, N_{\mu}) = \frac{\text{cov}(X_{\max}, N_{\mu})}{\sigma(X_{\max})\sigma(N_{\mu})} \quad (6.3)$$

For $\kappa = 0$ and a pure proton composition, there are only minor correlations between X_{\max} and N_{μ} ($r(X_{\max}, N_{\mu}) = -0.06$). With the introduction of LV into the shower, $\langle N_{\mu} \rangle$ increases, while $\langle X_{\max} \rangle$ decreases by $\approx 66 \text{ g cm}^{-2}$, shifting the distribution. In addition to this shift, the correlation increases to $r(X_{\max}, N_{\mu}) = 0.51$ at $\kappa = -6 \times 10^{-21}$.

The changes in the distributions of showers induced by heavier primary particles are less pronounced, with the effects of LV diminishing with an increase in primary particle mass. It follows that iron induced showers are least affected by LV for any given energy. Iron induced showers in general have a lower $\langle X_{\max} \rangle$ as well as higher $\langle N_{\mu} \rangle$ than showers induced by lighter particles, which is well reflected here. In addition to this, showers

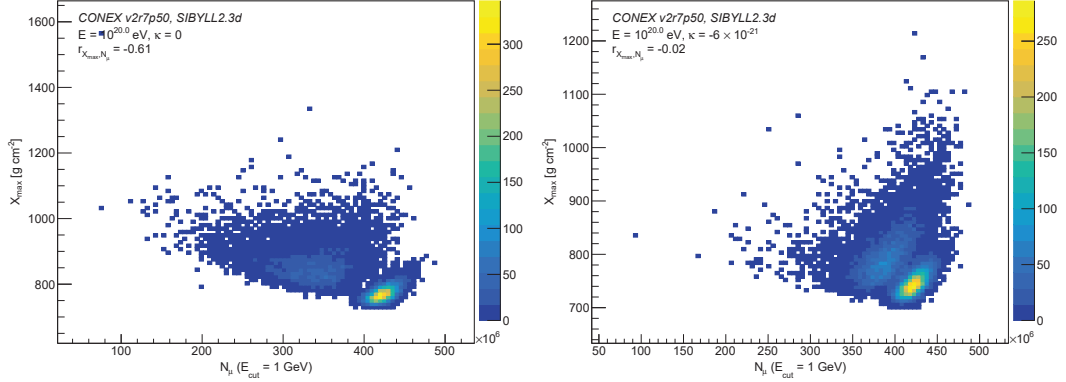


FIGURE 6.12: Visual example of the changes in the distribution of X_{\max} and the number of muons observed at ground level N_{μ} and their correlation for $\kappa = 0$ (left) and $\kappa = -6 \times 10^{-21}$ (right) and an energy of 10^{20} eV. Shown is the maximally mixed composition of a cosmic ray spectrum consisting of 50% protons and 50% iron nuclei for $\kappa = 0$ and $\kappa = -6 \times 10^{-21}$.

with higher X_{\max} tend to have a higher N_{μ} , which leads to a correlation of $r(X_{\max}, N_{\mu}) = 0.58$ for unmodified showers. The changes in the showers due to LV are less pronounced in comparison to protons, due to the lower energy per nucleon leading to lower energies of secondary particles and less particles above the thresholds of effects due to LV. At $\kappa = -6 \times 10^{-21}$, no noticeable changes in N_{μ} can be observed, but $\langle X_{\max} \rangle$ decreases by ≈ 27 g cm⁻². A minor increase in the correlation to a value of $r(X_{\max}, N_{\mu}) = 0.66$ can also be observed.

In summary, the introduction of LV into shower simulations decreases $\langle X_{\max} \rangle$, as already discussed in Sec. 6.2.1, increases $\langle N_{\mu} \rangle$ (see also Sec. 6.2.3) and increases the correlation $r(X_{\max}, N_{\mu})$ for pure compositions, with the effects being stronger for lighter primary particles.

Since the CRs are not necessarily consisting of only one particle type for any energy and the composition is expected to change with higher primary particle energies, mixed compositions have to be taken into account again. The pure compositions are the least mixed compositions, in the following paragraphs maximally mixed compositions are examined. Here, this is a composition with 50% protons and 50% iron nuclei as primaries, as those are the lightest and heaviest primaries considered. For maximally mixed compositions the effects on $r(X_{\max}, N_{\mu})$ due to differences between primaries are expected to become most pronounced, as a larger difference in mass number A translates to a large difference in both $\langle X_{\max} \rangle$ and $\langle N_{\mu} \rangle$.

In Fig. 6.12 the effects of LV on the combined distribution of X_{\max} and N_{μ} for maximally mixed distributions is displayed. For unmodified simulations ($\kappa = 0$), a significant negative correlation of $r(X_{\max}, N_{\mu}) = -0.61$ can be seen. This is due to the combination of 50% protons and 50% iron, as protons have both a higher $\langle X_{\max} \rangle$ and lower $\langle N_{\mu} \rangle$. The combination of those two

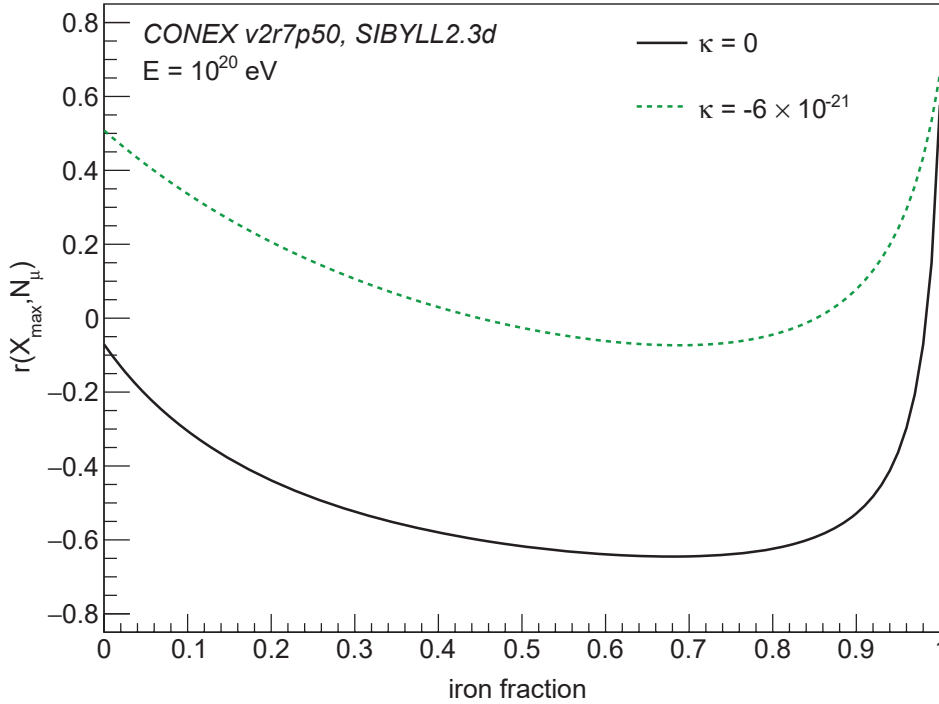


FIGURE 6.13: The correlation $r(X_{\max}, N_{\mu})$ between X_{\max} and N_{μ} for showers with a primary particle composition of only protons and iron. The correlation is shown for different fractions of both primaries, ranging from a pure proton composition to pure iron. Showers were simulated for a primary particle energy of 10^{20} eV.

distributions with different mean values in both parameters naturally leads to an increased correlation.

The increase in $\langle N_{\mu} \rangle$ with the accompanying decrease of $\langle X_{\max} \rangle$ for proton initiated showers incorporating LV leads to both distributions becoming significantly less separated. While $\sigma(N_{\mu})$ decreases, this is less significant than the decrease in the difference between the values of $\langle N_{\mu} \rangle$ of protons and $\langle N_{\mu} \rangle$ of heavier particles. For the proton-iron composition shown here, this is a reduction in the difference of $\langle X_{\max} \rangle$ between both primaries from $\approx 120 \text{ g cm}^{-2}$ to $\approx 75 \text{ g cm}^{-2}$. The value of $\langle N_{\mu} \rangle$ for iron is unchanged under LV in this case, while $\langle N_{\mu} \rangle$ of protons increases by 18%. As $\langle N_{\mu} \rangle$ is only 27% higher for iron primaries than for unmodified proton primaries, this reduces the difference between the means of the two N_{μ} distributions by $\approx 2/3$, while the width of the iron N_{μ} distribution is unchanged and that of protons decreases by $\approx 1/3$. In addition to this, the proton distribution gains a significant positive correlation of $r(X_{\max}, N_{\mu}) = 0.51$. As a result of both these effects, the correlation for the maximally mixed composition is greatly reduced to $r(X_{\max}, N_{\mu}) = -0.02$.

In Fig. 6.13, the dependence of the correlation $r(X_{\max}, N_{\mu})$ of a mixed CR composition consisting of protons and iron primary particles on the fraction of iron primaries can be seen, once for the SM case of $\kappa = 0$ and once for

$\kappa = -6 \times 10^{-21}$. In both cases, the correlation is larger for pure compositions, with the minimum value of $r(X_{\max}, N_{\mu})$ at a combination of $\approx 30\%$ protons and 70% iron. It is worth noting that the minimum is not at the maximally mixed composition of $\approx 50\%$ protons and 50% iron investigated before, with a difference of about 0.05 in $r(X_{\max}, N_{\mu})$. The reason for this can be found in the different values for the spread of both the X_{\max} and N_{μ} distributions for protons and iron, where the proton induced showers show a much larger spread. Thus, an iron-dominated composition has a lower overall spread than a $50/50$ composition, which leads to a higher impact of the proton-induced shower in the set on $r(X_{\max}, N_{\mu})$, while showing the same general features.

The correlation $r(X_{\max}, N_{\mu})$ is increased by ≈ 0.6 for $\kappa = -6 \times 10^{-21}$ in comparison to $\kappa = 0$ for most proton-iron compositions. This is not the case for heavily iron-dominated compositions ($> 90\%$), where the impact of LV vanishes, as the development of iron showers is barely affected by LV at the shown energy. For $\kappa = 0$, all compositions with an iron content of less than 98% show a negative correlation between X_{\max} and N_{μ} , with a strongest negative correlation of $r(X_{\max}, N_{\mu})_{\min} = -0.65$ at $\approx 70\%$ iron content. For $\kappa = -6 \times 10^{-21}$, most compositions show a positive correlation, while the minimum of the correlation is also reached at $\approx 70\%$ iron content with $r(X_{\max}, N_{\mu})_{\min} = -0.07$.

The observed effects of LV on $r(X_{\max}, N_{\mu})$ can be exploited to aid in setting new limits on κ through several approaches. A straightforward approach is the comparison of the correlation observed in air showers to the lower limit on $r(X_{\max}, N_{\mu})$ obtained through simulations. As $r(X_{\max}, N_{\mu})$ increases with larger negative values of κ , accordance between measurements and simulations for different κ can be tested. Building on this, a comparison between measurements and simulations of $r(X_{\max}, N_{\mu})$ can be used to constrain the primary particle composition, i.e. to set a lower limit on the purity of the composition $\sigma(\ln A)$.

However, all improvements discussed before are dependent on measurements of X_{\max} and N_{μ} . While X_{\max} can be measured directly by, e.g., the FD of the Pierre Auger Observatory, no such direct measurements exist for N_{μ} with a sufficiently high number of observed showers at the energies investigated here. The addition of muon counters at the AMIGA component of the Pierre Auger Observatory enables the direct measurement of muons at ground level (see Sec. 3.3), but covers only a small area compared to the entire array and its primary purpose is the measurement of lower energy air showers. With the addition of scintillators to all SD stations of the Pierre Auger Observatory planned with AugerPrime, the disentanglement of the muon content from the electromagnetic component of the shower will be possible for a large number of showers at the highest energies, enabling further investigation of LV incorporating N_{μ} as an additional observable. A currently measured observable closely correlated to N_{μ} is $S(1000)$, with muons contributing between 40% and 90% of $S(1000)$ at a primary particle energy of 10^{19} eV [Keg13]. For a meaningful comparison, the effects of LV on N_{μ}

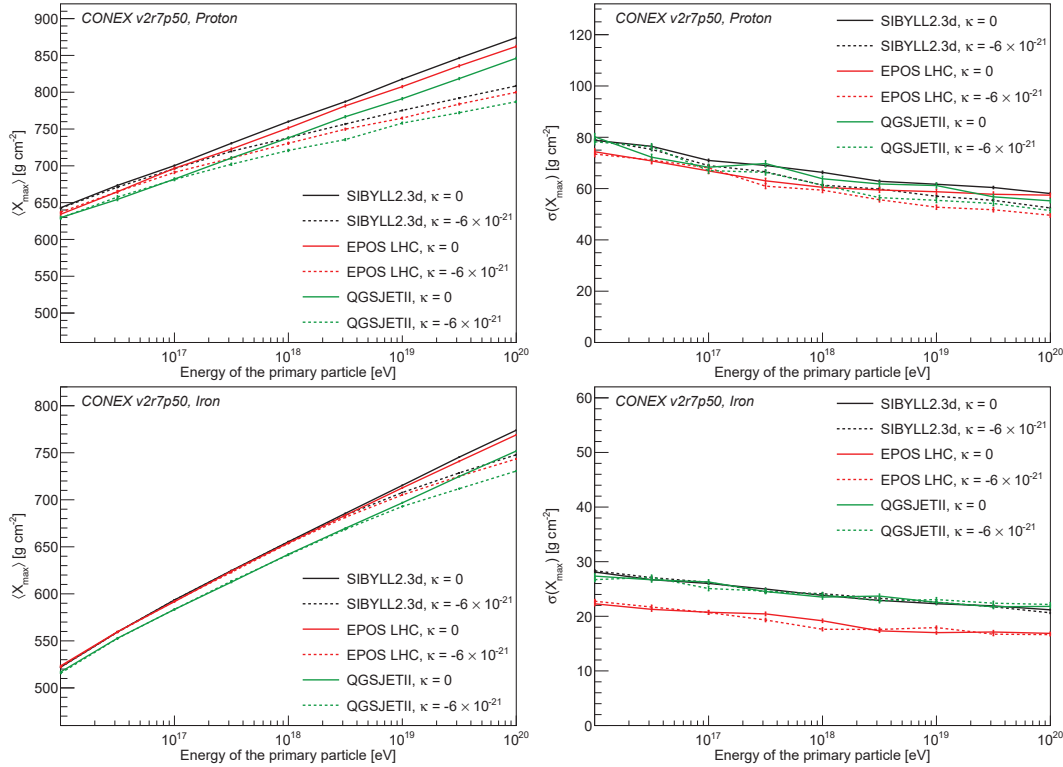


FIGURE 6.14: The simulated values of $\langle X_{\max} \rangle$ and $\sigma(X_{\max})$ as a function of the primary energy for primary protons and iron nuclei for the absence of LV ($\kappa = 0$) and for $\kappa = -6 \times 10^{-21}$. Shown are simulations with the three hadronic interaction models SIBYLL 2.3d [Rie+20], EPOS LHC [Pie+15] and QGSJET-II-04 [Ost11].

have to be translated to $S(1000)$ or vice versa. To gain an insight into the impact of LV on $S(1000)$, the simulation of showers incorporating LV with CORSIKA [Hec+98] can be used, however this is beyond the scope of this work.

6.2.5 Differences between hadronic interaction models

When hadronic interaction models other than SIBYLL 2.3d are used, the values of both $\langle X_{\max} \rangle$ and $\sigma(X_{\max})$ change. The differences between models are mostly caused by different treatment of the first interactions of the shower, i.e. the first interactions between the proton/nucleus and air as well as the pion-air interactions. The different models use different cross sections as well as multiplicities for those first hadronic interactions, which results in different predictions for the shower development [Pie17].

The relative changes of $\langle X_{\max} \rangle$ and $\sigma(X_{\max})$ introduced by LV are the same for all models. Differences in both $\langle X_{\max} \rangle$ and $\sigma(X_{\max})$ between models are unaffected by the introduction of LV. This is expected, since the differences in the hadronic interaction models impact the hadronic component

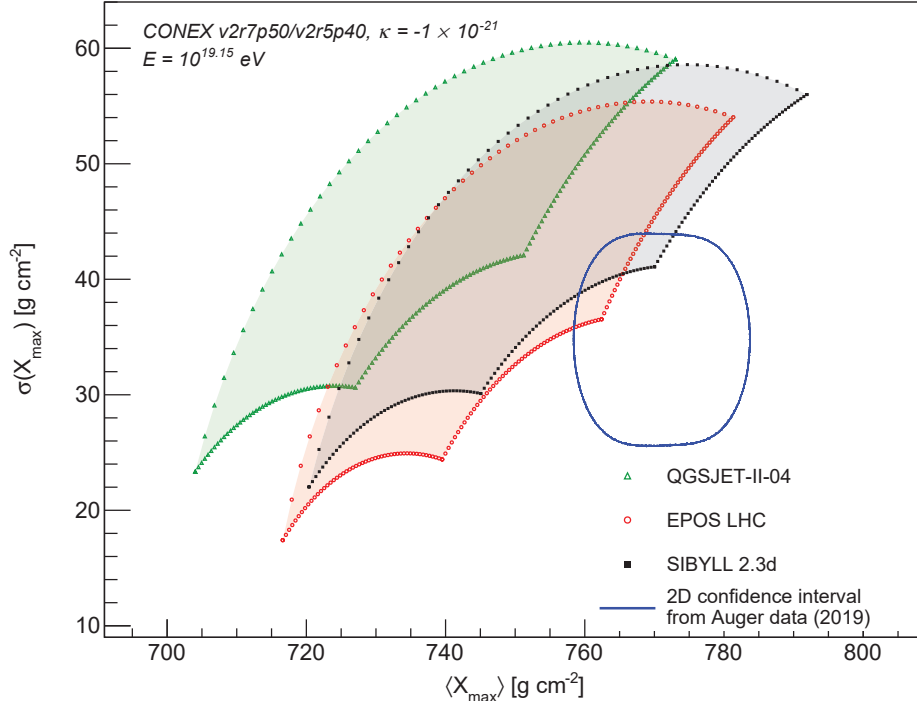


FIGURE 6.15: Comparison of the combinations of $\langle X_{\max} \rangle$ and $\sigma(X_{\max})$ which were derived from simulations with different hadronic interaction models which incorporate LV to the 2D confidence intervals given by the measurements of the Pierre Auger Observatory for $\kappa = -1 \times 10^{-21}$ and a primary particle energy of $10^{19.15}$ eV.

of the shower, not the electromagnetic component, where the most impactful change due to LV, the decay of the photon, is situated. Simulations with SIBYLL 2.3d produce the highest $\langle X_{\max} \rangle$ values, followed by EPOS LHC and QGSJET-II-04. The simulated values of $\langle X_{\max} \rangle$ and $\sigma(X_{\max})$ for protons and iron primaries in all three hadronic interaction models in the cases of $\kappa = 0$ (SM) and $\kappa = -6 \times 10^{-21}$ are shown in Fig 6.14.

For protons, the difference in $\langle X_{\max} \rangle$ between SIBYLL 2.3d and EPOS LHC is $\approx 10 \text{ g cm}^{-2}$, between EPOS LHC and QGSJET-II-04 $\approx 15 \text{ g cm}^{-2}$ of difference can be observed. In $\sigma(X_{\max})$ for protons, SIBYLL 2.3d and QGSJET-II-04 match considering statistical fluctuations in the sample, while EPOS LHC produces a $\sigma(X_{\max})$ which is reduced by $\approx 4 \text{ g cm}^{-2}$, with the difference reducing at higher energies.

For iron primaries, $\langle X_{\max} \rangle$ of SIBYLL 2.3d and EPOS LHC closely match, with values for EPOS LHC only decreasing by $\approx 4 \text{ g cm}^{-2}$ in comparison to SIBYLL 2.3d at the highest energies. Values of $\langle X_{\max} \rangle$ for QGSJET-II-04 are consistently lower than both other interaction models, with a difference of only $\approx 4 \text{ g cm}^{-2}$ at $E = 10^{13}$ eV increasing to $\approx 15 \text{ g cm}^{-2}$ at $E = 10^{20}$ eV. In $\sigma(X_{\max})$ for iron primaries, SIBYLL 2.3d and QGSJET-II-04 closely match, with $\sigma(X_{\max})$ values of EPOS LHC consistently $\approx 5 \text{ g cm}^{-2}$ below other models.

In $\langle X_{\max} \rangle$, changes due to LV are significantly greater than differences between hadronic interaction models. For $\sigma(X_{\max})$, where changes due to LV are less pronounced, differences due to different interaction models are greater, especially for heavier primaries. Due to the differences between models, all models were tested in the analysis. Where no qualitative differences between the models in the context of this analysis are apparent, it is focused on SIBYLL 2.3d, which is used to derive the most conservative limits, where model differences are important, the differences between models are explained.

As the different hadronic interaction models SIBYLL 2.3d, EPOS LHC and QGSJET-II-04 result in different shower development, changing both $\langle X_{\max} \rangle$ and $\sigma(X_{\max})$, this changes the parameter space $\langle X_{\max} \rangle$ and $\sigma(X_{\max})$ covered by all possible compositions used to set a new bound on κ . An illustration of the differences between the regions covered by values of $\langle X_{\max} \rangle$ and $\sigma(X_{\max})$ for each model at $E = 10^{19.15}$ eV and $\kappa = -1 \times 10^{-21}$ can be seen in Fig. 6.15. While SIBYLL 2.3d and EPOS LHC show the previously discussed differences in $\langle X_{\max} \rangle$ and $\sigma(X_{\max})$, with SIBYLL 2.3d resulting in higher values of both $\langle X_{\max} \rangle$ and $\sigma(X_{\max})$, both overlap with the shown confidence region. Simulations with QGSJET-II-04 result in showers with much lower values of $\langle X_{\max} \rangle$ combined with higher values of $\sigma(X_{\max})$, thus no overlap with the shown confidence region is found.

For the different hadronic interaction models, different values of κ_{crit} are produced due to the differences in both $\langle X_{\max} \rangle$ and $\sigma(X_{\max})$. The most conservative κ_{crit} is the one above gained by using the SIBYLL 2.3d model. This is due to the high $\langle X_{\max} \rangle$ values and low $\sigma(X_{\max})$ values in the energy bins which determine κ_{crit} , when compared to the other models. A slightly stricter limit is achieved using the EPOS LHC model, resulting in a limit of

$$\kappa_{\text{crit, EPOS LHC}} = -5 \times 10^{-21} \quad (98\% \text{ CL}). \quad (6.4)$$

Due to the much shallower showers simulated with QGSJET-II-04 the simulations are not able to reproduce the data in a self-consistent way, even for $\kappa = 0$ (no LV). This known fact (see e.g. [Yus19]) indicates shortcomings in this specific hadronic interaction model.

The changes on the muon numbers discussed in Sec. 6.2.3 were gained using the hadronic interaction model SIBYLL2.3d, but the same qualitative effects are seen for the different models. The relative differences in $\langle N_{\mu} \rangle$ and $\sigma(N_{\mu})$ between the hadronic interactions models without LV for the investigated energy range can be found in appendix B.2 and B.3, normalized to SIBYLL2.3d. The values of $\langle N_{\mu} \rangle$ are slightly increased by $\approx 2 - 3\%$ for simulations with EPOS LHC in comparison to SIBYLL2.3d, while QGSJET-II-04 shows $\approx 5 - 7\%$ less muons. The differences between models are more pronounced at higher energies and converge at lower energies. The $\sigma(N_{\mu})$ values of SIBYLL2.3d and EPOS LHC show differences of the order $\approx 5\%$, while $\sigma(N_{\mu})$ for QGSJET-II-04 is lower than those by $\approx 20\%$.

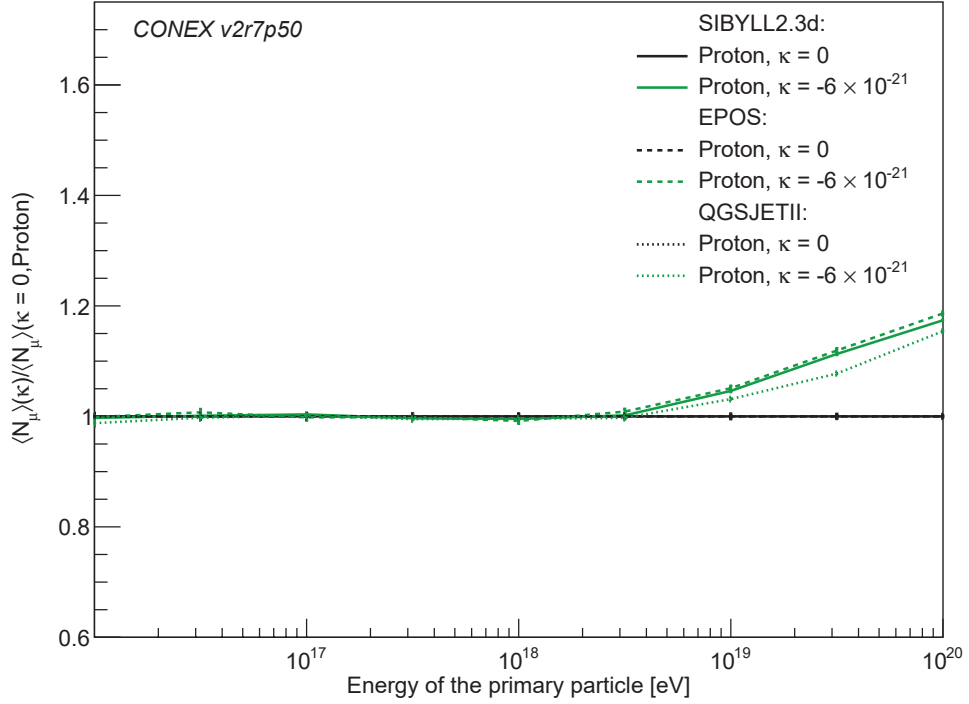


FIGURE 6.16: The simulated values of $\langle N_\mu \rangle$ as a function of the primary energy for different interaction models in the absence of LV ($\kappa = 0$) and for $\kappa < 0$. All values are normalized to the value of $\langle N_\mu \rangle$ for unmodified protons of the model at the corresponding energy, to show the relative effect of LV on the muon number.

Fig. 6.16 shows the relative change in the muon number of proton-induced showers for all three interaction models. For all models, $\langle N_\mu \rangle$ is normalized to the respective muon number of unmodified showers in the model. The relative increase of $\langle N_\mu \rangle$ for SIBYLL2.3d and EPOS is very similar, with QGSJET-II-04 showing a smaller relative impact of LV on $\langle N_\mu \rangle$, with $\approx 3\%$ difference between models at $E = 10^{20}$ eV. All three models also show similar behaviour for the changes in $\sigma(N_\mu)$ due to LV, which are displayed in Fig. 6.17 for primary protons.

6.3 Results for $\kappa > 0$

Here, changes in the shower development for a LV parameter $\kappa > 0$ are discussed and used to constrain κ . This section has a structure similar to the one of the preceding Sec. 6.2. The changes in the longitudinal shower development and the resulting changes in the atmospheric depth of the shower maximum X_{\max} are discussed in Sec. 6.3.1. The observed decreases of $\langle X_{\max} \rangle$, as well as the additional restriction on possible primary particle composition due to VCh radiation are employed in Sec. 6.3.2 to set a new limit on $\kappa > 0$. In Sec. 6.3.3, changes in the number of muons N_μ contained in showers are discussed. Sec. 6.3.4 covers the changes in the correlation between X_{\max} and

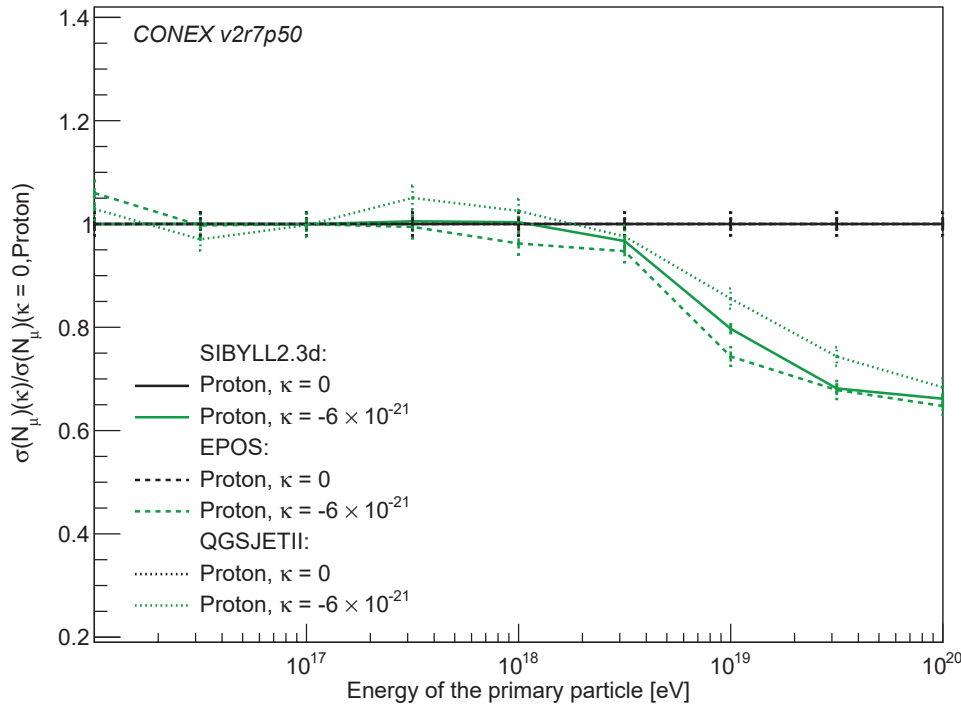


FIGURE 6.17: The simulated values of $\sigma(N_\mu)$ as a function of the primary energy for different interaction models in the absence of LV ($\kappa = 0$) and for $\kappa < 0$. All values are normalized to the value of $\sigma(N_\mu)$ for unmodified protons of the model at the corresponding energy, to show the relative effect of LV on the muon number.

N_μ and possible ways to use these changes to further improve the gained bounds on κ . The differences between the results using different hadronic interaction models are discussed in Sec. 6.2.5.

6.3.1 Changes in X_{\max}

For LV with a positive value of κ , changes in the shower development are caused by the introduction of VCh radiation for charged particles of high energies. The expected changes of processes occurring in the simulated showers are discussed in Sec. 4.5.

In Fig. 6.18, the distribution of X_{\max} values of proton-induced showers simulated at a primary energy of 10^{18} eV with $\kappa = 0$ and $\kappa = 3 \times 10^{-20}$ is shown. The energy was chosen as it is slightly below the maximum energy for protons at $\kappa = 3 \times 10^{-20}$, which is $E_{\text{VCh}}^{\max} = 2.1 \times 10^{18}$ eV, showing the effect of VCh radiation on X_{\max} where the impact of LV on shower development near its maximum. Still, this effect is relatively small in comparison to the changes seen for $\kappa < 0$, resulting in a shift of the distribution by $\approx 15 \text{ g cm}^{-2}$ towards lower values, while the overall shape of the distribution, as well as its width remain unchanged.

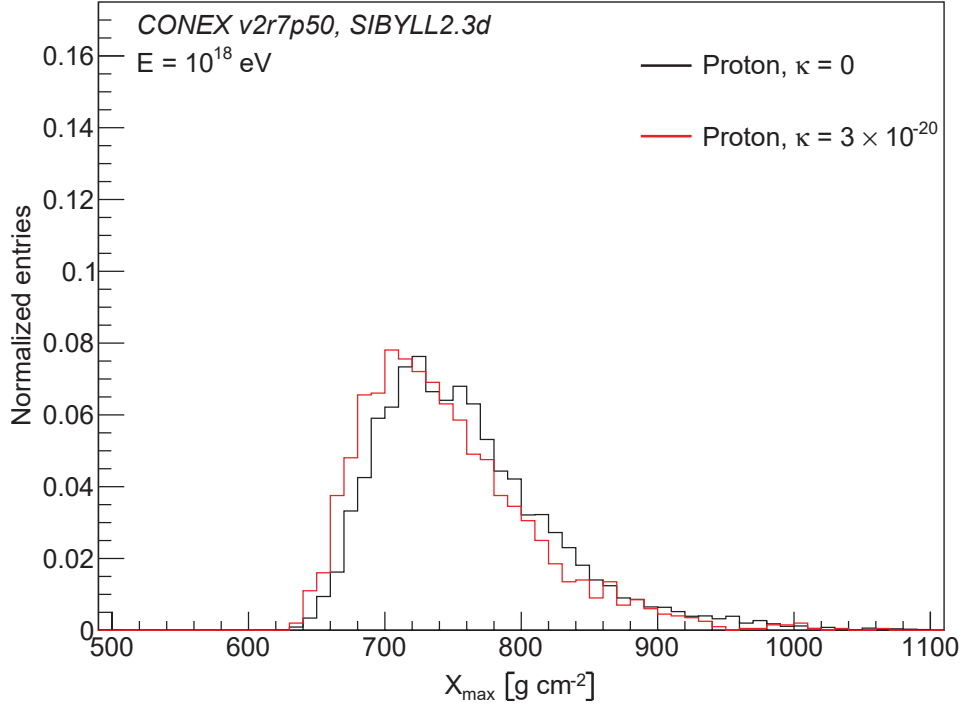


FIGURE 6.18: The distribution of simulated values of X_{\max} for primary protons with an energy of 10^{18} eV for the absence of LV ($\kappa = 0$) and for a value of $\kappa = 3 \times 10^{-20}$.

The impact of VCh radiation on $\langle X_{\max} \rangle$ for protons and iron primaries with energies between 10^{16} eV and 10^{20} eV is shown in Fig. 6.19. Similar to $\kappa < 0$, $\langle X_{\max} \rangle$ decreases for $\kappa > 0$ in comparison to the SM for energies above a given energy threshold. For noticeable changes in $\langle X_{\max} \rangle$, enough particles above their respective energy thresholds described by Eq. (4.18) have to be produced inside the shower. Changes in $\langle X_{\max} \rangle$ are mostly dependent on VCh radiation of electrons and positrons. For brevity, electrons and positrons are jointly referred to as electrons in the followings sections, as the effects of VCh radiation on both are equivalent due to their equivalent masses (see Eq. (4.19)). Changes to $\langle X_{\max} \rangle$ are seen at lower energies for greater values of κ , due to the relation between the energy threshold for VCh radiation and κ shown in Eq. (4.18). The threshold for noticeable changes in the elongation rate of the shower, dependent on primary particle energy and mass can be described by:

$$E_{\text{ER}}^{\text{th}}(A, \kappa) \approx s A E_{\text{VCh}}^{\text{th}}(\kappa) \quad (6.5)$$

This is equivalent to the description of the energy threshold of changes in the elongation rate for $\kappa < 0$ in Eq. (6.1), with the mass number A of the primary particle, the threshold energy for VCh radiation of electrons $E_{\text{VCh}}^{\text{th}}(\kappa)$ and a constant factor s . Here, the constant factor is found empirically to be $s \approx 100$. Above this threshold, enough electrons undergo VCh radiation to significantly change the development of the electromagnetic part of the shower.

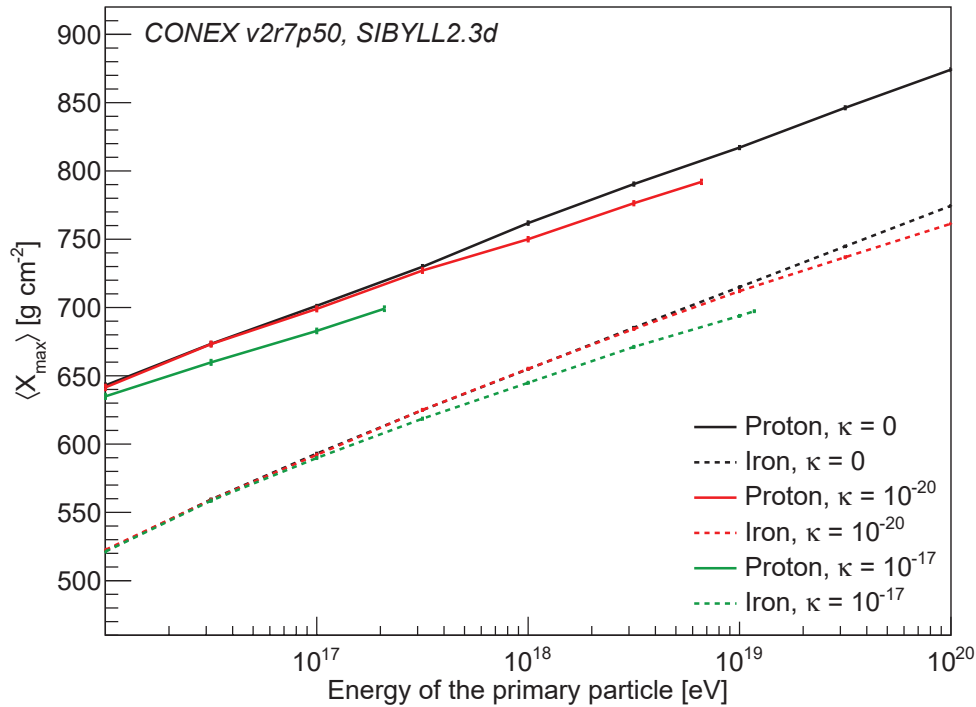


FIGURE 6.19: The simulated values of $\langle X_{\max} \rangle$ as a function of the primary energy for primary protons and iron nuclei for the absence of LV ($\kappa = 0$) and for different values of $\kappa > 0$. Lines are only plotted up to the maximum energy given by the onset of VCh radiation, see Eq. (4.18).

A significant feature which can also be seen in Fig. 6.19 is the introduction of a maximum energy for primary particles depending on their masses. As discussed in Sec. 4.5, VCh radiation would not only affect the secondary particles produced in the shower, but also the primary particles, making it impossible for lighter particles to arrive at higher energies. This maximum energy for a particle with a given mass m behaves according to the energy threshold given in Eq. (4.18):

$$E_{\text{VCh}}^{\max}(\kappa, A) \simeq \frac{m}{\sqrt{2\kappa}} \quad (6.6)$$

Here, A is the atomic mass number of the primary particle, with a resulting particle mass of $m \approx A \cdot 1u$. This upper limit on the particle energy scales linearly with the particle mass, leading to a restriction on the composition, which can only include heavier particles at higher energies. The lower limit of the allowed primary particle masses is described by rearranging Eq. (4.18):

$$m \geq E_0 \sqrt{2\kappa} \quad (6.7)$$

In this equation, E_0 is the energy of the primary particle. The lower bound on masses for primary particles depending on their energy is displayed in Fig. 6.20 for selected values of κ . Consequently, the values displayed in

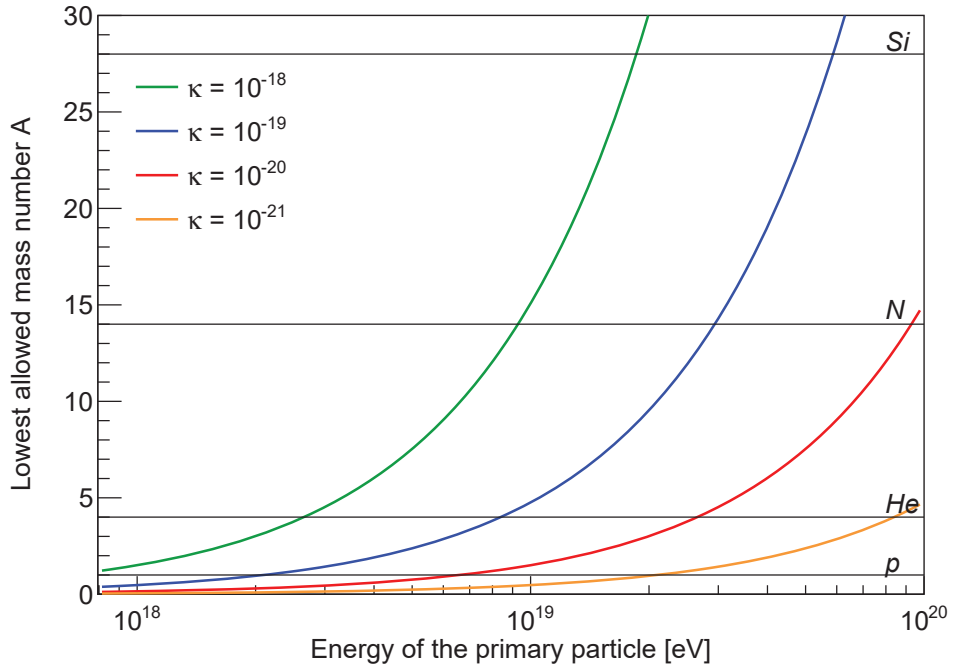


FIGURE 6.20: Mass threshold (in terms of mass number A) related to VCh radiation for different values of κ as a function of primary energy, cf. Eq. (6.7). For a given κ , only primaries above the line can reach the Earth.

Fig. 6.19 are also only plotted up to the maximum energy of the respective primary particle.

The maximum change in $\langle X_{\max} \rangle$, as seen both in Fig. 6.19 and Fig. 6.18, is much smaller than for $\kappa < 0$, with a maximum difference of about 15 g cm^{-2} between simulations with $\kappa = 0$ and any $\kappa > 0$ for the highest allowed energies for the respective particle. This maximum difference is independent of the particle type. The differing magnitude of the changes between $\kappa < 0$ and $\kappa > 0$ can be explained by the difference in shower behaviour of sub-showers initiated by electrons and photons. For VCh radiation, additional photons are produced from electrons in the electromagnetic part of the shower, for showers where photon decay was implemented ($\kappa < 0$), photons decay into electron-positron pairs. In both cases, the energy of the original particle is distributed to both secondary particles. The atmospheric depths of showers initiated by photons and electrons differ significantly, with $\langle X_{\max} \rangle$ values of photon induced showers approximately 30 g cm^{-2} higher than electron induced sub-showers of the same energy. This difference is reproduced using air shower simulations, results of which are added in the appendix in Fig. B.1.

For $\kappa < 0$, photon decay transforms one photon into an electron-positron pair, where the photon energy is distributed to both secondary particles. Both the decrease in particle energy as well as the change from photon to electron/positron lead to a shortening of the resulting sub-showers, explaining the significant impact of photon decay on $\langle X_{\max} \rangle$ which can be seen.

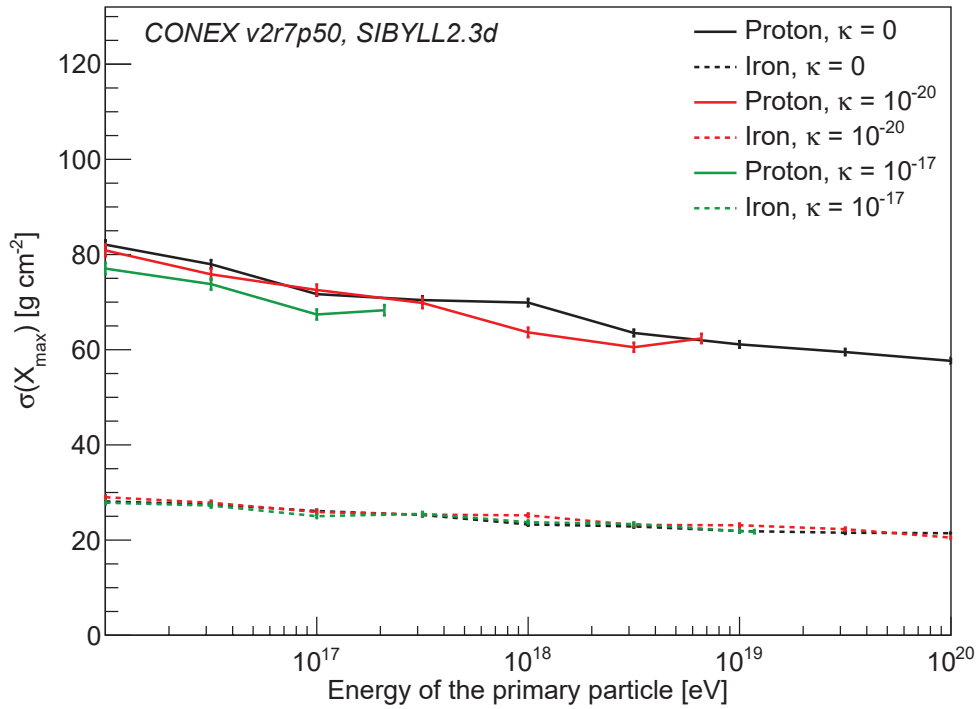


FIGURE 6.21: The simulated values of $\sigma(X_{\max})$ as a function of the primary energy for primary protons and iron nuclei for the absence of LV ($\kappa = 0$) and for different values of $\kappa > 0$. Lines are only plotted up to the maximum energy given by the onset of VCh radiation, see Eq. (4.18).

In the case of $\kappa > 0$, the lower energy of the secondary particles is expected to lead to a decrease of shower depth. This is counteracted by the energy lost by the electron onto a photon through VCh radiation. While the depth of the electron-induced sub-shower will decrease due to energy loss, the sub-shower induced by a photon inheriting a significant share of the electron energy may well be deeper than the sub-shower expected for the original electron for $\kappa = 0$. This can explain the much less pronounced reduction in $\langle X_{\max} \rangle$ for $\kappa > 0$ in comparison to $\kappa < 0$.

A comparison of $\sigma(X_{\max})$ for simulations with and without LV is displayed in Fig. 6.21. Concerning $\sigma(X_{\max})$, similar to the case of negative κ , no strong effect can be seen. This is expected, since a major contributor to shower fluctuations is the variance in the depth of the first interaction, which takes place well before the appearance of VCh radiation in the shower. However, similar to $\kappa < 0$ a minor decrease in $\sigma(X_{\max})$ of less than 5 g cm^{-2} can be seen for protons in the last decade of energy before E_{VCh}^{\max} , with decreasing effects for heavier particles and no visible decrease in $\sigma(X_{\max})$ for iron induced showers.

6.3.2 New limit on $\kappa > 0$ using X_{\max} measurements

The method used to derive an upper limit on $\kappa > 0$ through a comparison of $\langle X_{\max} \rangle$ and $\sigma(X_{\max})$ values for simulations incorporating LV and air shower

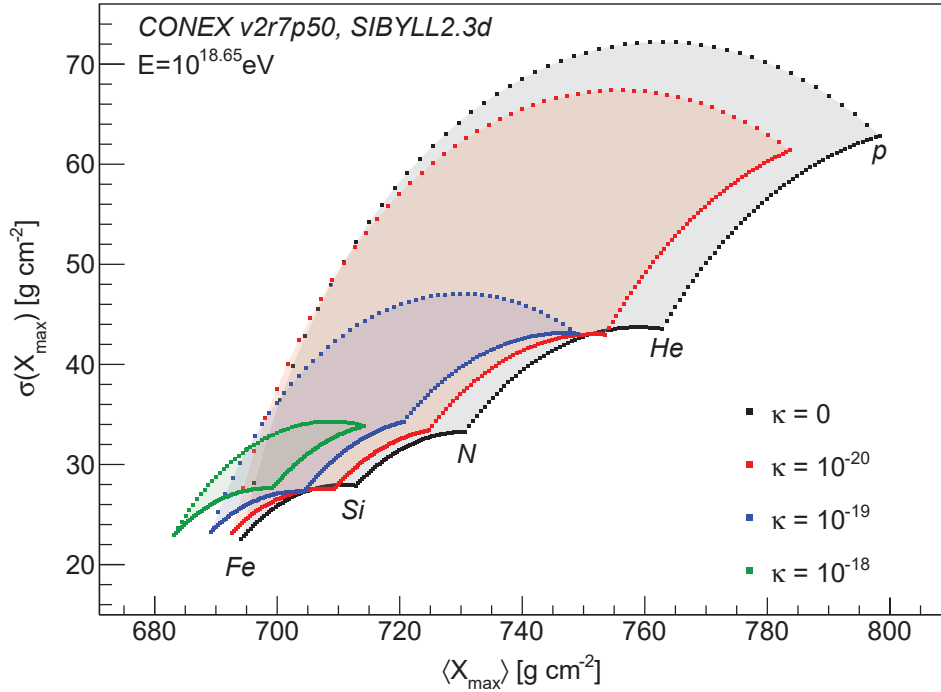


FIGURE 6.22: Comparison of combinations of $\langle X_{\max} \rangle$ and $\sigma(X_{\max})$ derived by simulations, excluding combinations with particles above the VCh radiation threshold, for different values of κ and a primary energy of $10^{18.65}$ eV. The "tips" of the umbrella refer to pure beams with primaries as indicated (proton, helium, nitrogen, silicon, iron). For a given κ , the corresponding "umbrella" covers all values allowed by arbitrary combinations of these primaries. With increasing κ , a reduction of $\langle X_{\max} \rangle$ can be seen as well as a successive removal of light primaries if above VCh radiation threshold.

observations is parallel to the method used in Sec. 6.2.2. The simulations of air showers produced by different primary particles are combined as described in Sec. 5.3.2 to cover all possible primary particle compositions. The results of these combinations for a fixed energy of $E = 10^{18.65}$ eV and differing values of κ are displayed in Fig. 6.22.

The primary particle energy, primary particles, as well as the different values of κ displayed were chosen to show the effect of the progressive exclusion of lighter primary particles with increasing κ according to Eq. (6.7), as well as the changes of X_{\max} discussed in the preceding section. The exclusion of lighter particles is shown by the disappearance of the tips associated with the respective particles for larger values of κ . An example of this is protons disappearing for $\kappa = 1 \times 10^{-19}$, as Eq. (6.7) results in $m \geq 2.15$ u for $E = 10^{18.65}$ eV and $\kappa = 1 \times 10^{-19}$. This results in a minimum mass number of $A \geq 3$ for primary particles. Unstable isotopes, such as tritium ($A = 3$) as well as isotopes with a low natural abundance like helium-3 ($A = 3$) are excluded from this analysis, as the probability of them accounting for a significant fraction of measured cosmic rays is negligible. This leaves helium

as the lightest possible particle for $E = 10^{18.65}$ eV and $\kappa = 1 \times 10^{-19}$. For $\kappa = 1 \times 10^{-18}$, the lower mass threshold is increased to $m \geq 6.78$ u, resulting in the restriction $A \geq 7$ on the mass of the primary particle. Of the primary particles chosen to be displayed in Fig. 6.22, the lightest remaining primary particle is nitrogen. For the determination of the limit on κ , the lightest allowed element is always chosen, which would here be lithium ($A = 7$).

The reduction in $\langle X_{\max} \rangle$ with increasing κ , as well as the lack of significant change in $\sigma(X_{\max})$ discussed in Sec. 6.3.1 can be observed as well. Lighter particles are affected at lower values of κ , with the reduction of $\langle X_{\max} \rangle$ increasing with κ to a maximum of 15 g cm^{-2} , before the particle is excluded from the allowed compositions.

The compatibility of simulations to observations is again tested by comparing the possible $\langle X_{\max} \rangle$ - $\sigma(X_{\max})$ combinations of simulations and measurements for each energy bin and different values of κ . The two highest-energy bins (above $10^{19.50}$ eV) are again excluded from the analysis due to the comparably small statistics. A κ value is treated as compatible with observations, if there is a possible simulated primary particle composition falling into the confidence region for every energy. This composition does not have to necessarily be the same for every energy interval, as the composition may change with different primary particle energies and the exclusion of lower-mass primaries due to VCh radiation.

The number of simulated primary particle compositions inside the confidence region for all energy bins of the X_{\max} moments from the Pierre Auger Observatory for $\kappa = 1 \times 10^{-19}$, $\kappa = 6 \times 10^{-20}$, $\kappa = 3 \times 10^{-20}$, $\kappa = 1 \times 10^{-20}$ and $\kappa = 0$ are shown in Tab. 6.2. The simulated primary particles used here include protons, helium, oxygen and iron as before, with an addition of lithium, beryllium, boron and nitrogen to include elements as close to the respective mass thresholds as possible for all simulated κ -energy combinations. As the allowed compositions are changed in comparison to the analysis done for $\kappa < 0$, the number of accepted compositions is also changed for $\kappa = 0$ between both analyses.

A zero in the table corresponds to no compositions at the edge of possible $\langle X_{\max} \rangle$ - $\sigma(X_{\max})$ combinations inside the determined confidence region for the respective energy. At low energies ($E < 10^{18.2}$ eV), entries marked with X are again due to the confidence region falling entirely into the $\langle X_{\max} \rangle$ and $\sigma(X_{\max})$ values spanned by the simulated showers. Those are thus ignored in this analysis, as well as the energy bins 23 and 24, which are excluded due to small statistics in the observations. A zero at high energies $E > 10^{18.2}$ eV corresponds to no simulated combinations falling into the respective confidence region. These can be found for $\kappa \leq 3 \times 10^{-20}$, with exactly one energy bin having no overlap for $\kappa = 3 \times 10^{-20}$. This excluded energy bin is at $E = 10^{18.65}$ eV, for $\kappa = 3 \times 10^{-20}$ this is the bin with the lowest energy, for which protons are not allowed as primary particles, thus helium is the lightest particle allowed in this composition. This leads to the proton-helium compositions, which were inside the confidence region for smaller κ , being

| Bin # | $\log_{10}(E/\text{eV})$ | $\kappa =$ | | | | |
|-------|--------------------------|---------------------|---------------------|---------------------|---------------------|-----|
| | | 1×10^{-19} | 6×10^{-20} | 3×10^{-20} | 1×10^{-20} | 0 |
| 0 | 17.26 | X | X | X | X | X |
| 1 | 17.35 | 2 | X | 4 | X | X |
| 2 | 17.45 | 5 | X | X | X | X |
| 3 | 17.55 | 5 | X | X | X | X |
| 4 | 17.65 | 9 | 5 | X | X | X |
| 5 | 17.75 | 12 | 9 | 4 | X | X |
| 6 | 17.85 | 10 | 9 | 4 | X | X |
| 7 | 17.95 | 15 | 13 | 8 | 2 | X |
| 8 | 18.05 | 19 | 18 | 13 | 8 | X |
| 9 | 18.15 | 21 | 20 | 16 | 11 | 2 |
| 10 | 18.25 | 26 | 25 | 21 | 16 | 6 |
| 11 | 18.35 | 0 | 29 | 26 | 20 | 9 |
| 12 | 18.45 | 0 | 0 | 29 | 23 | 11 |
| 13 | 18.55 | 0 | 0 | 28 | 23 | 11 |
| 14 | 18.65 | 0 | 0 | 0 | 24 | 7 |
| 15 | 18.75 | 35 | 38 | 46 | 57 | 82 |
| 16 | 18.85 | 31 | 35 | 43 | 55 | 91 |
| 17 | 18.95 | 0 | 47 | 57 | 82 | 136 |
| 18 | 19.05 | 0 | 0 | 65 | 90 | 146 |
| 19 | 19.15 | 6 | 23 | 91 | 123 | 184 |
| 20 | 19.25 | 0 | 15 | 30 | 125 | 178 |
| 21 | 19.35 | 0 | 19 | 106 | 179 | 214 |
| 22 | 19.44 | 0 | 44 | 130 | 222 | 206 |
| 23 | 19.55 | | 0 | 36 | 176 | 194 |
| 24 | 19.73 | | | 100 | 204 | 93 |

TABLE 6.2: Number of points in the contour around the $\langle X_{\text{max}} \rangle - \sigma(X_{\text{max}})$ values allowed by all compositions simulated using CONEX with the hadronic interaction model SIBYLL 2.3d inside the Auger confidence region determined from recent X_{max} moments published in [Yus19]. Selected values of $\kappa > 0$ are shown with decreasing strength of LV from left to right. For each value of κ , the comparison is done separately for each energy bin of the measurements from the Pierre Auger Observatory. Entries where the Auger confidence region is entirely inside the region covered by simulated showers are marked with an X. The two highest energy bins are excluded from the analysis due to low statistics, but listed here for completeness.

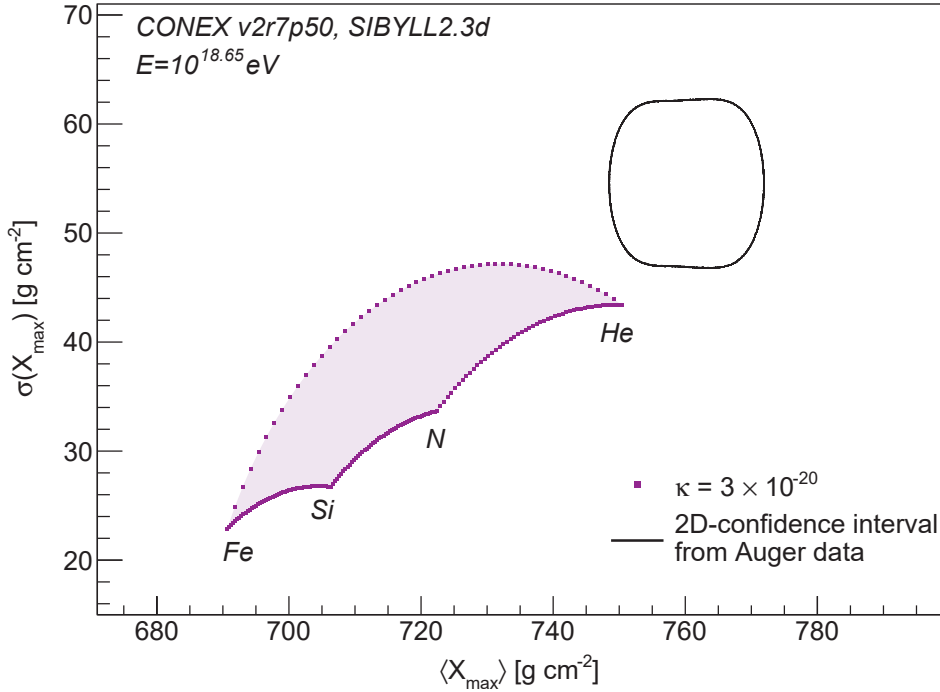


FIGURE 6.23: Comparison of the combinations of $\langle X_{\max} \rangle$ and $\sigma(X_{\max})$ derived by simulations which incorporate LV to the 2D confidence interval (98 % CL) given by the measurements of the Pierre Auger Observatory [Yus19] for the critical value of $\kappa = 3 \times 10^{-20}$ and a primary particle energy of $10^{18.65}$ eV. The umbrella shape covers all combinations of iron, silicon, nitrogen and helium primary particles, since protons are excluded due to VCh radiation for these values of energy and κ .

excluded, resulting in no more overlap between simulations and data. Plots for energy bins 0 to 23 at $\kappa = 3 \times 10^{-20}$ can be found in appendix B.12, B.13 and B.14, including all particles used for the results depicted in Tab. 6.2.

For higher values of κ , the zeroes at $E = 10^{18.35}$ eV to $E = 10^{18.65}$ eV can be explained by the same effect for higher masses. At $E = 10^{18.95}$ eV and $E = 10^{19.05}$ eV, no overlap is found for $\kappa = 6 \times 10^{-20}$ and $\kappa = 1 \times 10^{-19}$, as at this point helium is also excluded from possible primary particle compositions. Overall, discrepancies between simulations and data for $\kappa > 0$ are mainly caused by the exclusion of primary particles at high energies and greater values of κ , with the changes in X_{\max} increasing the effect.

As in the analysis for $\kappa < 0$, if an energy bin without a primary particle combination fitting the confidence region exists for a value of κ , this κ is not compatible with observations and can thus be excluded. By repeating this process for different κ , a value κ_{crit} can be established, for which all $\kappa \geq \kappa_{\text{crit}}$ are excluded while all $\kappa < \kappa_{\text{crit}}$ do fit with measurements. This leads to the new upper bound on $\kappa > 0$ of [DNR23]

$$\kappa < \kappa_{\text{crit}} = 3 \times 10^{-20} \quad (98\% \text{ CL}) . \quad (6.8)$$

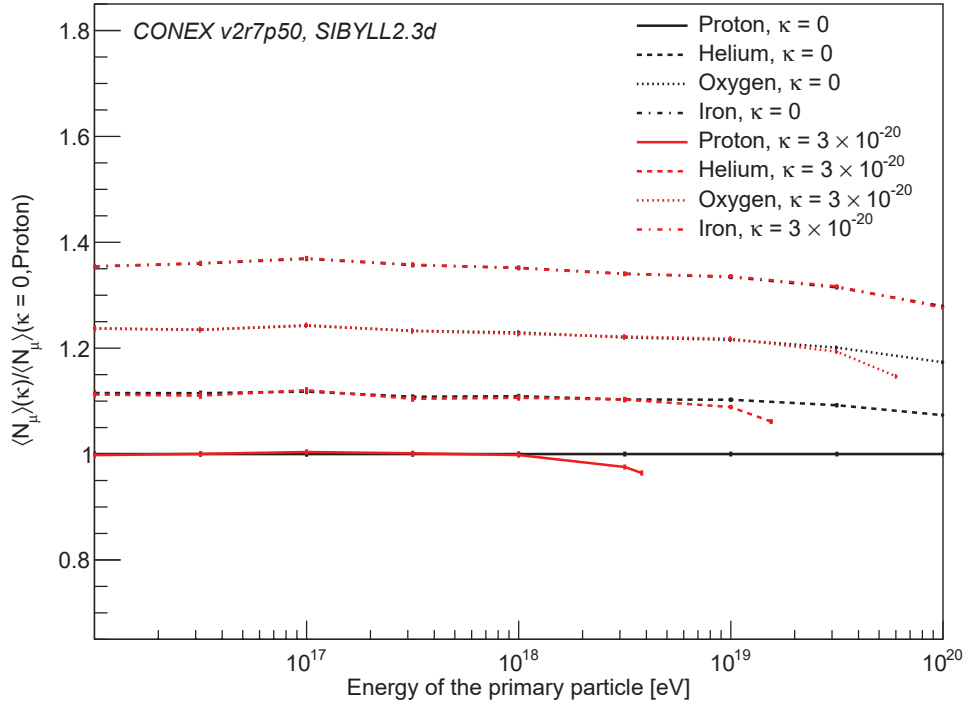


FIGURE 6.24: The simulated values of $\langle N_\mu \rangle$ as a function of the primary energy for different primary particles in the absence of LV ($\kappa = 0$) and for $\kappa = 3 \times 10^{-20}$. All values are normalized to the value of $\langle N_\mu \rangle$ for unmodified protons at the corresponding energy, to show the relative effect of LV on the muon number.

This confirms the previous limit derived from the observation of UHE cosmic rays using an independent method and improves this previous limit referenced in Eq. (4.24) by a factor of 2. The distribution of both $\langle X_{\max} \rangle$ and $\sigma(X_{\max})$ values simulated using SIBYLL2.3d as well as the confidence region for this critical bin at $E = 10^{18.65}$ eV are shown in Fig. 6.23. As seen in the plot, the compositions closest to the confidence region in the energy region used for the new bound are again very helium-heavy. As the disappearance of lighter particles at higher energies is crucial for determining the new bound, decreases in measurement uncertainties at the highest energies are expected to be able to be used to gain further improvements upon this bound.

6.3.3 Changes in N_μ

The effects of LV on the muon number N_μ of the shower for $\kappa > 0$ are found to be generally opposite to those for $\kappa < 0$ discussed in Sec. 6.3.3. While the mean number of muons $\langle N_\mu \rangle$ increases for $\kappa < 0$, a decrease can be seen for $\kappa > 0$, which is displayed in Fig. 6.24. The magnitude of the change is also smaller, with a maximal decrease in $\langle N_\mu \rangle$ of $\approx 4\%$ in comparison to the SM value. Changes in $\langle N_\mu \rangle$ also only appear near the highest allowed energies of the respective primary particles. For energies lower than approximately half the maximum energy described by Eq. (6.6), the muon number shows no changes incompatible with statistical fluctuations. This can be explained

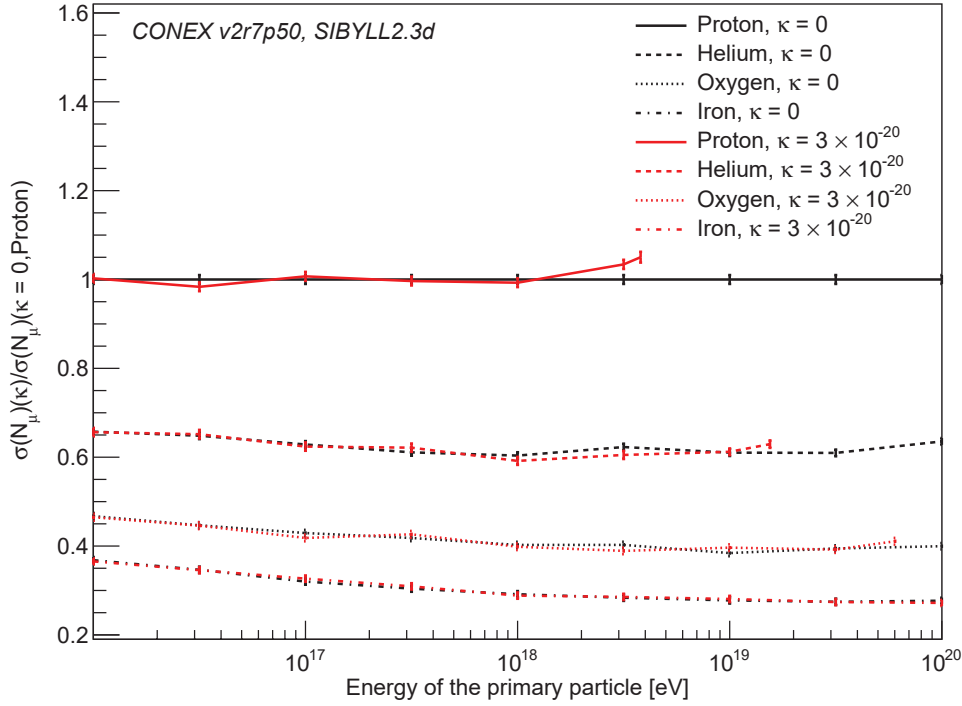


FIGURE 6.25: The simulated values of $\sigma(N_\mu)$ as a function of the primary energy for different primary particles in the absence of LV ($\kappa = 0$) and for $\kappa = 3 \times 10^{-20}$. All values are normalized to the value of $\sigma(N_\mu)$ for unmodified protons at the corresponding energy, to show the relative effect of LV on the muon number.

by examining the type of secondary particles emitting VCh radiation inside the shower.

The emission of VCh radiation by electrons was identified to produce the majority of the changes observed in X_{\max} in Sec. 6.3.1, while VCh radiation of other particles can be mostly neglected. However, changes in the electromagnetic part of the air shower do not affect the number of muons produced in a significant way, thus VCh radiation of electrons can be excluded as the reason for the change in $\langle N_\mu \rangle$. Other candidate particles for VCh radiation inside showers, as discussed in Sec. 4.5, are secondary pions and muons produced in the start-up phase of the shower. Those particles have significantly higher masses than electrons, thus, according to Eq. (4.18) their threshold energies for VCh radiation are also significantly higher. In extensive air showers, pions can be produced from the first hadronic interactions, while muons typically are the result of the decay of charged pions [MR18]. This makes the occurrence of VCh radiation produced by muons highly improbable, since the maximum of the energy of the producing pion following Eqs. (4.30) and (4.31) is only:

$$E_{\text{VCh},\pi^\pm}^{\text{th}} = \frac{m_{\pi^\pm}}{m_{\mu^\pm}} E_{\text{VCh},\mu^\pm}^{\text{th}}(\kappa) \approx 1.32 E_{\text{VCh},\mu^\pm}^{\text{th}}(\kappa) \quad (6.9)$$

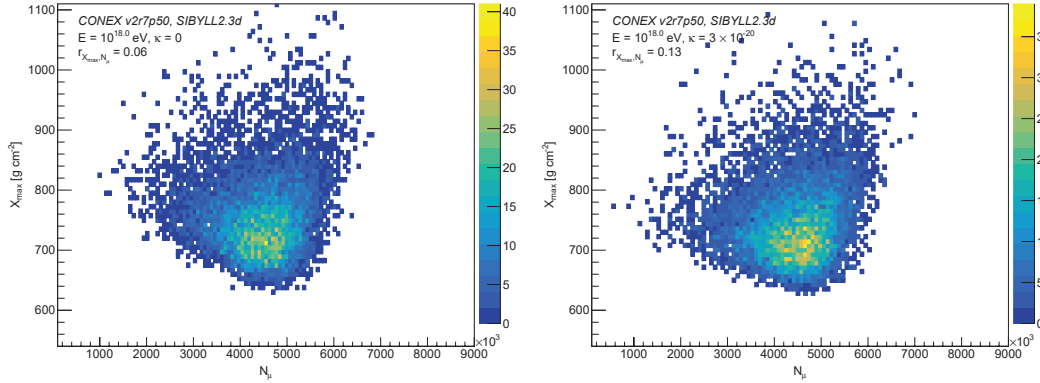


FIGURE 6.26: Visual example of the changes in the distribution of X_{\max} and the number of muons observed at ground level N_{μ} and their correlation for $\kappa = 0$ (left) and $\kappa = 3 \times 10^{-20}$ (right) and an energy of 10^{18} eV. Shown is a pure CR composition of only protons.

Overall, the majority of the changes in N_{μ} are thus driven by the VCh radiation of high-energy pions during the first interactions of the shower.

Although the value of $\langle N_{\mu} \rangle$ decreases for individual particles, the minimal value of $\langle N_{\mu} \rangle$ of possible primary particle compositions increases at higher energies in comparison to the SM, once the lightest particles are excluded due to VCh radiation. This is due to the higher number of muons occurring in showers caused by heavier primaries. For example, helium-induced showers simulated with $\kappa = 3 \times 10^{-20}$, even with the maximally possible reduction in $\langle N_{\mu} \rangle$ due to VCh radiation, still shows $\approx 6\%$ more muons than a proton-induced shower at the same energy with $\kappa = 0$.

While the value of $\sigma(N_{\mu})$ decreases for $\kappa < 0$, it is increasing for $\kappa > 0$. This is illustrated in Fig. 6.25. This increase is minor, only resulting in a maximal change of 5%. As for $\langle N_{\mu} \rangle$, showers with energies below half of the maximally allowed energy for the respective particle show no changes in $\sigma(N_{\mu})$ due to VCh radiation. The relative width of the N_{μ} distribution increases up to $\approx 8\%$ due to the decrease in $\langle N_{\mu} \rangle$ with the simultaneous increase in $\sigma(N_{\mu})$.

6.3.4 Changes in the correlation between X_{\max} and N_{μ}

The changes due to the introduction of VCh radiation on the correlation $r(X_{\max}, N_{\mu})$ between X_{\max} and N_{μ} for individual particles are much less pronounced than for $\kappa < 0$. In Fig. 6.26, the comparison between the distributions of X_{\max} and N_{μ} for $\kappa = 0$ and $\kappa = 3 \times 10^{-20}$ are shown at an energy of 10^{18} eV. A visible effect of the introduction of LV is the shift to lower values of X_{\max} , especially for showers with a low number of muons. This leads to a minor increase in $r(X_{\max}, N_{\mu})$ from 0.06 for $\kappa = 0$ to 0.13 for $\kappa = 3 \times 10^{-20}$.

In the case of a positive value of κ , a major contribution for the change in $r(X_{\max}, N_{\mu})$ for maximally mixed composition is the exclusion of lighter

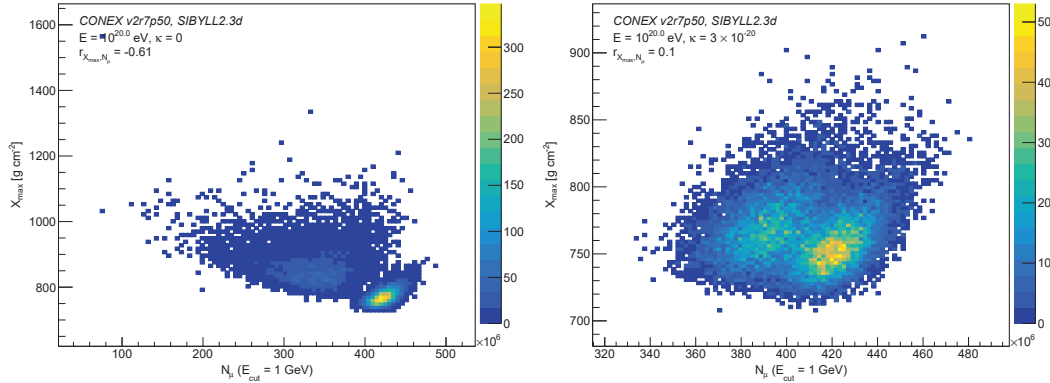


FIGURE 6.27: Visual example of the changes in the distribution of X_{\max} and the number of muons observed at ground level N_{μ} and their correlation for $\kappa = 0$ (left) and $\kappa = 3 \times 10^{-20}$ (right) and an energy of 10^{20} eV. Shown are the maximally mixed compositions of a cosmic ray spectrum consisting of 50 % protons and 50 % iron nuclei for $\kappa = 0$ and 50 % aluminium and 50 % iron nuclei for $\kappa = 3 \times 10^{-20}$.

particles from compositions at higher energies. Changes in both X_{\max} and N_{μ} are less pronounced than for $\kappa < 0$. This leads to less changes in the correlation $r(X_{\max}, N_{\mu})$ between both observables due to changing means of distributions resulting from simulations of showers initiated by primary particles of different masses. Instead, the majority of the effect on $r(X_{\max}, N_{\mu})$ is produced by a change in the maximally mixed composition possible for different κ at the same energies. As lighter primary particles become increasingly excluded by VCh radiation for larger values of κ , the maximally mixed composition changes accordingly to a mixture of 50 % of the lightest remaining primary particle and 50 % iron nuclei. The change in the distribution of X_{\max} and N_{μ} is displayed in Fig. 6.27 for $\kappa = 3 \times 10^{-20}$ and a primary particle energy of 10^{20} eV.

It can be observed that the distributions of aluminium and iron, which form the maximally mixed composition for $\kappa = 3 \times 10^{-20}$, are much less distinct than those of protons and iron for $\kappa = 0$. This is due to the lower difference in masses between aluminium and iron, which results in less difference in $\langle X_{\max} \rangle$ and $\langle N_{\mu} \rangle$ for those particles, as $\langle X_{\max} \rangle$ decreases with mass while $\langle N_{\mu} \rangle$ increases with increasing primary particle mass. The correlation for the maximally mixed composition decreases in magnitude from $r(X_{\max}, N_{\mu}) = -0.61$ to $r(X_{\max}, N_{\mu}) = 0.1$.

The correlation $r(X_{\max}, N_{\mu})$ at $E = 10^{20}$ eV for different two-particle compositions with a maximal spread in A between both particles for $\kappa = 0$ and $\kappa = 3 \times 10^{-20}$ can be seen in Fig. 6.28. For $\kappa = 0$, a proton-iron composition is shown, with the iron fraction ranging from 0 % to 100 %. For $\kappa = 3 \times 10^{-20}$, the lightest primary particle not affected by VCh radiation is aluminium, thus an aluminium-iron composition is chosen. Similar to $\kappa < 0$, $r(X_{\max}, N_{\mu})$ increases with the introduction of LV. The minimum of $r(X_{\max}, N_{\mu})$ for $\kappa < 0$ is again at a composition with 30 % protons and 70 % iron, with a minimum

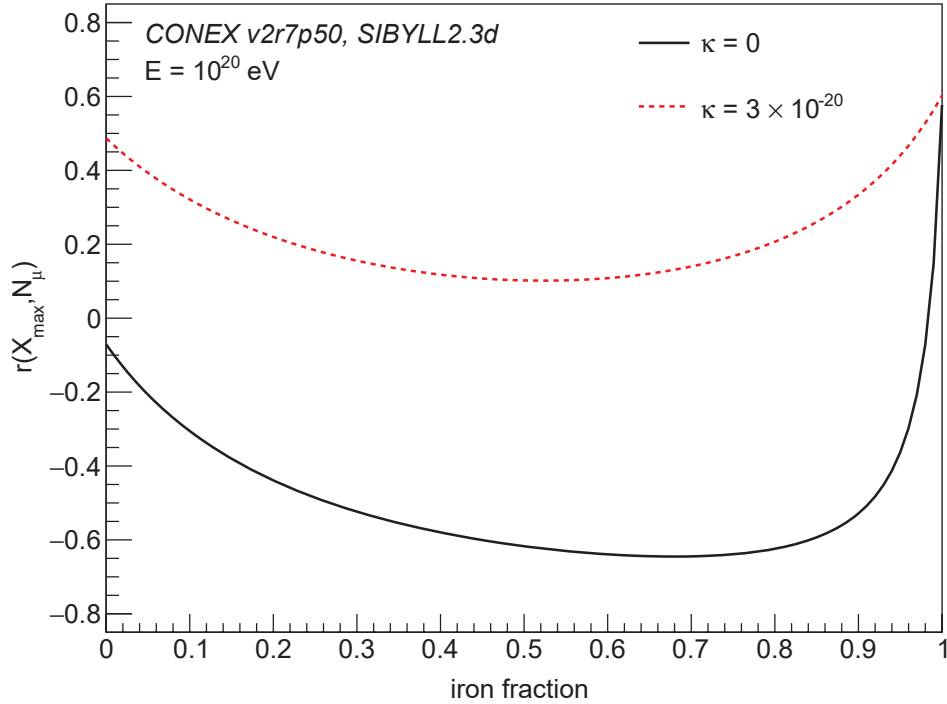


FIGURE 6.28: The correlation $r(X_{\max}, N_{\mu})$ between X_{\max} and N_{μ} for showers with a primary particle composition of only protons and iron ($\kappa = 0$) and aluminium and iron ($\kappa = 3 \times 10^{-20}$). The correlation is shown for different fractions of both primaries, ranging from a pure proton (aluminium) composition to pure iron for $\kappa = 0$ ($\kappa = 3 \times 10^{-20}$). Showers were simulated for a primary particle energy of 10^{20} eV.

value of $r(X_{\max}, N_{\mu})_{\min} = -0.65$. For $\kappa = 3 \times 10^{-20}$, the minimal value of $r(X_{\max}, N_{\mu})$ is reached at the maximally mixed composition of 50% aluminium and 50% iron, with a minimum of $r(X_{\max}, N_{\mu})_{\min} = 0.1$. The minimum correlation for aluminium and iron is at an approximately equal composition as both particles are much closer in mass, with the widths of both X_{\max} and N_{μ} distributions being more similar than those of protons and iron.

As was discussed already in Sec. 6.2.4, a comparison of $r(X_{\max}, N_{\mu})$ to observations is a possible way to set a bound on κ , as the minimum of the possible correlation increases with greater values in κ . As $r(X_{\max}, N_{\mu})$ increases for both $\kappa < 0$ and $\kappa > 0$, a two sided bound can be set by a single measurement of $r(X_{\max}, N_{\mu})$.

6.3.5 Differences between hadronic interaction models

The differences in both $\langle X_{\max} \rangle$ and $\sigma(X_{\max})$ between the three hadronic interaction models SIBYLL 2.3d, EPOS LHC and QGSJET-II is illustrated in Fig. 6.29 for modified simulations of both proton and iron primaries. As the unmodified showers are the same as the ones used before for the model comparison done in Sec. 6.2.1, the differences between unmodified showers simulated with the different models are not repeated here. For modified showers

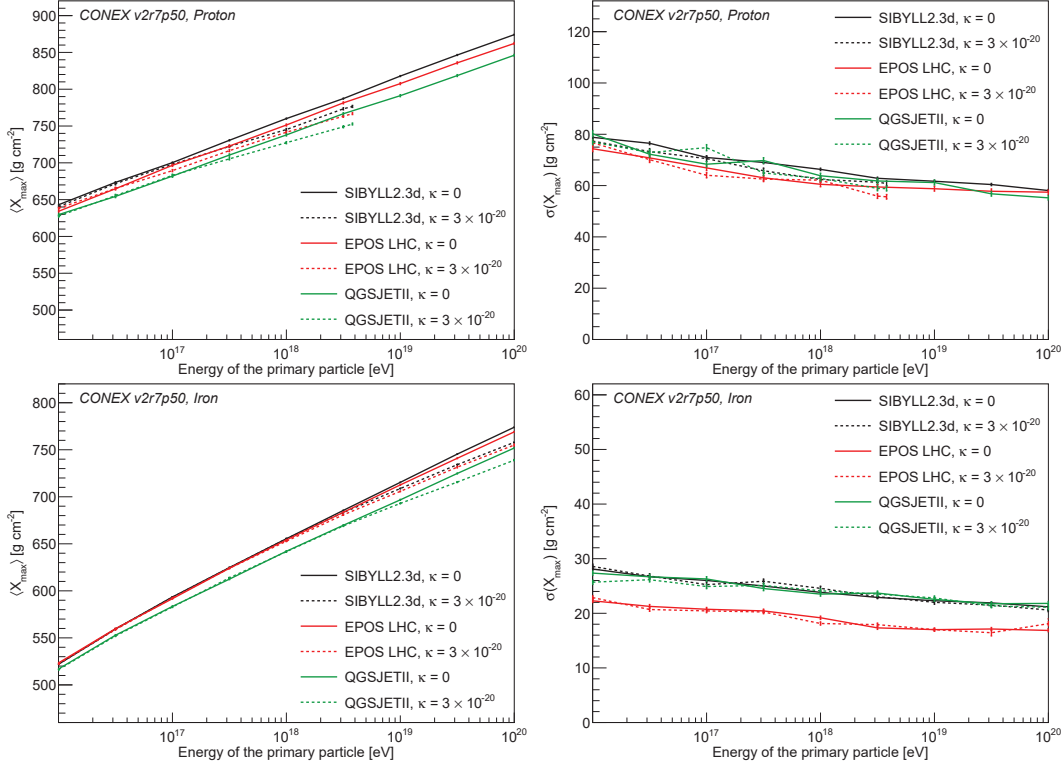


FIGURE 6.29: The simulated values of $\langle X_{\max} \rangle$ and $\sigma(X_{\max})$ as a function of the primary energy for primary protons and iron nuclei for the absence of LV ($\kappa = 0$) and for $\kappa > 0$. Shown are simulations with the three hadronic interaction models SIBYLL 2.3d [Rie+20], EPOS LHC [Pie+15] and QGSJET-II-04 [Ost11].

with $\kappa < 0$, the relative changes in both $\langle X_{\max} \rangle$ and $\sigma(X_{\max})$ are equivalent in each model. Consequently, SIBYLL 2.3d produces the highest values of $\langle X_{\max} \rangle$, independent of primary particle mass, followed by EPOS LHC with a $\approx 10 \text{ g cm}^{-2}$ smaller $\langle X_{\max} \rangle$ and QGSJET-II with an additional $\approx 15 \text{ g cm}^{-2}$ difference. In $\sigma(X_{\max})$, values for SIBYLL 2.3d and QGSJET-II match closely, while EPOS LHC produces $\approx 5 \text{ g cm}^{-2}$ less shower to shower fluctuations.

The new bound on $\kappa > 0$ derived in Sec. 6.3.2 does not change if the analysis is repeated using EPOS LHC as the hadronic interaction model. In simulations generated with both models, the energy bin from $10^{18.6} \text{ eV}$ to $10^{18.7} \text{ eV}$ is critical to determine the limit. This bin is the lowest energy bin for the critical value of $\kappa = 3 \times 10^{-20}$ in which the removal of protons from the composition of primaries leads to a loss of compatibility between simulations and measurements, with helium now taking its place as the lowest-mass particle in the composition. As both $\langle X_{\max} \rangle$ and $\sigma(X_{\max})$ are lower for EPOS LHC, this bin remains excluded in that model. For the next lower value of κ investigated, $\kappa = 2 \times 10^{-20}$, protons are again allowed as the lightest particle of the primary particle composition, leading to an overlap between both regions in both models.

Since showers produced using QGSJET-II-04 are much shallower than

those produced with the other two models, they are again not able to reproduce the data in a self-consistent way, even in the absence of LV for $\kappa = 0$.

A comparison of the impact of VCh radiation on $\langle N_\mu \rangle$ and $\sigma(N_\mu)$ in different hadronic interaction models can be found in appendix B.4 and B.5. The relative change of $\langle N_\mu \rangle$ is greatest for SIBYLL 2.3d, followed by EPOS LHC and QGSJET-II-04, although the difference between models is of the order of only 1%. For $\sigma(N_\mu)$, no differences between the relative changes not compatible with statistical fluctuations are seen.

6.4 Outlook

The new bounds on the LV parameter κ gained in this chapter can possibly be improved further in various ways. A straightforward way for improved limits is repeating the analysis done in this chapter once more CR observations are available, with higher statistics and smaller uncertainties in the measured observables. With smaller uncertainties, the size of the confidence regions in the investigated $\langle X_{\max} \rangle$ - $\sigma(X_{\max})$ parameter space is reduced, thus less simulated compositions match this region. In general, the energy of the CRs used to set narrower bounds will increase with smaller values of κ , as the energy thresholds for LV processes increases.

As an example, a reduction of systematic and statistical uncertainties of the used measurements by a factor of two, keeping the mean values of both $\langle X_{\max} \rangle$ and $\sigma(X_{\max})$, would result in an expected improvement of the limit on $\kappa < 0$ by a factor of ≈ 10 . The energy of the bin critical for this improved limit would be at $E = 10^{19.15}$ eV, two bins above the energy at the bin used for the current bound. For $\kappa > 0$, the same reduction of uncertainties has only negligible impact on the bound. The only energy bin showing no overlap in addition to the one at $E = 10^{18.65}$ eV used for the current limit of $\kappa = 3 \times 10^{-20}$ is at $E = 10^{19.25}$ eV. This is due to the exclusion of helium and lithium taking over as the lightest possible particle in the composition. However, this does not lead to any improvement on the limit, as for $\kappa = 2 \times 10^{-20}$, protons become allowed at $E = 10^{18.65}$ eV, while helium also does not undergo VCh radiation at $E = 10^{19.25}$ eV. With those particles again included in the possible CR compositions, simulations and the confidence region match again at $\kappa = 2 \times 10^{-20}$ for all energies, leaving the upper bound at $\kappa < 3 \times 10^{-20}$.

A second method to improve the bounds on κ is the inclusion of additional observables into the analysis, such as the number of muons per shower arriving at the ground N_μ investigated here. For $\kappa < 0$, significant changes caused by LV in both $\langle N_\mu \rangle$ and $\sigma(N_\mu)$ can be seen already for pure particle compositions. For $\kappa > 0$, the changes in N_μ for individual particles are less pronounced, with changes on the range of $\langle N_\mu \rangle$ and $\sigma(N_\mu)$ covered by all possible primary particle compositions primarily being caused by the introduction of a minimum mass of primary particles arriving at earth due to VCh

radiation. In both cases the minimal value of $\langle N_\mu \rangle$ for all possible compositions increases with primary particle energy and magnitude of κ , while the maximal value of $\sigma(N_\mu)$ decreases. At the current bounds, those effects are seen at energies of $\approx 10^{19}$ eV and above.

Adding N_μ as an additional observable to the analysis can be done in several ways. When the muon content in air showers is known, the comparison done for $\langle X_{\max} \rangle$ and $\sigma(X_{\max})$ can be expanded from two to four dimensions, including $\langle N_\mu \rangle$ and $\sigma(N_\mu)$. For the standard SD stations of the Pierre Auger Observatory, the direct measurements of the muon content of air showers is currently not possible, as the water Cherenkov detector does not distinguish signals caused by electrons and muons. Instead, the signal strength $S(1000)$ can be used as a replacement for the muon number, as muons are produced higher up in the atmosphere and have thus a wider lateral profile at the ground than electrons. For the determination of changes in $S(1000)$ due to LV, a three-dimensional shower simulation program like CORSIKA has to be used with the appropriate modifications to include LV, as CONEX simulates only the longitudinal shower development. Through modified simulations using CORSIKA, the expected lateral distributions of secondary particles at the ground can be found and compared to the detector responses of CR observations.

The introduction of LV into shower simulations also impacts the range of possible correlations $r(X_{\max}, N_\mu)$ between X_{\max} and N_μ reachable by combinations of different primary particles. For both $\kappa < 0$ and $\kappa > 0$, the minimal correlation $r(X_{\max}, N_\mu)$ increases significantly for the current bounds of κ in comparison to $\kappa = 0$. Thus, observations of a negative correlation $r(X_{\max}, N_\mu)$ can be used to set bounds on κ . When direct measurements of the muon number are unavailable, $S(1000)$ can be used as a replacement in an approach similar to that used in [Aab+16b], again requiring three-dimensional simulations of shower development. Through a combination of comparisons in $\langle X_{\max} \rangle$ and $\sigma(X_{\max})$, as well as $r(X_{\max}, N_\mu)$, further improvements of the bounds can be expected. This is due to mostly pure compositions being used to set bounds on κ in the analysis described here, as those define the outline of the $\langle X_{\max} \rangle$ - $\sigma(X_{\max})$ region allowed by simulations, while the lowest $r(X_{\max}, N_\mu)$ are reached by mixed compositions. Due to the necessity of one possible simulated composition matching measurements in $\langle X_{\max} \rangle$, $\sigma(X_{\max})$ and $r(X_{\max}, N_\mu)$, even stronger bounds of κ can be expected to be determined by a combined analysis of X_{\max} and N_μ .

Chapter 7

Conclusion

In this thesis, a method producing the currently most stringent bounds on nonbirefringent, isotropic Lorentz Violation in the photon sector by analyzing extensive air showers was presented. New bounds on the LV parameter κ were gained by analyzing the changes in air shower development for both $\kappa < 0$ and $\kappa > 0$, focusing on the average depth of the shower maximum $\langle X_{\max} \rangle$ and the variations between showers $\sigma(X_{\max})$. Shower parameters from showers simulated using the one-dimensional shower simulation code CONEX were compared to observations done by the Pierre Auger Observatory, allowing for any possible primary particle composition for simulated showers. Significant decreases in $\langle X_{\max} \rangle$ for $\kappa < 0$ as well as a restriction on possible primary particle masses for $\kappa > 0$ for simulations incorporating LV were used in the two dimensional comparison between simulations and observations to gain new bounds on κ :

$$-6 \times 10^{-21} < \kappa < 3 \times 10^{-20} \quad (98\% \text{ CL}). \quad (7.1)$$

The new limits on κ improve both the two-sided bound of $-9 \times 10^{-16} < \kappa < 6 \times 10^{-20}$, which was based on the observed energies of UHE photons and CRs [KS08], as well as the lower bound of $\kappa > -6 \times 10^{-19}$, which was gained by analyzing the impact of LV on $\langle X_{\max} \rangle$ [KNR17]. The previously strongest bound on κ is improved by a factor 50 for $\kappa < 0$. For $\kappa > 0$, the previous bound is improved by a factor of two, also confirming the previous bound with an independent method.

Possible further improvements of the limits derived here were discussed, with the reduction of statistical uncertainties in observations leading to improved bounds on κ , particularly in the case of $\kappa < 0$.

The introduction of the number of muons N_μ into the analysis can also lead to further improvements of the bounds on κ . Changes in N_μ for showers with $\kappa \neq 0$ were shown, with a significant increase in $\langle N_\mu \rangle$ for pure CR compositions at $\kappa < 0$. For $\kappa > 0$, the minimal value of $\langle N_\mu \rangle$ of possible primary particle compositions increases due to the restriction to higher primary particle masses at higher energies.

The changes in the shower development due to LV also result in an increase in the correlation $r(X_{\max}, N_{\mu})$ between X_{\max} and N_{μ} , both for pure and mixed CR compositions. The increase of the minimal correlation for simulated air showers $r(X_{\max}, N_{\mu})_{\min}$ through the introduction of LV for both $\kappa < 0$ and $\kappa > 0$ can be used to set new bounds on κ through simultaneous observations of muon content and shower depth, as well as through three-dimensional simulations of LV air showers, which enable a comparison of the lateral distributions of particles between simulations and measurements.

Appendix A

Code

```

1      IF (IQ(NP).EQ.0) THEN
2          aKappa = -1e-19
3          aThreshold = 0
4          call lvomegathreshold(aKappa,aThreshold)
5          aThreshold=aThreshold/1e6
6      IF (E(NP).GE.aThreshold) THEN
7          aTempEnergy = E(NP)*1e6
8      C      print *, "found photon above threshold!",E(NP)
9          IQ(NP)=-1
10     C      E(NP)=0.78*aTempEnergy/1e6
11         aDrawnEnergy = 0
12         call lvdrawrandomenergy(aKappa,aTempEnergy,aDrawnenergy
13     )
14         E(NP)=aDrawnenergy/1e6
15         IQ(NP+1)=1
16         E(NP+1)=aTempEnergy/1e6-E(NP)
17         U(NP+1)=U(NP)
18         V(NP+1)=V(NP)
19         W(NP+1)=W(NP)
20         X(NP+1)=X(NP)
21         Y(NP+1)=Y(NP)
22         Z(NP+1)=Z(NP)
23         IR(NP+1)=IR(NP)
24         XM(NP+1)=XM(NP)
25         YM(NP+1)=YM(NP)
26         ZM(NP+1)=ZM(NP)
27         DM(NP+1)=DM(NP)
28         TM(NP+1)=TM(NP)
29         WT(NP+1)=WT(NP)
30         DNEAR(NP+1)=DNEAR(NP)
31         LATCH(NP+1)=LATCH(NP)
32         NP=NP+1
33     END IF
END IF

```

LISTING A.1: Implementation of the instantaneous decay of a photon above energy threshold into an electron-positron pair added into the EGS4 section of CONEX, inserted after line 398247 of the original code.

```

1  subroutine lvomegathreshold(kappa, threshold)
2  implicit none
3  real*8, intent(in) :: kappa
4  real*8, intent(out) :: threshold
5
6  threshold = 2*511000*sqrt((1-kappa)/(-2*kappa))
7  return
8  end

```

LISTING A.2: Implementation of the energy threshold for photon decay given in Eq. (4.10) in an additional subroutine in CONEX. Inserted at the end of the original CONEX code.

```

1  aPionKappa = -1e-19
2  aPionTempEnergy = E1*1e9
3  aGfactor = 1
4  call lvpizerogfactor(aPionKappa, aPionTempEnergy, aGfactor)
5 C  print *, "found pion!", E1
6  B= bdeca(6)*aGfactor
7 C  B= bdeca(6)

```

LISTING A.3: Code inserted into the propagation subroutine to modify the neutral pion decay time, replacing line 4484 of the original CONEX code.

```

1  subroutine lvpizerogfactor(kappa, energy, gfactor)
2  implicit none
3  real*8, intent(in) :: kappa, energy
4  real*8, intent(out) :: gfactor
5  real*8 :: ecut
6
7  ecut = 134.9766*1e6*sqrt((1-kappa)/(-2*kappa))
8
9  if(energy < ecut) then
10     gfactor = sqrt(1-kappa**2)/((1-kappa)**3)*(1-(energy**2
11 &   -(134.9766*1e6)**2)/((1-kappa)/(-2*kappa)*
12 &   (134.9766*1e6)**2))**2
13  end if
14  if(energy >= ecut) then
15     gfactor = 0
16  end if
17
18  return
19  end

```

LISTING A.4: Subroutine added to CONEX to implement the multiplicative factor of the pion decay rate. Inserted at the end of the original CONEX code.

```

1  subroutine lvdrawrandomenergy(kappa, omega, drawnenergy)
2  implicit none
3  real*8, intent(in) :: kappa, omega
4  real*8, intent(out) :: drawnenergy
5  real*8 :: Eminus, Eplus, Gamma, r
6  integer*4 :: nbins, i, j, low, high, mid, k
7  real*8, dimension(100000) :: x, y
8
9  Eminus = 0.5*omega*(1.0 - sqrt((1.0+kappa)/(1.0-kappa)))*sqrt
10 (1.0-
11 &(1022000.0*sqrt((1.-kappa)/(-2.0*kappa)))**2/(omega**2))
12
13 Eplus = 0.5*omega*(1.0 + sqrt((1.0+kappa)/(1.0-kappa)))*sqrt
14 (1.0-
15 &(1022000.0*sqrt((1.-kappa)/(-2.0*kappa)))**2/(omega**2))
16
17 Gamma = -1.0/(137.0*sqrt((1.0+kappa)/(1.0-kappa))*(1+kappa)
18 *(1+
19 &kappa))*((2*kappa/(3*omega**2)*Eplus**3)-(2*kappa/(3*omega*
20 omega)*
21 &Eminus**3)-(kappa/omega*Eplus**2)+(kappa/omega*Eminus**2)+
22 &(kappa/(1.0-kappa)-(1+kappa)*511000.0**2/(omega**2))*
23 &Eplus-(kappa/(1.0-kappa)-(1+kappa)*511000.0**2/(omega**2))*
24 Eminus)
25
26 nbins = 100000
27 i = 2
28 x(1) = Eminus
29 y(1) = 0.0
30
31 do while( i < nbins )
32 x(i) = Eminus + (Eplus-Eminus)/(nbins)*i
33
34 y(i) = -1.0/(Gamma*137.0*sqrt((1.0+kappa)/(1.0-kappa))*(1+
35 kappa)*
36 &(1+kappa))*((2*kappa/(3*omega*omega)*x(i)**3)-(2*kappa/(3*
37 &omega*omega)*Eminus**3)-(kappa/omega*x(i)**2)+(kappa/omega*
38 &Eminus**2)+(kappa/(1.0-kappa)-(1+kappa)*511000.0**2/
39 &(omega**2))*x(i)-(kappa/(1.0-kappa)-(1+kappa)*511000.0**2/
40 &(omega**2))*Eminus)
41
42 i = i + 1
43 end do
44
45 call random_number(r)
46 low = 0
47 high = nbins - 1
48 do while (low <= high)
49 mid = (low + high)/2
50 if(r < y(mid)) then
51 if(y(mid-1) <= r .and. y(mid) >= r) then
52 drawnenergy = x(mid-1) + (x(mid)-x(mid-1))/(y(mid)-y(
53 mid-1
54 &))*r-y(mid-1))
55 return
56 end if
57 high = mid - 1

```

```
51     end if
52     if (r >= y(mid)) then
53         if (y(mid) <= r .and. y(mid+1) >= r) then
54             drawnenergy = x(mid) + (x(mid+1)-x(mid))/(y(mid+1)-
55 &y(mid))*(r-y(mid))
56             return
57         end if
58         low = mid + 1
59     end if
60 end do
61 return
62 end
```

LISTING A.5: Subroutine added to CONEX to implement drawing the energy of the first product of the photon decay. Inserted at the end of the original CONEX code.


```

1      IF (ABS(IQ(NP)).EQ.1) THEN
2          aKappa = 6e-20
3          avcmass = 511000.0
4          aThreshold = 0
5          call lvomegathreshold(aKappa,avcmass,aThreshold)
6          aThreshold=aThreshold/1e6
7
8          IF (E(NP).GE.aThreshold) THEN
9 C             print *, "VC_e: ",E(NP),aThreshold,NP
10             aTempEnergy = E(NP)*1e6
11 C         print *, "found photon above threshold!",E(NP)
12             aDrawnEnergy = 0
13             call lvdrawrandomenergy(aKappa,aTempEnergy,avcmass,
14             &             aDrawnEnergy)
15 C         print *, "VC_P:",aDrawnEnergy/1e6
16 C         print *, "Maximum Energy ",aTempEnergy/1e6
17             E(NP)=aDrawnEnergy/1e6
18             IQ(NP+1)=IQ(NP)
19             IQ(NP)=0
20             E(NP+1)=aTempEnergy/1e6-E(NP)
21             U(NP+1)=U(NP)
22             V(NP+1)=V(NP)
23             W(NP+1)=W(NP)
24             X(NP+1)=X(NP)
25             Y(NP+1)=Y(NP)
26             Z(NP+1)=Z(NP)
27             IR(NP+1)=IR(NP)
28             XM(NP+1)=XM(NP)
29             YM(NP+1)=YM(NP)
30             ZM(NP+1)=ZM(NP)
31             DM(NP+1)=DM(NP)
32             TM(NP+1)=TM(NP)
33             WT(NP+1)=WT(NP)
34             DNEAR(NP+1)=DNEAR(NP)
35             LATCH(NP+1)=LATCH(NP)
36             NP=NP+1
37 C         ELSE
38 C         print *, "BT_e:",E(NP),aThreshold,NP
39             END IF
40         END IF

```

LISTING A.6: Implementation of instantaneous VCh radiation of electrons above the given energy threshold added into the EGS4 section of CONEX, inserted after line 398247 of the original code.

```

1 C      VC Particle counter
2      aKappa = 6e-20
3      avcmass = 105658
4      aThreshold = 0
5      call lvomegathreshold(aKappa, avcmass, aThreshold)
6      aThreshold=aThreshold/1e6
7
8      IF(E1.GE. aThreshold) THEN
9 C          print *, "VC_mu: ", E1, aThreshold
10         imode=100
11         goto 9999
12 C      ELSE
13 C          print *, "BT_mu: ", E1, aThreshold
14      END IF

```

LISTING A.7: Code inserted into the propagation subroutine to add VCh radiation for muons, inserted after line 4446 of the original CONEX code.

```

1 C      VC Particle counter
2      aKappa = 6e-20
3      avcmass = 134976.0
4      aThreshold = 0
5      call lvomegathreshold(aKappa, avcmass, aThreshold)
6      aThreshold=aThreshold/1e6
7
8      IF(E1.GE. aThreshold) THEN
9 C          print *, "VC_pi0: ", E1, aThreshold
10         imode=100
11         goto 9999
12 C      ELSE
13 C          print *, "BT_pi0: ", E1, aThreshold
14      END IF

```

LISTING A.8: Code inserted into the propagation subroutine to add VCh radiation for neutral pions, inserted after line 4481 of the original CONEX code.

```

1 C      VC Particle counter
2      aKappa = 6e-20
3      avcmass = 139570.0
4      aThreshold = 0
5      call lvomegathreshold(aKappa, avcmass, aThreshold)
6      aThreshold=aThreshold/1e6
7
8      IF(E1.GE. aThreshold) THEN
9 C          print *, "VC_pic: ", E1, aThreshold
10         imode=100
11         goto 9999
12 C      ELSE
13 C          print *, "BT_pic: ", E1, aThreshold
14      END IF

```

LISTING A.9: Code inserted into the propagation subroutine to add VCh radiation for charged pions, inserted after line 4499 of the original CONEX code.

```
1      elseif(imode.eq.100)then
2 C      print *, 'Special VC interaction'
3      call VCPionInteraction
```

LISTING A.10: Additional imode case for added VCh interaction for particles other than electrons. Inserted after line 3384 of the original CONEX code.

```
1  subroutine lvomegathreshold(kappa, vcmass, threshold)
2  implicit none
3  double precision kappa, vcmass, threshold
4
5  threshold = vcmass*sqrt((1+kappa)/(2*kappa))
6  return
7  end
```

LISTING A.11: Implementation of the energy threshold for VCh radiation given in Eq. (4.18) in an additional subroutine in CONEX. Inserted at the end of the original CONEX code.

```

1  subroutine lvdrawrandomenergy(kappa, omega, vcmass,
drawnenergy)
2  implicit none
3  double precision kappa, omega, vcmass, drawnenergy
4  double precision Eminus, Eplus, Gamma, r, drangen
5  integer nbins, i, j, low, high, mid, k
6  double precision x(100000), y(100000)
7
8  Eminus = 0
9
10 Eplus = (omega-vcmass**2/(2.0*omega*kappa))*(1.0-kappa)
11
12 Gamma = 0
13
14 nbins = 100000
15 i = 2
16 x(1) = Eminus
17 y(1) = 0.0
18
19 do while( i < nbins )
20 x(i) = Eminus + (Eplus-Eminus)/(nbins)*i
21
22 y(i) = (2.0*kappa*omega/(1.0-kappa*kappa)*
23 &(omega*x(i)-x(i)*x(i)/2.0)
24 &-vcmass**2/(1.0-kappa)*x(i)
25 &+kappa/((1.0-kappa*kappa)*(1.0-kappa))*x(i)*x(i)*x(i)/3)/
26 &(2.0*kappa*omega/(1.0-kappa*kappa)*
27 &(omega*Eplus-Eplus*Eplus/2.0)
28 &-vcmass**2/(1.0-kappa)*Eplus
29 &+kappa/((1.0-kappa*kappa)*(1.0-kappa))*Eplus*Eplus*Eplus/3)
30
31 i = i + 1
32 end do
33
34 call random_number(r)
35 C r = drangen(omega)
36 low = 0
37 high = nbins - 1
38 do while (low <= high)
39 mid = (low + high)/2
40 if(r < y(mid)) then
41 if(y(mid-1) <= r .and. y(mid) >= r) then
42 drawnenergy = x(mid-1) + (x(mid)-x(mid-1))/(y(mid)-y(
mid-1
43 &))*r-y(mid-1))
44 return
45 end if
46 high = mid - 1
47 end if
48 if(r >= y(mid)) then
49 if(y(mid) <= r .and. y(mid+1) >= r) then
50 drawnenergy = x(mid) + (x(mid+1)-x(mid))/(y(mid+1)-
&y(mid))*r-y(mid))
51 return
52 end if
53 low = mid + 1
54 end if
55

```

```
56     end do  
57     return  
58     end
```

LISTING A.12: Subroutine added to CONEX to implement drawing the energy of the photon resulting from VCh radiation of an electron. Inserted at the end of the original CONEX code.

```

1 C-----
2      SUBROUTINE VCPionInteraction
3 C-----
4 C   modified QBall interaction for Pi0 VC radiation
5 C-----
6      implicit none
7 #include "conex.h"
8 #include "conex.incnex"
9      double precision epq(5),epp(5), aKappa, vcmass, omega,
drawnenergy
10     integer i,id,iret,nptl0,iptl
11     external drangen
12     double precision drangen,dummy,efrac
13
14 c   Initialize temporary stack
15     do i=1,2
16         epp(i)=0.d0
17         istptlxs(i)=1
18         xsptl(1,i)=dptl(1)      !px
19         xsptl(2,i)=dptl(2)      !py
20         xsptl(3,i)=dptl(3)      !pz
21         xsptl(4,i)=dptl(4)      !E
22         xsptl(5,i)=dptl(5)      !m
23         ityptlxs(i)=0
24         iorptlxs(i)=1
25         jorptlxs(i)=1
26         ifrptlxs(1,i)=0
27         ifrptlxs(2,i)=0
28         xsorptl(1,i)=0.d0      !x
29         xsorptl(2,i)=0.d0      !y
30         xsorptl(3,i)=0.d0      !z
31         xsorptl(4,i)=0.d0      !t
32         xstivptl(1,i)=0.d0
33         xstivptl(2,i)=0.d0
34         idptlxs(i)=0          !id
35     enddo
36
37     nptlxs=0                  !number of secondaries
38
39
40     aKappa = 6e-20
41     vcmass = dptl(5)          !134976.0
42     omega = dptl(4)
43     drawnenergy = 0
44
45 C     print *, 'original particle px:',xsptl(1,1), 'py:',xsptl(2,1),
46 C     &      'pz:',xsptl(3,i), 'E:',xsptl(4,1), 'm:',xsptl(5,1)
47 C     call lvdrawrandomenergy(aKappa, omega, vcmass, drawnenergy)
48 C     print *, 'drawn energy',drawnenergy
49
50     epp(4)=drawnenergy
51     epp(1)=dptl(1)*epp(4)/dptl(4)
52     epp(2)=dptl(2)*epp(4)/dptl(4)
53     epp(3)=dptl(3)*epp(4)/dptl(4)
54     epp(5)=0.d0
55     id=nint(dptl(10))
56     nptlxs=nptlxs+1

```

```

57     do i=1,4
58         xsptl(i,nptlxs)=xsptl(i,nptlxs)-epp(i)
59     enddo
60     idptlxs(nptlxs)=id
61     istptlxs(nptlxs)=0
62
63     id=10
64     nptlxs=nptlxs+1
65     do i=1,5
66         xsptl(i,nptlxs)=epp(i)
67     enddo
68     idptlxs(nptlxs)=id
69     istptlxs(nptlxs)=0
70 C     do i=1,2
71 C         print *, 'particle ',i,'px:',xsptl(1,i),'py:',xsptl(2,i),
72 C         &      'pz:',xsptl(3,i),'E:',xsptl(4,i),'m:',xsptl(5,i)
73 C     enddo
74 #ifdef __CXDEBUG__
75     if(isx.ge.4) write(ifck,*) 'decay ',id,' --> ',nptlxs-nptl0,'
       ptls'
76     if(isx.ge.6) call cxalist('QBallInt&',1,nptlxs,2)
77 #endif
78
79     END

```

LISTING A.13: Subroutine added to CONEX to implement VCh radiation of particles other than electrons and positrons occurring in the shower above their respective threshold energies, i.e., pions and muons. Inserted at the end of the original CONEX code.

Appendix B

Additional Figures

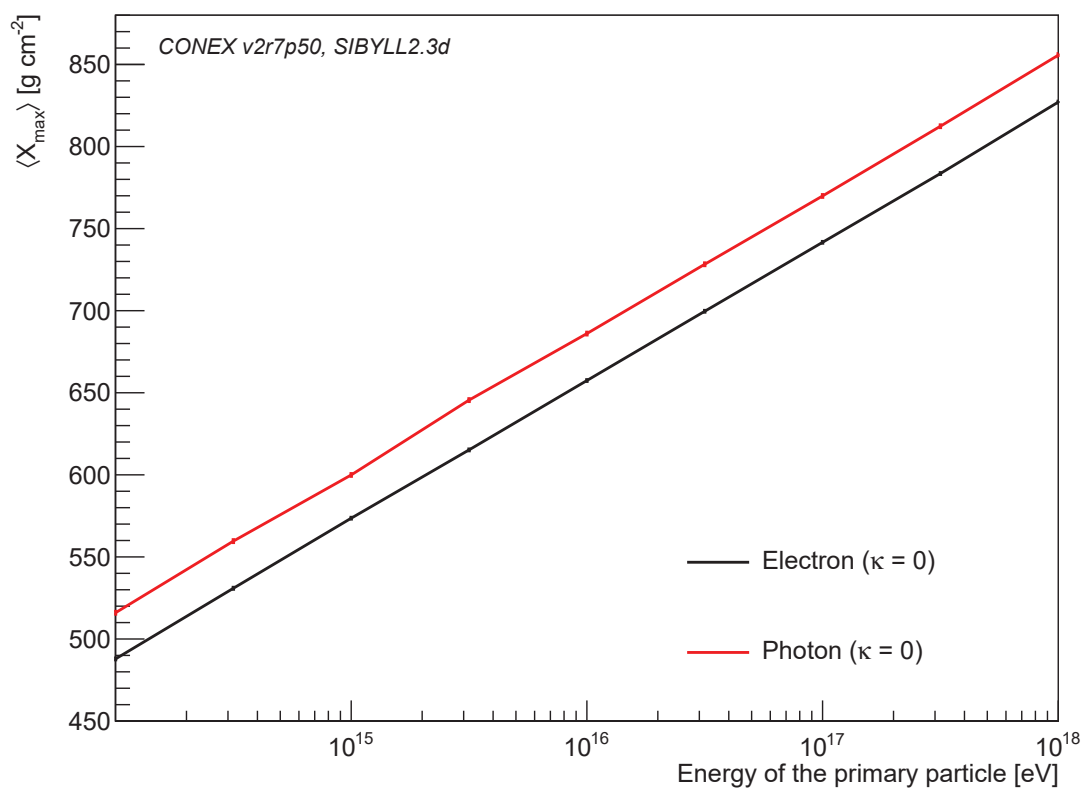


FIGURE B.1: The simulated values of $\langle X_{\max} \rangle$ as a function of the primary energy for primary photons and electrons in the absence of LV.

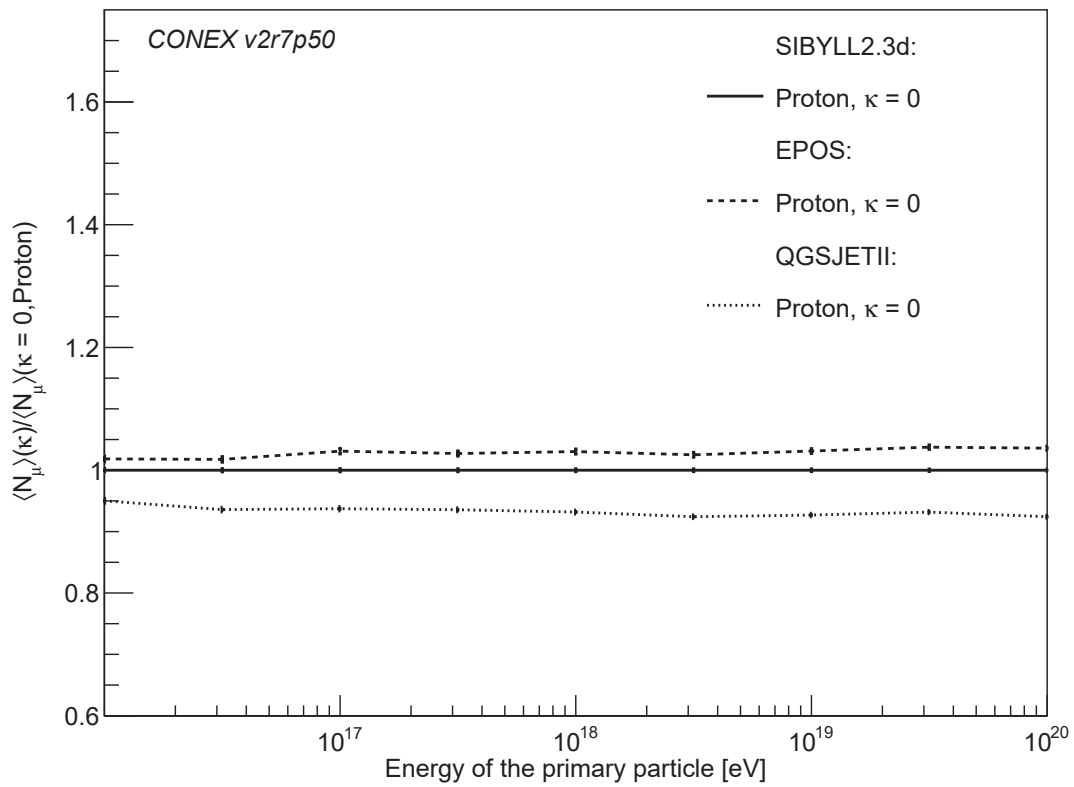


FIGURE B.2: The simulated values of $\langle N_\mu \rangle$ as a function of the primary energy for different interaction models in the absence of LV ($\kappa = 0$). All values are normalized to the value of $\langle N_\mu \rangle$ for unmodified protons of the hadronic interaction model SIBYLL2.3d at the corresponding energy, to show the relative effect of LV on the muon number.

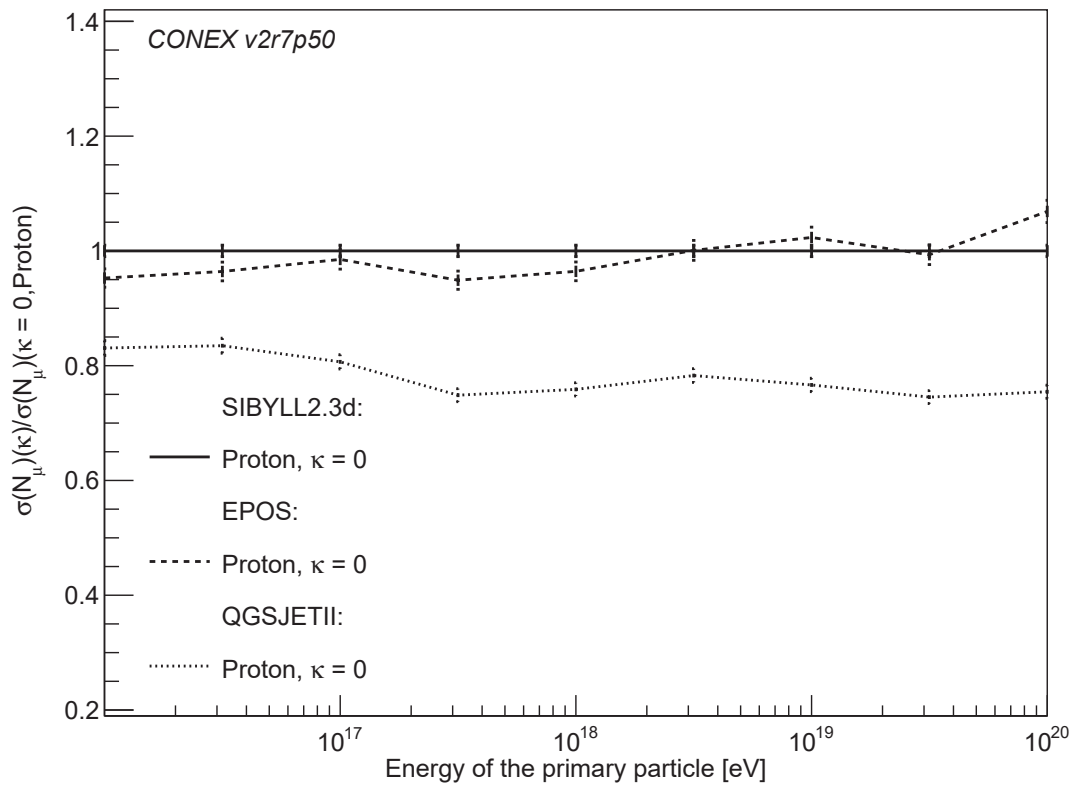


FIGURE B.3: The simulated values of $\sigma(N_\mu)$ as a function of the primary energy for different interaction models in the absence of LV ($\kappa = 0$). All values are normalized to the value of $\sigma(N_\mu)$ for unmodified protons of the hadronic interaction model SIBYLL2.3d at the corresponding energy, to show the relative effect of LV on the muon number.

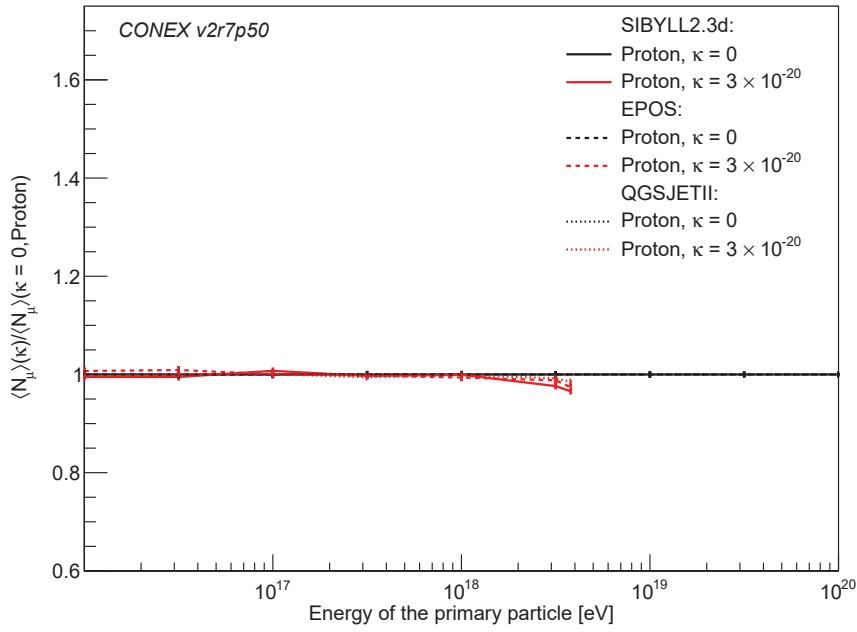


FIGURE B.4: The simulated values of $\langle N_\mu \rangle$ as a function of the primary energy for different interaction models in the absence of LV ($\kappa = 0$) and for $\kappa > 0$. All values are normalized to the value of $\langle N_\mu \rangle$ for unmodified protons of the model at the corresponding energy, to show the relative effect of LV on the muon number.

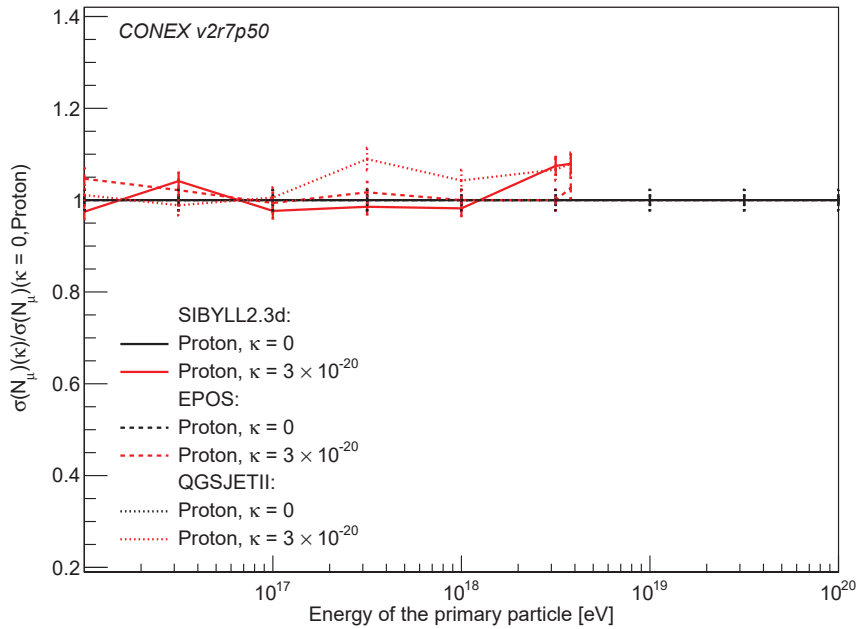


FIGURE B.5: The simulated values of $\sigma(N_\mu)$ as a function of the primary energy for different interaction models in the absence of LV ($\kappa = 0$) and for $\kappa > 0$. All values are normalized to the value of $\langle N_\mu \rangle$ for unmodified protons of the model at the corresponding energy, to show the relative effect of LV on the muon number.

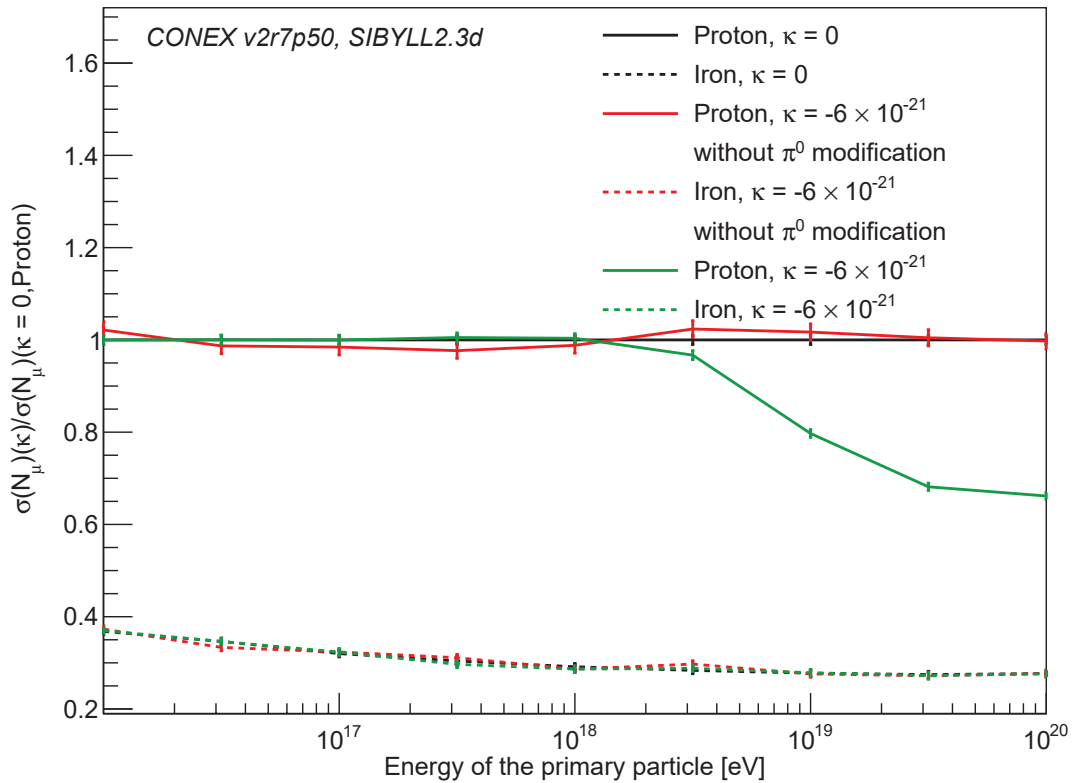


FIGURE B.6: The simulated values of $\sigma(N_\mu)$ as a function of the primary energy for different primary particles in the absence of LV ($\kappa = 0$) and for $\kappa = -6 \times 10^{-21}$. All values are normalized to the value of $\sigma(N_\mu)$ for unmodified protons at the corresponding energy, to show the relative effect of LV on the muon number. Depicted is also the result of a partial modification of the CONEX code, incorporating only photon decay and no modification of the pion decay time.

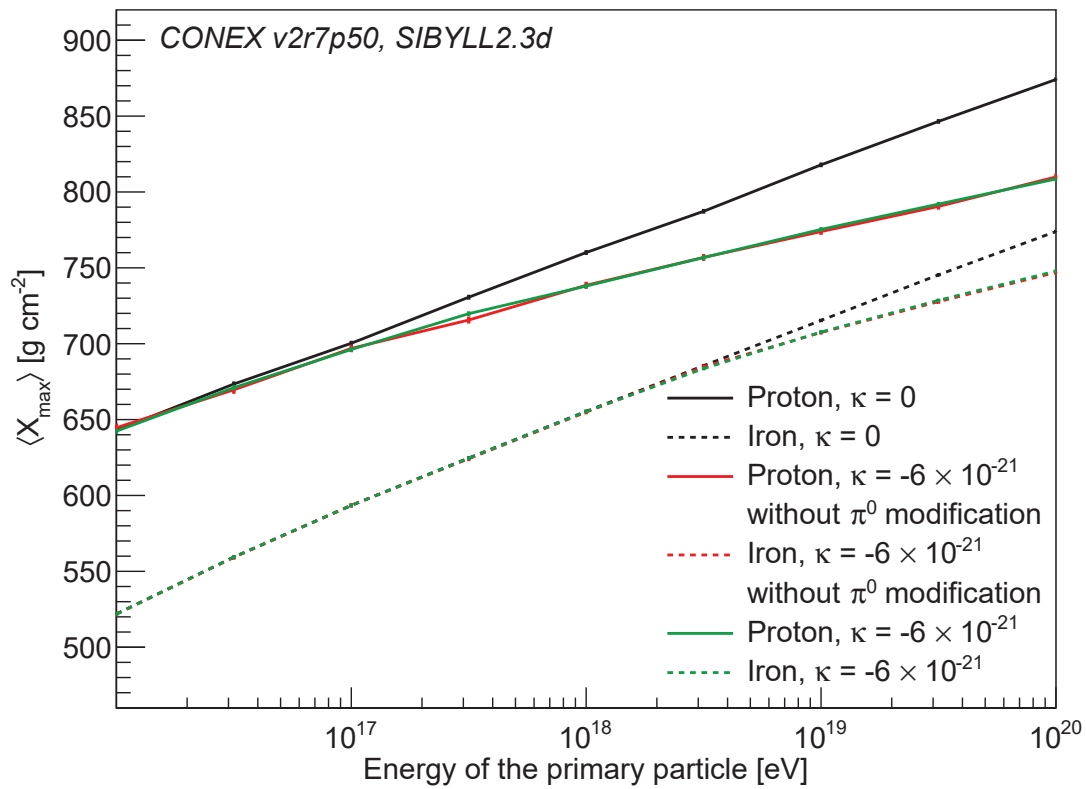


FIGURE B.7: The simulated values of $\langle X_{\max} \rangle$ as a function of the primary energy for primary protons and iron nuclei for the absence of LV ($\kappa = 0$) and for $\kappa = -6 \times 10^{-21}$. Depicted is also the result of a partial modification of the CONEX code, incorporating only photon decay and no modification of the pion decay time.

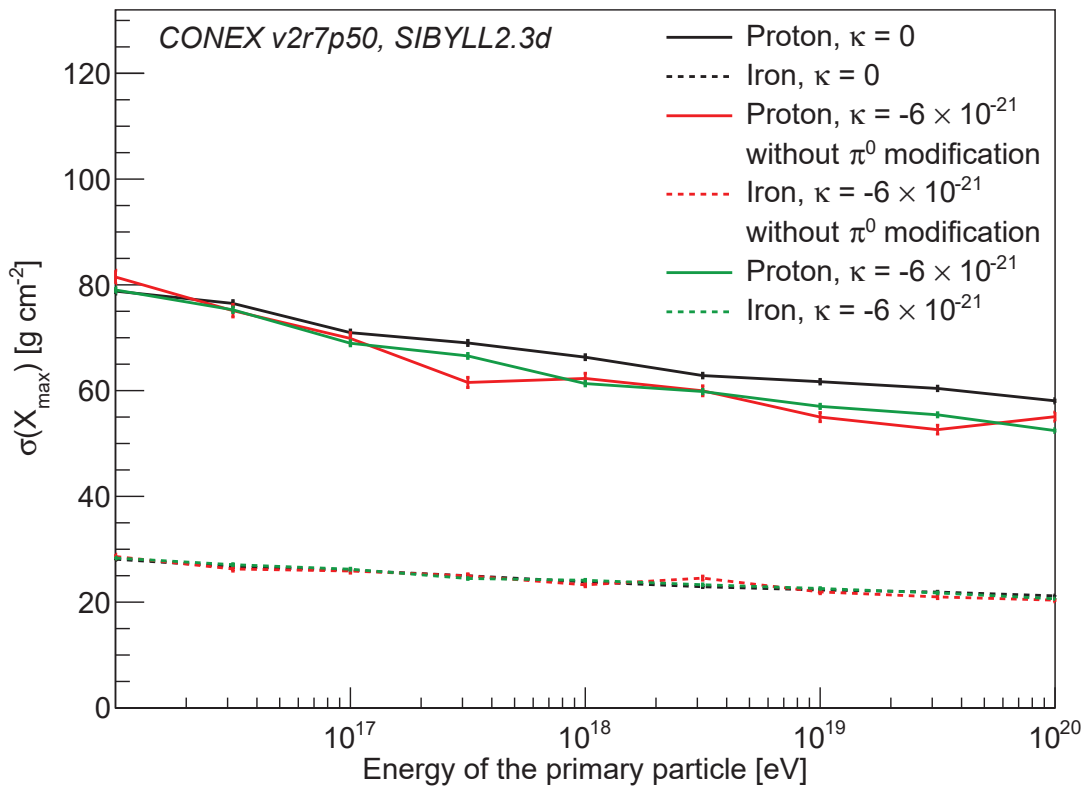


FIGURE B.8: The simulated values of $\sigma(X_{\max})$ as a function of the primary energy for primary protons and iron nuclei for the absence of LV ($\kappa = 0$) and for $\kappa = -6 \times 10^{-21}$. Depicted is also the result of a partial modification of the CONEX code, incorporating only photon decay and no modification of the pion decay time.

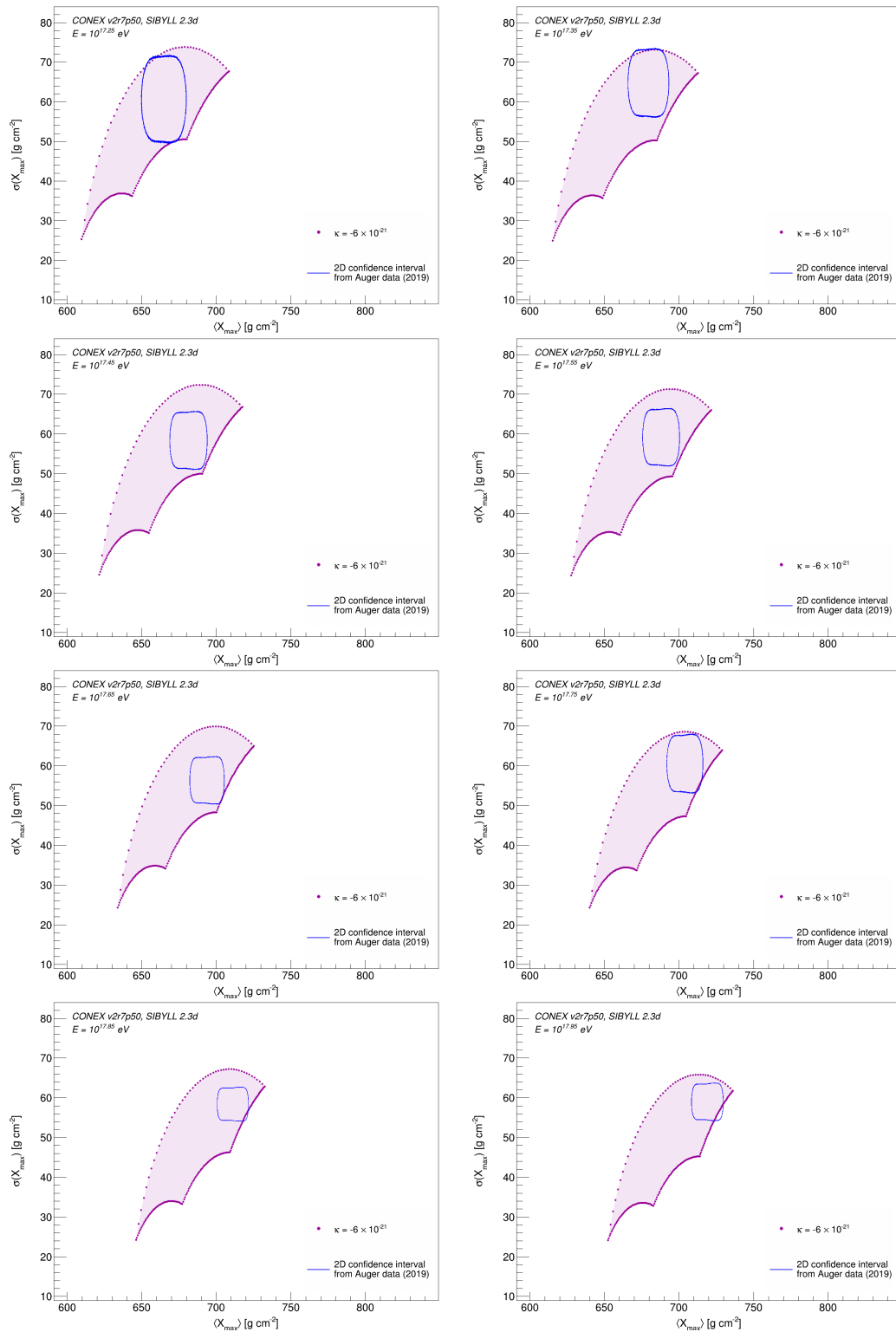


FIGURE B.9: Comparison of the $\langle X_{\max} \rangle$ - $\sigma(X_{\max})$ -combinations derived by simulations which incorporate LV to the 2D confidence intervals given by the measurements of the Pierre Auger Observatory [Yus19] for $\kappa = -6 \times 10^{-21}$ and different primary particle energies between $10^{17.2}$ eV and $10^{18.0}$ eV.

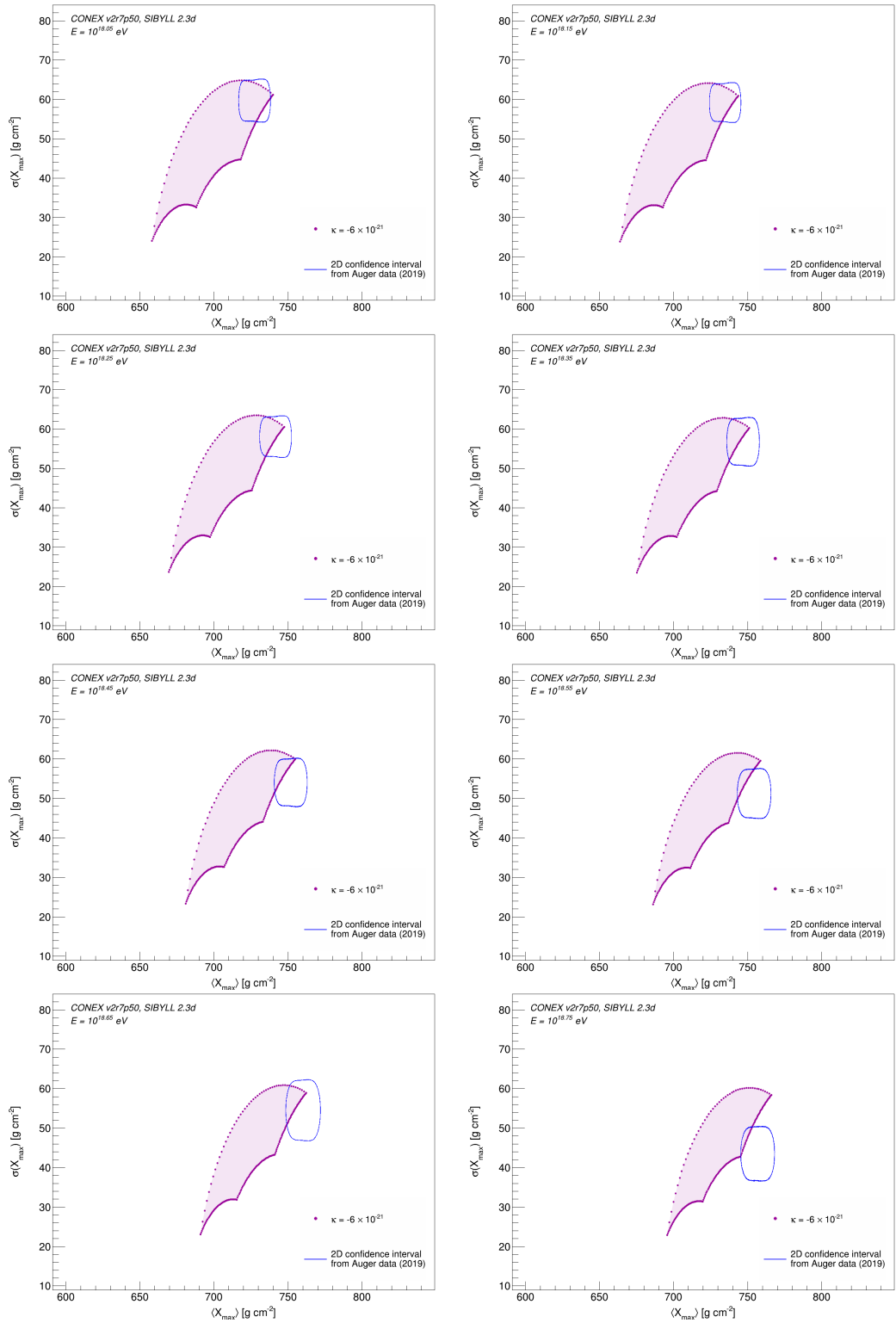


FIGURE B.10: Comparison of the $\langle X_{\max} \rangle$ - $\sigma(X_{\max})$ -combinations derived by simulations which incorporate LV to the 2D confidence intervals given by the measurements of the Pierre Auger Observatory [Yus19] for $\kappa = -6 \times 10^{-21}$ and different primary particle energies between $10^{18.0}$ eV and $10^{18.8}$ eV.

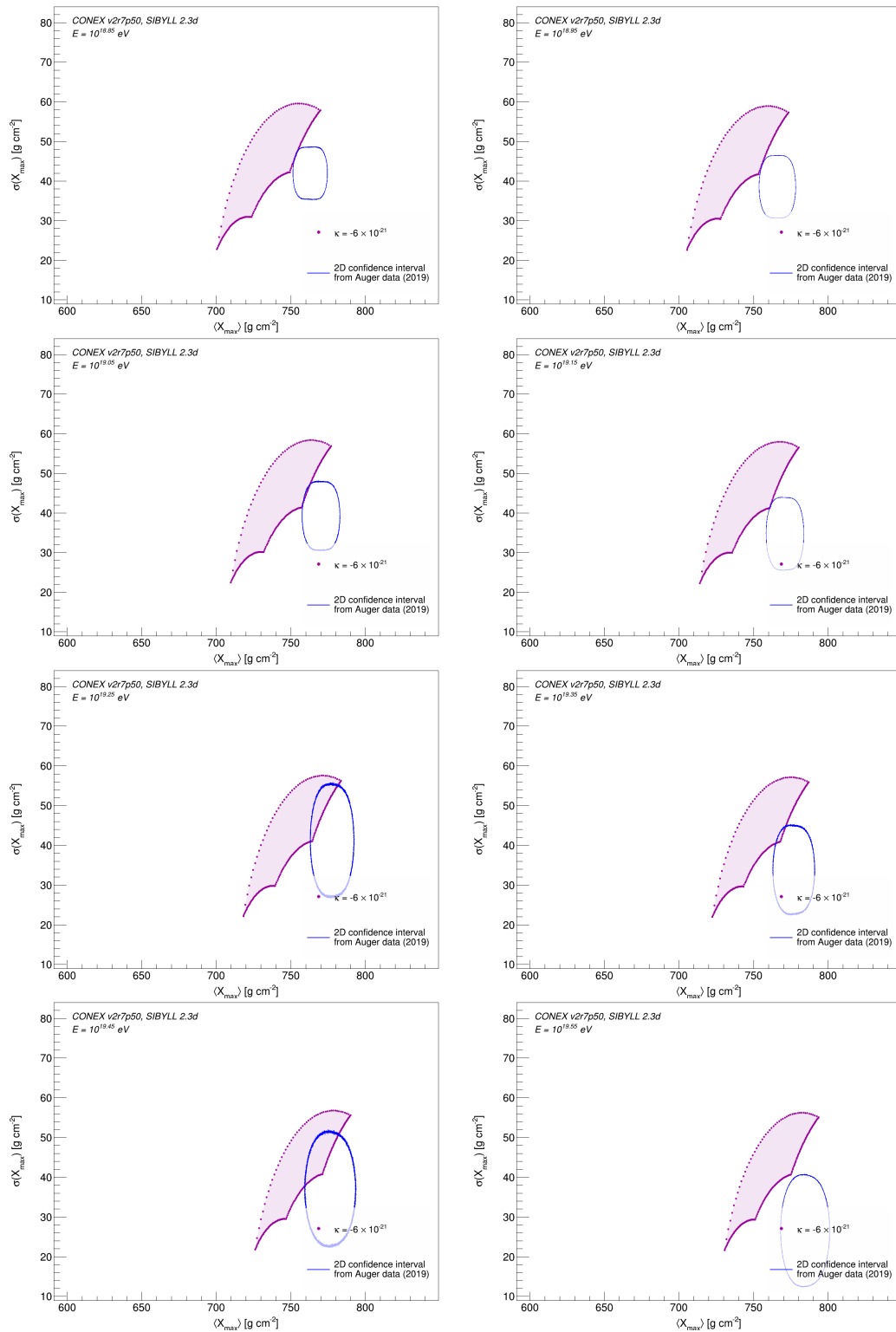


FIGURE B.11: Comparison of the $\langle X_{\max} \rangle$ - $\sigma(X_{\max})$ -combinations derived by simulations which incorporate LV to the 2D confidence intervals given by the measurements of the Pierre Auger Observatory [Yus19] for $\kappa = -6 \times 10^{-21}$ and different primary particle energies between $10^{18.8}$ eV and $10^{19.6}$ eV.

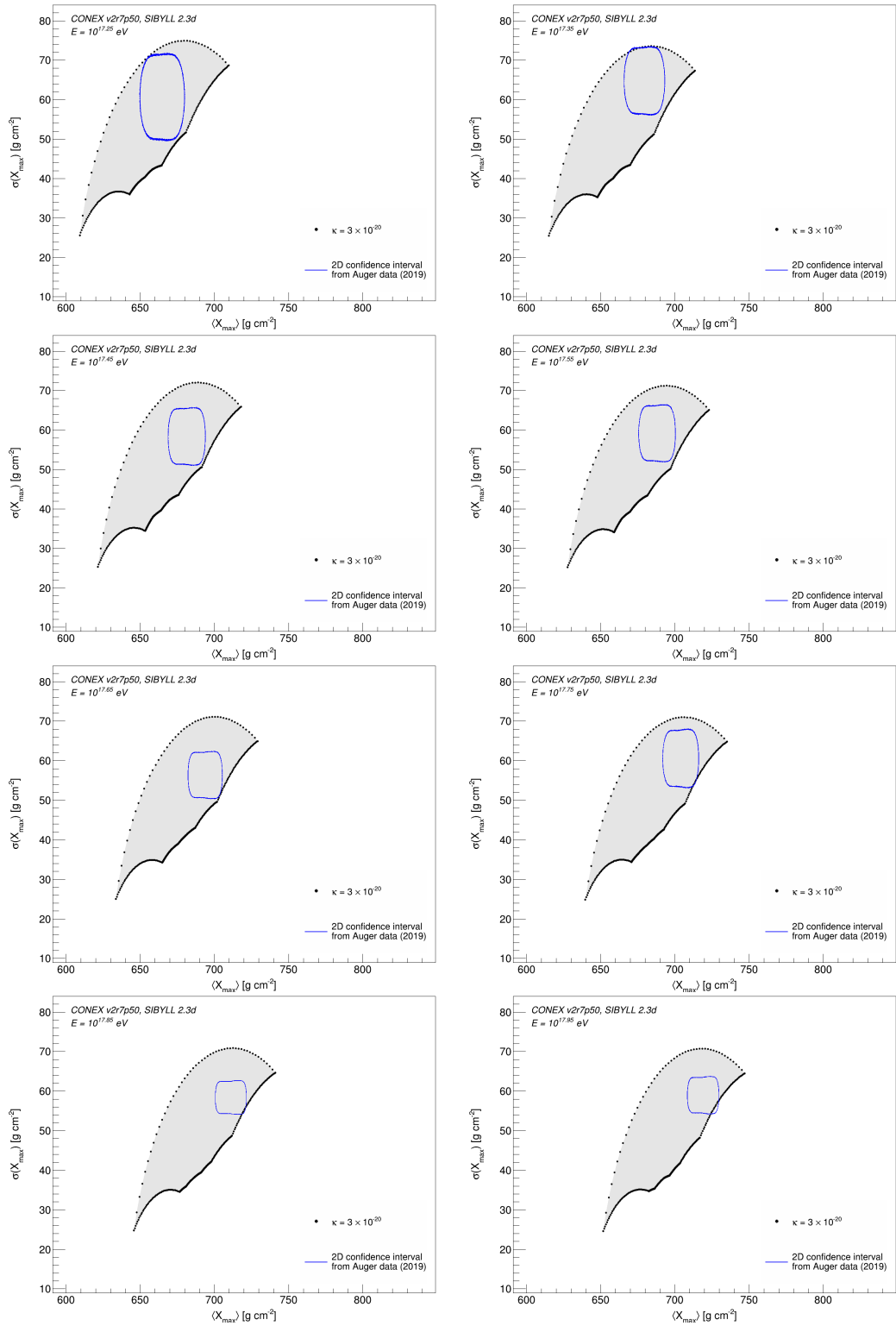


FIGURE B.12: Comparison of the $\langle X_{\max} \rangle$ - $\sigma(X_{\max})$ -combinations derived by simulations which incorporate LV to the 2D confidence intervals given by the measurements of the Pierre Auger Observatory [Yus19] for $\kappa = 3 \times 10^{-20}$ and different primary particle energies between $10^{17.2}$ eV and $10^{18.0}$ eV.

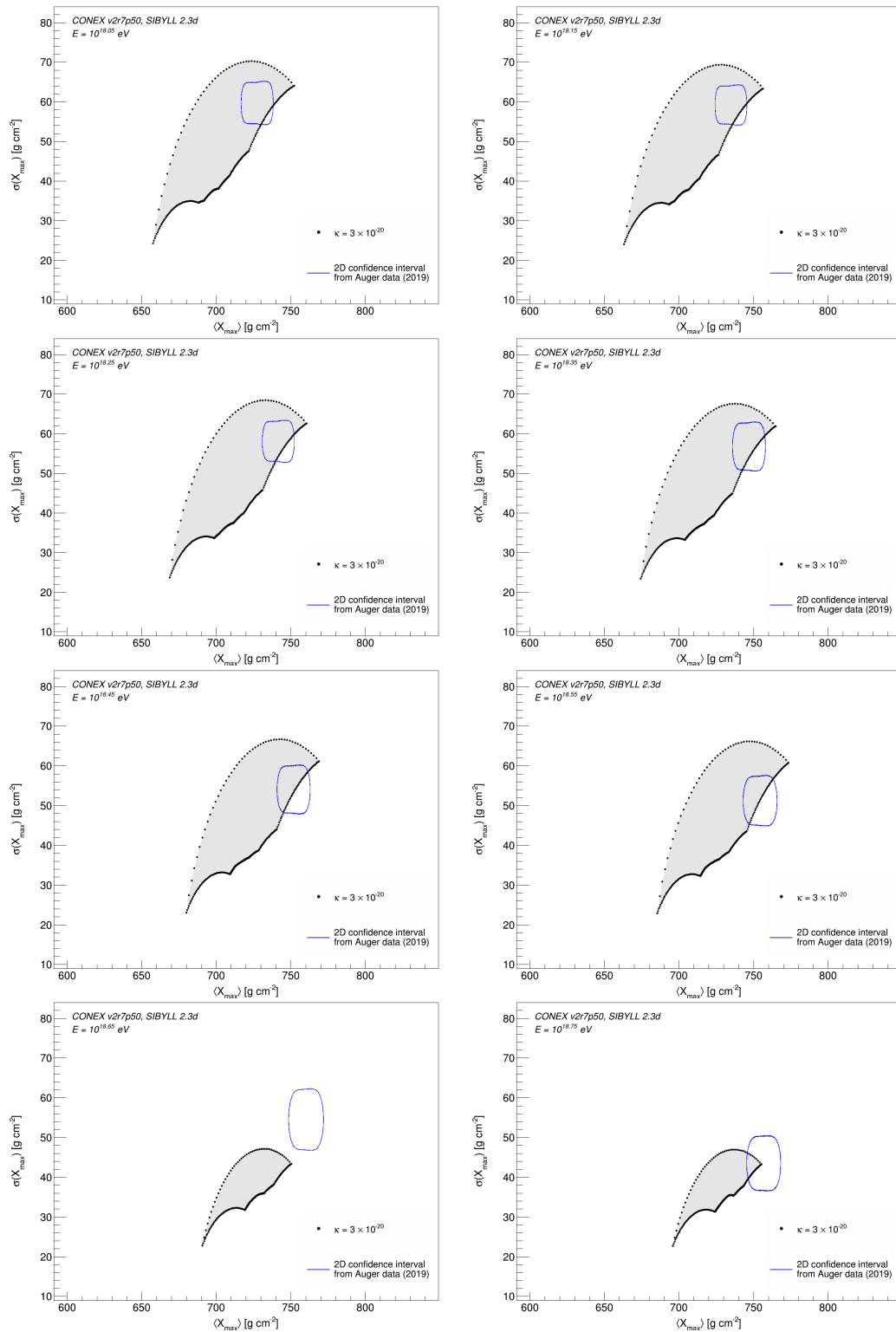


FIGURE B.13: Comparison of the $\langle X_{\max} \rangle$ - $\sigma(X_{\max})$ -combinations derived by simulations which incorporate LV to the 2D confidence intervals given by the measurements of the Pierre Auger Observatory [Yus19] for $\kappa = 3 \times 10^{-20}$ and different primary particle energies between $10^{18.0}$ eV and $10^{18.8}$ eV.

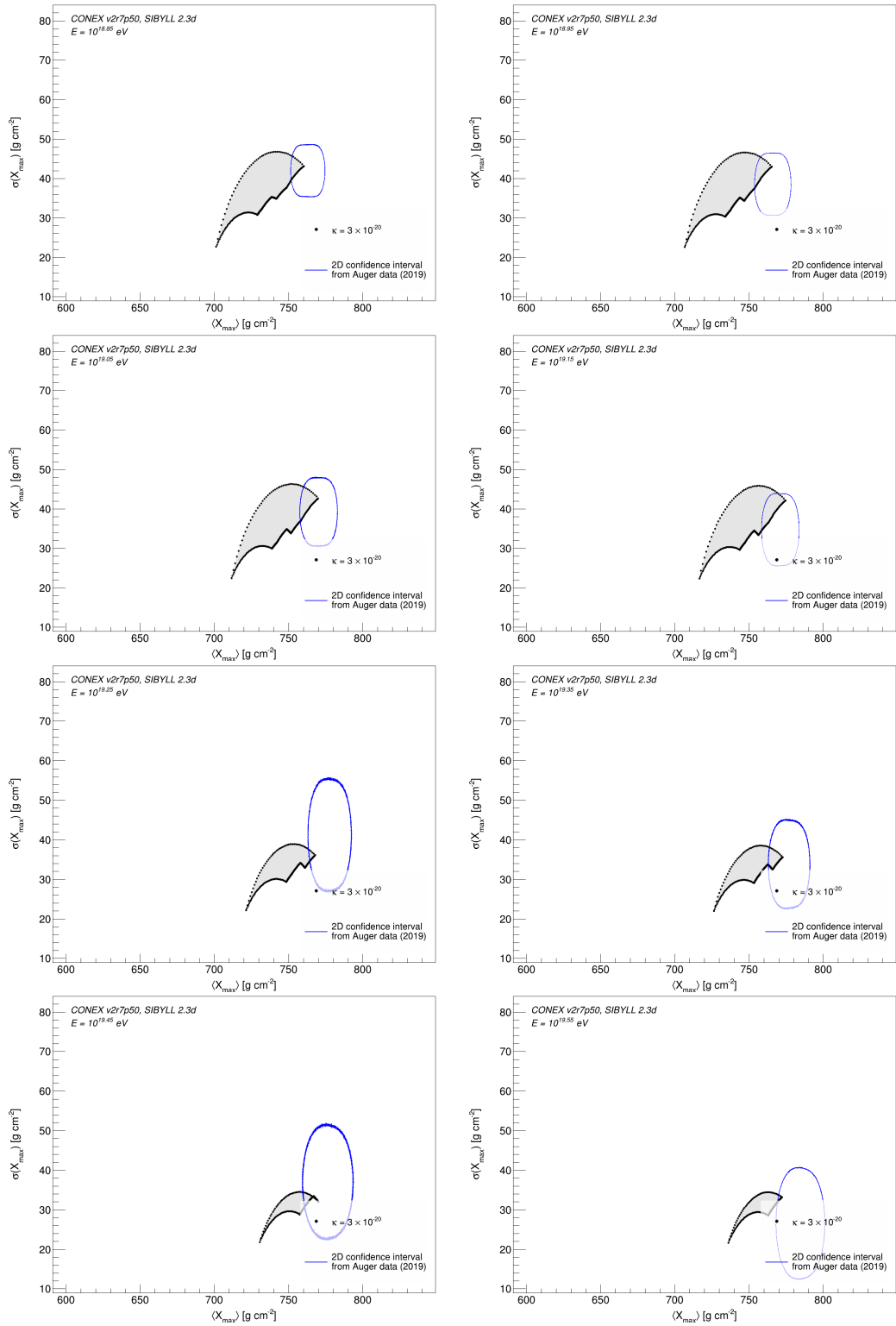


FIGURE B.14: Comparison of the $\langle X_{\max} \rangle$ - $\sigma(X_{\max})$ -combinations derived by simulations which incorporate LV to the 2D confidence intervals given by the measurements of the Pierre Auger Observatory [Yus19] for $\kappa = 3 \times 10^{-20}$ and different primary particle energies between $10^{18.8}$ eV and $10^{19.6}$ eV.

Appendix C

Additional Tables

| Bin # | $\log_{10}(E/\text{eV})$ | $\kappa =$ | | | | |
|-------|--------------------------|----------------------|----------------------|----------------------|----------------------|-----|
| | | -1×10^{-19} | -1×10^{-20} | -6×10^{-21} | -1×10^{-21} | 0 |
| 0 | 17,85 | 42 | X | X | X | X |
| 1 | 17,95 | 32 | 22 | 15 | 11 | X |
| 2 | 18,05 | 35 | 32 | 30 | X | X |
| 3 | 18,15 | 12 | 31 | 29 | 14 | X |
| 4 | 18,25 | 0 | 22 | 19 | 13 | 10 |
| 5 | 18,35 | 5 | 39 | 40 | 42 | 5 |
| 6 | 18,45 | 0 | 28 | 39 | 40 | 17 |
| 7 | 18,55 | 0 | 32 | 45 | 39 | 10 |
| 8 | 18,65 | 15 | 48 | 54 | 50 | X |
| 9 | 18,75 | 0 | 24 | 37 | 44 | 36 |
| 10 | 18,85 | 0 | 0 | 26 | 41 | 37 |
| 11 | 18,95 | 0 | 25 | 44 | 51 | 36 |
| 12 | 19,05 | 0 | 16 | 31 | 44 | 36 |
| 13 | 19,14 | 0 | 19 | 29 | 45 | 36 |
| 14 | 19,25 | 16 | 56 | 69 | 91 | 44 |
| 15 | 19,34 | 14 | 52 | 57 | 65 | 49 |
| 16 | 19,45 | 52 | 83 | 94 | 119 | 106 |
| 17 | 19,62 | 0 | 0 | 0 | 53 | 49 |

TABLE C.1: Number of points in the contour around the $\langle X_{\text{max}} \rangle / \sigma(X_{\text{max}})$ values allowed by all compositions simulated using CONEX with the hadronic interaction model SIBYLL 2.3d inside the Auger confidence region determined from X_{max} moments published in [Aab+14a]. Selected values of κ are shown with decreasing strength of LV from left to right. For each value of κ , the comparison is done separately for each energy bin of the measurements from the Pierre Auger Observatory. Entries where the Auger confidence region is entirely inside the region covered by simulated showers are marked with an X. The two highest energy bins are excluded from the analysis due to low statistics, but listed here for completeness.

Bibliography

- [Aab+14a] A. Aab et al. “Depth of maximum of air-shower profiles at the Pierre Auger Observatory. I. Measurements at energies above $10^{17.8}$ eV”. In: *Physical Review D* 90.12 (Dec. 2014).
- [Aab+14b] A. Aab et al. “Depth of maximum of air-shower profiles at the Pierre Auger Observatory. II. Composition implications”. In: *Physical Review D* 90.12 (Dec. 2014).
- [Aab+15a] A. Aab et al. “Muons in air showers at the Pierre Auger Observatory: Mean number in highly inclined events”. In: *Phys. Rev. D* 91 (3 Feb. 2015), p. 032003.
- [Aab+15b] A. Aab et al. “The Pierre Auger cosmic ray observatory”. In: *Nuclear Instruments and Methods in Physics Research Section A: Accelerators, Spectrometers, Detectors and Associated Equipment* 798 (Oct. 2015), pp. 172–213.
- [Aab+16a] A. Aab et al. *The Pierre Auger Observatory Upgrade - Preliminary Design Report*. 2016. arXiv: 1604.03637 [astro-ph.IM].
- [Aab+16b] A. Aab et al. “Evidence for a mixed mass composition at the ‘ankle’ in the cosmic-ray spectrum”. In: *Phys. Lett. B* 762 (2016), pp. 288–295.
- [Aab+17a] A. Aab et al. “Observation of a large-scale anisotropy in the arrival directions of cosmic rays above 8×10^{18} eV”. In: *Science* 357.6357 (Sept. 2017), pp. 1266–1270.
- [Aab+17b] A. Aab et al. “Spectral calibration of the fluorescence telescopes of the Pierre Auger Observatory”. In: *Astroparticle Physics* 95 (Oct. 2017), pp. 44–56.
- [Aab+17c] A. Aab et al. “Combined fit of spectrum and composition data as measured by the Pierre Auger Observatory”. In: *Journal of Cosmology and Astroparticle Physics* 2017.04 (Apr. 2017), pp. 038–038.
- [Aab+18a] A. Aab et al. “Large-scale Cosmic-Ray Anisotropies above 4 EeV Measured by the Pierre Auger Observatory”. In: *The Astrophysical Journal* 868.1 (Nov. 2018), p. 4.
- [Aab+18b] A. Aab et al. “Observation of inclined EeV air showers with the radio detector of the Pierre Auger Observatory”. In: *Journal of Cosmology and Astroparticle Physics* 2018.10 (Oct. 2018), pp. 026–026.
- [Aab+20a] A. Aab et al. “Measurement of the cosmic-ray energy spectrum above 2.5×10^{18} eV using the Pierre Auger Observatory”. In: *Physical Review D* 102.6 (Sept. 2020).

- [Aab+20b] A. Aab et al. "Reconstruction of events recorded with the surface detector of the Pierre Auger Observatory". In: *Journal of Instrumentation* 15.10 (Oct. 2020), P10021.
- [Aab+20c] A. Aab et al. "Features of the Energy Spectrum of Cosmic Rays above 2.5×10^{18} eV Using the Pierre Auger Observatory". In: *Phys. Rev. Lett.* 125 (12 Sept. 2020), p. 121106.
- [Abb+13] R. Abbasi et al. "IceTop: The surface component of IceCube". In: *Nuclear Instruments and Methods in Physics Research Section A: Accelerators, Spectrometers, Detectors and Associated Equipment* 700 (Feb. 2013), pp. 188–220.
- [Abb+18] R. U. Abbasi et al. "Depth of Ultra High Energy Cosmic Ray Induced Air Shower Maxima Measured by the Telescope Array Black Rock and Long Ridge FADC Fluorescence Detectors and Surface Array in Hybrid Mode". In: *The Astrophysical Journal* 858.2 (May 2018), p. 76.
- [Abb+22] R. Abbasi et al. "Searches for Neutrinos from Gamma-Ray Bursts Using the IceCube Neutrino Observatory". In: *The Astrophysical Journal* 939.2 (Nov. 2022), p. 116.
- [Abd+23] A. Abdul Halim et al. "A Catalog of the Highest-energy Cosmic Rays Recorded during Phase I of Operation of the Pierre Auger Observatory". In: *The Astrophysical Journal Supplement Series* 264.2 (Feb. 2023), p. 50.
- [Abr+08] J. Abraham et al. "Correlation of the highest-energy cosmic rays with the positions of nearby active galactic nuclei". In: *Astroparticle Physics* 29.3 (Apr. 2008), pp. 188–204.
- [Abr+09] J. Abraham et al. "Atmospheric effects on extensive air showers observed with the surface detector of the Pierre Auger observatory". In: *Astroparticle Physics* 32.2 (2009), pp. 89–99.
- [Abr+10a] J. Abraham et al. "The fluorescence detector of the Pierre Auger Observatory". In: *Nuclear Instruments and Methods in Physics Research Section A: Accelerators, Spectrometers, Detectors and Associated Equipment* 620.2–3 (Aug. 2010), pp. 227–251.
- [Abr+10b] J. Abraham et al. "Trigger and aperture of the surface detector array of the Pierre Auger Observatory". In: *Nuclear Instruments and Methods in Physics Research Section A: Accelerators, Spectrometers, Detectors and Associated Equipment* 613.1 (Jan. 2010), pp. 29–39.
- [Abr+22] P. Abreu et al. "A Search for Photons with Energies Above 2×10^{17} eV Using Hybrid Data from the Low-Energy Extensions of the Pierre Auger Observatory". In: *The Astrophysical Journal* 933.2 (July 2022), p. 125.
- [Abu+00] T. Abu-Zayyad et al. "The prototype high-resolution Fly's Eye cosmic ray detector". In: *Nuclear Instruments and Methods in Physics Research Section A: Accelerators, Spectrometers, Detectors and Associated Equipment* 450.2 (2000), pp. 253–269.
- [Abu+12] T. Abu-Zayyad et al. "The surface detector array of the Telescope Array experiment". In: *Nuclear Instruments and Methods in*

- Physics Research Section A: Accelerators, Spectrometers, Detectors and Associated Equipment* 689 (Oct. 2012), pp. 87–97.
- [Ach+06] A. Achterberg et al. “First year performance of the IceCube neutrino telescope”. In: *Astroparticle Physics* 26.3 (2006), pp. 155–173.
- [Act+11] M. Actis et al. “Design concepts for the Cherenkov Telescope Array CTA: An advanced facility for ground-based high-energy gamma-ray astronomy”. In: *Exper. Astron.* 32 (2011), pp. 193–316.
- [Add+22] A. Addazi et al. “Quantum gravity phenomenology at the dawn of the multi-messenger era—A review”. In: *Prog. Part. Nucl. Phys.* 125 (2022), p. 103948.
- [Ade+16] P. A. R. Ade et al. “Planck2015 results: XIII. Cosmological parameters”. In: *Astronomy & Astrophysics* 594 (Sept. 2016), A13.
- [Agu+15a] M. Aguilar et al. “Precision Measurement of the Helium Flux in Primary Cosmic Rays of Rigidities 1.9 GV to 3 TV with the Alpha Magnetic Spectrometer on the International Space Station”. In: *Phys. Rev. Lett.* 115 (21 Nov. 2015), p. 211101.
- [Agu+15b] M. Aguilar et al. “Precision Measurement of the Proton Flux in Primary Cosmic Rays from Rigidity 1 GV to 1.8 TV with the Alpha Magnetic Spectrometer on the International Space Station”. In: *Phys. Rev. Lett.* 114 (17 Apr. 2015), p. 171103.
- [Aha+06] F. Aharonian et al. “A detailed spectral and morphological study of the gamma-ray supernova remnant RX J1713.7-3946 with HESS”. In: *Astronomy & Astrophysics* 449.1 (Mar. 2006), pp. 223–242.
- [Ahn+07] H. Ahn et al. “The Cosmic Ray Energetics And Mass (CREAM) instrument”. In: *Nuclear Instruments and Methods in Physics Research Section A: Accelerators, Spectrometers, Detectors and Associated Equipment* 579.3 (2007), pp. 1034–1053.
- [Ahn+09] H. S. Ahn et al. “Energy spectra of cosmic-ray nuclei at high energies”. In: *The Astrophysical Journal* 707.1 (Nov. 2009), pp. 593–603.
- [All+08] I. Allekotte et al. “The surface detector system of the Pierre Auger Observatory”. In: *Nuclear Instruments and Methods in Physics Research Section A: Accelerators, Spectrometers, Detectors and Associated Equipment* 586.3 (Mar. 2008), pp. 409–420.
- [Ame+19] M. Amenomori et al. “First Detection of Photons with Energy beyond 100 TeV from an Astrophysical Source”. In: *Physical Review Letters* 123.5 (July 2019).
- [Ame+97] G. Amelino-Camelia et al. “Distance Measurement and Wave Dispersion in a Liouville-String Approach to Quantum Gravity”. In: *International Journal of Modern Physics A* 12.03 (Jan. 1997), pp. 607–623.
- [AMU02] J. Alfaro, H. A. Morales-Técotl, and L. F. Urrutia. “Loop quantum gravity and light propagation”. In: *Physical Review D* 65.10 (Apr. 2002).

- [Ant+03] T. Antoni et al. "The cosmic-ray experiment KASCADE". In: *Nuclear Instruments and Methods in Physics Research Section A: Accelerators, Spectrometers, Detectors and Associated Equipment* 513.3 (2003), pp. 490–510.
- [Ape+09] W. Apel et al. "Energy spectra of elemental groups of cosmic rays: Update on the KASCADE unfolding analysis". In: *Astroparticle Physics* 31.2 (Mar. 2009), pp. 86–91.
- [Ape+10] W. Apel et al. "The KASCADE-Grande experiment". In: *Nuclear Instruments and Methods in Physics Research Section A: Accelerators, Spectrometers, Detectors and Associated Equipment* 620.2 (2010), pp. 202–216.
- [Ape+13] W. Apel et al. "KASCADE-Grande measurements of energy spectra for elemental groups of cosmic rays". In: *Astroparticle Physics* 47 (July 2013), pp. 54–66.
- [Aug+39] P. Auger et al. "Extensive Cosmic-Ray Showers". In: *Rev. Mod. Phys.* 11 (3-4 July 1939), pp. 288–291.
- [Ave+13] M. Ave et al. "Precise measurement of the absolute fluorescence yield of the 337 nm band in atmospheric gases". In: *Astroparticle Physics* 42 (2013), pp. 90–102.
- [Avr+22] A. V. Avrorin et al. "Deep-Underwater Cherenkov Detector in Lake Baikal". In: *J. Exp. Theor. Phys.* 134.4 (2022), pp. 399–416.
- [Bac+21] S. Bacholle et al. "Mini-EUSO Mission to Study Earth UV Emissions on board the ISS". In: *The Astrophysical Journal Supplement Series* 253.2 (Mar. 2021), p. 36.
- [Bat98] R. Battiston. "The Alpha Magnetic Spectrometer (AMS): search for antimatter and dark matter on the International Space Station". In: *Nuclear Physics B - Proceedings Supplements* 65.1-3 (June 1998), pp. 19–26.
- [Bea+00] D. Bear et al. "Limit on Lorentz and CPT Violation of the Neutron Using a Two-Species Noble-Gas Maser". In: *Phys. Rev. Lett.* 85 (24 Dec. 2000), pp. 5038–5041.
- [Bea+02] D. Bear et al. "Erratum: Limit on Lorentz and CPT Violation of the Neutron Using a Two-Species Noble-Gas Maser [Phys. Rev. Lett. 85, 5038 (2000)]". In: *Phys. Rev. Lett.* 89 (20 Oct. 2002), p. 209902.
- [Bea+19] J. Beacham et al. "Physics beyond colliders at CERN: beyond the Standard Model working group report". In: *Journal of Physics G: Nuclear and Particle Physics* 47.1 (Dec. 2019), p. 010501.
- [Bec96] H. Becquerel. "Sur les radiations émises par phosphorescence". In: *Comptes rendus de l'Académie des Sciences, Paris* 122 (1896), pp. 420–421.
- [Bel78] A. R. Bell. "The acceleration of cosmic rays in shock fronts – I". In: *Monthly Notices of the Royal Astronomical Society* 182.2 (Feb. 1978), pp. 147–156.
- [Ber+07] T. Bergmann et al. "One-dimensional hybrid approach to extensive air shower simulation". In: *Astropart. Phys.* 26 (2007), pp. 420–432.

- [Ber+14] M. Bertaina et al. “Performance and air-shower reconstruction techniques for the JEM-EUSO mission”. In: *Advances in Space Research* 53.10 (2014). Cosmic Ray Origins: Viktor Hess Centennial Anniversary, pp. 1515–1535.
- [Ber10] K. Bergwitz. “Die Gammastrahlung des Erdkörpers und ihr Anteil an der spontanen Ionisierung der Atmosphäre”. In: *Jahresbericht des Braunschweiger Vereins für Naturwissenschaft* 10 (1910), pp. 196–239.
- [Ber23] C. Berat for the Pierre Auger Collaboration. “AugerPrime status and prospects”. In: *EPJ Web Conf.* 283 (2023), p. 06001.
- [Bez+15] P. Bezyazeev et al. “Measurement of cosmic-ray air showers with the Tunka Radio Extension (Tunka-Rex)”. In: *Nuclear Instruments and Methods in Physics Research Section A: Accelerators, Spectrometers, Detectors and Associated Equipment* 802 (Dec. 2015), pp. 89–96.
- [BG86] L. S. Brown and G. Gabrielse. “Geonium theory: Physics of a single electron or ion in a Penning trap”. In: *Rev. Mod. Phys.* 58 (1 Jan. 1986), pp. 233–311.
- [Bir+95] D. J. Bird et al. “Detection of a cosmic ray with measured energy well beyond the expected spectral cutoff due to cosmic microwave radiation”. In: *The Astrophysical Journal* 441 (Mar. 1995), p. 144.
- [BK29] W. Bothe and W. Kolhörster. “Das Wesen der Höhenstrahlung”. In: *Zeitschrift für Physik* 56.11 (Nov. 1929), pp. 751–777.
- [Bot21] A. M. Botti for the Pierre Auger Collaboration. “The AMIGA underground muon detector of the Pierre Auger Observatory - performance and event reconstruction”. In: *PoS ICRC2019* (2021), p. 202.
- [Bra+13] J. T. Brack et al. “Absolute calibration of a large-diameter light source”. In: *Journal of Instrumentation* 8.05 (May 2013), P05014–P05014.
- [BT19] I. Brivio and M. Trott. “The standard model as an effective field theory”. In: *Physics Reports* 793 (Feb. 2019), pp. 1–98.
- [Bur+57] E. M. Burbidge et al. “Synthesis of the Elements in Stars”. In: *Rev. Mod. Phys.* 29 (4 Oct. 1957), pp. 547–650.
- [Car+01] S. M. Carroll et al. “Noncommutative Field Theory and Lorentz Violation”. In: *Physical Review Letters* 87.14 (Sept. 2001).
- [Cas18] M. Casolino. “The EUSO program to study UHECR from space: status and perspectives.” In: *35th International Cosmic Ray Conference*. Vol. 301. SISSA Medialab. 2018, p. 370.
- [Cas19] A. Castellina for the Pierre Auger Collaboration. “AugerPrime: the Pierre Auger Observatory Upgrade”. In: *EPJ Web Conf.* 210 (2019). Ed. by I. Lhenry-Yvon et al., p. 06002.
- [CCB98] P. Curie, M. Curie, and G. Bémont. “Sur une nouvelle substance fortement radioactive, contenue dans la pechblende”. In: *Comptes rendus de l’Academie des Sciences, Paris* 127 (1898), pp. 1215–1217.

- [CD11] P. Carlson and A. De Angelis. “Nationalism and internationalism in science: the case of the discovery of cosmic rays”. In: *The European Physical Journal H* 35.4 (Mar. 2011), pp. 309–329.
- [CK97] D. Colladay and V. A. Kostelecký. “CPT violation and the standard model”. In: *Physical Review D* 55.11 (June 1997), pp. 6760–6774.
- [CK98] D. Colladay and V. A. Kostelecký. “Lorentz-violating extension of the standard model”. In: *Physical Review D* 58.11 (Oct. 1998).
- [Cla27] J. Clay. “Penetrating radiation”. In: *Proceedings of the Royal Academy of Sciences at Amsterdam* 30 (1927), pp. 1115–1127.
- [Cla28] J. Clay. “Penetrating radiation II”. In: *Proceedings of the Royal Academy of Sciences at Amsterdam* 31 (1928), pp. 1091–1097.
- [CN83] S. Chadha and H. B. Nielsen. “Lorentz invariance as a low-energy phenomenon”. In: *Nucl. Phys. B* 217 (1983), p. 125.
- [DK15] J. S. Díaz and F. R. Klinkhamer. “Parton-model calculation of a nonstandard decay process in isotropic modified Maxwell theory”. In: *Phys. Rev. D* 92 (2015), p. 025007.
- [DKR16] J. S. Díaz, F. R. Klinkhamer, and M. Risse. “Changes in extensive air showers from isotropic Lorentz violation in the photon sector”. In: *Phys. Rev. D* 94 (2016), p. 085025.
- [DNR21] F. Duenkel, M. Niechciol, and M. Risse. “Photon decay in ultrahigh-energy air showers: Stringent bound on Lorentz violation”. In: *Phys. Rev. D* 104 (1 July 2021), p. 015010.
- [DNR23] F. Duenkel, M. Niechciol, and M. Risse. “New bound on Lorentz violation based on the absence of vacuum Cherenkov radiation in ultrahigh energy air showers”. In: *Phys. Rev. D* 107 (8 Apr. 2023), p. 083004.
- [EG00] J. Elster and H. Geitel. “On electricity dissipation in air”. In: *Ann. Phys* 2 (1900), pp. 425–446.
- [Ell+00] J. Ellis et al. “A Search in Gamma-Ray Burst Data for Nonconstancy of the Velocity of Light”. In: *The Astrophysical Journal* 535.1 (May 2000), pp. 139–151.
- [Eng+90] J. Engelmann et al. “Charge composition and energy spectra of cosmic-ray nuclei for elements from Be to Ni - Results from HEAO-3-C2”. In: *Astronomy and Astrophysics* 233 (June 1990), pp. 96–111.
- [Fer06] E. Fernandez. “The MAGIC gamma-ray telescope: status and first results”. In: *Nuclear Physics B - Proceedings Supplements* 151.1 (2006), pp. 381–392.
- [Fer49] E. Fermi. “On the Origin of the Cosmic Radiation”. In: *Phys. Rev.* 75 (8 Apr. 1949), pp. 1169–1174.
- [Fix09] D. J. Fixsen. “The Temperature of the Cosmic Microwave Background”. In: *The Astrophysical Journal* 707.2 (Nov. 2009), pp. 916–920.
- [Fri+20] A. S. Friedman et al. “Improved constraints on anisotropic birefringent Lorentz invariance and CPT violation from broadband

- optical polarimetry of high redshift galaxies". In: *Phys. Rev. D* 102 (4 Aug. 2020), p. 043008.
- [FS12] R. Fricke and K. Schlegel. "100th anniversary of the discovery of cosmic radiation: the role of Günther and Tegetmeyer in the development of the necessary instrumentation". In: *History of Geo-and Space Sciences* 3.2 (2012), pp. 151–158.
- [Fun15] S. Funk. "Ground- and Space-Based Gamma-Ray Astronomy". In: *Annual Review of Nuclear and Particle Science* 65.1 (2015), pp. 245–277.
- [GH77] T. K. Gaisser and A. M. Hillas. "Reliability of the Method of Constant Intensity Cuts for Reconstructing the Average Development of Vertical Showers". In: *International Cosmic Ray Conference*. Vol. 8. International Cosmic Ray Conference. Jan. 1977, p. 353.
- [Gia+71] R. Giacconi et al. "Discovery of periodic X-ray pulsations in Centaurus X-3 from Uhuru". In: *Astrophysical Journal*, vol. 167, p. L67 167 (1971), p. L67.
- [GM08] M. Gonzalez-Garcia and M. Maltoni. "Phenomenology with massive neutrinos". In: *Physics Reports* 460.1–3 (Apr. 2008), pp. 1–129.
- [Goc11] A. Gockel. "Measurement of penetrating radiation during balloon flights". In: *Phys. Zeit* 12 (1911), pp. 595–597.
- [Gre56] K. Greisen. "The extensive air showers". In: *Progress in cosmic ray physics* 3.1 (1956).
- [Gre60] K. Greisen. "Cosmic Ray Showers". In: *Annual Review of Nuclear Science* 10.1 (1960), pp. 63–108.
- [Gri08] D. Griffiths. *Introduction to Elementary Particles*. Wiley-VCH, 2008. ISBN: 9783527834631.
- [Gru20] C. Grupen. *Astroparticle Physics*. Jan. 2020. ISBN: 978-3-030-27341-5.
- [Hea08] A. Heavens. "The cosmological model: an overview and an outlook". In: *Journal of Physics: Conference Series* 120.2 (July 2008), p. 022001.
- [Hec+98] D. Heck et al. *CORSIKA: a Monte Carlo code to simulate extensive air showers*. 1998.
- [Hei54] W. Heitler. *The quantum theory of radiation*. Courier Corporation, 1954, p. 386.
- [Her+61] J. Hersil et al. "Observations of Extensive Air Showers near the Maximum of Their Longitudinal Development". In: *Phys. Rev. Lett.* 6 (1961), pp. 22–23.
- [Hes12] V. F. Hess. "Über Beobachtungen der durchdringenden Strahlung bei sieben Freiballonfahrten". In: *Phys. Z.* 13 (1912), pp. 1084–1091.
- [Hil84] A. M. Hillas. "The Origin of Ultra-High-Energy Cosmic Rays". In: *Annual Review of Astronomy and Astrophysics* 22 (Jan. 1984), pp. 425–444.

- [HRR03] A. Haungs, H. Rebel, and M. Roth. “Energy spectrum and mass composition of high-energy cosmic rays”. In: *Reports on Progress in Physics* 66.7 (June 2003), p. 1145.
- [Huc+12] J. P. Huchra et al. “The 2mass Redshift Survey—Description and Data Release”. In: *The Astrophysical Journal Supplement Series* 199.2 (Mar. 2012), p. 26.
- [Hue13] T. Huege. “Theory and simulations of air shower radio emission”. In: *AIP Conference Proceedings*. AIP, 2013.
- [JLM06] T. Jacobson, S. Liberati, and D. Mattingly. “Lorentz violation at high energy: Concepts, phenomena, and astrophysical constraints”. In: *Annals of Physics* 321.1 (Jan. 2006), pp. 150–196.
- [KC62] W. L. Kraushaar and G. W. Clark. “Search for Primary Cosmic Gamma Rays with the Satellite Explorer XI”. In: *Phys. Rev. Lett.* 8 (3 Feb. 1962), pp. 106–109.
- [Keg13] B. Kegl for the Pierre Auger Collaboration. “Measurement of Muon Signal Using the Temporal and Spectral Structure of the Signals in Surface Detectors of the Pierre Auger Observatory”. In: *PoS ICRC2013* (2013), p. 415.
- [Kei04] B. G. Keilhauer. “Investigation of atmospheric effects on the development of extensive air showers and their detection with the Pierre Auger Observatory”. Ph.D. thesis. Feb. 2004.
- [Kel11] J. L. Kelley. “AERA: The Auger Engineering Radio Array”. In: *32nd International Cosmic Ray Conference*. Vol. 3. Aug. 2011, p. 112.
- [Kim19] S. S. Kimura. “High-energy emissions from neutron star mergers”. In: *EPJ Web of Conferences* 210 (2019). Ed. by I. Lhenry-Yvon et al., p. 03001.
- [Kli18] F. R. Klinkhamer. “Lorentz-violating neutral-pion decays in isotropic modified Maxwell theory”. In: *Mod. Phys. Lett. A* 33 (2018), p. 1850104.
- [KM02] V. A. Kostelecký and M. Mewes. “Signals for Lorentz violation in electrodynamics”. In: *Phys. Rev. D* 66 (2002), p. 056005.
- [KN58] K. Kamata and J. Nishimura. “The Lateral and the Angular Structure Functions of Electron Showers”. In: *Progress of Theoretical Physics Supplement* 6 (Feb. 1958), pp. 93–155.
- [KNR17] F. R. Klinkhamer, M. Niechciol, and M. Risse. “Improved bound on isotropic Lorentz violation in the photon sector from extensive air showers”. In: *Phys. Rev. D* 96.11 (2017), p. 116011.
- [Kol13] W. Kolhörster. “Messungen der durchdringenden Strahlung im Freiballon in größeren Höhen”. In: *Physikalische Zeitschrift* 14 (1913).
- [Kol14] W. Kolhörster. “Messung der durchdringenden Strahlung bis in Höhen von 9300m”. In: *Verhandlungen der Deutschen Physikalischen Gesellschaft* 16 (1914), p. 719.
- [KR08] F. R. Klinkhamer and M. Risse. “Addendum: Ultrahigh-energy cosmic-ray bounds on non-birefringent modified-Maxwell theory”. In: *Phys. Rev. D* 77 (2008), p. 117901.

- [KR11] V. A. Kostelecký and N. Russell. “Data tables for Lorentz and CPT violation”. In: *Rev. Mod. Phys.* 83 (2011), p. 11.
- [KS06] M. Kachelrieß and P. Serpico. “The Compton–Getting effect on ultra-high energy cosmic rays of cosmological origin”. In: *Physics Letters B* 640.5–6 (Sept. 2006), pp. 225–229.
- [KS08] F. R. Klinkhamer and M. Schreck. “New two-sided bound on the isotropic Lorentz-violating parameter of modified Maxwell theory”. In: *Phys. Rev. D* 78 (2008), p. 085026.
- [KS11a] F. R. Klinkhamer and M. Schreck. “Consistency of isotropic modified Maxwell theory: Microcausality and unitarity”. In: *Nucl. Phys. B* 848 (2011), pp. 90–107.
- [KS11b] F. Klinkhamer and M. Schreck. “Consistency of isotropic modified Maxwell theory: Microcausality and unitarity”. In: *Nuclear Physics B* 848.1 (July 2011), pp. 90–107.
- [KS89] V. A. Kostelecky and S. Samuel. “Spontaneous Breaking of Lorentz Symmetry in String Theory”. In: *Phys. Rev. D* 39 (1989), p. 683.
- [Lav+13] K. A. Lave et al. “Elemental GCR Observations During the 2009–2010 Solar Minimum Period”. In: *33rd International Cosmic Ray Conference*. 2013, p. 0793.
- [Lin63] J. Linsley. “Evidence for a Primary Cosmic-Ray Particle with Energy 10^{20} eV”. In: *Phys. Rev. Lett.* 10 (4 Feb. 1963), pp. 146–148.
- [Lod03] K. Lodders. “Solar System Abundances and Condensation Temperatures of the Elements”. In: *The Astrophysical Journal* 591.2 (July 2003), p. 1220.
- [Mar01] G. S. Martin Lemoine. *Physics and Astrophysics of Ultra High Energy Cosmic Rays*. Heidelberg: Springer Berlin, 2001. ISBN: 978-3-540-45615-5.
- [Mat05a] J. Matthews. “A Heitler model of extensive air showers”. In: *Astroparticle Physics* 22 (Jan. 2005), pp. 387–397.
- [Mat05b] D. Mattingly. “Modern Tests of Lorentz Invariance”. In: *Living Reviews in Relativity* 8.1 (Sept. 2005).
- [Mat11] T. H.-J. Mathes for the Pierre Auger Collaboration. “The HEAT telescopes of the Pierre Auger Observatory: Status and first data”. In: *32nd International Cosmic Ray Conference*. Vol. 3. Aug. 2011, p. 153.
- [MB26] R. A. Millikan and I. S. Bowen. “High Frequency Rays of Cosmic Origin I. Sounding Balloon Observations at Extreme Altitudes”. In: *Phys. Rev.* 27 (4 Apr. 1926), pp. 353–361.
- [Mit+99] R. K. Mittleman et al. “Bound on CPT and Lorentz Symmetry with a Trapped Electron”. In: *Phys. Rev. Lett.* 83 (11 Sept. 1999), pp. 2116–2119.
- [MPR00] I. Mocioiu, M. Pospelov, and R. Roiban. “Low-energy limits on the antisymmetric tensor field background on the brane and on the non-commutative scale”. In: *Physics Letters B* 489.3–4 (Sept. 2000), pp. 390–396.

- [MR18] S. Mollerach and E. Roulet. “Progress in high-energy cosmic ray physics”. In: *Progress in Particle and Nuclear Physics* 98 (Jan. 2018), pp. 85–118.
- [Mül+08] D. Müller et al. “The TRACER Project: Instrument Concept, Balloon Flights, and Analysis Procedures”. In: *Proceedings of the 30th International Cosmic Ray Conference, ICRC 2007 2* (Jan. 2008).
- [Nie] M. Niechciol. private communication.
- [OH23] S. Ohm and S. W. for the H.E.S.S. Collaboration. “Current status and operation of the H.E.S.S. array of imaging atmospheric Cherenkov telescopes”. In: *Nuclear Instruments and Methods in Physics Research Section A: Accelerators, Spectrometers, Detectors and Associated Equipment* 1055 (Oct. 2023), p. 168442.
- [Ost11] S. Ostapchenko. “Monte Carlo treatment of hadronic interactions in enhanced Pomeron scheme: QGSJET-II model”. In: *Physical Review D* 83 (2011), p. 014018.
- [Pet61] B. Peters. “Primary cosmic radiation and extensive air showers”. In: *Il Nuovo Cimento (1955-1965)* 22.4 (Nov. 1961), pp. 800–819.
- [Phi+01] D. F. Phillips et al. “Limit on Lorentz and CPT violation of the proton using a hydrogen maser”. In: *Physical Review D* 63.11 (Apr. 2001).
- [Pic+07] P. Picozza et al. “PAMELA – A payload for antimatter matter exploration and light-nuclei astrophysics”. In: *Astroparticle Physics* 27.4 (Apr. 2007), pp. 296–315.
- [Pie+06] T. Pierog et al. “First Results of Fast One-dimensional Hybrid Simulation of EAS Using CONEX”. In: *Nucl. Phys. Proc. Suppl.* 151 (2006), pp. 159–162.
- [Pie+15] T. Pierog et al. “EPOS LHC: Test of collective hadronization with data measured at the CERN Large Hadron Collider”. In: *Phys. Rev. C* 92 (2015), p. 034906.
- [Pie15a] Pierre Auger Observatory. *Pierre Auger Observatory @ flickr*. accessed on January 14, 2024. July 2015. URL: <https://www.flickr.com/photos/134252569@N07/>.
- [Pie15b] Pierre Auger Observatory. *Pierre Auger Observatory @ flickr*. accessed on January 11, 2024. Oct. 2015. URL: <https://www.flickr.com/photos/134252569@N07/>.
- [Pie17] T. Pierog. “Open issues in hadronic interactions for air showers”. In: *EPJ Web Conf.* 145 (2017), p. 18002.
- [Pie20] Pierre Auger Observatory. *Pierre Auger Observatory @ flickr*. accessed on January 14, 2024. Oct. 2020. URL: <https://www.flickr.com/photos/134252569@N07/>.
- [Pro+14] V. Prosin et al. “Tunka-133: Results of 3 year operation”. In: *Nuclear Instruments and Methods in Physics Research Section A: Accelerators, Spectrometers, Detectors and Associated Equipment* 756 (2014), pp. 94–101.
- [PS95] M. E. Peskin and D. V. Schroeder. *An introduction to quantum field theory*. Reading, USA: Addison Wesley, 1995.

- [Ptu+93] V. Ptuskin et al. “Diffusion and drift of very high energy cosmic rays in galactic magnetic fields”. In: *Astronomy and Astrophysics* 268 (Jan. 1993), pp. 726–735.
- [Rie+20] F. Riehn et al. “Hadronic interaction model Sibyll 2.3d and extensive air showers”. In: *Phys. Rev. D* 102.6 (2020), p. 063002.
- [Rou21] E. Roulet. “Large-scale anisotropies above 0.03 EeV measured by the Pierre Auger Observatory”. In: *PoS ICRC2019* (2021), p. 408.
- [Sch16] J. Schulz for the Pierre Auger Collaboration. “Status and Prospects of the Auger Engineering Radio Array ”. In: *Proceedings of The 34th International Cosmic Ray Conference — PoS(ICRC2015)*. Vol. 236. 2016, p. 615.
- [Sch17] F. G. Schröder. “Radio detection of cosmic-ray air showers and high-energy neutrinos”. In: *Progress in Particle and Nuclear Physics* 93 (Mar. 2017), pp. 1–68.
- [Sch38] B. Schmidt. “Ein lichtstarkes komafreies Spiegelsystem”. In: *Mitteilungen der Hamburger Sternwarte in Bergedorf, vol. 7*, pp. 15–17 7 (1938), pp. 15–17.
- [Swo01] S. Swordy. “The Energy Spectra and Anisotropies of Cosmic Rays”. In: *Space Science Reviews* 99 (Oct. 2001), pp. 85–94.
- [Tom17] G. Tomar. “Lorentz invariance violation as an explanation of the muon excess in Auger data”. In: *Physical Review D* 95.9 (May 2017).
- [TT04] J.-L. Tassoul and M. Tassoul. *A Concise History of Solar and Stellar Physics*. Princeton: Princeton University Press, 2004. ISBN: 9781400865390.
- [Ung+08] M. Unger et al. “Reconstruction of longitudinal profiles of ultra-high energy cosmic ray showers from fluorescence and Cherenkov light measurements”. In: *Nuclear Instruments and Methods in Physics Research Section A: Accelerators, Spectrometers, Detectors and Associated Equipment* 588.3 (Apr. 2008), pp. 433–441.
- [Ung16] M. Unger for the Pierre Auger Collaboration and the Telescope Array Collaboration. “Report of the Working Group on the Composition of Ultra-High Energy Cosmic Rays ”. In: *PoS ICRC2015* (2016), p. 307.
- [Veb20] D. Veberič. *Maps of the Pierre Auger Observatory*. accessed on January 08, 2024. Aug. 2020. URL: <https://web.iap.kit.edu/darko/auger/auger-array>.
- [Wax95] E. Waxman. “Cosmological Gamma-Ray Bursts and the Highest Energy Cosmic Rays”. In: *Physical Review Letters* 75.3 (July 1995), pp. 386–389.
- [WBM97] B. Wiebel-Sooth, P. L. Biermann, and H. Meyer. “Cosmic Rays VII. Individual element spectra: prediction and data”. In: *Astronomy and Astrophysics* 330 (1997), p. 389.
- [Wik19] Wikipedia contributors. *Standard Model of Elementary Particles*. accessed on February 06, 2024. Aug. 2019. URL:

- wikipedia.org/wiki/File:Standard_Model_of_Elementary_Particles.svg.
- [Wil01] C. T. R. Wilson. “On the ionisation of atmospheric air”. In: *Proceedings of the Royal Society of London* 68.442-450 (1901), pp. 151–161.
- [Wor+22] R. L. Workman et al. “Review of Particle Physics”. In: *PTEP* 2022.8 (Aug. 2022), p. 083C01.
- [Wul09] T. Wulf. “On the radiation of high penetrating power that exists in the atmosphere”. In: *Phys. Zeit* 1.152-157 (1909), p. 124.
- [Yoo+17] Y. S. Yoon et al. “Proton and Helium Spectra from the CREAM-III Flight”. In: *The Astrophysical Journal* 839.1 (Apr. 2017), p. 5.
- [Yos+04] T. Yoshida et al. “BESS-polar experiment”. In: *Advances in Space Research* 33.10 (2004). The Next Generation in Scientific Ballooning, pp. 1755–1762.
- [YR12] P. Younk and M. Risse. “Sensitivity of the correlation between the depth of shower maximum and the muon shower size to the cosmic ray composition”. In: *Astroparticle Physics* 35.12 (July 2012), pp. 807–812.
- [Yus19] A. Yushkov for the Pierre Auger Collaboration. “Mass Composition of Cosmic Rays with Energies above $10^{17.2}$ eV from the Hybrid Data of the Pierre Auger Observatory”. In: *PoS ICRC2019* (2019), p. 482.
- [Yus23] A. Yushkov for the Pierre Auger Collaboration and the Telescope Array Collaboration. “Depth of maximum of air-shower profiles: testing the compatibility of the measurements at the Pierre Auger Observatory and the Telescope Array”. In: *PoS ICRC2023* (2023), p. 249.
- [ZK66] G. T. Zatsepin and V. A. Kuzmin. “Upper limit of the spectrum of cosmic rays”. In: *JETP Lett.* 4 (1966), pp. 78–80.

List of Figures

- | | | |
|-----|--|---|
| 1.1 | Shown on the left is the cross section of the electroscope developed and used by Wulf, on the right a picture of the same. The electric charge of the metal filaments (F) held by a quartz string (Q) can be determined from the spread of the filament through the microscope (M). The quartz strings are connected to an amber insulator (B) and the chambers can be connected to a sodium-drying device by two openings (Na). Image taken from [FS12]. | 2 |
| 1.2 | Measurements of the atmospheric ionisation in different altitudes. The results of the balloon flights by Viktor Hess [Hes12] are shown on the left. On the right, Werner Kolhörster's results are shown, extending the measurements to altitudes up to 9.2 km and confirming the results of Hess [Kol13; Kol14]. Image taken from [CD11]. | 3 |
| 1.3 | Measurements of the number of coincident events in two detectors in different distances [Aug+39]. The x-axis corresponds to the distance between the detectors in meters, the y-axis to the number of measured coincident events. The solid line shows the interpolation between measurements (dots), while the dashed line corresponds to the prediction of coincident events made by Hans Euler. Auger explained the increased rate at high distances through the production of highly penetrating "mesotrons" (mesons) in the shower. | 4 |
| 1.4 | The cosmic-ray energy spectrum, aggregated from both direct measurements and indirect measurements using air-showers in the Earth's atmosphere [Nie]. Covered are 11 orders of magnitude in energy and 32 orders of magnitude in CR flux. Marked are significant milestones of particle fluxes as well as the energy reached by protons accelerated by the LHC. | 6 |
| 1.5 | The CR energy spectrum as observed by the Pierre Auger Observatory [Aab+20c]. In the top plot, the CR energy spectrum is scaled by E^2 , as well as the number of events observed in each bin is noted. In the bottom plot, the CR energy spectrum is scaled by E^3 and fitted with a sequence of four power laws, showing how the spectral index changes with the different energy ranges. | 7 |

- 1.6 Flux of CRs with energies above 8 EeV by arrival direction in galactic coordinates as measured by the Pierre Auger Observatory [Aab+18a]. The direction of the reconstructed dipole is indicated by the cross, the surrounding ellipses denote the 68 % CL and 95 % CL regions. The direction of the flux weighted dipole of galaxies in the 2MRS catalog [Huc+12] is denoted by the diamond. The two arrows show the modifications to the dipole moment due to the Galactic magnetic field as modeled in [Ade+16] for particles with E/Z of 5 EeV and 2 EeV respectively. Image taken from [MR18]. 10
- 1.7 The Hillas plot shows size and magnetic field strength of possible UHECR source candidates [MR18]. The solid and dashed purple lines indicate the necessary source parameters needed to accelerate protons and iron respectively to energies above 100 EeV. For sources with relativistic jets, e.g. GRBs, the shifted lines for the case of a boost of $\Gamma = 100$ are shown in cyan, indicating the relaxed parameters in size and magnetic field. Shown sources are Neutron stars (n-star), GRBs, AGNs involving both radio-quiet Seyfert galaxies (Sy) and radio galaxies (RG) with acceleration both in the inner black hole (BH) or the inner jets, and the hot-spots and radio lobes of Fanaroff-Riley Class II galaxies. The parameters of SNRs as well as the acceleration of CRs in large scale shocks in starburst galaxies and galaxy clusters are also displayed. 11
- 1.8 The relative abundances of elements up to nickel (Ni) in the solar system [Lod03] and from galactic CRs at low energies [Lav+13]. The relative abundances are normalized to 10^6 for silicon (Si, $Z = 14$). Image taken from [MR18]. 13
- 1.9 Cosmic ray spectra of different elements [MR18] in the energy range between 1 GeV and 0.2 EeV. Below the knee, the spectrum is measured by the satellite experiments AMS-02 [Agu+15b; Agu+15a] and HEAO-3 [Eng+90] and the balloon flights CREAM-I, CREAM-II and CREAM-III [Yoo+17; Ahn+09]. For energies above the knee, results from the Air-shower experiments KASCADE [Ape+09] as well as KASCADE-Grande [Ape+13] are shown, where the elements are taken as representative of the flux of their respective mass ranges due to the indirect detection method. 14
- 1.10 Fractions of elements of four different elemental mass groups as determined by the Pierre Auger Observatory [Aab+14b]. Results are shown for the three hadronic interaction models EPOS-LHC, QGSJET-II-04 and Sibyll 2.1. In the upper panels, the fractions of individual elements are shown, the lower panel shows the p-values of the fits. 15

| | | |
|-----|--|----|
| 2.1 | Schematic depiction of the Heitler model adapted from [Mat05a]. Shown is the shower development over the first four interaction lengths. Electrons and positrons are depicted as straight lines, photons as wavy lines. | 18 |
| 2.2 | Schematic depiction of the shower development and the individual shower components [HRR03]. | 20 |
| 2.3 | Average longitudinal profile of the electromagnetic (blue) and muonic (red) components of simulated showers initiated by a 10 EeV proton [Abr+09]. The solid black line shows a Gaisser-Hillas function fitted to the electromagnetic component. | 22 |
| 2.4 | Lateral distribution of particle densities of the different air shower components in showers initiated by different primary particles [HRR03]. The values were derived from MC simulations of vertical showers with a primary energy of 1 PeV using CORSIKA [Hec+98]. | 23 |
| 2.5 | A sketch of different detection techniques of air showers [Sch17]. | 25 |
| 3.1 | Layout of the Pierre Auger Observatory [Veb20]. The black markers correspond to the 1660 detector stations of the SD. The four sites of the FD as well as the field of view of individual telescopes are marked in blue, with the additional high-elevation telescopes of HEAT at Coihueco marked in dark orange. Also shown are the 750 m array and AERA near Coihueco, as well as laser (XLF, CLF) and weather balloon launching (BLS) facilities. | 28 |
| 3.2 | (A) The FD building at Los Morados at night [Pie20]. (B) Schematic layout of a FD detector location with six fluorescence telescopes [Abr+10a]. | 29 |
| 3.3 | (A) Schematic depiction of a fluorescence telescope, with main components labeled [Abr+10a]. (B) Photo of the Camera module of a fluorescence telescope [Pie15a]. | 30 |
| 3.4 | (A) Camera view of an event measured by the FD telescope at Coihueco. The time at which each pixel is activated is indicated by the colors, with violet pixels being early and red pixels late occurrences. Grey pixels indicate coincident signals excluded from the event reconstruction [Abd+23]. (B) Schematic depiction of the shower as seen from the FD telescope and the shower detector plane [Abr+10a]. | 31 |
| 3.5 | Reconstruction of the longitudinal profile of a shower measured by the FD [Abd+23]. The line overlaying the measurements is the fitted Gaisser-Hillas function. | 32 |
| 3.6 | A water Cherenkov detector station of the Pierre Auger Observatory. (A) Photograph of a deployed SD station. Main hardware components visible from the outside, as well as the position of the photomultipliers inside the tank, are labeled. Image taken from [Pie15b]. (B) Schematic view of an SD station filled with pure water, adapted from [Kei04]. | 33 |

| | | |
|------|---|----|
| 3.7 | Schematic depictions of the air shower development from [Aab+20b]. (A) Approximation in a planar front described by the shower axis \hat{a} and the barycenter \vec{x}_b . (B) Spherical shower development originating at a center point \vec{x}_o at the time t_o | 35 |
| 3.8 | Shower behavior of extensive air showers at ground in dependence on the distance from the shower axis. In both plots, points with error bars correspond to triggered stations, the black line is the result of the model fit and the shaded area represents its uncertainties. (A) Delay of the signal start times compared to a plane shower front [Aab+15b]. (B) Signal size in VEM [Aab+15b]. | 36 |
| 3.9 | (A) $S(1000)$ as a function of $\sec(\theta)$ as described in Eq. (3.6) [Aab+20a]. The lines correspond to the fits at intensities associated with the approximate energies 3×10^{18} eV (I_1), 8×10^{18} eV (I_2) and 2×10^{19} eV (I_3). The dots correspond to the data gained using the CIC method. (B) Correlation between S_{38} and E_{FD} [Aab+20a]. The red line is the best fit of the data points with the function given in Eq. (3.7). | 37 |
| 3.10 | (A) Layout of the 750 m infill array of AMIGA and HEAT near Coihueco [Abr+22]. (B) Cross section of a HEAT telescope in both horizontal and tilted configuration [Mat11]. | 38 |
| 4.1 | The particles of the Standard Model of particle physics [Wik19]. The particles are divided into six quarks and six leptons, which are further divided into three generations or flavours each. The forces between those particles are mediated by four gauge bosons and the Higgs boson. | 42 |
| 4.2 | The photon decay length l_{PhD} due to LV induced photon decay dependent on photon energy ω . Values of $\kappa = -10^{-16}$, $\kappa = -10^{-18}$ and $\kappa = -10^{-20}$ are used. The threshold energies $\omega_{th}(\kappa)$ for the respective values of κ are marked by the vertical lines. | 47 |
| 4.3 | Differential emission rates of VCh photons in dependence of the energy fraction ω/E_e inherited from a primary electron for $\kappa = 6 \times 10^{-20}$ and different electron energies E_e | 50 |
| 4.4 | Rate of emitted energy from a electron emitting VCh radiation in relation to the electron energy for different values of κ . The energy thresholds of VCh radiation for different κ is marked by the black vertical lines. | 51 |
| 4.5 | Schematic depiction of the Heitler model modified to include photon decay. Shown is the shower development over the first three interaction lengths. Electrons and positrons are depicted as straight lines, the initial photon as a wavy line. While the initial photon is depicted for illustration purposes, all photons decay immediately into electron-positron pairs, leading to a multiplicity of three at each vertex after the first interaction. | 53 |

- 5.1 Comparison between 1000000 energy values for an electron produced by photon decay drawn by `lvdrawrandomenergy` (red) and the differential energy spectrum $\frac{d\Gamma_{\text{PhD}}}{dE}$ (black). The values were drawn for a primary photon energy $\omega = 10^{16}$ eV and $\kappa = -6 \times 10^{-20}$ 59
- 5.2 Comparison between 1000000 values for a VCh photon drawn by `lvdrawrandomenergy` (red) and the differential energy spectrum $\frac{d\Gamma_{\text{PhD}}}{dE}$ (black). The values were drawn for a primary electron with energy $E = 10^{16}$ eV and $\kappa = 6 \times 10^{-20}$ 60
- 5.3 The range of all possible $\langle X_{\text{max}} \rangle / \sigma(X_{\text{max}})$ -values inside the contours of the two-dimensional confidence interval derived from Auger X_{max} data. The contours are shown for select energy bins, statistical errors are indicated by lines, systematic errors by brackets. 64
- 5.4 The range of all possible $\langle X_{\text{max}} \rangle / \sigma(X_{\text{max}})$ -values for combinations of simulated air showers induced by primary protons, helium, oxygen and iron nuclei for $\kappa = 0$ and a primary particle energy of $10^{19.15}$ eV. Displayed are only proton-helium, helium-oxygen, oxygen-iron and iron-proton combinations, since all other possible combinations of those four elements produce $\langle X_{\text{max}} \rangle / \sigma(X_{\text{max}})$ -values inside the umbrella-shaped area defined by those. Any point is differing 2% in composition from the neighboring points. 65
- 5.5 Distributions of X_{max} for simulated showers initiated by protons and iron nuclei (A), as well as the sum of both distributions (B). The primary particle energy is $E = 10^{19}$ eV in both cases. The mean values of each distribution are marked by the vertical continuous lines, the corresponding 1σ widths are shown by the shaded areas. 66
- 6.1 The distribution of simulated values of X_{max} for primary protons with an energy of 10^{19} eV for the absence of LV ($\kappa = 0$) and for different values of $\kappa < 0$ 71
- 6.2 The simulated values of $\langle X_{\text{max}} \rangle$ as a function of the primary energy for primary protons and iron nuclei for the absence of LV ($\kappa = 0$) and for different values of $\kappa < 0$ 72
- 6.3 Distribution of the number of photon decays per shower for 2000 showers simulated with $\kappa = -1 \times 10^{21}$ and different energies of a primary proton. 73
- 6.4 The simulated values of $\sigma(X_{\text{max}})$ as a function of the primary energy for primary protons and iron nuclei for the absence of LV ($\kappa = 0$) and for different values of $\kappa < 0$ 74
- 6.5 Comparison of the $\langle X_{\text{max}} \rangle - \sigma(X_{\text{max}})$ -combinations derived by simulations which incorporate LV to the 2D confidence intervals given by the measurements of the Pierre Auger Observatory [Yus19] for different values for κ and a primary particle energy of $10^{19.15}$ eV. 75

| | | |
|------|--|----|
| 6.6 | Comparison of the $\langle X_{\max} \rangle$ - $\sigma(X_{\max})$ -combinations derived by simulations to the 2D confidence intervals given by the measurements of the Pierre Auger Observatory for different values of κ and a primary particle energy of $10^{17.55}$ eV. | 78 |
| 6.7 | Comparison of the $\langle X_{\max} \rangle$ - $\sigma(X_{\max})$ -combinations derived by LV simulations to the 2D confidence interval given by the measurements of the Pierre Auger Observatory for $\kappa = -6 \times 10^{-21}$ and a primary particle energy of $10^{18.95}$ eV. | 79 |
| 6.8 | The simulated values of $\langle N_{\mu} \rangle$ as a function of the primary energy for different primary particles in the absence of LV ($\kappa = 0$) and for $\kappa < 0$. All values are normalized to the value of $\langle N_{\mu} \rangle$ for unmodified protons at the corresponding energy, to show the relative effect of LV on the muon number. | 80 |
| 6.9 | The simulated values of $\langle N_{\mu} \rangle$ as a function of the primary energy for different primary particles in the absence of LV ($\kappa = 0$) and for $\kappa = -6 \times 10^{-21}$. All values are normalized to the value of $\langle N_{\mu} \rangle$ for unmodified protons at the corresponding energy, to show the relative effect of LV on the muon number. Depicted is also the result of a partial modification of the CONEX code, incorporating only photon decay and no modification of the pion decay time. | 82 |
| 6.10 | The simulated values of $\sigma(N_{\mu})$ as a function of the primary energy for different primary particles in the absence of LV ($\kappa = 0$) and for $\kappa < 0$. All values are normalized to the value of $\sigma(N_{\mu})$ for unmodified protons at the corresponding energy, to show the relative effect of LV on the muon number. | 83 |
| 6.11 | Visual example of the changes in the distribution of X_{\max} and the number of muons observed at ground level N_{μ} and their correlation for $\kappa = 0$ (left) and $\kappa = -6 \times 10^{-21}$ (right) and an energy of 10^{20} eV. Shown are pure compositions with CRs consisting of 100 % protons (top) or 100 % iron nuclei (bottom). | 84 |
| 6.12 | Visual example of the changes in the distribution of X_{\max} and the number of muons observed at ground level N_{μ} and their correlation for $\kappa = 0$ (left) and $\kappa = -6 \times 10^{-21}$ (right) and an energy of 10^{20} eV. Shown is the maximally mixed composition of a cosmic ray spectrum consisting of 50 % protons and 50 % iron nuclei for $\kappa = 0$ and $\kappa = -6 \times 10^{-21}$ | 85 |
| 6.13 | The correlation $r(X_{\max}, N_{\mu})$ between X_{\max} and N_{μ} for showers with a primary particle composition of only protons and iron. The correlation is shown for different fractions of both primaries, ranging from a pure proton composition to pure iron. Showers were simulated for a primary particle energy of 10^{20} eV. | 86 |

- 6.14 The simulated values of $\langle X_{\max} \rangle$ and $\sigma(X_{\max})$ as a function of the primary energy for primary protons and iron nuclei for the absence of LV ($\kappa = 0$) and for $\kappa = -6 \times 10^{-21}$. Shown are simulations with the three hadronic interaction models SIBYLL 2.3d [Rie+20], EPOS LHC [Pie+15] and QGSJET-II-04 [Ost11]. 88
- 6.15 Comparison of the combinations of $\langle X_{\max} \rangle$ and $\sigma(X_{\max})$ which were derived from simulations with different hadronic interaction models which incorporate LV to the 2D confidence intervals given by the measurements of the Pierre Auger Observatory for $\kappa = -1 \times 10^{-21}$ and a primary particle energy of $10^{19.15}$ eV. 89
- 6.16 The simulated values of $\langle N_{\mu} \rangle$ as a function of the primary energy for different interaction models in the absence of LV ($\kappa = 0$) and for $\kappa < 0$. All values are normalized to the value of $\langle N_{\mu} \rangle$ for unmodified protons of the model at the corresponding energy, to show the relative effect of LV on the muon number. 91
- 6.17 The simulated values of $\sigma(N_{\mu})$ as a function of the primary energy for different interaction models in the absence of LV ($\kappa = 0$) and for $\kappa < 0$. All values are normalized to the value of $\sigma(N_{\mu})$ for unmodified protons of the model at the corresponding energy, to show the relative effect of LV on the muon number. 92
- 6.18 The distribution of simulated values of X_{\max} for primary protons with an energy of 10^{18} eV for the absence of LV ($\kappa = 0$) and for a value of $\kappa = 3 \times 10^{-20}$ 93
- 6.19 The simulated values of $\langle X_{\max} \rangle$ as a function of the primary energy for primary protons and iron nuclei for the absence of LV ($\kappa = 0$) and for different values of $\kappa > 0$. Lines are only plotted up to the maximum energy given by the onset of VCh radiation, see Eq. (4.18). 94
- 6.20 Mass threshold (in terms of mass number A) related to VCh radiation for different values of κ as a function of primary energy, cf. Eq. (6.7). For a given κ , only primaries above the line can reach the Earth. 95
- 6.21 The simulated values of $\sigma(X_{\max})$ as a function of the primary energy for primary protons and iron nuclei for the absence of LV ($\kappa = 0$) and for different values of $\kappa > 0$. Lines are only plotted up to the maximum energy given by the onset of VCh radiation, see Eq. (4.18). 96

- 6.22 Comparison of combinations of $\langle X_{\max} \rangle$ and $\sigma(X_{\max})$ derived by simulations, excluding combinations with particles above the VCh radiation threshold, for different values of κ and a primary energy of $10^{18.65}$ eV. The "tips" of the umbrella refer to pure beams with primaries as indicated (proton, helium, nitrogen, silicon, iron). For a given κ , the corresponding "umbrella" covers all values allowed by arbitrary combinations of these primaries. With increasing κ , a reduction of $\langle X_{\max} \rangle$ can be seen as well as a successive removal of light primaries if above VCh radiation threshold. 97
- 6.23 Comparison of the combinations of $\langle X_{\max} \rangle$ and $\sigma(X_{\max})$ derived by simulations which incorporate LV to the 2D confidence interval (98 % CL) given by the measurements of the Pierre Auger Observatory [Yus19] for the critical value of $\kappa = 3 \times 10^{-20}$ and a primary particle energy of $10^{18.65}$ eV. The umbrella shape covers all combinations of iron, silicon, nitrogen and helium primary particles, since protons are excluded due to VCh radiation for these values of energy and κ 100
- 6.24 The simulated values of $\langle N_{\mu} \rangle$ as a function of the primary energy for different primary particles in the absence of LV ($\kappa = 0$) and for $\kappa = 3 \times 10^{-20}$. All values are normalized to the value of $\langle N_{\mu} \rangle$ for unmodified protons at the corresponding energy, to show the relative effect of LV on the muon number. 101
- 6.25 The simulated values of $\sigma(N_{\mu})$ as a function of the primary energy for different primary particles in the absence of LV ($\kappa = 0$) and for $\kappa = 3 \times 10^{-20}$. All values are normalized to the value of $\sigma(N_{\mu})$ for unmodified protons at the corresponding energy, to show the relative effect of LV on the muon number. 102
- 6.26 Visual example of the changes in the distribution of X_{\max} and the number of muons observed at ground level N_{μ} and their correlation for $\kappa = 0$ (left) and $\kappa = 3 \times 10^{-20}$ (right) and an energy of 10^{18} eV. Shown is a pure CR composition of only protons. 103
- 6.27 Visual example of the changes in the distribution of X_{\max} and the number of muons observed at ground level N_{μ} and their correlation for $\kappa = 0$ (left) and $\kappa = 3 \times 10^{-20}$ (right) and an energy of 10^{20} eV. Shown are the maximally mixed compositions of a cosmic ray spectrum consisting of 50 % protons and 50 % iron nuclei for $\kappa = 0$ and 50 % aluminium and 50 % iron nuclei for $\kappa = 3 \times 10^{-20}$ 104
- 6.28 The correlation $r(X_{\max}, N_{\mu})$ between X_{\max} and N_{μ} for showers with a primary particle composition of only protons and iron ($\kappa = 0$) and aluminium and iron ($\kappa = 3 \times 10^{-20}$). The correlation is shown for different fractions of both primaries, ranging from a pure proton (aluminium) composition to pure iron for $\kappa = 0$ ($\kappa = 3 \times 10^{-20}$). Showers were simulated for a primary particle energy of 10^{20} eV. 105

- 6.29 The simulated values of $\langle X_{\max} \rangle$ and $\sigma(X_{\max})$ as a function of the primary energy for primary protons and iron nuclei for the absence of LV ($\kappa = 0$) and for $\kappa > 0$. Shown are simulations with the three hadronic interaction models SIBYLL 2.3d [Rie+20], EPOS LHC [Pie+15] and QGSJET-II-04 [Ost11]. 106
- B.1 The simulated values of $\langle X_{\max} \rangle$ as a function of the primary energy for primary photons and electrons in the absence of LV. 123
- B.2 The simulated values of $\langle N_{\mu} \rangle$ as a function of the primary energy for different interaction models in the absence of LV ($\kappa = 0$). All values are normalized to the value of $\langle N_{\mu} \rangle$ for unmodified protons of the hadronic interaction model SIBYLL2.3d at the corresponding energy, to show the relative effect of LV on the muon number. 124
- B.3 The simulated values of $\sigma(N_{\mu})$ as a function of the primary energy for different interaction models in the absence of LV ($\kappa = 0$). All values are normalized to the value of $\sigma(N_{\mu})$ for unmodified protons of the hadronic interaction model SIBYLL2.3d at the corresponding energy, to show the relative effect of LV on the muon number. 125
- B.4 The simulated values of $\langle N_{\mu} \rangle$ as a function of the primary energy for different interaction models in the absence of LV ($\kappa = 0$) and for $\kappa > 0$. All values are normalized to the value of $\langle N_{\mu} \rangle$ for unmodified protons of the model at the corresponding energy, to show the relative effect of LV on the muon number. 126
- B.5 The simulated values of $\sigma(N_{\mu})$ as a function of the primary energy for different interaction models in the absence of LV ($\kappa = 0$) and for $\kappa > 0$. All values are normalized to the value of $\langle N_{\mu} \rangle$ for unmodified protons of the model at the corresponding energy, to show the relative effect of LV on the muon number. 126
- B.6 The simulated values of $\sigma(N_{\mu})$ as a function of the primary energy for different primary particles in the absence of LV ($\kappa = 0$) and for $\kappa = -6 \times 10^{-21}$. All values are normalized to the value of $\sigma(N_{\mu})$ for unmodified protons at the corresponding energy, to show the relative effect of LV on the muon number. Depicted is also the result of a partial modification of the CONEX code, incorporating only photon decay and no modification of the pion decay time. 127
- B.7 The simulated values of $\langle X_{\max} \rangle$ as a function of the primary energy for primary protons and iron nuclei for the absence of LV ($\kappa = 0$) and for $\kappa = -6 \times 10^{-21}$. Depicted is also the result of a partial modification of the CONEX code, incorporating only photon decay and no modification of the pion decay time. 128
- B.8 The simulated values of $\sigma(X_{\max})$ as a function of the primary energy for primary protons and iron nuclei for the absence of LV ($\kappa = 0$) and for $\kappa = -6 \times 10^{-21}$. Depicted is also the result of a partial modification of the CONEX code, incorporating only photon decay and no modification of the pion decay time. 129

- B.9 Comparison of the $\langle X_{\max} \rangle$ - $\sigma(X_{\max})$ -combinations derived by simulations which incorporate LV to the 2D confidence intervals given by the measurements of the Pierre Auger Observatory [Yus19] for $\kappa = -6 \times 10^{-21}$ and different primary particle energies between $10^{17.2}$ eV and $10^{18.0}$ eV. 130
- B.10 Comparison of the $\langle X_{\max} \rangle$ - $\sigma(X_{\max})$ -combinations derived by simulations which incorporate LV to the 2D confidence intervals given by the measurements of the Pierre Auger Observatory [Yus19] for $\kappa = -6 \times 10^{-21}$ and different primary particle energies between $10^{18.0}$ eV and $10^{18.8}$ eV. 131
- B.11 Comparison of the $\langle X_{\max} \rangle$ - $\sigma(X_{\max})$ -combinations derived by simulations which incorporate LV to the 2D confidence intervals given by the measurements of the Pierre Auger Observatory [Yus19] for $\kappa = -6 \times 10^{-21}$ and different primary particle energies between $10^{18.8}$ eV and $10^{19.6}$ eV. 132
- B.12 Comparison of the $\langle X_{\max} \rangle$ - $\sigma(X_{\max})$ -combinations derived by simulations which incorporate LV to the 2D confidence intervals given by the measurements of the Pierre Auger Observatory [Yus19] for $\kappa = 3 \times 10^{-20}$ and different primary particle energies between $10^{17.2}$ eV and $10^{18.0}$ eV. 133
- B.13 Comparison of the $\langle X_{\max} \rangle$ - $\sigma(X_{\max})$ -combinations derived by simulations which incorporate LV to the 2D confidence intervals given by the measurements of the Pierre Auger Observatory [Yus19] for $\kappa = 3 \times 10^{-20}$ and different primary particle energies between $10^{18.0}$ eV and $10^{18.8}$ eV. 134
- B.14 Comparison of the $\langle X_{\max} \rangle$ - $\sigma(X_{\max})$ -combinations derived by simulations which incorporate LV to the 2D confidence intervals given by the measurements of the Pierre Auger Observatory [Yus19] for $\kappa = 3 \times 10^{-20}$ and different primary particle energies between $10^{18.8}$ eV and $10^{19.6}$ eV. 135

List of Tables

| | | |
|-----|--|-----|
| 5.1 | Auger X_{\max} moments published in [Yus19]. | 62 |
| 6.1 | Number of points in the contour around the $\langle X_{\max} \rangle - \sigma(X_{\max})$ values allowed by all compositions simulated using CONEX with the hadronic interaction model SIBYLL 2.3d inside the Auger confidence region determined from recent X_{\max} moments published in [Yus19]. Selected values of $\kappa < 0$ are shown with decreasing strength of LV from left to right. For each value of κ , the comparison is done separately for each energy bin of the measurements from the Pierre Auger Observatory. Entries where the Auger confidence region is entirely inside the region covered by simulated showers are marked with an X. The two highest energy bins are excluded from the analysis due to low statistics, but listed here for completeness. | 77 |
| 6.2 | Number of points in the contour around the $\langle X_{\max} \rangle - \sigma(X_{\max})$ values allowed by all compositions simulated using CONEX with the hadronic interaction model SIBYLL 2.3d inside the Auger confidence region determined from recent X_{\max} moments published in [Yus19]. Selected values of $\kappa > 0$ are shown with decreasing strength of LV from left to right. For each value of κ , the comparison is done separately for each energy bin of the measurements from the Pierre Auger Observatory. Entries where the Auger confidence region is entirely inside the region covered by simulated showers are marked with an X. The two highest energy bins are excluded from the analysis due to low statistics, but listed here for completeness. | 99 |
| C.1 | Number of points in the contour around the $\langle X_{\max} \rangle / \sigma(X_{\max})$ values allowed by all compositions simulated using CONEX with the hadronic interaction model SIBYLL 2.3d inside the Auger confidence region determined from X_{\max} moments published in [Aab+14a]. Selected values of κ are shown with decreasing strength of LV from left to right. For each value of κ , the comparison is done separately for each energy bin of the measurements from the Pierre Auger Observatory. Entries where the Auger confidence region is entirely inside the region covered by simulated showers are marked with an X. The two highest energy bins are excluded from the analysis due to low statistics, but listed here for completeness. | 137 |

Danksagung

An dieser Stelle möchte ich mich bei den Menschen bedanken, die mich bei meinem Studium und meiner Promotion begleitet haben und ohne die diese Arbeit kaum möglich gewesen wäre.

Als erstes möchte ich mich bei Prof. Dr. Markus Risse dafür bedanken, dass er mir die Möglichkeit gegeben hat, unter seiner Betreuung zu promovieren. Die zahlreichen hilfreichen Ratschläge und Diskussionen werden mir immer als bereichernder und konstruktiver Austausch in Erinnerung bleiben. Ich habe unsere Unterhaltungen stets als hilfreich und motivierend empfunden.

Außerdem möchte ich Prof. Dr. Markus Cristinziani dafür danken, dass er sich dazu bereit erklärt hat, die Rolle des Zweitgutachters zu übernehmen, sowie Prof. Dr. Otfried Gühne und Prof. Dr. Wolfgang Kilian für ihre Bereitschaft, an meiner Promotionskommission mitzuwirken.

Des weiteren danke ich Dr. Marcus Niechciol für die vielen Anregungen und Verbesserungsvorschläge, sowie das geduldige Beantworten meiner Fragen.

Bei Dr. Tanguy Pierog bedanke ich mich für seine Bereitschaft, bei der Modifikation des CONEX-Codes zu helfen.

Bei der gesamten Arbeitsgruppe für experimentelle Teilchen- und Astroteilchenphysik an der Universität Siegen möchte ich mich für das jederzeit angenehme und freundliche Arbeitsklima bedanken. Insbesondere möchte ich Dr. Wolfgang Walkowiak danken, der mir bei meiner Einarbeitung als Co-Administrator des lokalen Clusters "SiMPLE" viel Geduld und Vertrauen entgegengebracht hat.

Ich möchte mich ebenso bei meinen Mit-Doktoranden in der Arbeitsgruppe bedanken, ohne die meine Zeit an der Universität bestimmt weniger spannend gewesen wäre. Philip und Chiara, die mir bei der Einarbeitung meiner Promotion und mit Korrekturlesen geholfen haben, gebührt hier mein besonderer Dank.

Der größte Dank gilt jedoch meiner Familie. Zunächst meinen Eltern, die mir diesen Bildungsweg ermöglicht haben und mich jederzeit unterstützt haben. Außerdem meiner Frau Larissa, die mich seit meinem Masterstudium begleitet und mir in jeder Situation den nötigen Rückhalt gegeben hat, sowie meinem Sohn Lars, der stets eine zusätzliche Motivation war.